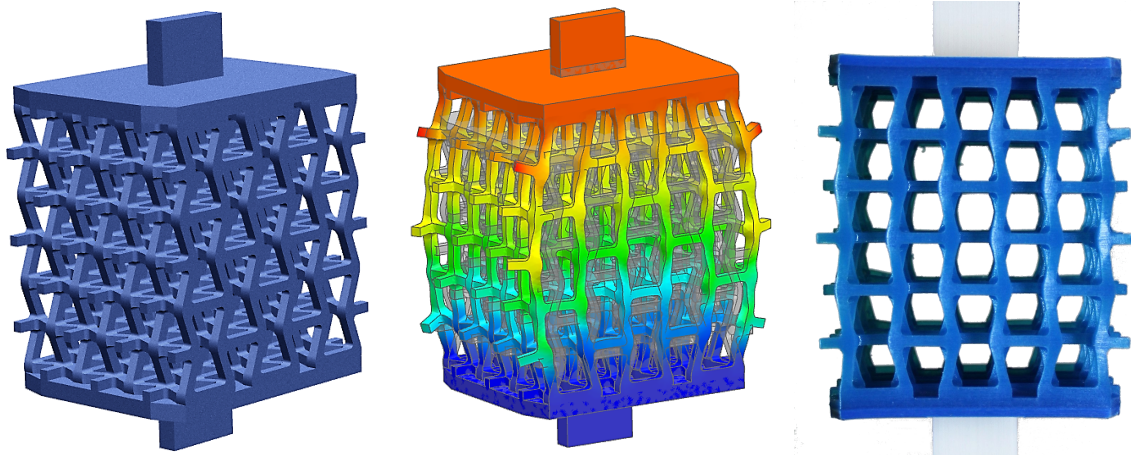


Computational Vademecums for Lattice Materials using algebraic PGD



by

Alberto Pedro Sibileau

Thesis submitted for the Doctor of Philosophy degree in
Computational Mechanics and Advanced Materials

to

Dipartimento di Ingegneria Civile ed Architettura
Università degli Studi di Pavia

and

Departament d'Enginyeria Civil i Ambiental
Universitat Politècnica de Catalunya

Advisors: Prof. Pedro Díez

Prof. Ferdinando Auricchio

Co-Advisors: Dr. Alberto García González Dr. Simone Morganti

Pavia & Barcelona, June 2019

“ Ever tried, ever failed. No matter, try again. Fail again. Fail better. ”
Samuel Beckett (1906, Dublin - 1989, Paris).

ABSTRACT

Computational Vademecums for Lattice Materials using algebraic PGD

Alberto Pedro Sibileau

This thesis is motivated by the *materials by design* concept. Focusing on structures, this states that the properties in a mechanical component are not only inherited by its constituent material, but also by the shape in which this one is distributed in space. This absolutely adds a new degree of freedom to the process of conceiving new material properties. Although this notion has been developed for thousand of years in architecture, at a bigger scale, its relevance has not been conceived until the arrival of additive manufacturing technologies.

The *materials by design* approach is certainly multidisciplinary, from the study of the shape, its representation in CAD, to the final manufacturing by 3D printing. We here focus on the first one, by means of numerical simulations. These play an important role, reinforcing our physical intuition in addressing the following problem: which is the material structure at a small scale or meso-structure, that features some prescribed properties at a global scale or material bulk.

We introduce the material meso-structure as a lattice model with a parametric shape. The mechanical properties arising at the global scale are recovered by solving an equilibrium problem. Naturally, this one acquires the parametric nature of the lattice model. The main difficulty to handle the emerging mechanical properties of the bulk parametrically, is that the computational complexity of numerical simulations increases exponentially with the number of parameters.

To overcome this, we resort to the Proper Generalized Decomposition (PGD), which provides explicit parametric solutions of our equilibrium problem. As a major contribution, we obtain the parametric solutions of the algebraic equations arising from different lattice structures using the same PGD framework. In this sense, the algebraic PGD works as a non-intrusive solver, which is not limited to structural problems but in general, any discrete form of a parametrized linear PDE. The intrusive part, however, remains in the construction of the algebraic equations, by taking care of its parametric dependence in a separated manner. For our structural problems, we undertake this part following a systematic methodology, based on familiar

procedures for finite element programmers.

The parametric mechanical properties of 2D and 3D lattice materials are explicitly represented by the PGD solutions or computational *vademecums*. In particular, we reproduce the response of orthotropic Poisson's ratios in terms of the design parameters. Extreme negative values are identified, a feature that is relevant regarding the outperforming of some *auxetic* (or negative Poisson's ratios) properties compared to conventional materials. Moreover, these computational *vademecums* could be further exploited to tailor the material design through multi-objective and constraint optimizations, providing an efficient tool to browse the parametric design space.

Finally, we extend our parametric analysis using geometrically nonlinear finite elements to compute equilibrium, and the algebraic PGD a posteriori to interpolate their response. This is achieved with very good accuracy, for engineering purposes, at a considerably low number of modes. The nonlinear parametric framework surely broadens the range of applications, and we highlight this in two distinctive situations. First, we demonstrate its capability to describe the loading magnitude as an extra parameter to the material properties behavior. Last but not least, we show its potential to perform buckling analysis of lattice structures, as a function of the geometric parameters and the loading magnitude itself.

ACKNOWLEDGMENTS

“ ¡Gracias... totales! ”

Gustavo Cerati (1959-2014, Buenos Aires).

I begin by declaring my genuine recognition to Prof. Pedro Díez and Prof. Ferdinando Auricchio, who gave me the opportunity to work under their supervision. Moreover, it has been priceless to count on Dr. Alberto García González and Dr. Simone Morganti mentorship. I have really appreciated all their encouragement and generous advices.

This work would not have been possible without the financial support of the European Education, Audiovisual and Culture Executive Agency (EACEA) under the programme: “Simulation in Engineering and Entrepreneurship Development” (SEED). I would like to state my truly acknowledgment for the promotion of European higher education to non-Europeans.

This joint research has been done through the cooperation between Università degli Studi di Pavia and Universitat Politècnica de Catalunya. During these three years, I have shared my work with many colleagues and people I really enjoyed to have met, Alessandro, Michele, Sergio, Guillermo, Sonia, Lelia, Massimo, Margherita, Rodrigo, Gianluca - who made the 3D printing possible - and all who I might ungenerously missed. Among the SEED community, I was fortunate to share the office and out of office hours together with Xi, Karim, Alex, Andrea, Hasini, Arash and Tuong. Likewise, my sincere thanks to Olga, David and the many hours devoted to climbing that kept me grounded.

I am also indebted to our compatriots in Barcelona, without naming the long list of Argentinians, Ludmila, Lucas, Costi y Sebas, for your kindest support and close friendship, and to our families, for their endless generosity and love. Last but not least, I express my deepest gratitude unto Pepi, for being my soul-mate along this learning experience, holding the true costs of this thesis and the confidence of its future returns.

Contents

Abstract	v
Acknowledgments	vii
Contents	ix
List of Figures	xi
List of Tables	xvii
1 Introduction	1
1.1 Bringing architecture to materials	1
1.2 Metamaterials	6
1.3 Computational tools for architected materials	12
1.4 Outline and objectives of this work	19
2 Parametric lattice structures	21
2.1 2D parametric structural problem	21
2.2 Affine decomposition of input data	26
3 An algebraic PGD solver for parametric systems of linear equations	33
3.1 Problem statement	33
3.2 Separable approximations	34
3.3 PGD algebraic solver	35
3.4 Proposed 2D problems for PGD solver	44
4 Numerical solutions in 2D lattices	45
4.1 Unit-cell problem using homogenization	46
4.2 Periodic pattern of hexagonal honeycomb cells	56
5 Application to 3D lattices and nonlinear problems	63
5.1 Problem statement: 3D parametric lattices	66
5.2 Affine decomposition of input data	73
5.3 3D parametric lattice structures solved with algebraic PGD	85

5.4	Nonlinear parametric formulations treated with PGD a posteriori . . .	105
6	PGD web app: displaying parametric solutions online	109
6.1	Program structure	110
6.2	A PGD interactive post-processing example	120
7	Conclusions	121
7.1	Contributions of the present thesis	121
7.2	Concluding remarks	122
7.3	Future works	123
	Bibliography	125
A	Algebraic PGD solver: Algorithm	135
B	PGD compression: Algorithm	137
C	Parametric honeycomb unit-cell analytical solution	139
D	Singular Value Decomposition (SVD)	145
D.1	Geometrical parameters constraint in the scaffold structure	145
D.2	Application	146
D.3	Results	148
E	Parametric functions for the scaffold unit-cell problem	151

List of Figures

1.1	“Hanging strings” naturally take a catenary shape, and Gaudí used mirrors below to visualize them downside-up as arches. Courtesy of KK Clark under license CC BY SA.	3
1.2	Bird wing’s bone cross section. Courtesy of OpenStax under license CC BY 4.0.	3
1.3	Architected materials are built as tessellations of small-scale structures into a bulk.	4
1.4	Mechanical influence of the material cell architecture in the macro-scaling between stiffness and density. Adapted with permission of Annual Reviews, from Schaedler and Carter (2016) via Copyright Clearance Center.	5
1.5	Sketch of refraction comparing a left-handed material (LHM) with a conventional one (CM). Supposing that refraction indexes $n_2 > n_1 > 0$, the incident beam enters with an angle θ_1 and refracts with an angle $\pm\theta_2$. Adapted from Wiki Commons.	6
1.6	Thermal cloaking experiment measured by infrared camera. Metamaterial is machined from a 2 mm copper plate (black) filled after with polydimethylsiloxane (white). Reproduced with permission from Schittny et al. (2013). Copyright (2013) by the American Physical Society.	7
1.7	Isotropic Poisson’s ratio and the so-called “Milton map”, as reported in Kadic et al. (2013).	10
1.8	Characterization of the Poisson’s ratio effect in materials under uniaxial stretch.	11
1.9	CAD of a smart fastening prototype featuring an helical auxetic pattern.	11
1.10	Poisson’s ratio effect in doubly curved shapes of thick plates under bending.	12
1.11	Structure of a sandwich panel.	12
1.12	Sketch of a periodic material response at the local scale, when homogeneous strain is imposed on the global scale.	14
1.13	Unit-cell dimensions of a perfect honeycomb, as reported by Sigmund (1994a).	14
1.14	Prescribed strains at the global scale used as unit-cell loading cases.	15
2.1	Diagram of external loads q , internal forces V and moments M in a differential element of Euler-Bernoulli beam.	22

2.2	Planar beam element of length L . Local degrees of freedom denoted at their tip points 1 and 2.	22
2.3	Parametrization of a periodic hexagonal honeycomb.	24
2.4	Data structure of $\mathbf{K}(\boldsymbol{\mu})$ affine decomposition in a Matlab [©] cell array variable “Ksep”. Honeycomb material sheet with spatial mesh size: $n_{\text{dof}} = 2880$ and $n_p = 4$ number of parameters.	32
4.1	PGD modal amplitudes β^m , $m = 1, 2, \dots, n$ (with or without PGD compression). Parametric unit-cell subjected to periodic loading cases.	47
4.2	Unit-cell load case XX with PGD compression. Normalized spatial modes 1 and 4 scaled for illustration.	47
4.3	Unit-cell load case YY with PGD compression. Normalized spatial modes 1 and 2 scaled for illustration.	48
4.4	Unit-cell load case XY with PGD compression. Normalized spatial modes 1 and 4 scaled for illustration.	48
4.5	Unit-cell load case XX with PGD compression. Normalized parametric functions weighted for illustration.	49
4.6	Unit-cell load case YY with PGD compression. Normalized parametric functions weighted for illustration.	50
4.7	Unit-cell load case XY with PGD compression. Normalized parametric functions weighted for illustration.	50
4.8	Honeycomb unit-cell configurations given by the sets of random values of the parameters.	51
4.9	Unit-cell load cases: relative error of PGD solution against FE computed at different sets of parameters values.	52
4.10	Relative error of $\mathbf{U}_{\text{PGD}}^n(\boldsymbol{\mu})$ in the unit-cell depending on the n number of PGD modes, measured in a global parametric norm.	53
4.11	ν_{12}^{eff} response in $a \times \alpha$ for specified values of b and t	55
4.12	ν_{21}^{eff} response in $a \times \alpha$ for specified values of b and t	55
4.13	Periodic 5×5 array of honeycomb cells subjected to tensile loads.	56
4.14	PGD modal amplitudes β^m , $m = 1, 2, \dots, n$ (with or without PGD compression). Honeycomb periodic structure subjected to uni-axial tensile loads.	57
4.15	Normalized spatial modes 1 and 2 scaled for illustration. PGD compressed solution of the periodic honeycomb structure under uni-axial loads.	58
4.16	Periodic honeycomb structure under X -direction tensile load with PGD compression. Normalized parametric functions weighted for illustration.	59
4.17	Periodic honeycomb structure under Y -direction tensile load with PGD compression. Normalized parametric functions weighted for illustration.	59
4.18	Measurement of ν_{12} in the honeycomb structure subjected to uniform load in X direction.	60

4.19	PGD modal evolution of relative error of Poisson's ratios computed in the full lattice material against the effective ones, measured in a global parametric norm.	61
5.1	Auxetic stent-like structures.	64
5.2	Buckling effect observed in a honeycomb sheet subjected to a tensile vertical load. Loaded strain is 9% for the 3D-printed sample and 10% for the FE simulation.	65
5.3	Local beam element system and nodal degrees of freedom.	66
5.4	Parametrization of a scaffold unit-cell.	68
5.5	Scaffold unit-cell geometry for characteristic values of parameters α and ϕ , and fixed values of parameters $a = 0.5$ and $b = 1$	69
5.6	Vector \mathbf{d} expressed in components $[d_{\hat{x}} d_{\hat{y}} d_{\hat{z}}]^T$ or $[d_x d_y d_z]^T$, either in the coordinate system $(\hat{x}, \hat{y}, \hat{z})$ or (x, y, z) respectively.	72
5.7	Stent unwrap and wrap configurations.	81
5.8	Orientation of the stent oblique elements.	82
5.9	Scaffold unit-cell characterization.	87
5.10	PGD modal amplitudes β^m , $m = 1, 2, \dots, n$ (with or without PGD compression). Parametric scaffold unit-cell model with homogenization.	87
5.11	Scaffold unit-cell under normal strain load cases. Normalized spatial modes with PGD compression scaled for illustration.	88
5.12	Scaffold unit-cell under shear strain load cases. Normalized spatial modes with PGD compression scaled for illustration.	89
5.13	ν_{12}^{eff} in $a \times \alpha$ for specified values of b and t . Response for a scaffold unit-cell with a fixed value of $\phi = 1$	93
5.14	ν_{21}^{eff} in $a \times \alpha$ for specified values of b and t . Response for a scaffold unit-cell with a fixed value of $\phi = 1$	93
5.15	ν_{13}^{eff} in $\phi \times \alpha$ for specified values of a and t . Response for a scaffold unit-cell with a fixed value of $b = 1$	94
5.16	ν_{31}^{eff} in $\alpha \times \phi$ for specified values of a and t . Response for a scaffold unit-cell with a fixed value of $b = 1$	94
5.17	ν_{23}^{eff} in $\alpha \times \phi$ for specified values of a and t . Response for a scaffold unit-cell with a fixed value of $b = 1$	95
5.18	ν_{32}^{eff} in $\alpha \times \phi$ for specified values of a and t . Response for a scaffold unit-cell with a fixed value of $b = 1$	95
5.19	Scaffold unit-cell under uni-axial traction loads: relative error of PGD solution against FE computed at different sets of parameters values (Table 5.4).	97
5.20	Relative error of Poisson's ratios PGD response in $\alpha \times \phi$ against FE, for a scaffold unit-cell with parameters values: $\{a = 0.3; b = 1; t = \frac{1}{50}\}$	98
5.21	Parametric lattice scaffold made by a $5 \times 5 \times 5$ unit-cells composition.	99
5.22	PGD modal amplitudes β^m , $m = 1, 2, \dots, n$ (with or without PGD compression). Parametric lattice scaffold subjected to uni-axial loads.	99

5.23	Periodic scaffold subjected to XX displacements (5% equivalent strain), comparing deformations using FE or PGD, for parameters $\{a = 0.3; b = 1; \alpha = 45^\circ; \phi = 0.75; t = \frac{1}{50}\}$	100
5.24	Periodic scaffold subjected to YY displacements (10% equivalent strain), comparing deformations using FE or PGD, for parameters $\{a = 0.3; b = 1; \alpha = 45^\circ; \phi = 0.75; t = \frac{1}{50}\}$	101
5.25	Stent-like structure under two different load cases.	102
5.26	PGD modal amplitudes (with or without PGD compression), stent-like structure under axial and radial loads.	102
5.27	$\nu_{\text{ax-rad}}$ in $a \times \alpha$ for specified values of b and t in the stent-like structure.	103
5.28	$\nu_{\text{rad-ax}}$ in $a \times \alpha$ for specified values of b and t in the stent-like structure.	104
5.29	Modal amplitudes of the PGD least square approximation for the stent-like structure solved using nonlinear finite elements, sampled at points of the parametric space $a \times \alpha$, and subjected to axial and radial loads.	106
5.30	$\nu_{\text{rad-ax}}$ in $a \times \alpha$ for the PGD nonlinear solution of a stent-like structure, given at different load magnitudes.	106
5.31	$\nu_{\text{ax-rad}}$ in $a \times \alpha$ for the PGD nonlinear solution of a stent-like structure, given at different load magnitudes.	107
5.32	Stent-like structure subjected to axial loads (8% equivalent strain), comparing deformed configurations obtained by PGD and LS-PGD of a nonlinear response affected by buckling. The set of parameters are: $\{a = 0.4; b = 1.2; \alpha = 50^\circ; t = \frac{2}{25}\}$	108
6.1	Main web-page graphical interface parts.	111
6.2	Different graphical interface windows for a PGD solution loaded into the working area.	112
6.3	A detailed look at the Control bar.	113
6.4	Interactive PGD solution of a parametric stent-like structure subjected to axial and radial load cases. The set of values of the parameters is indicated using the notation: $\boldsymbol{\mu} = [\mu_1; \mu_2; \mu_3; \mu_4] = [a; b; \alpha; t]$	120
C.1	Scaled $\mathbf{U}_R^{\text{xx}}(\boldsymbol{\mu})$ evaluated at $(a = 0.5, b = 1, \alpha = 60^\circ, t = \frac{1}{40})$.	140
C.2	Scaled $\mathbf{U}_R^{\text{yy}}(\boldsymbol{\mu})$ evaluated at $\boldsymbol{\mu}=[a = 0.5, b = 1, \alpha = 60^\circ, t = \frac{1}{40}]$.	141
C.3	Scaled $\mathbf{U}_R^{\text{xy}}(\boldsymbol{\mu})$ evaluated at $\boldsymbol{\mu}=[a = 0.5, b = 1, \alpha = 60^\circ, t = \frac{1}{40}]$.	142
D.1	Scaffold unit-cell parameterization ($\boldsymbol{\mu} = [a \ b \ \alpha \ \phi \ t]^\top$).	146
D.2	SVD factorization of \mathbf{A} into the product of three matrices. Adapted from Wiki Commons.	147
D.3	SVD evolution of modal amplitudes and parametric functions, these latter shown for $\ell = 1, \dots, \mathbf{n}_{\text{svd}} = 5$.	148
D.4	Plot of the function $f(\alpha, \phi)$ and relative error of an approximation with $\mathbf{n}_{\text{svd}} = 5$ SVD terms.	149

E.1	Scaffold unit-cell load case XX with PGD compression. Normalized parametric functions weighted for illustration.	152
E.2	Scaffold unit-cell load case YY with PGD compression. Normalized parametric functions weighted for illustration.	153
E.3	Scaffold unit-cell load case ZZ with PGD compression. Normalized parametric functions weighted for illustration.	154
E.4	Scaffold unit-cell load case XY with PGD compression. Normalized parametric functions weighted for illustration.	155
E.5	Scaffold unit-cell load case XZ with PGD compression. Normalized parametric functions weighted for illustration.	156
E.6	Scaffold unit-cell load case YZ with PGD compression. Normalized parametric functions weighted for illustration.	157

List of Tables

1.1	Designing materials architecture. Adapted with permission of Annual Reviews, from Schaedler and Carter (2016) via Copyright Clearance Center.	5
2.1	Parametric functions $O_{i,ob}^f$ in the hexagonal honeycomb cell.	28
2.2	Parametric functions L_i^g in the hexagonal honeycomb cell.	29
2.3	There is a total number $n_q = 6$ of multisets of length 2 on $n_T = 3$, representing the unique combinations of unordered pairs of summing indexes $\{g, h\}$, for $g, h = 1, \dots, n_T$	30
2.4	Global parametric functions $B_i^k(\mu_i)$ for the lattice structure.	31
4.1	Unit-cell sets of parameters where PGD error is evaluated against finite element solutions.	51
5.1	Parametric functions $O_{i,xz}^f(\mu_i)$ in the scaffold structure.	74
5.2	Functions $L_{i,xy}^g$ and $L_{i,xz}^g$ describing the separated parametric dependence of transformation matrices $\mathbf{T}_{e,xy}(\boldsymbol{\mu})$ and $\mathbf{T}_{e,xz}(\boldsymbol{\mu})$	76
5.3	Parametric functions $B_{i,xy}^d$ describing stiffness of the oblique elements “ $e \in xy$ ” in the scaffold, for $d = 1, \dots, n_{k_{xy}}$ and $i = 1, \dots, n_p$	78
5.4	Scaffold sets of parameters (a, α, ϕ) , where PGD against finite element error is computed (Figure 5.19). The remaining parameters are constant at $b = 1$ and $t = 0.11$	97

Chapter 1

Introduction

The present work develops an application of a PGD-based reduced order model in the parametric analysis of lattice materials. Within the computational mechanics framework, it features a contribution that supplements the standard finite element procedures with an efficient treatment of their parametric dimensions. From the architected materials point of view, it analyzes parametric structures capable of exhibiting auxetic or negative Poisson's ratio. In order to embrace this multidisciplinary character, we present in the following the background on which we base our analysis and the motivations we found to propose our thesis objectives.

In section 1.1 we first describe the research trend that is bringing architecture to materials, in a methodology that explores the materials meso-structure as a new design variable in the search of novel properties. The emergence of additive manufacturing has certainly consolidate this design approach by building more complex topologies. Section 1.2 highlights some of the achievements in terms of novel material properties that have coined the term metamaterials. In particular, we focus our attention in a type of mechanical metamaterials that show auxetic behavior.

The reader with expertise in metamaterials might skip sections 1.1 and 1.2 directly to 1.3, where computational tools for materials design are presented. We introduce homogenization theory, supporting the computation of effective properties (the materials *forward* problem), and the optimization approach to the materials *inverse* problem. Due to the multiple queries required to attempt a numerical solution to the latter, we identify the potential of applying a PGD-based reduced order model to approach the parametric response of auxetic materials efficiently, through computational vademecums.

Finally, the thesis objectives and chapter organization is discussed in section 1.4.

1.1 Bringing architecture to materials

Material science is a very wide field of studies and research, where many sciences converge. From the process where materials are conceived until they are actually

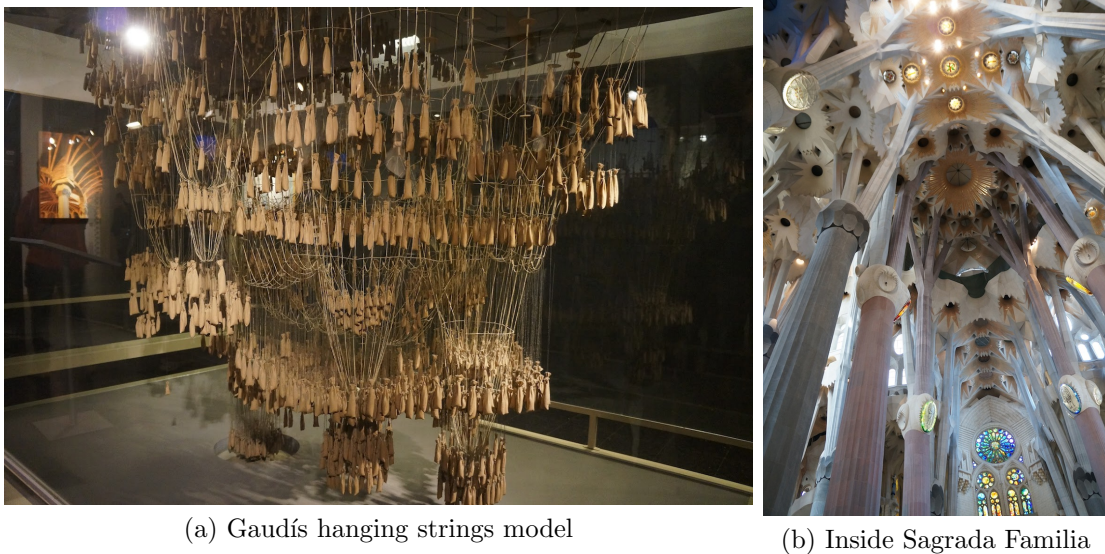
manufactured, chemical processes occur, like change of phases, heat transfers and mechanical plastic deformations take place. In addition, engineering practices require different type of materials with diverse behavior. Naturally, this complexity can not be approached in only one expertise and therefore different material science branches like metallurgy, polymers, ceramics, composites and many others have evolved in time. Even if the differences between these fields are broad, their material design process shares a common goal, which is the modification of the material constituent from a chemical point of view. As noted by [Reis et al. \(2015\)](#), this is the reason why traditionally, the material design effort has been focused on the micro-scale - or equivalently, the size of the material constituent building blocks.

On the other hand, material scientists and engineers have recently shifted their attention to a new material design trend, where the focus is placed on the structure role at a mesoscopic scale. This term is defined by [Reis et al. \(2015\)](#) as an intermediate scale between the material continuum at the macro-scale and the micro-scale. The novelty here is that the material properties at the macro-scale, those of practical interest for engineering applications, are function of a new variable, their meso-structure, in addition to the constituent chemistry at micro-scale.

Along history, architecture and structural engineering have developed a deep knowledge about how a solid body of a certain material responds differently to the same load, depending on how this material is distributed in space. In fact, the relation between geometry and mechanical performance is appreciated in the evolution of structures. In monuments, for example, a clearly contrast is observed from the pyramids of Egypt to the Eiffel Tower. [Schaedler and Carter \(2016\)](#) provide another example in a mechanical component like wheels, stating that from the ones made of solid stone to those in modern bicycles, at least 95% of the material in the original design has been just replaced by air.

The evolution of these structures has been driven by the same question: how could the same fraction of material be placed in space such that it maximizes the relation between load-bearing capability and self weight. It is worth mentioning here a historic note about the Catalan architect Antoni Gaudí (1852-1926), who approached this issue in his architecture designs using creative experiments. One of these models is shown in [Figure 1.1](#), and allowed the architect to extend a well known idea by his time - that catenary arches posses an optimal structural performance - to more complex designs involving superimposed arches. Even more impressive is to consider the ability of these “hanging chains” to perform what we know today as *parametric design*, in the sense that the optimal structural configuration was *automatically updated* while the hanging strings length or their anchor positions were modified ([Gómez-Moriana \(2012\)](#)).

There is a recent research tendency that is bringing architecture to materials. This means that principles that has been long used, for example to increase mechanical efficiency of structures, are being now applied at the material scale. Indeed, solid materials that are found in nature are closely connected with this approach. Evolution has sorted out that a higher ratio of stiffness or strength to density could be achieved



(a) Gaudí's hanging strings model

(b) Inside Sagrada Família

Figure 1.1: “Hanging strings” naturally take a catenary shape, and Gaudí used mirrors below to visualize them downside-up as arches. Courtesy of [KK Clark](#) under license [CC BY SA](#).

if voids are properly added to the solid. Figure 1.2 shows an extreme example of this, in a longitudinal cut of a bird's bone. As described by [Schaedler and Carter \(2016\)](#), this whole piece is made of a thin solid skin internally connected by a highly porous core.



Figure 1.2: Bird wing's bone cross section. Courtesy of [OpenStax](#) under license [CC BY 4.0](#).

The internal structure of bones evoke the idea of randomly distributed voids, and some manufactured materials like foams have reproduced this kind of meso-structure. On the other hand, the same concept of adding voids inside a solid can be retained, but replacing the random distribution by an ordered repetition of a so-called “unit-cell”. The unit-cell is tessellated in space into a bulk, which in turn becomes the material at the macro-scale. This concept is illustrated in Figure 1.3 and becomes the shared bond in a broad family of materials denominated as *Architected materials*. Often, the unit-cell topology is defined by a grid of points that are linked together

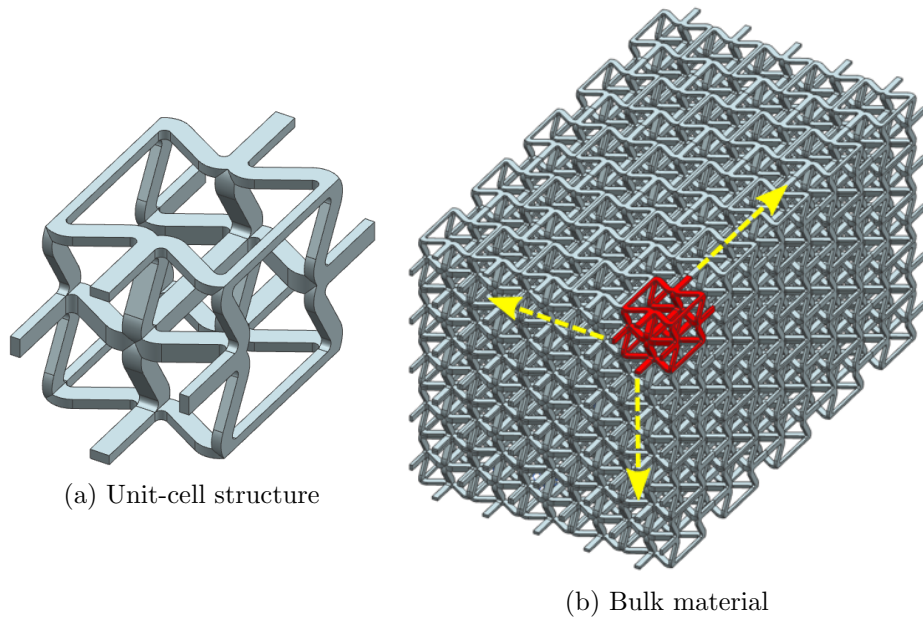


Figure 1.3: Architectured materials are built as tessellations of small-scale structures into a bulk.

by straight elements conforming a truss. These type of architected materials are also referred to as *Lattice materials*.

In this framework, material properties at the bulk can be modified by changing the unit-cell architecture. This introduces a new degree of freedom to materials design, allowing additional routes in the search of desirable properties. According to their meso-structure and design variables, [Schaedler and Carter \(2016\)](#) suggested a categorization of materials as shown in [Table 1.1](#).

In the following, it is explained with an example, how unit-cells architecture influences the materials mechanical properties. Materials with a random meso-structure like foams, hold cells whose deformation is dominated by bending. The reason behind this is their open meso-structure, in the sense that cells are interconnected without a triangulated pattern, see [Figure 1.4b](#). In contrast, the deformation of closed unit-cells in lattice materials, such as the *octet truss* shown in [Figure 1.4b](#), is governed by stretching. The distinction between these types of meso-structure is a key concept when designing lightweight materials without compromising stiffness. As seen in [Figure 1.4a](#), the drop of stiffness at the macro-scale is higher in a foam compared to an octet truss, for the same reduction in density. Further studies in architected materials have been covered by [Gibson and Ashby \(1999\)](#); [Guest \(2000\)](#); [Deshpande et al. \(2001a,b\)](#), analyzing how different mechanical properties are scaled with density at the bulk.


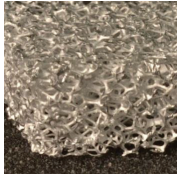
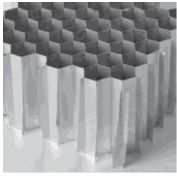
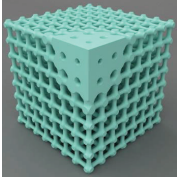
				
Meso-structure	None	Random	Ordered	Ordered and location specific
Properties	Continuous and homogeneous	Homogeneous at scales > cell	Homogeneous and highly anisotropic	Inhomogeneous and highly anisotropic
Design variables	Solid constituent	Solid constituent, cell size	Solid constituent, cell size, shape and orientation	Cell size, shape, topology, material

Table 1.1: Designing materials architecture. Adapted with permission of Annual Reviews, from [Schaedler and Carter \(2016\)](#) via Copyright Clearance Center.

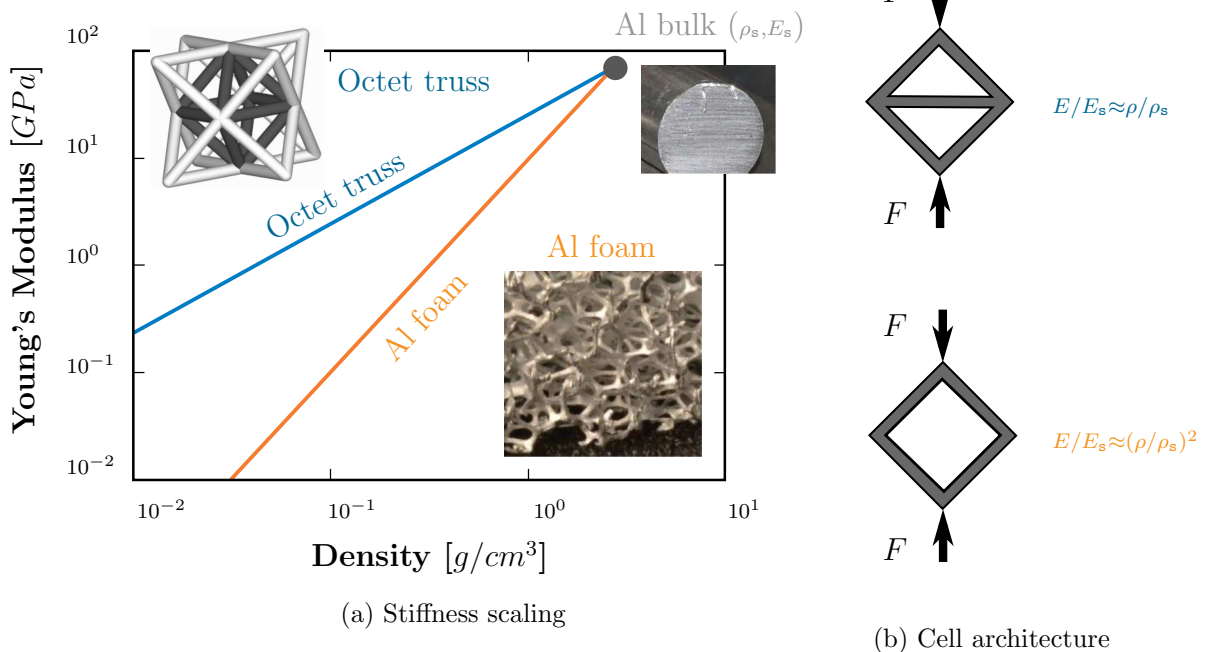


Figure 1.4: Mechanical influence of the material cell architecture in the macro-scaling between stiffness and density. Adapted with permission of Annual Reviews, from [Schaedler and Carter \(2016\)](#) via Copyright Clearance Center.

1.2 Metamaterials

Scientific and technical communities trend toward obtaining specific material properties at the macro-scale through the design of tailored unit-cells. The initial goal was improving the materials performance, but it has already reached the point where researchers seek beyond what nature seems to offer us. This explains the actual popularity in the material scientific community of the word “*meta*”, meaning beyond or after in Greek.

Although metamaterials are introduced in this section separately, we will refer to them generically as members of the broad family of architected materials. In this work, we will focus on the mechanical response of metamaterials. However, about two decades ago, the first metamaterial that attracted a lot of attention was the photonic crystal, as presented by [Sievenpiper et al. \(1996\)](#), in relation to electromagnetic material properties. For this historical reason, we will briefly present a categorization of metamaterials in the following order, regarding first to electromagnetic, then thermal and finally mechanical material properties.

1.2.1 Electromagnetic metamaterials

In this case, the manufactured unit-cell characteristic length is comparable with the propagating electromagnetic wavelength, such that it can alter its scattering. Some astonishing metamaterials have been discovered and manufactured in this field of research, in the sense that their material properties are not found in nature. One example of this are the materials with negative index of refraction, that change the intuitive idea we have about electromagnetic phenomena occurring at the interface between two phases. Figure 1.5 illustrates Snell’s law and the effect of negative index of refraction or *left-handed* materials. An experimental setup that measures this phenomenon is presented by [Shelby et al. \(2001\)](#).

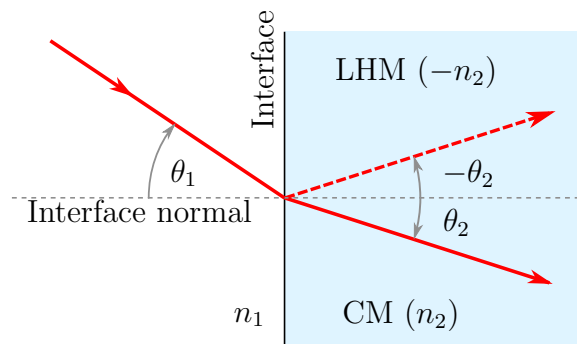


Figure 1.5: Sketch of refraction comparing a left-handed material (LHM) with a conventional one (CM). Supposing that refraction indexes $n_2 > n_1 > 0$, the incident beam enters with an angle θ_1 and refracts with an angle $\pm\theta_2$. Adapted from Wiki Commons.

Another fascinating topic that have raised interest in the physics community, also related to electromagnetic metamaterial properties, is the invisibility cloak. This term is referred to the idea in which the light could be redirected to avoid an object and flow around it like a fluid, to return undisturbed to its original trajectory. From a mathematical point of view, invisibility is ideally impossible, as derived by [Nachman \(1988\)](#), from the uniqueness of the inverse-scattering wave problem. As explained by [Leonhardt \(2006\)](#), due to the wave nature of light, only its propagation through empty space is consistent with the scattering data of light in an empty space. However, within the limits of geometrical optics, that is for objects that are much larger than the light wavelength, [Pendry et al. \(2006\)](#) and [Leonhardt \(2006\)](#) described a theoretical framework where a metamaterial could guide the light rays around an object, such that they return to their original trajectory. This would create a *cloaking device*, that is providing the covered object with an invisible appearance. Despite being an appealing idea, manufacturing an invisibility cloak still presents a technological challenge in three dimensions, as reported by [Soukoulis and Wegener \(2011\)](#). For example, when many unit-cells of these photonic metamaterials are put together into a 3D bulk, the light absorption (losses) is so high that actually turns these objects into useless opaque materials.

1.2.2 Thermal Metamaterials

The theoretical framework supporting the invisibility cloak, applied in Maxwell's equations by [Pendry et al. \(2006\)](#) and [Leonhardt \(2006\)](#), was enforced into Fourier's heat equation by [Guenneau et al. \(2012\)](#), adopting the term thermal cloaking. This study proofs that the time-dependent heat equation behaves in a form-invariant way under a curvilinear coordinate transformation. In practice, this transformation can be used to map a fictitious curved domain onto a metamaterial. In fact, the result can be interpreted as a highly anisotropic and spatially inhomogeneous thermal conductivity, such that the cloaking effect works.

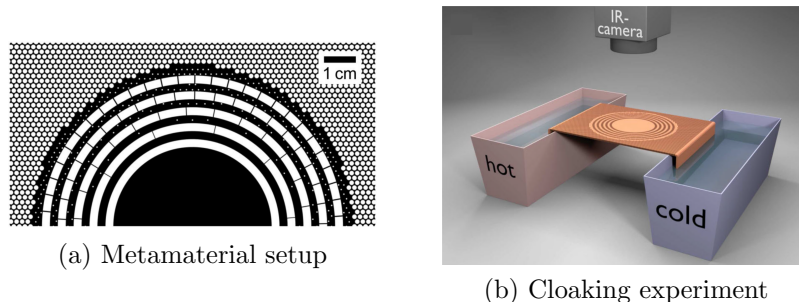


Figure 1.6: Thermal cloaking experiment measured by infrared camera. Metamaterial is machined from a 2 mm copper plate (black) filled after with polydimethylsiloxane (white). Reproduced with permission from [Schittny et al. \(2013\)](#). Copyright (2013) by the American Physical Society.

Unlike thermal insulators, a thermal cloaking device not only isolates an object from its surrounding but also does not perturb the heat flow. This comparison is provided by [Schittny et al. \(2013\)](#), who constructed the metamaterial and the experimental setup shown in [Figure 1.6](#), to support evidences of a material performing thermal cloaking.

In general, thermal cloaking inspires the idea that heat flow can be tailored by means of metamaterials. For example, in the works by [Narayana and Sato \(2012\)](#) and [Guenneau and Amra \(2013\)](#), a design is proposed such that the heat fluxes are rotated like a vortex. Therefore, in an experiment that prescribes hot and cold temperatures as depicted in [Figure 1.6b](#), a local heat flux in the center of the vortex is obtained opposite to the global heat flowing from the hot to the cold. From the material properties point of view, this effect is surprisingly explained as a local apparent negative heat conductivity.

1.2.3 Mechanical Metamaterials

Following the previous discussion about metamaterials, the new question we can raise is: could we design anisotropic materials such that we can control the propagation of waves in an elastic media? The straightforward answer from a mathematical point of view is not very optimistic, since it has been proved by [Milton et al. \(2006\)](#) that the elastodynamics equation is not form-invariant under an arbitrary curvilinear coordinate transformation. The reason behind it is given by the constitutive relation, which has both non-zero bulk and shear modulus in an homogeneous isotropic elastic solid. Thus, mechanical waves in an homogenous solid not only propagate longitudinally (pressure waves, like sound propagates in air or water) but also transversely (shear waves).

A simple explanation is provided by [Kadic et al. \(2013\)](#) that clarifies why the general cloaking idea in elastodynamics does not work. Suppose that a pressure wave is traveling in an homogeneous isotropic body, in absence of obstacles and damping effects, this will stay forever as a longitudinal wave. In contrast, whenever this pressure wave gets into an inhomogeneous and anisotropic solid, namely the metamaterial designed for mechanical cloaking, the emerging waves will no longer be only longitudinal but also shear waves will arise. The impossibility of recovering the incident wave without perturbations inhibit the design of mechanical cloaking.

Despite this, there are feasible solutions to overcome the general impossibility of forging the path where waves propagate in solids, and mechanical metamaterials are a topic that attracts intense research efforts, as it has been addressed by [Kadic et al. \(2013\)](#) and [Christensen et al. \(2015\)](#). One possibility that has been explored is to reduce the generic 3D elastodynamics problem to particular geometries, for example thin elastic plates described by Mindlin-Reissner theory ([Reissner \(1945\)](#) and [Mindlin \(1951\)](#)). Under the thin plate assumption, and supposing the loads have a much bigger wavelength than the plate thickness, [Kadic et al. \(2013\)](#) characterize this as a flexural or bending wave problem, meaning that only displacements with

a normal component to the plate propagate. Farhat et al. (2009) demonstrate that the elastodynamics equations for bending waves propagating along an infinitely large homogeneous plate is form-invariant upon a curvilinear coordinates transformation. In practice, this transformation or mapping can be shaped into an heterogeneous orthotropic metamaterial, namely the elastic cloak, which is appealing from the engineering point of view at least for two reasons. First, Stenger et al. (2012) suggest that manufacturing metamaterials with elastic cloaking is fairly inexpensive. Secondly, Brûlé et al. (2013) point out that elastic cloaking could be exploited in civil engineering for the infrastructure protection against earthquakes. In particular, the behavior of one type of seismic loads known as Rayleigh waves can be modeled under the assumptions of flexural waves. Thus, the idea of scaling up an elastic cloak holds in principle, providing that a design with the required heterogeneous anisotropy could be achieved in the soil.

1.2.3.1 Auxetic (and anti-auxetic) metamaterials

Given that this work is focused in the study of *auxetic* metamaterials, we present in the following a separated subsection discussing about their characteristics and why are they considered relevant in the mechanical metamaterials research community. On the other hand, anti-auxetic materials are out of the scope of this study. However, we briefly introduce them since they are relevant to the elastic cloaking problem previously described.

Auxetic and anti-auxetic metamaterials are located at two opposite extremes in the ratio between bulk - B - and shear modulus - G - in isotropic solids, as categorized by Milton (2002) in a map, depicted in Figure 1.7b. In isotropic media, the bulk and shear modulus are related by the Poisson's ratio ν following

$$\frac{B}{G} = \frac{2(1 + \nu)}{3(1 - 2\nu)},$$

whose plot is shown in Figure 1.7a. The values of the isotropic Poisson's ratio are restricted to the interval $-1 < \nu < 0.5$, such that the elastic energy is positive under all possible deformations. Most common isotropic solids have Poisson's ratio around $\nu \approx 0.3$, meaning that B and G are of the same order (see Figure 1.7a).

On one hand, the relation B/G becomes very high when $\nu \rightarrow 0.5$, which is the case for fluids, rubber, and also for anti-auxetic materials, which are often referred to as *pentamode* metamaterials. Originally proposed by Milton and Cherkaev (1995), pentamodes are a type of isotropic lattice metamaterials that have been successfully constructed, for example by Kadic et al. (2012) and Amendola et al. (2016), using additive manufacturing. Their architecture is thought such that from the six independent ways that an elastic solid can be deformed, five - or *penta* in Greek - can be ideally performed with zero force (resisting only hydrostatic pressure). In practice, Kadic et al. (2012) report experimental tests showing ratios between modulus $B/G > 1000$, two orders of magnitude above the highest $B/G \approx 13$ found in gold.

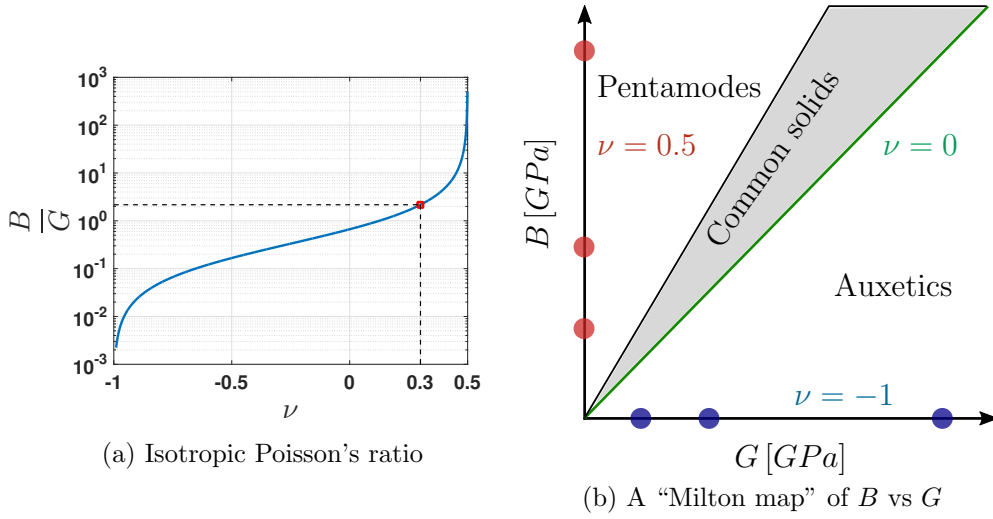


Figure 1.7: Isotropic Poisson's ratio and the so-called "Milton map", as reported in [Kadic et al. \(2013\)](#).

A stable solid exhibiting a very high $B/G \gg 1$ ratio allows only the propagation of pressure waves, and elastodynamics could be simplified as a scalar problem. Thus, as reported by [Bückmann et al. \(2014\)](#), pentamode metamaterials have opened the path to design a 3D elastic cloak.

On the opposite limit, the relation $B/G \ll 1$ is very small when $\nu \rightarrow -1$. In general, materials with negative-Poisson's-ratio $\nu < 0$ are called *auxetics*, and lie on the horizontal axis of Figure 1.7b in the ideal case. According to [Grima et al. \(2015\)](#), the term was taken from the Greek *auxetos* - meaning: "that may be increased" - and proposed by [Evans et al. \(1991\)](#) to avoid the long phrase "negative-Poisson's-ratio materials". We are accustomed to the fact that, when materials are stretched, they become thinner in the transverse directions to loading, as depicted in Figure 1.8b. However, *auxetics* get thicker when stretched, being this characteristic the one that gave rise to its denomination (see Figure 1.8c).

The French mathematician Siméon Denis Poisson (1787-1840) was the first one to introduce in [Poisson \(1811\)](#), an analysis of the shape and volume changes of a fluid under an arbitrary loading. The interested reader in this historical note is referred to [Greaves et al. \(2011\)](#). Today, the Poisson's ratio - ν - is a fundamental characteristic of an isotropic material, its effect is depicted in Figure 1.8, and formally is defined as the negative of a transverse strain divided by the applied uniaxial strain. Although the auxetic behavior $\nu < 0$ is found in nature, for example [Gatt et al. \(2015\)](#) encountered it in the human Achilles tendon, it is also a subject of dedicated research since the early works of [Evans and Alderson \(2000\)](#) featuring auxetic properties outperforming conventional materials. In the following, we describe two of them, being simple yet functional.

Figure 1.9 shows a prototype that highlights an auxetic property that could be

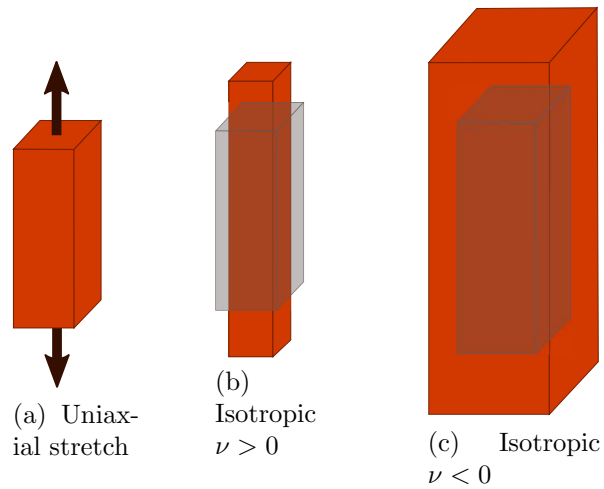


Figure 1.8: Characterization of the Poisson's ratio effect in materials under uniaxial stretch.

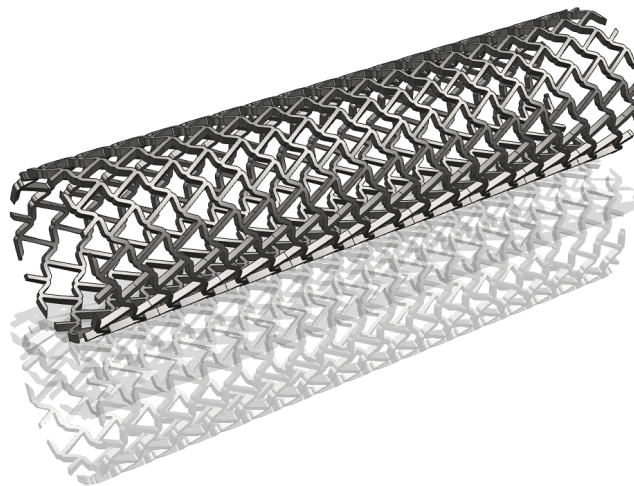


Figure 1.9: CAD of a smart fastening prototype featuring an helical auxetic pattern.

used in fasteners: the lateral contraction produced by compression eases the insertion into a hole, while pulling out the fastener actually enhances its grip, since stretching provokes lateral expansion. In addition, the helical pattern would help extraction if torque is applied.

Auxetic materials naturally form dome shapes, effect that is known as *synclastic* curvatures, while ordinary materials tend to conform themselves into saddle shapes or *anticlastic* curvatures. As depicted in Figure 1.10, if a thick plate is subjected to bending, the orthogonal curvature to bending direction depends on the Poisson's ratio.

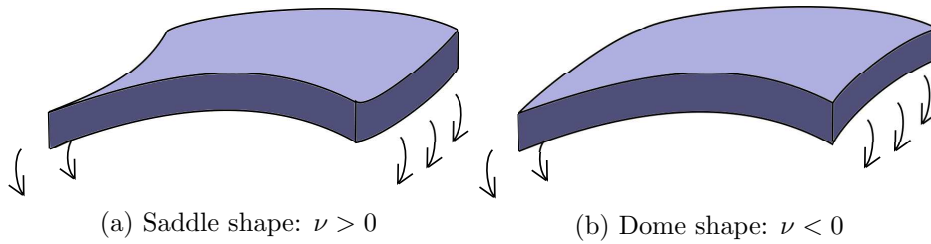


Figure 1.10: Poisson's ratio effect in doubly curved shapes of thick plates under bending.

Sandwich panels are very much used in aerospace industry because of their high bending stiffness to density ratio. As shown in Figure 1.11, these are formed by two face thin sheets and a thick hexagonal honeycomb core. For structures like the airplane nose, manufacturing sandwich panels could be improved by placing an auxetic honeycomb in the core (as originally proposed by Evans (1991)), instead of the most common hexagonal honeycomb fabricated by Hexcel (1999).

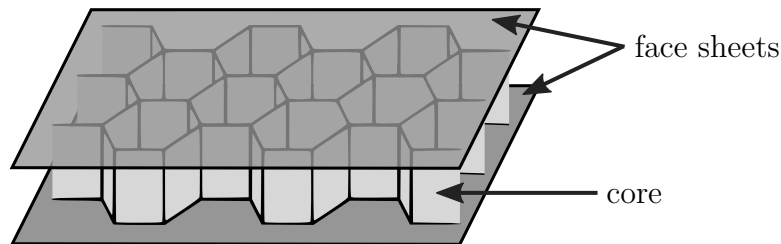


Figure 1.11: Structure of a sandwich panel.

1.3 Computational tools for architected materials

In this section, we will first introduce two topics, homogenization theory and design optimization, originally developed as independent issues and afterward exploited jointly to approach the materials inverse problem in computational mechanics. Last but not least, we present the perspectives of using reduced order models (ROM) for the design of architected materials, which is a less established subject and constitutes the main focus of this work.

Among these three topics, homogenization is the one at its highest stage of maturity, then is chosen to be presented first. This theory supports the mathematical background to prove that whenever we have a periodic architected material, as shown in Figure 1.3, one can benefit from the study of only one unit-cell, and still predict how

the bulk material will behave in the macro-scale. The material properties obtained at the macro-scale using homogenization, are often referred to as effective properties.

In terms of the material design process, obtaining effective properties is the so-called *forward* problem. By means of homogenization, the reduction of the computational effort in the forward problem is evident. On the other hand, the so-called *inverse* problem in material design is formulated like this: which is the meso-structure, formed by some set of constituent materials (which could possibly include voids), that features some prescribed effective material properties. The inverse problem is definitely harder to solve, quoting experts in the field, [Kadic et al. \(2013\)](#) say: “there is no general explicit analytical solution for this step” and [Reis et al. \(2015\)](#) state: “this problem is generally ill-posed, and making progresses requires a combination of computational strategies to strengthen our physical intuition”. In this sense, we present an optimization framework, which is the mostly used approach to attempt a numerical solution to the material design inverse problem.

As a general idea, design optimization or other numerical approaches to tackle inverse problems, rely on solving multiple times an updated forward problem in a smart procedure. Accordingly, the forward problem must be formulated as a parametric problem, such that each time it is solved, the design variables or parameters are updated and allow us to compute afterward a different solution. In the design of materials, the main difficulty of handling a parametric description of the meso-structure and to determine its influence in the emerging properties of the bulk is the multidimensional character of the problem. The computational complexity increases exponentially with the number of parameters and hence the burden of the inverse problem. A possible solution to affordably deal with the so-called *curse of dimensionality* is using reduced order models (ROM).

1.3.1 Computing effective properties using homogenization

The basic idea of homogenization consists in the possibility of measuring effective constitutive properties in a periodic material at the global scale, just by considering the behavior of a repetitive cell at the local scale. Take for example a plane test specimen of honeycomb, as shown in [Figure 1.12](#), which is subjected to a state of homogeneous stress Σ or strain \mathbf{E} at the global scale, see [Figure 1.12a](#). Experimental tests can be done in order to measure the components of the homogeneous or effective constitutive relation between Σ and \mathbf{E} , given by \mathbf{C}^{eff} . If these tests are reproduced by numerical simulations, for example using finite elements, the computational cost is reduced by performing analysis at a local scale only. In fact, as observe in [Figure 1.12b](#), an homogeneous state of strain in the global scale conforms into a periodic arrangement of strain and stress fields at the local scale, ϵ and σ respectively. This justifies that the computational analysis can be done on a single unit-cell. The interested reader is referred to [Anthoine \(1995\)](#) and [Michel et al. \(1999\)](#) for a complete description of the homogenization mechanical principles using basic mathematics. In addition, [Sánchez-](#)

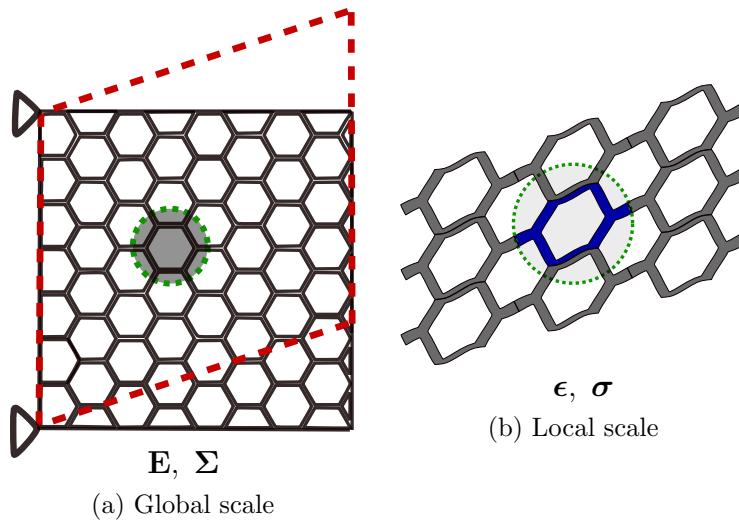


Figure 1.12: Sketch of a periodic material response at the local scale, when homogeneous strain is imposed on the global scale.

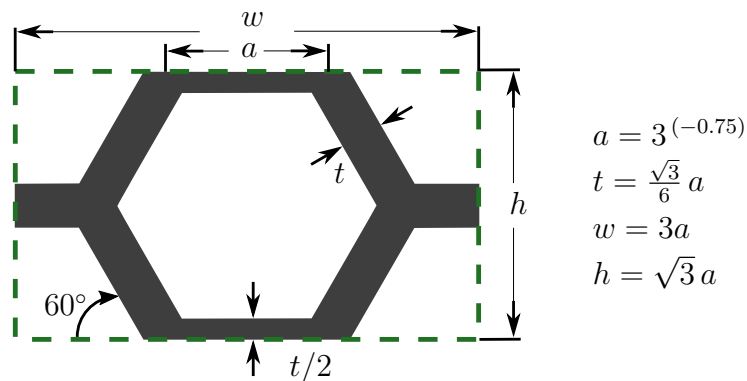


Figure 1.13: Unit-cell dimensions of a perfect honeycomb, as reported by [Sigmund \(1994a\)](#).

[Palencia \(1980\)](#) and [Benssousan et al. \(2011\)](#) cover further technical aspects such as functional settings, existence and uniqueness theorems and convergence properties.

For simplicity, we present here an overview of homogenization applied to a 2D periodic material. The reader is referred to the work by [Nguyen et al. \(2011\)](#), for an extended version approaching a 3D random composite. Nevertheless, as noted by [Hernández et al. \(2014\)](#), the same theory in homogenization is used with different terminologies, adopting *representative volume element* (RVE) to indicate a domain showing statistical homogeneity in a random composite, whereas *unit-cell* is employed to indicate a meso-structure displaying periodicity.

Implementing homogenization with finite elements is exactly as discretizing the domain of a unit-cell, see the perfect honeycomb example in [Figure 1.13](#), and solve

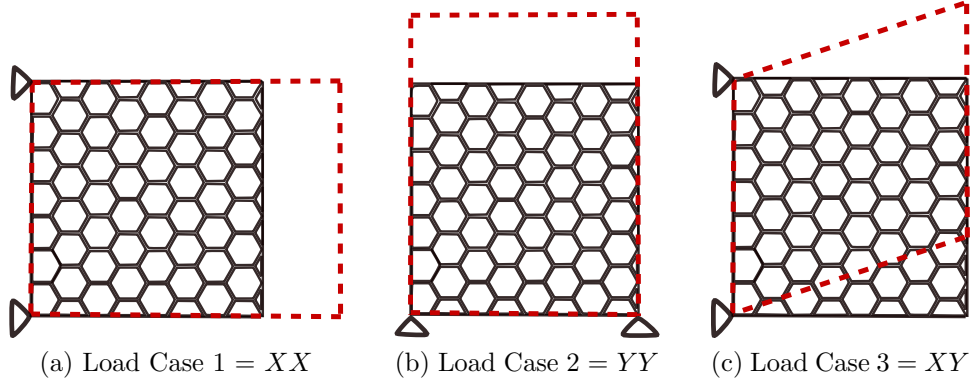


Figure 1.14: Prescribed strains at the global scale used as unit-cell loading cases.

an equilibrium problem where:

- Periodic boundary conditions must be prescribed at the degrees of freedom located in the unit-cell external boundary (marked in Figure 1.13 with dotted lines).
- The generalized load in the unit-cell is given by a prescribed homogeneous strain at the global scale. Figure 1.14 depicts three independent load cases in 2D, that applied in the unit-cell, allow the recovery of all the effective material properties at the global scale.

Once the unit-cell equilibrium problem is solved, subjected to the conditions above, we obtain the displacements denoted by \mathbf{u}^{XX} , \mathbf{u}^{YY} and \mathbf{u}^{XY} . As a post-process, homogenization theory allows us to compute the material effective constitutive tensor \mathbf{C}^{eff} , which in 2D Voigt notation is written

$$\mathbf{C}^{\text{eff}} = \begin{bmatrix} C_{11}^{\text{eff}} & C_{12}^{\text{eff}} & C_{13}^{\text{eff}} \\ C_{21}^{\text{eff}} & C_{22}^{\text{eff}} & C_{23}^{\text{eff}} \\ C_{31}^{\text{eff}} & C_{32}^{\text{eff}} & C_{33}^{\text{eff}} \end{bmatrix}, \quad (1.1)$$

with components

$$C_{IJ}^{\text{eff}} = \frac{1}{wh} (\mathbf{u}^I)^\top \mathbf{K} \mathbf{u}^J, \quad \text{for } I, J = 1, 2, 3. \quad (1.2)$$

In the expression above, the following definitions hold for displacements: $\mathbf{u}^1 \equiv \mathbf{u}^{XX}$, $\mathbf{u}^2 \equiv \mathbf{u}^{YY}$ and $\mathbf{u}^3 \equiv \mathbf{u}^{XY}$, wh stands for the area occupied by the unit-cell (see Figure 1.13), and \mathbf{K} is the unit-cell stiffness matrix obtained by finite element discretization. It is worth noting that both left and right hand sides of equation (1.2) have physical units of stress. On the left-hand side, there are components of the 2D constitutive tensor, whereas on the right-hand side we have units of energy divided by area. Thus, assuming plane elasticity, the latter corresponds to units of stress as well.

1.3.2 The architected material inverse problem

The goal here is to briefly introduce the material design inverse problem, and stated formally in an optimization framework, since it is the most frequent formulation found in computational mechanics literature. Naturally, when applying this procedure to the design of materials, the optimization problem must contain the embedded tools capable of analyzing the material physical behavior. Typically, a unit-cell model is used to reduce the computational cost, and this analysis is upscale using homogenization theory, such that the material bulk or effective properties can be recovered. This is known as an inverse homogenization approach and was first addressed by the works of Sigmund (1994b, 1995).

The general optimization problem is stated below following the notation by Osanov and Guest (2016), where the unit-cell architecture is defined by the vector of design variables (or parameters) $\boldsymbol{\rho}$:

$$\begin{aligned} & \min_{\boldsymbol{\rho}} f(\boldsymbol{\rho}, \mathbf{C}^{\text{eff}}(\boldsymbol{\rho})), \\ \text{subject to } & \begin{cases} \mathbf{h}(\boldsymbol{\rho}, \mathbf{C}^{\text{eff}}(\boldsymbol{\rho})) = \mathbf{0}, \\ \mathbf{g}(\boldsymbol{\rho}, \mathbf{C}^{\text{eff}}(\boldsymbol{\rho})) \leq \mathbf{0}, \end{cases} \end{aligned} \quad (1.3)$$

where f is the objective or cost function, \mathbf{h} are the equality constraints, \mathbf{g} are the inequality constraints, and all of them are function of the design variables $\boldsymbol{\rho}$. In our inverse homogenization problem, \mathbf{h} contains at least the unit-cell equilibrium equations, subjected the illustrated loads of previous subsection (see Figure 1.14). The inequality constraints \mathbf{g} typically bound minimum allowable magnitudes of the design variables or the material effective properties. The objective function f can be set for the material mass or some combination of effective properties. As pointed out in a recent review by Osanov and Guest (2016), there are multiple alternatives to define the functions in (1.3) but these must be meaningful for the architected material design. In addition, it is remarked that either material symmetries or engineering moduli can be prescribed in (1.3), by properly combining the effective constitutive tensor coefficients (equations (1.1) and (1.2) from previous subsection).

Although it is out of the scope in this thesis, it is often differentiate in the literature the numerical methods used to solve the problem established in (1.3). Whenever the initial choice of the architecture drives the design, it is often referred to size or shape optimization, whereas topology optimization indicates that the exploration of the optimal design allows changes in the structural connectivities. A brief list is presented in the following that accounts for non-usual mechanical performances obtained by topology optimization: materials with zero or negative thermal expansion coefficients by Sigmund and Torquato (1997) and by Hopkins et al. (2013), isotropic auxetic materials in 3D by Andreassen et al. (2014), multifunctional materials (combined optimization of stiffness and fluid permeability) for biomedical applications by Guest and Prévost (2006) and Wang et al. (2016), and pentamode metamaterial for an acoustic cloak by Gustavo Méndez et al. (2017).

1.3.3 Perspectives of using reduced order models for the design of architected materials

In the past decade, reduced order models (ROM) have had a big development by contributing to scale down the computational cost and data storage requirements of simulations in many fields of applied science and engineering. Numerical methods like finite elements (FE) are well established given their ability to approximate *high-fidelity* solutions of partial differential equations (PDEs), the mathematical models of many different physical phenomena. Whenever the same PDE has to be solved for diverse inputs, it can be reformulated as a parametrized PDE. Different inputs to a PDE can be considered as parameters, naturally one may think about material properties, but it is also the case of boundary conditions, or geometrical parameters that modify the domain where the PDE holds.

If a PDE solution by FE is a vector field of size N , any time we demand an updated solution for a new set of parameters values, we are required to solve a *full-order* system of N equations. We will first refer to a class of ROM known as Reduced Basis (RB) and Proper Orthogonal Decomposition (POD)¹, that share the main concept behind answering to the PDE *multi-queries* effectively. Instead of updating the vector field of size N using FE, it is reconstructed by a linear combination of m basis vectors. Supposing that m is a relatively low number compared to N , the reconstruction implies solving a *reduced* system of m equations, at a much lower cost than the *full-order* one. The transformation from the *full-order* system to the *reduced* one is achieved through the so-called *projection matrix*, conformed by the m basis vectors. These are nothing but different solutions of the *full-order* system, often called *snapshots*, calculated at particular values of the parameters. Thus, one key question in RB and POD methods is related to selecting carefully where to calculate the snapshots and assessing properly the accuracy of the reduced basis through error estimation. The reader is referred to the works by Prud'Homme et al. (2002) and Rozza et al. (2007, 2013) for a comprehensive review on this topic and on goal-oriented error estimation of RB applied to parametrized PDEs.

Another ROM technique that has grown attention in the last decade is the so-called Proper Generalized Decomposition (PGD), see for example: Chinesta et al. (2011) and Chinesta and Ladevèze (2014). In contrast with RB and POD, the PGD does not base its approximation on snapshots, i.e. solutions of the PDE computed at prescribed values of the parameters. Instead, the solution of a generalized PDE is sought, where a number \mathbf{n}_p of different parameters are considered as extra coordinates. Now, the space where this solution belongs is not any more the size of the vector field N but the product $N \prod_{i=1}^{\mathbf{n}_p} n_i$, where n_i is the size of the vector field containing values of a parameter μ_i , for $i = 1, 2, \dots, \mathbf{n}_p$. This leads to the so-called *curse of dimensionality*, meaning that the computational cost of solving the parametrized PDE grows exponentially with respect to the number of added parameters \mathbf{n}_p . To avoid this,

¹Depending on the field of application, POD may also appear as Singular Value Decomposition (SVD), Principal Component Analysis (PCA) or Karhunen-Loève transform.

PGD introduces the following approximation to the parametrized PDE solution: a sum of terms containing a product of separated unknowns. The work by [Chinesta et al. \(2010\)](#) proposes to compute sequentially each one of these terms (greedy algorithm), using a fixed-point solver (alternated directions scheme) to deal with the nonlinearities introduced by the product of unknowns. By reducing the complexity of the parametrized PDE solution from exponential to linear, multidimensional problems have been efficiently approached by PGD, for example: in structural mechanics ([Bognet et al. \(2012\)](#) and [Vidal et al. \(2013\)](#)), optimization of structures ([Courard et al. \(2016\)](#)), computational fluid mechanics ([Leblond and Allery \(2014\)](#) and [Díez et al. \(2017\)](#)), and wave propagation in elastic media ([Signorini et al. \(2017\)](#)). In addition, once the parametrized PDE solution - a.k.a. the *computational vademecum* - has been built and stored at the *offline* phase, the solution for a prescribed value of the parameters is evaluated just by a linear combination of terms at the *online* stage. In contrast to RB, the PGD online step does not solve any reduced system, making it suitable for applications like haptic rendering of soft biological tissues ([Niroomandi et al. \(2013\)](#)), electrical power distribution ([García-Blanco et al. \(2018\)](#)), among others requiring fast responses ([Chinesta et al. \(2013\)](#) and [Modesto et al. \(2015\)](#)).

In a context closer to the interests of this work, the literature review shows a devoted research effort in ROM applied to the “Finite Element square method” (FE^2). This computational approach is focused on modeling the behavior of structures without defining any constitutive law at the global scale. Instead, another model is done at the local scale, where the material heterogeneities - and possible nonlinearities - are described in a unit-cell or an RVE (representative volume element). The procedure that links the two models is the following: at each point of the global scale, start with a guessed strain that loads the unit-cell problem at the local scale, whose solution retrieves back the stresses to the global scale. This procedure is addressed iteratively until equilibrium at the global scale is reached, as explained by [Feyel and Chaboche \(2000\)](#). Achieving the latter comes with high expenses, so the independent unit-cell problems have been implemented in parallel, for example by [Mosby and Matouš \(2015\)](#), but still remains the computational cost of exchanging information between scales. Instead, using POD to approach the multiple queries to the unit-cell problem in the framework of (FE^2), we highlight the works by [Yvonnet and He \(2007\)](#) and [Hernández et al. \(2014\)](#), where very significant computational time reductions are obtained. In addition, the works by [Lamari et al. \(2010\)](#), [El Halabi et al. \(2013\)](#) and [Cremonesi et al. \(2013\)](#) also report meaningful computational cost savings for this multiscale approach in structural analysis, but using PGD-based models instead.

In the architected materials literature review, there are very few but promising implementations of ROM, which is one of the motivations of the present thesis. In the works by [Ganapathysubramanian and Zabararas \(2007\)](#) and [Xia et al. \(2013\)](#), a POD image-based interpolation is presented to obtain an efficient parametrization of the unit-cell meso-structure. With respect to design, a RB approach is used in [Saa-Seoane et al. \(2012\)](#) to reduce the computational complexity of a metamaterial optimization

for wave propagation. In the previous, RB allows to keep the discrete binary nature of the unit-cell optimization problem (i.e. selecting either to place material or void in a FE mesh), which is more robust than continuous gradient-based methods but comes at a higher computational cost. Also in the context of topology optimization, the work by [Xia and Breitkopf \(2014\)](#) presents a POD approach that admits an efficient treatment of a two-scale problem: derive a structure with maximum stiffness for a given weight at the macro-scale, using a fixed unit-cell architecture of a nonlinear elastic constituent material.

A further step in the search of optimal structures is reported by [Ferrer et al. \(2016\)](#). There, the two-scale algorithm also searches for an optimum unit-cell topology in the design problem that maximizes structural stiffness for a given weight at the macro-scale. The high computational cost of simultaneously optimizing a structure and its material topology, is addressed by building a computational vademecum a priori. This outputs the optimal unit-cell topology among a large set of the same weight, taking as inputs the macroscopic stress state in 2D (parametrized with two parameters only). Given that this material vademecum has been calculated using brute force, we highlight the authors suggestion about using ROM to include more parameters, as it would be needed in the case of representing a 3D stress state, variations of the constituent material properties or ranges in the unit-cell weight (material volume fraction).

The need to explore efficient routes to computational vademecums in the material design problem is the key aspect that motivates the present research by means of a PGD algebraic approach applied to parametric lattice structures.

1.4 Outline and objectives of this work

This work is based on parametric lattices structures, formulated with beam finite elements. This is introduced and described in [Chapter 2](#). In addition, a distinct effort is committed to describe how the parametric input data must be decomposed in a separated way, which is a requirement for the algebraic PGD solver.

The algebraic PGD solver is one distinguished objective of this thesis and is developed in [Chapter 3](#). So far, many PGD solutions for parametric partial differential equations have been proposed, however, none of them features an integrated approach that could be used independently of the parametric PDE nature. Our approach stands as a solver for any parametric system of algebraic equations, that could be used as a black-box, provided that the input parametric data is given in a separated form. In addition, it highlights how the different parametric problems inside this black-box can be formulated independently such that they can be solved in parallel.

An application of the PGD algebraic solver for the solution of a 2D parametric honeycomb is detailed in [Chapter 4](#). The results show the PGD solution obtained for a unit-cell model with homogenization, supporting the explicit parametric analysis of effective mechanical properties, such as the negative orthotropic Poisson's ratios.

Chapter 5 shows the algebraic PGD solver applied to 3D parametric lattices. First, the parametrization of a scaffold is introduced, with a particular emphasis on the application of the Singular Value Decomposition (SVD) to handle the non-separable input parametric data. In addition, an insight is provided on the accuracy of the parametric 3D orthotropic Poisson's ratios recovered by our PGD strategy. Furthermore, the PGD solver is applied to a stent-like tubular structure capable of exhibiting auxetic behavior. Finally, the same parametric stent is analyzed using a geometrically nonlinear beam model in a commercial software. Although a fewer number of parameters are considered to approach the multidimensional sampling, a PGD response can be built a posteriori based on a least-squares approximation. This explicit parametric response is certainly appealing since it is capable of evaluating buckling, and the load magnitude as an extra parameter that modifies the material effective properties. Being the ultimate goal to build this explicit parametric response using PGD a priori, we state a possible route to exploit the algebraic PGD solver in a nonlinear scheme.

A web application is presented in Chapter 6, which has been developed to exploit the fast responses offered by the PGD online phase. This post-processing tool supplies an interactive graphical interface to explore the PGD parametric responses in lattice materials. In addition, the WebGL core combined with JavaScript admits a versatile rendering tool qualify to work across multiple platforms (i.e. any modern web browser).

Lastly, Chapter 7 gathers the contributions, conclusions and outlines of future works.

Chapter 2

Parametric lattice structures

In this chapter, the mechanical response at the macro-scale of an architected material is studied. Its periodic structure is formed by the repetition of a unit-cell in 2D. The focus is set on a hexagonal unit-cell, frequently found in honeycomb materials (Hexcel (1999)). In addition, the unit-cell shape is parametrized, with the particularity that an *auxetic* behavior could be achieved depending on the geometric configurations (Almgren (1985)). Since we are dealing with a lattice structure, the Euler-Bernoulli beam theory is chosen to describe the mechanical problem. In addition, we restrict the mechanical behavior to the linear elastic regime. The goal is to solve the parametric structural problem by means of the PGD method, such that the multidimensional space of parameters can be browsed in an efficient approach. In addition, the PGD provides an explicit parametric response that could be exploited to efficiently solve an inverse problem, such as the design of tailored material properties or multi-parameter identification. In such cases, multiple queries in the parametric design space are needed to evaluate the arising mechanical responses, which in the PGD framework can be obtained in real time.

2.1 2D parametric structural problem

2.1.1 Planar beam element

The Euler-Bernoulli beam theory proposes a continuous element with external loads q as depicted in Figure 2.1 (Timoshenko and Goodier (1951)). The external loads generate moments M , and internal shear forces V . These forces and moments generate a displacement field, which in the linear framework, is accounted only in the transverse direction to the beam dotted-line of centroids.

The Euler-Bernoulli beam hypothesis is an idealization in which the kinematics of a continuous solid is approximated by its line of centroids, provided that the solid body cross-sections remain undeformed. In addition, a decoupled axial strain is added to account for the extension or contraction produced by external axial forces. By this simplification, the axial strain becomes independent of the shear forces and moments.

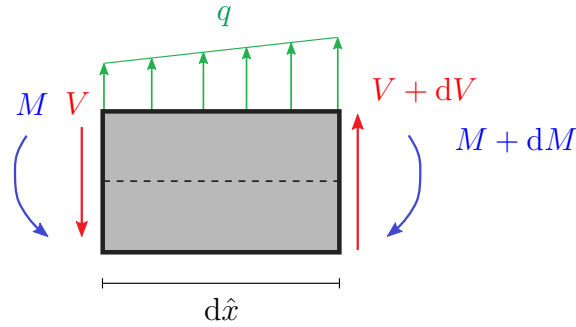


Figure 2.1: Diagram of external loads q , internal forces V and moments M in a differential element of Euler-Bernoulli beam.

In the 2D model, the beam's line of centroids is completely defined by a displacement $u_{\hat{y}}$ and a curvature $\theta_{\hat{z}}$, and together with the axial displacement $u_{\hat{x}}$, they account for a total of three degrees of freedom. The local beam axes defined in Figure 2.2 is denoted by $(\hat{x}, \hat{y}, \hat{z})$.

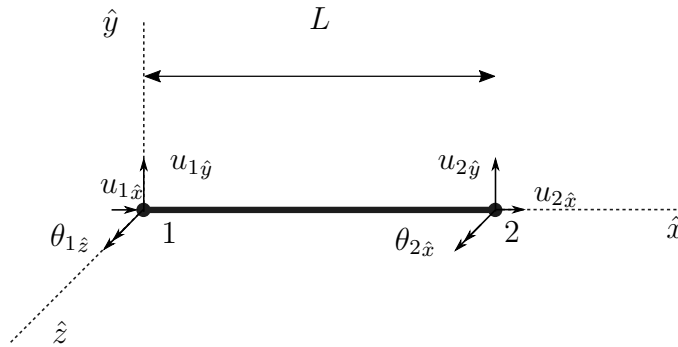


Figure 2.2: Planar beam element of length L . Local degrees of freedom denoted at their tip points 1 and 2.

2.1.2 Unit-cell parameterization

In the numerical solutions to structural problems, one often considers different parameters that take a particular set of values. As long as the problem is well posed, this leads to a unique solution valid for the determined set of parameters values.

In a parametrized problem instead, the parameters - previously defined as a particular set of values - are now left as variables, letting the solution be an expression in terms of them. In case it is possible to obtain an analytical expression, then all the possible solutions to the problem are written in a mathematical statement. This can be evaluated for any set of values without need of solving the same problem many times. However, even for small sized problems, the use of symbolic computation to obtain analytical solutions becomes computationally inefficient, or even unfeasible.

Alternatively, one can keep the parametric problem description but assigning admissible intervals where each of the parameters range. If the parametric dependence of the problem is separable, a PGD solver provides an explicit solution in the parameters. A detailed explanation is here presented about the process of building the PGD solver input data separable in the parameters. With respect to the PGD solver itself, this is comprehensively treated in Chapter 3.

The parametric structural problem is described for a periodic material with an hexagonal unit-cell (Figure 2.3). Two different structures arising from the same parametrization are shown as an example in Figures 2.3a and 2.3b (unit-cells depicted in red). Moreover, the unit-cell geometry is detailed in Figure 2.3c. The mechanical behavior is modeled by 8 beam elements in Figure 2.3d, which at the end it allows us to characterize the material shape by means of the following parameters:

- a : the length of the obliquely oriented beams.
- b : the length of the horizontal beams.
- α : the angle of the obliquely oriented beams, with respect to the horizontal axis.
- t : the beam elements thickness.

Thus, there are a total of $\mathbf{n}_p = 4$ parameters, collected in a vector $\boldsymbol{\mu}$:

$$\boldsymbol{\mu} = [\mu_1 \ \mu_2 \ \mu_3 \ \mu_4]^T = [a \ b \ \alpha \ t]^T.$$

As explained in section 1.3.1, one can exploit the material periodicity and recover its mechanical properties at the macro-scale, just by using a series of independent problems on the unit-cell subjected to proper boundary conditions. In such case, the unit-cell parametrization must take into account that:

1. $t/2$ is the thickness of the top and bottom horizontal beam elements (as shown in Figure 2.3c).
2. $b/2$ is the length of the horizontal beam elements in blue (see Figure 2.3d).

In addition, the material structure parametrization has physical sense only for a restricted parameters range. If we circumscribe the unit-cell into a rectangle, depicted in Figure 2.3c with dotted lines, one must take into account that this rectangle width - w - has to be larger than the horizontal elements length b . This leads to the constraint:

$$\begin{aligned} w &> b, \\ w = 2(b - a \cos(\alpha)) &> b, \\ \cos(\alpha) &< \frac{b}{2a}. \end{aligned} \tag{2.1}$$

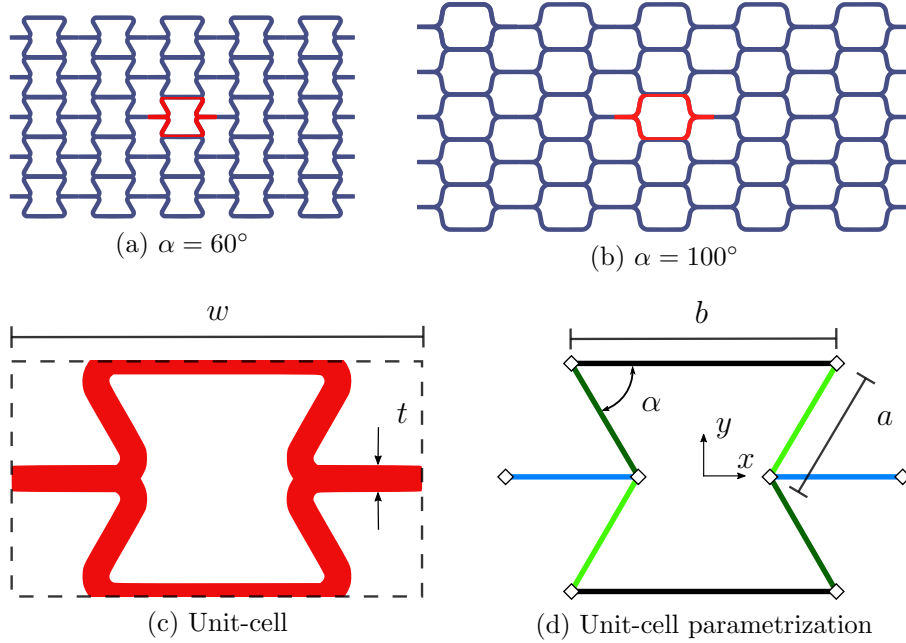


Figure 2.3: Parametrization of a periodic hexagonal honeycomb.

Besides, the intervals I_i , where the parameters μ_i range in our analysis, for $i = 1, \dots, n_p$, are chosen as follows:

$$a \in I_1 = [0.3, 0.7], b \in I_2 = [1, 1.5], \alpha \in I_3 = \left[\frac{\pi}{4}, \frac{3\pi}{4}\right] \text{ and } t \in I_4 = \left[\frac{1}{50}, \frac{1}{5}\right].$$

In this manner, we assure that all the values in the multidimensional parametric space formed by the Cartesian product $I_1 \times I_2 \times I_3$ fulfill the constraint given by equation (2.1). Following this approach, the algebraic PGD solver - Chapter 3 - builds the parametric dependence as a product of separated 1D functions. The reader is referred to the work by Zou et al. (2018) for an alternative approach of PGD with a constrained parametric space. There, the mutually dependent parameters are collected into non-separable (2D or 3D) spaces.

2.1.3 Finite Element formulation of planar beams

The discretization of the beams is done with a 2D element, which is classical in structural mechanics (Cook et al., 2002, Chapter 2). Two nodes are located at the beam tip points, each one associated to three degrees of freedom (Figure 2.2). Thus, a generalized displacement vector collects the element degrees of freedom at the beam local system of coordinates:

$$\hat{\mathbf{u}} = \{u_{1\hat{x}} \ u_{1\hat{y}} \ \theta_{1\hat{z}} \ u_{2\hat{x}} \ u_{2\hat{y}} \ \theta_{2\hat{z}}\}^T,$$

and a generalized force vector gathers analogously:

$$\hat{\mathbf{f}} = \{N_{1\hat{x}} \ V_{1\hat{y}} \ M_{1\hat{z}} \ N_{2\hat{x}} \ V_{2\hat{y}} \ M_{2\hat{z}}\}^\top,$$

where N represents axial forces, which are always in the beam local \hat{x} direction, V are shear forces, and M are bending moments. In the planar beam model, there is only one bending curvature, depending on shear forces and moments in the beam local \hat{y} and \hat{z} directions respectively. In the Bernoulli beam element, the relation between vectors of generalized forces and displacements can be obtained in a closed-form matrix, using a direct stiffness method (Cook et al., 2002, Chapter 2). In a mathematical sense, the same result is obtained using a variational formulation with some particular interpolation for the degrees of freedom, and integrating in space (Cook et al., 2002, Chapter 4). In both cases, the stiffness matrix becomes

$$\hat{\mathbf{K}}_e = \begin{bmatrix} X_e & 0 & 0 & -X_e & 0 & 0 \\ 0 & Y_{1,e} & Y_{2,e} & 0 & -Y_{1,e} & Y_{2,e} \\ 0 & Y_{2,e} & 2Y_{3,e} & 0 & -Y_{2,e} & Y_{3,e} \\ -X_e & 0 & 0 & X_e & 0 & 0 \\ 0 & -Y_{1,e} & -Y_{2,e} & 0 & Y_{1,e} & -Y_{2,e} \\ 0 & Y_{2,e} & Y_{3,e} & 0 & -Y_{2,e} & 2Y_{3,e} \end{bmatrix}, \quad (2.2)$$

where the superscript “ $\hat{}$ ” denotes the stiffness of an element “ e ” in its local coordinate system, as depicted in Figure 2.2. The elemental matrix coefficients read:

$$\begin{aligned} X_e &= \frac{E_e A_e}{L_e} & Y_{1,e} &= \frac{12E_e I_{\hat{z},e}}{L_e^3} \\ Y_{2,e} &= \frac{6E_e I_{\hat{z},e}}{L_e^2} & Y_{3,e} &= \frac{2E_e I_{\hat{z},e}}{L_e} \end{aligned} \quad (2.3)$$

In our parametric setup, we have that the beams cross-section area - A_e - and centroidal moment of inertia along \hat{z} axis - $I_{\hat{z},e}$ - are functions of the parameter “ t ”. Note that the subscript “ e ” is kept to distinguish that, in the unit-cell model, some elements must be defined with half-thickness $t/2$ (see Figure 2.3c). The beams length L_e is a function of either parameter “ b ” or parameter “ a ”, depending upon which element “ e ” are we considering in the unit-cell model (see Figure 2.3d, and note in blue the elements defined with half-length $b/2$). Finally, the beams Young’s modulus E_e can be neglected for all our analysis, given that we focus on the unit-cell geometric parametrization and therefore it is set unitary $E_e = 1$ for all elements in the structure.

The parametric dependence of the elemental matrix coefficients is indicated with the following notation - $X_e(\boldsymbol{\mu})$, $Y_{1,e}(\boldsymbol{\mu})$, $Y_{2,e}(\boldsymbol{\mu})$ and $Y_{3,e}(\boldsymbol{\mu})$ -, which implies that the parametric elemental stiffness matrix itself is - $\hat{\mathbf{K}}_e(\boldsymbol{\mu})$ -.

The elemental matrix $\hat{\mathbf{K}}_e(\boldsymbol{\mu})$ can be mapped to the global coordinate system (x, y, z) (Figure 2.3d) by a standard transformation (Cook et al., 2002, Chapter 2):

$$\mathbf{K}_e(\boldsymbol{\mu}) = \mathbf{T}_e^\top(\alpha) \hat{\mathbf{K}}_e(\boldsymbol{\mu}) \mathbf{T}_e(\alpha); \quad \mathbf{T}_e(\alpha) = \begin{bmatrix} \boldsymbol{\Lambda}_e(\alpha) & \mathbf{0} \\ \mathbf{0} & \boldsymbol{\Lambda}_e(\alpha) \end{bmatrix}. \quad (2.4)$$

The elemental matrices $\mathbf{\Lambda}_e(\alpha)$ represent a plane rotation through an angle $\vartheta_e(\alpha)$:

$$\mathbf{\Lambda}_e(\alpha) = \begin{bmatrix} \cos(\vartheta_e(\alpha)) & \sin(\vartheta_e(\alpha)) & 0 \\ -\sin(\vartheta_e(\alpha)) & \cos(\vartheta_e(\alpha)) & 0 \\ 0 & 0 & 1 \end{bmatrix}, \quad (2.5)$$

and depending upon the element in the unit-cell, $\vartheta_e(\alpha)$ becomes:

$$\vartheta_e(\alpha) = \begin{cases} \pi - \alpha, & \text{for depicted elements in dark green, see Figure 2.3d;} \\ \alpha, & \text{for depicted elements in light green, see Figure 2.3d.} \end{cases} \quad (2.6)$$

Note that for the horizontal elements in Figure 2.3d, the global coordinate system (x, y, z) coincides with the local one $(\hat{x}, \hat{y}, \hat{z})$ in the beams, therefore the transformation in equation (2.4) becomes the identity.

2.2 Affine decomposition of input data

Once we have defined the structural parametrization and the finite element discretization in our problem, the next goal is to build the discrete parametric mechanical equilibrium:

$$\mathbf{K}(\boldsymbol{\mu}) \mathbf{U}(\boldsymbol{\mu}) = \mathbf{F}(\boldsymbol{\mu}). \quad (2.7)$$

The information of the parametric problem is condensed in the global stiffness matrix $\mathbf{K}(\boldsymbol{\mu})$ and the global forcing term $\mathbf{F}(\boldsymbol{\mu})$, such that we will refer to them as the parametric input data. In our case, input data represents the discrete form of a mechanical equilibrium problem of a parametric structure, subjected to a loading state that also depends on the parameters. However, equation (2.7) could represent in general, the discrete form of any parametrized linear PDE.

Instead of solving the unknown $\mathbf{U}(\boldsymbol{\mu})$ as the finite element solution for any particular value of the parameters, it will be approximated using an algebraic PGD solver (Chapter 3). In this manner, the exponential growth of the computational cost, associated with the increasing number of parameters, can be prevented. The algebraic PGD solver relies, however, on the affine decomposition - or in other words, separability - of the parametric input data. We will here focus on the methodology to obtain the separated form of the stiffness matrix $\mathbf{K}(\boldsymbol{\mu})$, that is:

$$\mathbf{K}(\boldsymbol{\mu}) = \sum_{k=1}^{n_k} \mathbf{K}^k \prod_{i=1}^{n_p} B_i^k(\mu_i), \quad (2.8)$$

but analogously, the procedure can also be used to obtain the separated form of the forcing term $\mathbf{F}(\boldsymbol{\mu})$, such that

$$\mathbf{F}(\boldsymbol{\mu}) = \sum_{\ell=1}^{n_f} \mathbf{f}^\ell \prod_{i=1}^{n_p} S_i^\ell(\mu_i). \quad (2.9)$$

In order to approach the affine decomposition of the global stiffness matrix $\mathbf{K}(\boldsymbol{\mu})$ in (2.8), we will begin with (as usual in finite element procedures) an affine decomposition of the elementary contribution to the global stiffness matrix, precisely

$$\mathbf{K}_e(\boldsymbol{\mu}) = \sum_{d=1}^{\mathbf{n}_{k_e}} \mathbf{K}_e^d \prod_{i=1}^{\mathbf{n}_p} B_{i,e}^d(\mu_i). \quad (2.10)$$

The elementary stiffness matrix $\mathbf{K}_e(\boldsymbol{\mu})$ for our parametric structure has been described by equation (2.4). From this equation, we observe that the affine decomposition given by (2.10) implies the separability of $\widehat{\mathbf{K}}_e(\boldsymbol{\mu})$ - the beam element stiffness matrix in its local system of coordinates -, provided that the transformation matrix \mathbf{T}_e depends only on one parameter, “ α ”, so it is separable by definition. Thus, $\widehat{\mathbf{K}}_e(\boldsymbol{\mu})$ should be described as

$$\widehat{\mathbf{K}}_e(\boldsymbol{\mu}) = \sum_{f=1}^{\mathbf{n}_{\hat{k}}} \widehat{\mathbf{K}}_e^f \prod_{i=1}^{\mathbf{n}_p} O_{i,e}^f(\mu_i). \quad (2.11)$$

Note that the element subscript “ e ” has been dropped out from the notation “ $\mathbf{n}_{\hat{k}}$ ”, since the number of separated terms for $\widehat{\mathbf{K}}_e(\boldsymbol{\mu})$ results the same in all elements of our parametric structure, as it will be explained below.

The decomposition stated in (2.11) is constructed by observing the functions: $X_e(\boldsymbol{\mu})$ and $Y_{j,e}(\boldsymbol{\mu})$, for $j = 1, 2, 3$, that provide the dependence of matrix $\widehat{\mathbf{K}}_e$ on the parameters, see equation (2.2). In fact, it is noticed from (2.3) that all these four functions are a product of functions depending on one of the parameters only. This implies that the proposition in (2.11) is feasible.

Let us assume that all beam elements in our honeycomb material have a rectangular cross-section, with unitary width and thickness t . Then, for the set of oblique elements “ $e \in \text{ob}$ ”, i.e. those colored in Figure 2.3d in green, we use the following notation to denote their physical properties:

$$A_{\text{ob}} = t, \quad I_{\hat{z},\text{ob}} = t^3/12, \quad L_{\text{ob}} = a. \quad (2.12)$$

Using the properties above, together with equations (2.2) and (2.3), we decompose $\widehat{\mathbf{K}}_{\text{ob}}(\boldsymbol{\mu})$ in four terms:

$$\widehat{\mathbf{K}}_{\text{ob}}(\boldsymbol{\mu}) = \widehat{\mathbf{K}}_{\text{ob}}^1 t/a + \widehat{\mathbf{K}}_{\text{ob}}^2 t^3/a + \widehat{\mathbf{K}}_{\text{ob}}^3 t^3/a^2 + \widehat{\mathbf{K}}_{\text{ob}}^4 t^3/a^3. \quad (2.13)$$

This expression is nothing but equation (2.11), with $\mathbf{n}_{\hat{k}} = 4$, and the parametric functions $O_{i,\text{ob}}^f$, for $f = 1, \dots, \mathbf{n}_{\hat{k}}$ and $i = 1, \dots, \mathbf{n}_p$, being the following:

$\mu_i \setminus^f$	1	2	3	4
μ_1	$1/a$	$1/a$	$1/a^2$	$1/a^3$
μ_2	1	1	1	1
μ_3	1	1	1	1
μ_4	t	t^3	t^3	t^3

 Table 2.1: Parametric functions $O_{i,\text{ob}}^f$ in the hexagonal honeycomb cell.

In the table above, parametric functions depending on $\mu_2 = b$ and $\mu_3 = \alpha$ remain constant. This is natural, given that the oblique elements length is $L_{\text{ob}} = a$, and matrix $\widehat{\mathbf{K}}_{\text{ob}}$ is defined locally, without considering its orientation in the global system. Finally, equation (2.13) is completely described using the following matrices $\widehat{\mathbf{K}}_{\text{ob}}^f$, for $f = 1, \dots, n_{\widehat{\mathbf{k}}} = 4$:

$$\begin{aligned}
 \widehat{\mathbf{K}}_{\text{ob}}^1 &= \begin{bmatrix} 1 & 0 & 0 & -1 & 0 & 0 \\ 0 & 0 & 0 & 0 & 0 & 0 \\ 0 & 0 & 0 & 0 & 0 & 0 \\ -1 & 0 & 0 & 1 & 0 & 0 \\ 0 & 0 & 0 & 0 & 0 & 0 \\ 0 & 0 & 0 & 0 & 0 & 0 \end{bmatrix}, & \widehat{\mathbf{K}}_{\text{ob}}^2 &= \frac{1}{3} \begin{bmatrix} 0 & 0 & 0 & 0 & 0 & 0 \\ 0 & 0 & 0 & 0 & 0 & 0 \\ 0 & 0 & 1 & 0 & 0 & \frac{1}{2} \\ 0 & 0 & 0 & 0 & 0 & 0 \\ 0 & 0 & 0 & 0 & 0 & 0 \\ 0 & 0 & 1 & 0 & 0 & \frac{1}{2} \end{bmatrix}, \\
 \widehat{\mathbf{K}}_{\text{ob}}^3 &= \frac{1}{2} \begin{bmatrix} 0 & 0 & 0 & 0 & 0 & 0 \\ 0 & 0 & 1 & 0 & 0 & 1 \\ 0 & 1 & 0 & 0 & -1 & 0 \\ 0 & 0 & 0 & 0 & 0 & 0 \\ 0 & 0 & -1 & 0 & 0 & -1 \\ 0 & 1 & 0 & 0 & -1 & 0 \end{bmatrix}, & \widehat{\mathbf{K}}_{\text{ob}}^4 &= \begin{bmatrix} 0 & 0 & 0 & 0 & 0 & 0 \\ 0 & 1 & 0 & 0 & -1 & 0 \\ 0 & 0 & 0 & 0 & 0 & 0 \\ 0 & 0 & 0 & 0 & 0 & 0 \\ 0 & -1 & 0 & 0 & 1 & 0 \\ 0 & 0 & 0 & 0 & 0 & 0 \end{bmatrix}.
 \end{aligned} \tag{2.14}$$

Eventually, notice that each term of the decomposition $\widehat{\mathbf{K}}_{\text{ob}}^f \prod_{i=1}^{n_p} O_{i,\text{ob}}^f$, for $f = 1, \dots, n_{\widehat{\mathbf{k}}} = 4$, describes one of the functions from equation (2.3), $X_e(\boldsymbol{\mu})$ and $Y_{j,e}(\boldsymbol{\mu})$, for $j = 1, 2, 3$, in the matrix order given by (2.2). In this case, we have considered beam properties (equation (2.12)) for the set of oblique elements. For the remaining elements in the honeycomb cell (see Figure 2.3d), the procedure is alike but taking into account other beam properties properly.

So far, we have described in equation (2.14) and Table 2.1, the terms characterizing the affine decomposition of the elemental local stiffness matrix $\widehat{\mathbf{K}}_e$. In order to provide an affine decomposition for the elemental global stiffness matrix \mathbf{K}_e , it remains to consider the parametric dependence of the orientation angle α . For this purpose, we refer to the transformation matrix $\mathbf{T}_e(\alpha)$ in equation (2.4), and the decomposition:

$$\mathbf{T}_e(\boldsymbol{\mu}) = \sum_{g=1}^{n_r} \mathbf{T}_e^g \prod_{i=1}^{n_p} L_{i,e}^g(\mu_i). \tag{2.15}$$

The number of terms $\mathbf{n}_T = 3$ is readily obtained by decomposition of rotation matrix $\mathbf{\Lambda}_e(\alpha)$, from equation (2.5), as follows:

$$\mathbf{\Lambda}_e(\alpha) = \begin{bmatrix} 0 & 0 & 0 \\ 0 & 0 & 0 \\ 0 & 0 & 1 \end{bmatrix} + \begin{bmatrix} 1 & 0 & 0 \\ 0 & 1 & 0 \\ 0 & 0 & 0 \end{bmatrix} \underbrace{\cos(\vartheta_e(\alpha))}_{L_{3,e}^2} + \begin{bmatrix} 0 & 1 & 0 \\ -1 & 0 & 0 \\ 0 & 0 & 0 \end{bmatrix} \underbrace{\sin(\vartheta_e(\alpha))}_{L_{3,e}^3}. \quad (2.16)$$

We remark that $\vartheta_e(\alpha)$ takes values $(\pi - \alpha)$ or (α) depending on the elements in the honeycomb unit-cell, as defined in (2.6). This only changes the sign of the second term in equation (2.16), according to $\cos(\pi - \alpha) = -\cos(\alpha)$. Then, we can take out the subscript “ e ” from the parametric functions in equation (2.15), becoming L_i^g as summarized below:

$\mu_i \setminus^g$	1	2	3
μ_1	1	1	1
μ_2	1	1	1
μ_3	1	$\cos(\alpha)$	$\sin(\alpha)$
μ_4	1	1	1

Table 2.2: Parametric functions L_i^g in the hexagonal honeycomb cell.

Naturally, all functions that do not depend on parameter $\mu_3 = \alpha$ remain constant. Finally, matrix \mathbf{T}_e^2 takes opposite signs, depending upon the elements in the unit-cell (equation (2.6)).

Using the matrix decompositions in (2.11) and (2.15), the parametric dependence of $\widehat{\mathbf{K}}_e(\boldsymbol{\mu})$ and $\mathbf{T}_e(\boldsymbol{\mu})$ is replaced in equation (2.4), to obtain the following expression:

$$\mathbf{K}_e(\boldsymbol{\mu}) = \sum_{f=1}^{\mathbf{n}_{\hat{\mathbf{k}}}} \sum_{h=1}^{\mathbf{n}_T} \sum_{g=1}^{\mathbf{n}_T} [\mathbf{T}_e^g \widehat{\mathbf{K}}_e^f \mathbf{T}_e^h] \prod_{i=1}^{\mathbf{n}_p} (L_i^g L_i^h O_{i,e}^f). \quad (2.17)$$

Here, the dependence of the parametric functions on (μ_i) has been omitted in behalf of a simplified notation. The equation above is a product of separated matrices, whose result is a collection of terms describing the affine decomposition of $\mathbf{K}_e(\boldsymbol{\mu})$. This is written in equation (2.10), with a number of terms - $\mathbf{n}_{\mathbf{k}_e}$ - depending on the element in the honeycomb structure.

In the simplest case, some elements have a fixed orientation, not depending on the parametrization. We referred to these as the set of horizontal elements “ $e \in \text{hor}$ ” (those horizontally aligned in Figure 2.3d). Thus, local and global stiffness matrices coincide: $\mathbf{K}_{\text{hor}}(\boldsymbol{\mu}) = \widehat{\mathbf{K}}_{\text{hor}}(\boldsymbol{\mu})$, implying that $\mathbf{n}_{\mathbf{k}_{\text{hor}}} = \mathbf{n}_{\hat{\mathbf{k}}} = 4$. On the other hand, the oblique elements have a parametrized orientation, so the number of separated terms - $\mathbf{n}_{\mathbf{k}_{\text{ob}}}$ - results from the evaluation of (2.17).

2. PARAMETRIC LATTICE STRUCTURES

Typically, the number of terms arising from three nested sums in equation (2.17) results $\mathbf{n}_{\mathbf{k}_{\text{ob}}}^{\text{max}} = \mathbf{n}_{\mathbf{T}}^2 \mathbf{n}_{\hat{\mathbf{k}}}$. In our parametric structure, we have that $\mathbf{n}_{\mathbf{T}} = 3$ and $\mathbf{n}_{\hat{\mathbf{k}}} = 4$, leading to $\mathbf{n}_{\mathbf{k}_{\text{ob}}}^{\text{max}} = 36$. However, the $\mathbf{n}_{\mathbf{T}}^2$ combinations of indexes $\{g, h\}$, for $g, h = 1, \dots, \mathbf{n}_{\mathbf{T}}$, reach twice the same commutative product $\prod_{i=1}^{\mathbf{n}_{\mathbf{p}}} L_i^g L_i^h, \forall g \neq h$. Thus, taking the repeated parametric functions in the sum as a common factor, the number $\mathbf{n}_{\mathbf{T}}^2$ is reduced to $\mathbf{n}_{\mathbf{q}}$, given by the simple formula:

$$\mathbf{n}_{\mathbf{q}} := \binom{\mathbf{n}_{\mathbf{T}}}{2} = \binom{\mathbf{n}_{\mathbf{T}} + 1}{2} = \frac{(\mathbf{n}_{\mathbf{T}} + 1)!}{2! (\mathbf{n}_{\mathbf{T}} - 1)!}. \quad (2.18)$$

This is often referred to as $\mathbf{n}_{\mathbf{T}}$ *multichoose* 2, denoted by $\binom{\mathbf{n}_{\mathbf{T}}}{2}$, by analogy with the binomial coefficient. The idea behind is simple, as it is shown in Table 2.3 for $\mathbf{n}_{\mathbf{T}} = 3$: it basically counts how many unordered pairs $\{g, h\}$ are collected without repetitions, for $g, h = 1, \dots, \mathbf{n}_{\mathbf{T}}$.

g	1	1	1	2	2	3
h	1	2	3	2	3	3

Table 2.3: There is a total number $\mathbf{n}_{\mathbf{q}} = 6$ of multisets of length 2 on $\mathbf{n}_{\mathbf{T}} = 3$, representing the unique combinations of unordered pairs of summing indexes $\{g, h\}$, for $g, h = 1, \dots, \mathbf{n}_{\mathbf{T}}$.

Having considered the previous, the number of terms arising from (2.17) can be reduced from $\mathbf{n}_{\mathbf{k}_{\text{ob}}}^{\text{max}} = \mathbf{n}_{\mathbf{T}}^2 \mathbf{n}_{\hat{\mathbf{k}}}$ to $\mathbf{n}_{\mathbf{k}_{\text{ob}}}^{\text{red}} = \mathbf{n}_{\mathbf{q}} \mathbf{n}_{\hat{\mathbf{k}}}$. In addition, we can define a one to one relation “ \mathcal{F} ” between the summing index $d = 1, \dots, \mathbf{n}_{\mathbf{k}_{\text{ob}}}^{\text{red}}$ in equation (2.10) and the multiple summing indexes from equation (2.17), being $f = 1, \dots, \mathbf{n}_{\hat{\mathbf{k}}}$ and the $\mathbf{n}_{\mathbf{q}}$ unrepeated-unordered pairs $\{g, h\}$, that is summarized by the following equations:

$$d = \mathcal{F}(g, h, f) \quad \text{for } d = 1, \dots, \mathbf{n}_{\mathbf{k}_{\text{ob}}}^{\text{red}} \quad (2.19)$$

$$\mathbf{K}_e^d = \begin{cases} \mathbf{T}_e^{g\top} \widehat{\mathbf{K}}_e^f \mathbf{T}_e^h & \text{if } g = h, \\ \mathbf{T}_e^{g\top} \widehat{\mathbf{K}}_e^f \mathbf{T}_e^h + \mathbf{T}_e^{h\top} \widehat{\mathbf{K}}_e^f \mathbf{T}_e^g & \text{if } g \neq h, \end{cases} \quad (2.20)$$

$$B_{i,e}^d = L_i^g L_i^h O_{i,e}^f \quad \text{for } i = 1, \dots, \mathbf{n}_{\mathbf{p}} \quad (2.21)$$

In our problem, we have that $\mathbf{n}_{\mathbf{q}} = 6$ and $\mathbf{n}_{\hat{\mathbf{k}}} = 4$, which gives $\mathbf{n}_{\mathbf{k}_{\text{ob}}}^{\text{red}} = 24$ matrices \mathbf{K}_e^d computed as stated in (2.20). However, in practice, many of these terms result in a null matrix. In our honeycomb material, after performing equation (2.20) for $d = 1, \dots, \mathbf{n}_{\mathbf{k}_{\text{ob}}}^{\text{red}}$, we end up collecting a final number of $\mathbf{n}_{\mathbf{k}_{\text{ob}}} = 9$ nonzero terms.

Once we have defined the affine decomposition for the elemental stiffness matrices in the parametric structure, we can proceed to build the global one, also in a separated form, specified in equation (2.8). For that purpose, we first note that the total number of terms in the global separated stiffness matrix - $\mathbf{n}_{\mathbf{k}}$ - is given by the collection of all the different parametric functions obtained for the elemental matrices. In our honeycomb structure, this turns out to be the sum of $\mathbf{n}_{\mathbf{k}_{\text{hor}}} = 4$ and $\mathbf{n}_{\mathbf{k}_{\text{ob}}} = 9$

distinctive parametric functions, collected for the different set of elements in the unit-cell. Table 2.4 presents this group of parametric functions, $B_i^k(\mu_i)$, for $k = 1, \dots, \mathbf{n}_k = 13$ (see notation from equation (2.8)).

$\mu_i \setminus k$	1	2	3	4	5	6	7	8	9	10	11	12	13
μ_1	1	1	1	1	$\frac{1}{a}$	$\frac{1}{a}$	$\frac{1}{a}$	$\frac{1}{a}$	$\frac{1}{a^2}$	$\frac{1}{a^2}$	$\frac{1}{a^3}$	$\frac{1}{a^3}$	$\frac{1}{a^3}$
μ_2	$\frac{1}{b}$	$\frac{1}{b}$	$\frac{1}{b^2}$	$\frac{1}{b^3}$	1	1	1	1	1	1	1	1	1
μ_3	1	1	1	1	$\cos^2(\alpha)$	$\sin(2\alpha)$	$\sin^2(\alpha)$	1	$\cos(\alpha)$	$\sin(\alpha)$	$\cos^2(\alpha)$	$\sin(2\alpha)$	$\sin^2(\alpha)$
μ_4	t	t^3	t^3	t^3	t	t	t	t^3	t^3	t^3	t^3	t^3	t^3

Table 2.4: Global parametric functions $B_i^k(\mu_i)$ for the lattice structure.

It is observed from Table 2.4, that an ordering criteria has been set for the $k = 1, \dots, \mathbf{n}_k$ separated terms of the global stiffness matrix, \mathbf{K}^k , each one of them associated to a product of parametric functions $\prod_{i=1}^{\mathbf{n}_p} B_i^k$. Now the methodology to build each of the global matrices \mathbf{K}^k follows pretty much the finite element procedures, with slight considerations that take into account the particularities of the parametric affine decomposition. In Algorithm 1 it is sketched the standard FE loop, together with some particular considerations that allow building separated matrices \mathbf{K}^k for our parametric honeycomb structure.

Data: FE connectivities, $e\ell Typ_e$: element type, for $e = 1, \dots, \mathbf{n}_e$.

Parametric functions B_i^k , for $k = 1, \dots, \mathbf{n}_k$.

Result: \mathbf{K}^k separated matrices, for $k = 1, \dots, \mathbf{n}_k$.

for $e = 1 \dots \mathbf{n}_e$ **do**

switch $e\ell Typ_e$ **do**

case “ $e \in hor$ ” **do**

 • Compute $\widehat{\mathbf{K}}_e^f$ from (2.11), for $f = 1, \dots, \mathbf{n}_{k\ hor}$.

 • Assign local $\widehat{\mathbf{K}}_e^f$ to global \mathbf{K}^k for $k = 1, \dots, \mathbf{n}_{k\ hor}$.

end

case “ $e \in ob$ ” **do**

 • Compute \mathbf{K}_e^d from (2.20), for $d = 1, \dots, \mathbf{n}_{k\ ob}$.

 • Assign local \mathbf{K}_e^d to global \mathbf{K}^k for $k = (\mathbf{n}_{k\ hor} + 1), \dots, \mathbf{n}_k$.

end

end

end

Build all sparse \mathbf{K}^k , for $k = 1, \dots, \mathbf{n}_k$.

Algorithm 1: Adapted FE loop building the separated matrices \mathbf{K}^k that provide an affine decomposition of the parametric honeycomb stiffness.

2. PARAMETRIC LATTICE STRUCTURES

Figure 2.4 illustrates how does the data structure look for the affine decomposition of the parametric stiffness matrix $\mathbf{K}(\boldsymbol{\mu})$. It is presented as a Matlab[©] cell array variable “Ksep”, for the hexagonal honeycomb material made of 15×15 periodic repetitions of unit-cells, with a total number of DOF denoted by $\mathbf{n}_{\text{dof}} = 2880$ and $\mathbf{n}_p = 4$ parameters. For each term $k = 1, \dots, \mathbf{n}_k$, there is a sparse matrix $\mathbf{K}^k \in \mathbb{R}^{\mathbf{n}_{\text{dof}} \times \mathbf{n}_{\text{dof}}}$, and the complementary functions B_i^k , these latter evaluated at the 1D parametric meshes of size $\mathbf{n}_{d,i}$, for $i = 1, \dots, \mathbf{n}_p$.

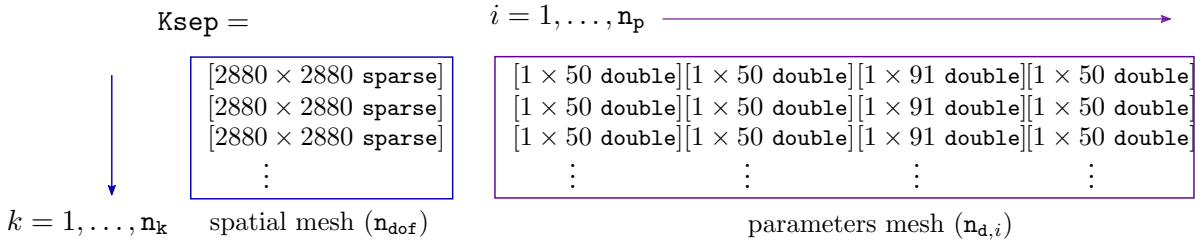


Figure 2.4: Data structure of $\mathbf{K}(\boldsymbol{\mu})$ affine decomposition in a Matlab[©] cell array variable “Ksep”. Honeycomb material sheet with spatial mesh size: $\mathbf{n}_{\text{dof}} = 2880$ and $\mathbf{n}_p = 4$ number of parameters.

In the next chapter, it is presented an algebraic PGD solver, which has the ability to take as inputs the stiffness matrix and force vector of a parametric structure - derived in the particular separated fashion - and produce as output an explicit solution in the multidimensional parametric space, avoiding the expensive calculations required with standard numerical solvers (e.g: finite elements). In addition, considering the algebraic nature of the solver and the flexibility of its implementation, it results very practical to treat different structural parametric problems, within the limits of linear elasticity. The user working load is limited to boiling down the parametric input data into the stiffness matrix and forcing term, both expressed in a separated structure.

Chapter 3

An algebraic PGD solver for parametric systems of linear equations

3.1 Problem statement

Consider a system of linear equations that depends on \mathbf{n}_p parameters, characterized by μ_i , for $i = 1, 2, \dots, \mathbf{n}_p$, each ranging in a real interval $I_i \subset \mathbb{R}$. For the sake of shortening the notation, the \mathbf{n}_p parameters are collected in a vector $\boldsymbol{\mu} = [\mu_1 \mu_2 \dots \mu_{\mathbf{n}_p}]^\top$. Accordingly, $\boldsymbol{\mu}$ ranges in the multidimensional parametric space $\mathcal{D} = I_1 \times I_2 \times \dots \times I_{\mathbf{n}_p} \subset \mathbb{R}^{\mathbf{n}_p}$.

Typically, this linear system would be the result of a parametric partial differential equation that has been discretized with finite elements. The unknowns of the parametric problem, *e.g.* displacements, are described by a vector $\mathbf{U}(\boldsymbol{\mu})$. The number of degrees of freedom of the problem is denoted by \mathbf{n}_{dof} and therefore for every value of the parameters, $\mathbf{U}(\boldsymbol{\mu}) \in \mathbb{R}^{\mathbf{n}_{\text{dof}}}$.

The parametric input data boils down to the stiffness matrix $\mathbf{K}(\boldsymbol{\mu}) \in \mathbb{R}^{\mathbf{n}_{\text{dof}} \times \mathbf{n}_{\text{dof}}}$ and the vector of nodal forces $\mathbf{F}(\boldsymbol{\mu}) \in \mathbb{R}^{\mathbf{n}_{\text{dof}}}$. Thus, the equilibrium equation reads

$$\mathbf{K}(\boldsymbol{\mu}) \mathbf{U}(\boldsymbol{\mu}) = \mathbf{F}(\boldsymbol{\mu}), \quad (3.1)$$

that must be solved to obtain $\mathbf{U}(\boldsymbol{\mu})$.

Equation (3.1) is stated in a parametric fashion, in the sense that input data \mathbf{K} and \mathbf{F} depend on $\boldsymbol{\mu}$ and therefore also the solution \mathbf{U} depends on $\boldsymbol{\mu}$. Thus, all these mathematical objects are fields taking values in the multidimensional parametric space \mathcal{D} . In the following, it is assumed that the parametric dependence of the input data is regular enough to be square integrable, that is $\mathbf{F}(\boldsymbol{\mu}) \in [\mathcal{L}_2(\mathcal{D})]^{\mathbf{n}_{\text{dof}}}$ and $\mathbf{K}(\boldsymbol{\mu}) \in [\mathcal{L}_2(\mathcal{D})]^{\mathbf{n}_{\text{dof}} \times \mathbf{n}_{\text{dof}}}$. Note that the parametric functional space $\mathcal{L}_2(\mathcal{D})$ is also expressed in terms of the sectional spaces $\mathcal{L}_2(I_i)$, with $i = 1, 2, \dots, \mathbf{n}_p$. Namely, $\mathcal{L}_2(\mathcal{D}) = \mathcal{L}_2(I_1) \otimes \mathcal{L}_2(I_2) \otimes \dots \otimes \mathcal{L}_2(I_{\mathbf{n}_p})$, which means that freezing all the parameters but one, the remaining functional dependence is square integrable.

In order to devise a numerical solver, the parametric space is also discretized. Finite-dimensional spaces $V_i \subset \mathcal{L}_2(I_i)$, whose dimension is $\mathbf{n}_{d,i}$, for $i = 1, 2, \dots, \mathbf{n}_p$, are introduced to approximate each sectional parametric space. Accordingly, the space where the discrete approximation to $\mathbf{U}(\boldsymbol{\mu})$ lies is $[V_1 \otimes V_2 \otimes \dots \otimes V_{\mathbf{n}_p}]^{\mathbf{n}_{\text{dof}}}$, with an overall dimension equal to

$$\mathbf{n}_{\text{Full}} = \mathbf{n}_{\text{dof}} \prod_{i=1}^{\mathbf{n}_p} \mathbf{n}_{d,i}. \quad (3.2)$$

The total number of unknowns \mathbf{n}_{Full} increases dramatically when the number of parameters \mathbf{n}_p is raised, producing the so-called *curse of dimensionality*. In other words, the number of degrees of freedom in the full multidimensional problem, \mathbf{n}_{Full} , grows exponentially with \mathbf{n}_p .

Reduced Order Models (ROM) are a possible alternative to overcome this difficulty. In particular, the Proper Generalized Decomposition (PGD) is a ROM based on the idea of producing a separable approximation of the multidimensional unknowns, such that the exponential computational complexity is reduced into a linear one.

Next section discusses the application of a PGD solver to the problem under consideration.

3.2 Separable approximations

The PGD solver output will be an approximated form of the unknown $\mathbf{U}(\boldsymbol{\mu})$ by a separable approximation $\mathbf{U}_{\text{PGD}}^n(\boldsymbol{\mu})$ with n terms, namely

$$\begin{aligned} \mathbf{U}(\boldsymbol{\mu}) \approx \mathbf{U}_{\text{PGD}}^n(\boldsymbol{\mu}) &= \sum_{m=1}^n \mathbf{u}^m G_1^m(\mu_1) G_2^m(\mu_2) \dots G_{\mathbf{n}_p}^m(\mu_{\mathbf{n}_p}), \\ &= \sum_{m=1}^n \mathbf{u}^m \prod_{i=1}^{\mathbf{n}_p} G_i^m(\mu_i), \\ &= \mathbf{U}_{\text{PGD}}^{n-1}(\boldsymbol{\mu}) + \mathbf{u}^n \prod_{i=1}^{\mathbf{n}_p} G_i^m(\mu_i). \end{aligned} \quad (3.3)$$

Each term, for $m = 1, 2, \dots, n$, is determined by a displacement vector \mathbf{u}^m and a set of parametric functions $G_i^m(\mu_i)$, for $i = 1, 2, \dots, \mathbf{n}_p$. Due to the similarity of (3.3) to a modal decomposition, for example the one frequently used in linear elastodynamics, (Cook et al., 2002, Chapter 11), \mathbf{u}^m is often referred to as the m^{th} spatial mode and the product $\prod_{i=1}^{\mathbf{n}_p} G_i^m(\mu_i)$ as the m^{th} parametric mode. In the following, in order to alleviate the notation and where there is no ambiguity, the explicit dependence on μ_i is omitted and $G_i^m(\mu_i)$ is written as G_i^m .

In order to use PGD, the input data, $\mathbf{K}(\boldsymbol{\mu})$ and $\mathbf{F}(\boldsymbol{\mu})$, must also be expressed in a separated form, that is

$$\mathbf{K}(\boldsymbol{\mu}) = \sum_{k=1}^{n_k} \mathbf{K}^k \prod_{i=1}^{n_p} B_i^k(\mu_i) \text{ and} \quad (3.4)$$

$$\mathbf{F}(\boldsymbol{\mu}) = \sum_{\ell=1}^{n_f} \mathbf{f}^\ell \prod_{i=1}^{n_p} S_i^\ell(\mu_i), \quad (3.5)$$

where n_k and n_f are the number of terms needed to express \mathbf{K} and \mathbf{F} in a separable manner, \mathbf{K}^k and \mathbf{f}^ℓ are the corresponding spatial modes and $B_i^k(\mu_i)$ and $S_i^\ell(\mu_i)$ are the parametric functions. For the sake of simplifying the notation, also the dependence of B_i^k and S_i^ℓ on the parameters is omitted in the following. In the case where input data can not be separated, a separable approximation has to be obtained as a pre-process. See for example [Zlotnik et al. \(2015\)](#), for a discussion on the errors introduced by this phase.

In the following, we will present a solution for equation (3.1), that is based on the weighted residuals idea. Thus, we first introduce the residual of (3.1) as

$$\mathbf{R}(\mathbf{U}(\boldsymbol{\mu})) := \mathbf{F}(\boldsymbol{\mu}) - \mathbf{K}(\boldsymbol{\mu}) \mathbf{U}(\boldsymbol{\mu}). \quad (3.6)$$

Then, one can state that $\mathbf{U}(\boldsymbol{\mu})$ is the solution of (3.1), if and only if

$$\int_{I_1} \int_{I_2} \cdots \int_{I_{n_p}} \delta \mathbf{U}(\boldsymbol{\mu})^\top \mathbf{R}(\mathbf{U}(\boldsymbol{\mu})) \, d\mu_{n_p} \cdots d\mu_2 \, d\mu_1 = 0 \quad (3.7)$$

for all $\delta \mathbf{U}(\boldsymbol{\mu}) \in [\mathcal{L}_2(\mathcal{D})]^{n_{\text{dof}}}$.

Note that no integration is performed in the physical space. The integrals involve only the parametric space \mathcal{D} . This is due to the algebraic nature of (3.1), which can be seen as already discretized in space. The role of the space integration (energy product) is played here by the scalar product of the residual (forces) and the test function (parametric virtual displacements).

3.3 PGD algebraic solver

The PGD solver is based on discretizing and solving the integral form presented in (3.7), using the separable approximations introduced in (3.3), (3.4) and (3.5). Formulating the PGD also requires to introduce sectional norms. These are norms defined only along each one of the independent parametric dimensions, which in turn will allow us to measure the PGD modes in the multidimensional space.

3.3.1 Sectional norms

The standard norm in $\mathcal{L}_2(I_i)$ is used to measure the parametric functions $G_i^m \in \mathcal{L}_2(I_i)$, namely

$$\|G_i^m\|^2 = \int_{I_i} (G_i^m)^2 d\mu_i. \quad (3.8)$$

The choice for the sectional norm affecting the space (or physical) dimension, that is the norm to measure the m^{th} spatial mode $\mathbf{u}^m \in \mathbb{R}^{\text{n}_{\text{dof}}}$, is not as basic. The obvious choice of selecting the Euclidean scalar product in $\mathbb{R}^{\text{n}_{\text{dof}}}$ would yield

$$\|\mathbf{u}^m\|^2 = [\mathbf{u}^m]^\top \mathbf{u}^m.$$

The Euclidean norm, however, does not take into account the nature of generalized nodal displacements, that are, for example, the ones that mix displacements and rotations, which are common in structural finite element formulations, such as beams, plates or shells. In these cases, the euclidean norm lacks of physical meaning, and a more suitable choice is using a structural mass matrix \mathbf{M}_u with sound physical rationale. The norm using \mathbf{M}_u results in

$$\|\mathbf{u}^m\|^2 = [\mathbf{u}^m]^\top \mathbf{M}_u \mathbf{u}^m. \quad (3.9)$$

The spatial modes and parametric functions are normalized using the sectional norms, that is

$$\tilde{\mathbf{u}}^m = \frac{1}{\|\mathbf{u}^m\|} \mathbf{u}^m \quad \text{and} \quad \tilde{G}_i^m = \frac{1}{\|G_i^m\|} G_i^m. \quad (3.10)$$

Thus, the separated representation of (3.3) is rewritten as

$$\mathbf{U}_{\text{PGD}}^n(\boldsymbol{\mu}) = \sum_{m=1}^n \beta^m \tilde{\mathbf{u}}^m \prod_{i=1}^{\text{n}_p} \tilde{G}_i^m, \quad (3.11)$$

where $\beta^m = \|\mathbf{u}^m\| \prod_{i=1}^{\text{n}_p} \|G_i^m\|$ is the amplitude of the m^{th} mode of the PGD.

Note that β^m provides a key information on the relative importance of the different modes in the separable approximation and therefore, it is used as one of the criteria to decide whether the number of terms, n , is sufficient to obtain a desirable accuracy.

A global norm in $[\mathcal{L}_2(\mathcal{D})]^{\text{n}_{\text{dof}}}$, the multidimensional space, is also introduced such that

$$\|\mathbf{U}(\boldsymbol{\mu})\|_{\text{G}_{\text{lob}}}^2 = \int_{I_1} \int_{I_2} \cdots \int_{I_{\text{n}_p}} \mathbf{U}(\boldsymbol{\mu})^\top \mathbf{M}_u \mathbf{U}(\boldsymbol{\mu}) d\mu_{\text{n}_p} \cdots d\mu_2 d\mu_1, \quad (3.12)$$

for any $\mathbf{U}(\boldsymbol{\mu}) \in [\mathcal{L}_2(\mathcal{D})]^{\text{n}_{\text{dof}}}$.

3.3.2 Greedy strategy and rank-one approximation

The PGD methodology aims at solving numerically equation (3.7) by using an approximation of the form shown in (3.3). This is performed using a greedy strategy, that is to compute the terms of the sum in (3.3) in a sequential approach. Thus, we start computing $\mathbf{U}_{\text{PGD}}^1$, and then, once $\mathbf{U}_{\text{PGD}}^1$ is available, we compute $\mathbf{U}_{\text{PGD}}^2$, and so on.

Each of the steps of the greedy algorithm, that is, updating some $\mathbf{U}_{\text{PGD}}^{n-1}$ into $\mathbf{U}_{\text{PGD}}^n$, consists in solving a rank-one approximation problem.

Accordingly, it is assumed that $\mathbf{U}_{\text{PGD}}^{n-1}$ is known and that

$$\mathbf{U}_{\text{PGD}}^n = \mathbf{U}_{\text{PGD}}^{n-1} + \mathbf{u} \prod_{i=1}^{n_p} G_i, \quad (3.13)$$

where the superscript n in \mathbf{u}^n and G_i^n is omitted here to simplify the notation.

The problem consists now in finding \mathbf{u} , G_1, G_2, \dots, G_{n_p} such that $\mathbf{U}_{\text{PGD}}^n$ fulfills (3.7). The complete unknown function $\mathbf{u} \prod_{i=1}^{n_p} G_i$ is said to be of rank one because it is built as the product of sectional functions. The problem at hand is nonlinear (because the unknown functions are multiplying each other) but with a number of degrees of freedom much lower than the original one. Recall that the discrete version of the full linear problem has a number of degrees of freedom n_{Full} given in (3.2). Instead, with the PGD strategy, each rank-one approximation problem is nonlinear but with a number of degrees of freedom n_{RankOne} , given by:

$$n_{\text{RankOne}} = n_{\text{dof}} + \sum_{i=1}^{n_p} n_{d,i}. \quad (3.14)$$

Typically, due to the additive nature of n_{RankOne} in terms of the sectional dimensions, $n_{\text{RankOne}} \ll n_{\text{Full}}$ holds and therefore the reduction of the dimension of the problem is well worth the difficulties associated with the newly acquired nonlinear character.

Due to the incremental character of (3.13), the expression of the residual (3.6) is rewritten as

$$\mathbf{R}(\mathbf{U}_{\text{PGD}}^n) = \mathbf{R}(\mathbf{U}_{\text{PGD}}^{n-1}) - \mathbf{K}(\boldsymbol{\mu}) \mathbf{u} \prod_{i=1}^{n_p} G_i, \quad (3.15)$$

which, using (3.4), becomes

$$\begin{aligned} \mathbf{R}(\mathbf{U}_{\text{PGD}}^n) &= \mathbf{R}(\mathbf{U}_{\text{PGD}}^{n-1}) - \left[\sum_{k=1}^{n_k} \mathbf{K}^k \prod_{i=1}^{n_p} B_i^k \right] \mathbf{u} \prod_{i=1}^{n_p} G_i \\ &= \mathbf{R}(\mathbf{U}_{\text{PGD}}^{n-1}) - \sum_{k=1}^{n_k} \left[\prod_{i=1}^{n_p} B_i^k G_i \right] \mathbf{K}^k \mathbf{u}. \end{aligned} \quad (3.16)$$

The test function $\delta \mathbf{U}(\boldsymbol{\mu})$ in (3.7) has to be selected in accordance with the unknowns of the rank-one problem, which consists in introducing in equation (3.7), the residual as defined in (3.16). Thus, the test function is taken as a variation of the actual unknowns $\mathbf{u} \prod_{i=1}^{n_p} G_i$, yielding

$$\delta \mathbf{U} = \delta \mathbf{u} \prod_{i=1}^{n_p} G_i + \mathbf{u} \sum_{i=1}^{n_p} \delta G_i \prod_{\substack{j=1 \\ j \neq i}}^{n_p} G_j, \quad (3.17)$$

where the explicit dependence on $\boldsymbol{\mu}$ has been omitted in the notation.

That is, instead of taking an arbitrary $\delta\mathbf{U} \in [\mathcal{L}_2(\mathcal{D})]^{\text{n}_{\text{dof}}}$ as in (3.7), one must take arbitrary $\delta\mathbf{u} \in \mathbb{R}^{\text{n}_{\text{dof}}}$ and $\delta G_i \in \mathcal{L}_2(I_i)$, for $i = 1, 2, \dots, \mathbf{n}_p$. Then, in the numerical version, the finite-dimensional sectional spaces V_i replace $\mathcal{L}_2(I_i)$.

The numerical strategy to deal with the nonlinearity of this problem is based on the alternated directions idea, [Ammar et al. \(2010\)](#), which is also referred to as fixed-point solver.

3.3.3 Alternated directions: fixed-point solver

The alternated directions strategy consists in successively solving each one of the nonlinear problem unknowns, assuming that the rest of them are known, until all these reach a stationary point.

3.3.3.1 Computing \mathbf{u}

The first step consists in, assuming all G_i known, for $i = 1, 2, \dots, \mathbf{n}_p$, compute \mathbf{u} such that $\mathbf{R}(\mathbf{U}_{\text{PGD}}^n)$ satisfies equation (3.7). Since all G_i are known, δG_i is taken to be zero, for $i = 1, 2, \dots, \mathbf{n}_p$, and $\delta\mathbf{U}$ in (3.17) reduces to

$$\delta\mathbf{U} = \delta\mathbf{u} \prod_{i=1}^{\mathbf{n}_p} G_i.$$

Thus, in this case, equation (3.7) becomes

$$\int_{\times_{j=1}^{\mathbf{n}_p} I_j} \delta\mathbf{u}^\top \mathbf{R}(\mathbf{U}_{\text{PGD}}^n) \prod_{i=1}^{\mathbf{n}_p} G_i \, d\mu_j = 0,$$

for all $\delta\mathbf{u} \in \mathbb{R}^{\text{n}_{\text{dof}}}$. Note that the notation has been shortened in a single multidimensional integral but using $\times_{j=1}^{\mathbf{n}_p} I_j$ instead of \mathcal{D} because this notation is going to be useful in the following. If the previous equation is fulfilled for all $\delta\mathbf{u} \in \mathbb{R}^{\text{n}_{\text{dof}}}$, it is equivalent to the following algebraic equation in $\mathbb{R}^{\text{n}_{\text{dof}}}$:

$$\int_{\times_{j=1}^{\mathbf{n}_p} I_j} \mathbf{R}(\mathbf{U}_{\text{PGD}}^n) \prod_{i=1}^{\mathbf{n}_p} G_i \, d\mu_i = \mathbf{0}.$$

Substituting $\mathbf{R}(\mathbf{U}_{\text{PGD}}^n)$ by the expression (3.16) one gets

$$\int_{\times_{j=1}^{\mathbf{n}_p} I_j} \left(\mathbf{R}(\mathbf{U}_{\text{PGD}}^{n-1}) - \sum_{k=1}^{\mathbf{n}_k} \left[\prod_{i=1}^{\mathbf{n}_p} B_i^k G_i \right] \mathbf{K}^k \mathbf{u} \right) \prod_{i=1}^{\mathbf{n}_p} G_i \, d\mu_i = \mathbf{0}.$$

The expression $\mathbf{R}(\mathbf{U}_{\text{PGD}}^{n-1})$ in the previous is expanded using the definition of the residual in (3.15), and the separable expressions for $\mathbf{K}(\boldsymbol{\mu})$ and $\mathbf{F}(\boldsymbol{\mu})$ in (3.4) and (3.5) respectively. All terms coming from $\mathbf{R}(\mathbf{U}_{\text{PGD}}^{n-1})$ are known quantities, and taking them to the right-hand side it results

$$\left[\sum_{k=1}^{\mathbf{n}_k} \mathbf{K}^k \underbrace{\prod_{i=1}^{\mathbf{n}_p} \int_{I_i} B_i^k (G_i)^2 d\mu_i}_{c^k} \right] \mathbf{u} = \sum_{\ell=1}^{\mathbf{n}_f} \mathbf{f}^\ell \underbrace{\prod_{i=1}^{\mathbf{n}_p} \int_{I_i} S_i^\ell G_i d\mu_i}_{\hat{c}^\ell} \quad (3.18)$$

$$- \sum_{m=1}^{n-1} \left[\sum_{k=1}^{\mathbf{n}_k} \mathbf{K}^k \underbrace{\prod_{i=1}^{\mathbf{n}_p} \int_{I_i} B_i^k G_i^m G_i d\mu_i}_{c^{k,m}} \right] \mathbf{u}^m.$$

That is, a linear system of equations for \mathbf{u} :

$$\left[\sum_{k=1}^{\mathbf{n}_k} \mathbf{K}^k c^k \right] \mathbf{u} = \sum_{\ell=1}^{\mathbf{n}_f} \mathbf{f}^\ell \hat{c}^\ell - \sum_{m=1}^{n-1} \left[\sum_{k=1}^{\mathbf{n}_k} \mathbf{K}^k c^{k,m} \right] \mathbf{u}^m, \quad (3.19)$$

where scalars c^k , \hat{c}^ℓ and $c^{k,m}$ are computable terms defined by:

$$c^k := \prod_{i=1}^{\mathbf{n}_p} \int_{I_i} B_i^k (G_i)^2 d\mu_i, \quad (3.20)$$

$$\hat{c}^\ell := \prod_{i=1}^{\mathbf{n}_p} \int_{I_i} S_i^\ell G_i d\mu_i \quad \text{and} \quad (3.21)$$

$$c^{k,m} := \prod_{i=1}^{\mathbf{n}_p} \int_{I_i} B_i^k G_i^m G_i d\mu_i. \quad (3.22)$$

3.3.3.2 Computing G_i , for $i = 1, 2, \dots, \mathbf{n}_p$

The subsequent steps consist in computing one parametric function, say G_i , assuming that \mathbf{u} and the rest of the parametric modes G_j - for $j = 1, 2, \dots, \mathbf{n}_p$ and $j \neq i$ - are known. Thus, the corresponding variations δG_j and $\delta \mathbf{u}$ are taken to be zero, and the variation $\delta \mathbf{U}$ in (3.17) becomes

$$\delta \mathbf{U} = \mathbf{u} \delta G_i \prod_{\substack{j=1 \\ j \neq i}}^{\mathbf{n}_p} G_j.$$

Using this variation in (3.7) for $\delta \mathbf{U}$ one gets that

$$\int_{I_i} \delta G_i \left[\int_{\times_{j \neq i} I_j} \mathbf{u}^\top \mathbf{R}(\mathbf{U}_{\text{PGD}}^n) \prod_{j \neq i} G_j d\mu_j \right] d\mu_i = 0, \quad (3.23)$$

3. ALGEBRAIC PGD SOLVER

which must hold for all $\delta G_i \in \mathcal{L}_2(I_i)$. In order to ease the reading, the range of j : $j = 1, 2, \dots, n_p$ and $j \neq i$ is omitted, emphasizing only the fact that $j \neq i$. Note that (3.23) is an equation for the unknown function $G_i(\mu_i)$, that appears explicitly in $\mathbf{R}(\mathbf{U}_{\text{PGD}}^n)$ - see (3.15) -. Indeed, the integral equation (3.23) results in the following equation for $G_i(\mu_i)$:

$$\int_{\times_{j \neq i} I_j} \mathbf{u}^\top \left[\mathbf{R}(\mathbf{U}_{\text{PGD}}^{n-1}) - G_i \mathbf{K}(\boldsymbol{\mu}) \mathbf{u} \prod_{j \neq i} G_j \right] \prod_{j \neq i} G_j d\mu_j = 0. \quad (3.24)$$

That is

$$G_i \left[\int_{\times_{j \neq i} I_j} \mathbf{u}^\top \mathbf{K}(\boldsymbol{\mu}) \mathbf{u} \prod_{j \neq i} (G_j)^2 d\mu_j \right] = \int_{\times_{j \neq i} I_j} \mathbf{u}^\top \mathbf{R}(\mathbf{U}_{\text{PGD}}^{n-1}) \prod_{j \neq i} G_j d\mu_j, \quad (3.25)$$

where both the term in brackets in the left-hand side and the right-hand side of (3.25) are computable functions in I_i . The expression for these functions is determined using the definition of the residual $\mathbf{R}(\mathbf{U}_{\text{PGD}}^{n-1})$ from (3.15) and the forms of the data given in (3.4) and (3.5). The resulting equation reads

$$G_i(\cdot) = \frac{\sum_{\ell=1}^{n_f} (\mathbf{u}^\top \mathbf{f}^\ell) \hat{d}_i^\ell(\cdot) - \sum_{m=1}^{n-1} \sum_{k=1}^{n_k} (\mathbf{u}^\top \mathbf{K}^k \mathbf{u}^m) d_i^{k,m}(\cdot)}{\sum_{k=1}^{n_k} (\mathbf{u}^\top \mathbf{K}^k \mathbf{u}) d_i^k(\cdot)}, \quad (3.26)$$

where the notation $G_i(\cdot)$ is used to stress that $G_i(\mu_i)$ takes values in the interval I_i , as well as the computable functions $d_i^k(\cdot)$, $\hat{d}_i^\ell(\cdot)$ and $d_i^{k,m}(\cdot)$, which in turn are defined by

$$d_i^k(\cdot) := \left(\prod_{\substack{j=1; \\ j \neq i}}^{n_p} \int_{I_j} B_j^k (G_j)^2 d\mu_j \right) B_i^k(\cdot), \quad (3.27)$$

$$\hat{d}_i^\ell(\cdot) := \left(\prod_{\substack{j=1; \\ j \neq i}}^{n_p} \int_{I_j} S_j^\ell G_j d\mu_j \right) S_i^\ell(\cdot) \text{ and} \quad (3.28)$$

$$d_i^{k,m}(\cdot) := \left(\prod_{\substack{j=1; \\ j \neq i}}^{n_p} \int_{I_j} B_j^k G_j^m G_j d\mu_j \right) B_i^k(\cdot) G_i^m(\cdot). \quad (3.29)$$

3.3.3.3 Convergence control and stopping criterion

For each term of the PGD solution, that is for each value of $m = 1, 2, \dots, n$, the fixed-point solver iterations are expected to converge to the best rank-one approximation of $(\mathbf{U}_{\text{PGD}}^n - \mathbf{U}_{\text{PGD}}^{n-1})$, being $\mathbf{U}_{\text{PGD}}^{n-1}$ known and $\mathbf{U}_{\text{PGD}}^n$ unknown. This iterative algorithm (see Appendix A) requires a stopping criterion to decide whether the current iteration is acceptable or not. The stopping criterion is based on the stationarity of the solution: the iteration is validated if the modification from the previous iteration is small enough. Thus, assume that \mathbf{u} and G_i , for $i = 1, 2, \dots, n_p$, characterize the previous iteration and that after the fixed-point solver loop, the new approximation is given by \mathbf{u}^{new} and G_i^{new} , for $i = 1, 2, \dots, n_p$. The stopping criterion is expressed in terms of the difference between the two successive iterations, measured with the norms introduced in section 3.3.1.

In particular, a typical convergence criterion is to continue iterating while

$$\left\| \mathbf{u}^{\text{new}} \prod_{i=1}^{n_p} G_i^{\text{new}} - \mathbf{u} \prod_{i=1}^{n_p} G_i \right\|_{\text{Glob}} > \eta_{\text{tol}} \left\| \mathbf{u}^{\text{new}} \prod_{i=1}^{n_p} G_i^{\text{new}} \right\|_{\text{Glob}}, \quad (3.30)$$

where the global norm has been introduced in (3.12) and η_{tol} is a small user-prescribed tolerance.

The computation of these norms is simplified by using the normalized spatial mode, parametric functions and modal amplitude: $\tilde{\mathbf{u}}$, \tilde{G}_i and β , given in equation (3.10). Then,

$$\begin{aligned} \left\| \mathbf{u}^{\text{new}} \prod_{i=1}^{n_p} G_i^{\text{new}} - \mathbf{u} \prod_{i=1}^{n_p} G_i \right\|_{\text{Glob}}^2 &= \left\| \mathbf{u}^{\text{new}} \prod_{i=1}^{n_p} G_i^{\text{new}} \right\|_{\text{Glob}}^2 + \left\| \mathbf{u} \prod_{i=1}^{n_p} G_i \right\|_{\text{Glob}}^2 \\ &\quad - 2 (\mathbf{u}^{\text{new}}, \mathbf{u}) \prod_{i=1}^{n_p} (G_i^{\text{new}}, G_i), \quad (3.31) \\ &= (\beta^{\text{new}})^2 + \beta^2 \\ &\quad - 2\beta^{\text{new}}\beta (\tilde{\mathbf{u}}^T \mathbf{M}_{\mathbf{u}} \tilde{\mathbf{u}}^{\text{new}}) \prod_{i=1}^{n_p} \int_{I_i} \tilde{G}_i^{\text{new}} \tilde{G}_i d\mu_i, \end{aligned}$$

where all the sectional scalar products are denoted in a unified fashion by the bilinear operator (\cdot, \cdot) . Note that, if the new iteration coincides with the previous one, this expression vanishes because the amplitudes are equivalent and the scalar products of identical and normalized spatial mode and parametric functions are equal to one.

In Appendix A, the fixed-point solver algorithm is detailed.

3.3.3.4 Remark on the algebraic PGD solver parallelization

It has been acknowledged in previous works that the fixed-point solver or alternate directions, used for the linearization of (3.7), has the drawback of being non parallelizable (Zou (2017)). In fact, what we observe is that each of the fixed-point iterations,

implies solving a sequence of equations given by (3.19) and (3.26), this latter being called once for each of the parameters μ_i , for $i = 1, \dots, n_p$. During this sequence, one can use the values of the unknowns \mathbf{u} and G_i , for $i = 1, \dots, n_p$, computed at the previous iteration or the values of the unknowns \mathbf{u}^{new} and G_i^{new} , for $i = 1, \dots, n_p$, computed at the current iteration. These strategies are analogous to the Jacobi Method or the Gauss-Seidel Method respectively, two well known iterative approaches for the solution of large linear systems (Black and Moore (2019)).

In this sense, we can apply any of the previous procedures to the PGD fixed-point iterations, and depending on our problem decide upon the advantages or drawbacks inherited by them. Typically, when performed in serial, the *Jacobi-like* approach is slower and requires to store the unknowns twice (at previous and current iterations). Nevertheless, it has the main advantage of being parallelizable, since equations (3.19) and (3.26) are treated independently, becoming irrelevant the order in which they are solved. On the other hand, the *Gauss-Seidel-like* approach is typically faster to converge - when performed in serial - and the unknowns are only stored once. However, serial computations can not be avoided and equations (3.19) and (3.26) can not be solved simultaneously. Although it is out of the scope of the present work, it is remarked that depending on the nature of the parametric problem, it might be interesting to choose smartly between one of these two approaches.

3.3.4 PGD compression

The n terms of PGD solution $\mathbf{U}_{\text{PGD}}^n$ may contain redundant information. This is associated with the greedy strategy employed to compute the successive terms, with no enforcement of any *orthogonality* between the successive modes. Thus, the number of terms in an *optimal* separable approximation required to achieve the same level of accuracy as in $\mathbf{U}_{\text{PGD}}^n$ could be lower than n . This can be checked a posteriori in the 2D case, where the Singular Value Decomposition (SVD) provides an optimal separation, with the least number of terms. For parametric problems of higher dimensions, the PGD lack of orthogonality still holds, but there is no optimal solution to compare with, given that the High Order SVD - or HO-SVD - is no longer optimal (Kolda and Bader (2009)).

In order to mitigate the effect of this phenomenon, a common practice in the PGD codes is to implement the so-called PGD compression, see Modesto et al. (2015), where it is referred to as “HO-PGD”. This compression consists in a least-squares projection of $\mathbf{U}_{\text{PGD}}^n$ into the same approximation space, computed with the very same PGD strategy, that is combining a greedy algorithm for the sequential terms and an alternated directions scheme for each of the spatial modes and parametric functions.

In the context of the algebraic PGD solver for parametric linear systems of equations (3.1), the PGD compression is formulated as follows. Let $\mathbf{U}_{\text{PGD}}^n$ indicate the *raw* PGD solution with n terms. Instead of solving the original equation (3.1) or its integral counterpart (3.7), now the objective is obtaining $\mathbf{U}_{\text{com}}^{\hat{n}}$ minimizing the

least-squares functional \mathcal{J} defined as

$$\mathcal{J}(\mathbf{U}_{\text{com}}^{\hat{n}}) = \|\mathbf{U}_{\text{com}}^{\hat{n}} - \mathbf{U}_{\text{PGD}}^n\|_{\text{Glob}}^2. \quad (3.32)$$

More precisely, the aim is at computing a separable approximation $\mathbf{U}_{\text{com}}^{\hat{n}}$, with \hat{n} terms expressed as

$$\mathbf{U}_{\text{com}}^{\hat{n}} = \sum_{\hat{m}=1}^{\hat{n}} \hat{\mathbf{u}}^{\hat{m}} \prod_{i=1}^{n_p} \hat{G}_i^{\hat{m}}, \quad (3.33)$$

using a PGD approach to minimize (3.32) with the objective of getting a sufficiently accurate approximation to $\mathbf{U}_{\text{PGD}}^n$ with $\hat{n} \ll n$.

Again, the main idea of the PGD strategy is to formulate a rank-one approximation of the minimization problem of (3.32). Thus, let us briefly describe how to compute the first term of $\mathbf{U}_{\text{com}}^{\hat{n}}$, taking

$$\mathbf{U}_{\text{com}} = \hat{\mathbf{u}} \prod_{i=1}^{n_p} \hat{G}_i.$$

Following the expansion in (3.31), the expression for $\mathcal{J}(\mathbf{U}_{\text{com}})$ is reduced to its dependence on the unknowns $\hat{\mathbf{u}}, \hat{G}_1, \dots, \hat{G}_{n_p}$ and reads

$$\begin{aligned} \mathcal{J}(\hat{\mathbf{u}}, \hat{G}_1, \dots, \hat{G}_{n_p}) &= \left\| \hat{\mathbf{u}} \prod_{i=1}^{n_p} \hat{G}_i \right\|_{\text{Glob}}^2 + \left\| \sum_{m=1}^n \mathbf{u}^m \prod_{i=1}^{n_p} G_i^m \right\|_{\text{Glob}}^2 \\ &\quad - 2 \sum_{m=1}^n (\hat{\mathbf{u}}, \mathbf{u}^m) \prod_{i=1}^{n_p} (\hat{G}_i, G_i^m). \end{aligned} \quad (3.34)$$

Again the alternated directions scheme is used here. The first step assumes that $\hat{G}_1, \dots, \hat{G}_{n_p}$ are known to compute $\hat{\mathbf{u}}$. Note that the previous functional is quadratic for $\hat{\mathbf{u}}$ and therefore the sectional minimization problem results in solving a linear system of equations for $\hat{\mathbf{u}}$. Indeed, for given values of $\hat{G}_1, \dots, \hat{G}_{n_p}$, the functional dependence on the remaining unknown reads

$$\begin{aligned} \mathcal{J}(\hat{\mathbf{u}}) &= (\hat{\mathbf{u}}^\top \mathbf{M}_{\mathbf{u}} \hat{\mathbf{u}}) \overbrace{\prod_{i=1}^{n_p} (\hat{G}_i, \hat{G}_i)}^{\lambda} + \left\| \sum_{m=1}^n \mathbf{u}^m \prod_{i=1}^{n_p} G_i^m \right\|_{\text{Glob}}^2 \\ &\quad - 2 \sum_{m=1}^n (\hat{\mathbf{u}}^\top \mathbf{M}_{\mathbf{u}} \mathbf{u}^m) \underbrace{\prod_{i=1}^{n_p} (\hat{G}_i, G_i^m)}_{\gamma^m}, \end{aligned} \quad (3.35)$$

and minimizing $\mathcal{J}(\hat{\mathbf{u}})$ requires solving $\frac{\partial \mathcal{J}(\hat{\mathbf{u}})}{\partial \hat{\mathbf{u}}} = 0$, that is

$$\mathbf{M}_{\mathbf{u}} \hat{\mathbf{u}} = \frac{1}{\lambda} \sum_{m=1}^n \gamma^m \mathbf{M}_{\mathbf{u}} \mathbf{u}^m \implies \hat{\mathbf{u}} = \frac{1}{\lambda} \sum_{m=1}^n \gamma^m \mathbf{u}^m. \quad (3.36)$$

Note that matrix \mathbf{M}_u cancels in both sides, and the solution of the linear system of equations is provided by an explicit expression.

The iteration to compute mode \hat{G}_i provided that $\hat{\mathbf{u}}$ and \hat{G}_j are available for $j = 1, 2, \dots, n_p$ and $j \neq i$ leads also to a simple equation. The sectional functional to be minimized reads

$$\begin{aligned} \mathcal{J}(\hat{G}_i) = & \left[\overbrace{(\hat{\mathbf{u}}^\top \mathbf{M}_u \hat{\mathbf{u}}) \prod_{j \neq i}^{n_i} (\hat{G}_j, \hat{G}_j)} \right] (\hat{G}_i, \hat{G}_i) + \left\| \sum_{m=1}^n \mathbf{u}^m \prod_{i=1}^{n_p} G_i^m \right\|_{\text{Glob}}^2 \\ & - 2 \sum_{m=1}^n \underbrace{(\hat{\mathbf{u}}^\top \mathbf{M}_u \mathbf{u}^m) \prod_{j \neq i} (\hat{G}_j, G_j^m)}_{\xi_i^m} (\hat{G}_i, G_i^m), \end{aligned} \quad (3.37)$$

which in turn gives as a result, the following function taking values in I_i :

$$\hat{G}_i(\cdot) = \frac{1}{\eta_i} \sum_{m=1}^n \xi_i^m G_i^m(\cdot). \quad (3.38)$$

Note that expressions (3.36) and (3.38) provide a very simple solver for each of the alternated directions iteration. In the case of the subsequent terms of $\mathbf{U}_{\text{com}}^{\hat{n}}$, that is for $\hat{n} > 1$, the expressions are very similar because one has to replace only $\mathbf{U}_{\text{PGD}}^n$ by $(\mathbf{U}_{\text{PGD}}^n - \mathbf{U}_{\text{com}}^{\hat{n}-1})$. Therefore, the expressions (3.36) and (3.38) are not significantly different, just slightly modified by a term involving a weighted sum of the $\hat{n} - 1$ previously computed terms. The reader is referred to Appendix B, where the complete PGD compression scheme is detailed.

The stopping criterion in this case is identical to that presented in Section 3.3.3.3. Again, what it is checked during the fixed-point solver iterations, is the stationarity of the solution. In fact, the same expression as in equation (3.31) can be straightforwardly used here taking $\hat{\mathbf{u}}$ instead of \mathbf{u} and \hat{G}_i instead of G_i .

3.4 Proposed 2D problems for PGD solver

Next chapter presents results about two different problems based on the parametric hexagonal honeycomb material. In one case, we model a parametric unit-cell and apply to it the homogenization theory. As a post-process, an explicit parametric effective constitutive tensor can be recovered for the material properties at the macro-scale. Moreover, a second problem is solved alternatively, using a tessellated structure made of periodic unit-cell repetitions. The full structure is subjected to a uni-axial tensile load in the horizontal and vertical directions. Finally, a comparison is made for some relevant mechanical properties, between measurements done in the periodic structure against the effective values recovered from the unit-cell with homogenization.

Chapter 4

Numerical solutions in 2D lattices

For all the structural elements, recall that Young’s modulus is set unitary: $E_e = 1$. The beam cross-section is assumed to be rectangular with a unitary width, and a thickness t . The parametric solutions are obtained using the PGD solver described in Chapter 3. In the following, it is described the information related to the problem boundary conditions, discretization of the parameters intervals and solver tolerances. Regarding the latter, a further insight is given in the PGD solver scheme presented in Appendix A.

Each of the parametric intervals I_i , for $i = 1, \dots, \mathbf{n}_p = 4$ is uniformly discretized with a number of points $\mathbf{n}_{d,1} = \mathbf{n}_{d,2} = 50$, $\mathbf{n}_{d,3} = 91$ and $\mathbf{n}_{d,4} = 50$ respectively.

The loads in all the problems are enforced via prescribed displacements (no tractions are applied on the boundary). In the analysis of the unit-cell, this includes periodicity constraints according to homogenization theory. An arbitrary prescribed PGD mode is introduced first such that it verifies the non-homogeneous Dirichlet boundary conditions (nonzero prescribed displacements). Afterward, the PGD solver is called to calculate the subsequent modes, where homogeneous essential conditions are enforced using Lagrange Multipliers. In this way, the sum of all terms verifies exactly the boundary conditions, whereas equilibrium is satisfied through a minimization of the parametrized PDE residual in the PGD framework described in Chapter 3.

The nonlinear iterations of the PGD fixed-point solver are stopped using the prescribed tolerance $\eta_{\text{tol}} = 10^{-6}$. In addition, the final number of terms in the PGD expansion is controlled by a criterion based on the modal amplitudes reduction. That means, the process computing PGD modes with amplitudes β^m , for $m = 1, 2, \dots, n$, is stopped at term number n if

$$\frac{\beta^n}{\max_{m=1,\dots,n}(\beta^m)} < \zeta,$$

where $\zeta = 10^{-3}$ or $\zeta = 10^{-4}$ are the tolerances typically used for the present structural problems. Once the PGD solution is obtained, a post-process called “PGD compression” (Díez et al. (2018)) is used to attempt a reduction of redundant PGD

modes. It is expected that the PGD compressed solution maintains the accuracy of the original one, but reduces the total number of modes. Despite a proper assessment of the error introduced by the PGD approximation is not presented in the following, the reader is referred to the works of [Ammar et al. \(2010\)](#); [Ladevèze and Chamoin \(2011\)](#); [Alfaro et al. \(2015\)](#); [Chamoin et al. \(2017\)](#).

The 2D problems presented next are, in section [4.1](#), the parametric solution of the honeycomb unit-cell model. Periodic boundary conditions (PBC) are prescribed for three independent load cases, that allow to build up the effective material properties at the bulk. The reader is referred to [Michel et al. \(1999\)](#) for the theoretical derivation of PBC in the context of homogenization, and [Theerakittayakorn and Nanakorn \(2013\)](#) for an insight in the implementation of PBC in structural beam models. Section [4.2](#) presents instead, the solution of the honeycomb parametric structure formed by periodic translations of the unit-cell.

It is well known that the present unit-cell architecture could exhibit auxetic performance depending on its parameters ([Elibe and Lantada \(2012\)](#)), therefore one of the most relevant mechanical properties is the effective Poisson's ratio. For both problems in the next sections, the Poisson's ratio can be obtained in an explicit parametric form. From the point of view of material design of auxetics, the PGD *vademecum* of mechanical properties is valued for analysis, since it provides an efficient browser for the parametric design space.

4.1 Unit-cell problem using homogenization

The goal here is to exploit the generalized solution of the parametric unit-cell to extract the effective mechanical properties at the macro-scale. Following the homogenization theory, the planar unit-cell has to be subjected to periodic boundary conditions, and loaded in the three independent cases described in [Figure 1.14](#). In addition, as explained in [Appendix C](#), the solution of the parametric unit-cell can be obtained analytically using a symbolic solver. Therefore, an insight on the PGD solver convergence is also presented in the following.

The first results show the evolution of the PGD modal amplitudes, for the parametric unit-cell subjected to three loading cases, see [Figure 4.1](#). It can be observed that the maximum number of PGD modes computed, i.e. the stopping criteria for the greedy algorithm, is set using $\zeta = 10^{-4}$. When the solution is post-processed with PGD compression, this condition is notably reached with a reduction in the number of modes, 38% and 26% for load cases XX and YY respectively. In all cases, it is observed that the modal amplitudes decrease more smoothly in the PGD post-process solution compared to the standard PGD greedy approach.

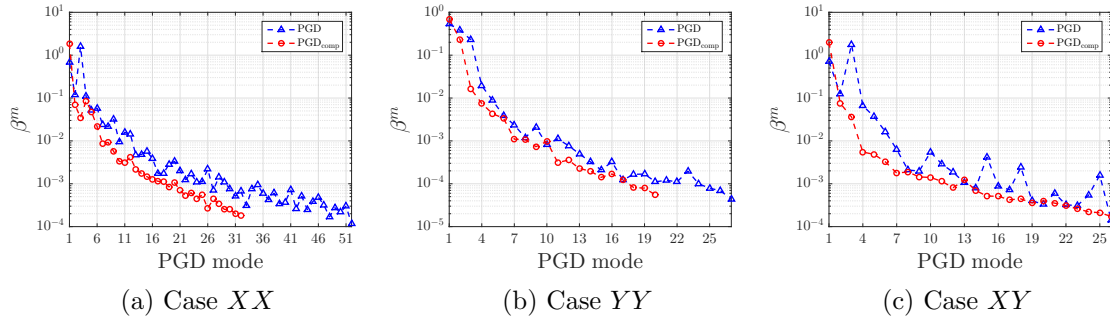


Figure 4.1: PGD modal amplitudes β^m , $m = 1, 2, \dots, n$ (with or without PGD compression). Parametric unit-cell subjected to periodic loading cases.

In our problem, each of the PGD spatial modes are vectors containing generalized displacements of the beam formulation. Their shape is depicted in Figures 4.2, 4.3 and 4.4, where two representative spatial modes are chosen, for the three unit-cell loading cases: XX , YY and XY respectively. In contrast to Reduced Basis approaches, the PGD spatial modes are not precisely FE solutions of the PDE at specific values of the parameters. They constitute instead, together with their complementary parametric functions, a term in the separated sum approximating the multidimensional solution of a parametric PDE. In the problem we are solving, a particular value is chosen for the parameters that modify the shape of the structure, in order to visualize the PGD spatial modes. For this purpose, we set $a = 0.6$, $b = 1.1$ and $\alpha = 75^\circ$, which results in the undeformed configuration of the unit-cell represented in Figures 4.2, 4.3 and 4.4, using dashed-blue lines.

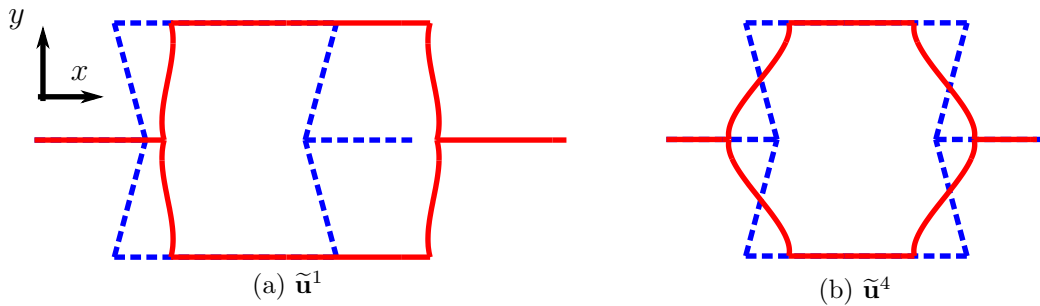


Figure 4.2: Unit-cell load case XX with PGD compression. Normalized spatial modes 1 and 4 scaled for illustration.

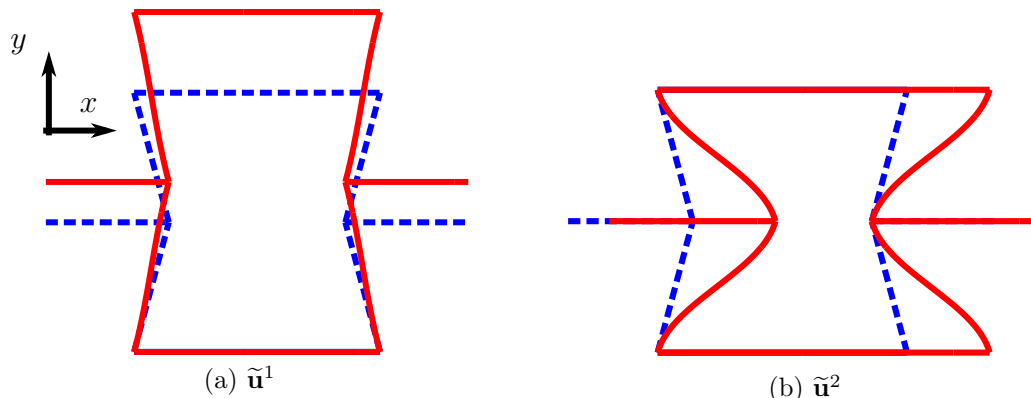


Figure 4.3: Unit-cell load case YY with PGD compression. Normalized spatial modes 1 and 2 scaled for illustration.

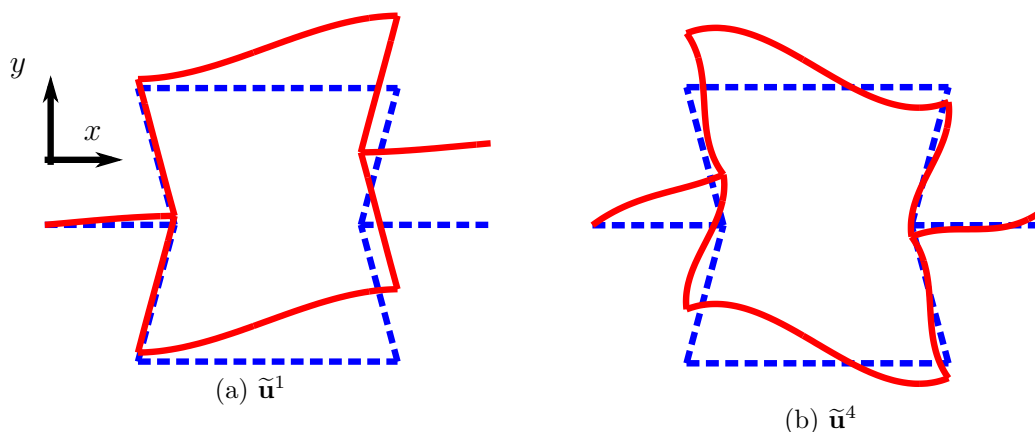


Figure 4.4: Unit-cell load case XY with PGD compression. Normalized spatial modes 1 and 4 scaled for illustration.

Naturally, the first spatial mode captures the essence of the unit-cell deformation under periodic boundary conditions, subjected to the imposed load cases. However, not all the features can be captured by the first mode, and some of them are very distinguished and relevant for the resulting material effective properties at the macro-scale. For this reason, it is necessary to introduce as well the normalized parametric functions \tilde{G}_i^m , being $i = 1, \dots, \mathbf{n}_p = 4$, that complement the PGD spatial modes presented before. In order to visualize the PGD mode significance, each parametric function \tilde{G}_i^m is weighted by $(\beta^m)^{\frac{1}{\mathbf{n}_p}}$, being β^m the amplitude of mode m and $\mathbf{n}_p = 4$ the number of parameters, see Figures 4.5, 4.6 and 4.7 for the unit-cell load cases XX , YY and XY .

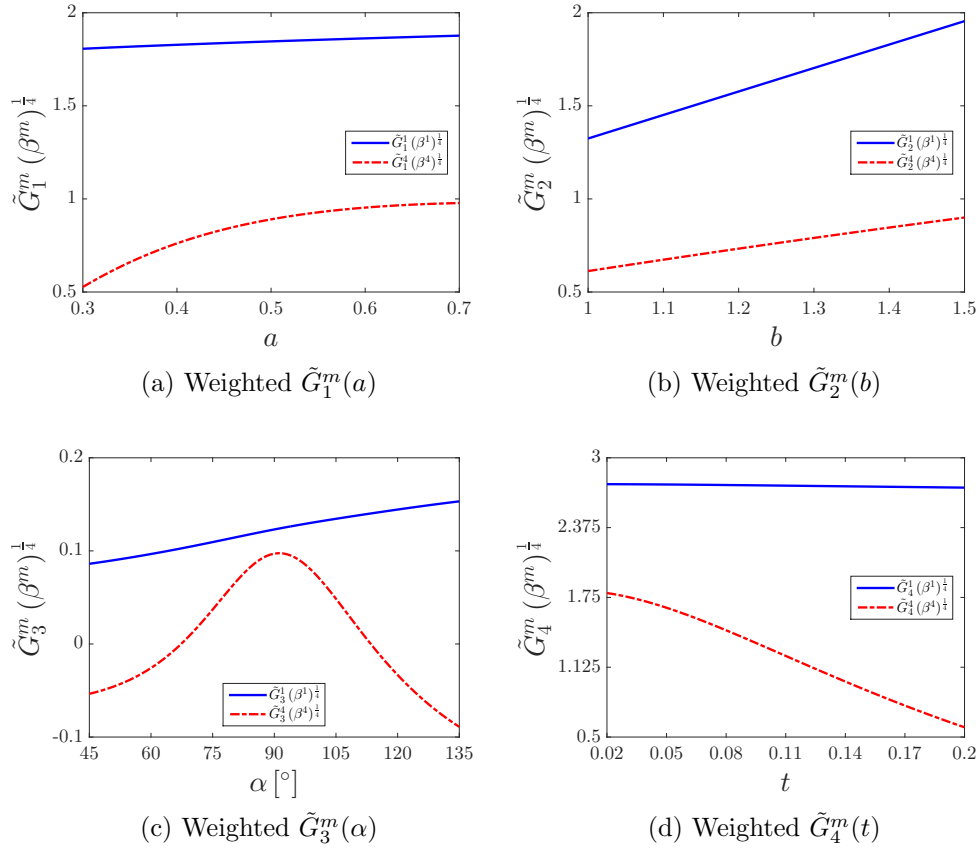


Figure 4.5: Unit-cell load case XX with PGD compression. Normalized parametric functions weighted for illustration.

Some remarkable considerations from the explicit parametric functions obtained by PGD are here reported. When observing the PGD spatial mode 2 shape in load case YY (Figure 4.3b), deformations of the unit-cell in the horizontal direction are present. These depend on parameter α by function \tilde{G}_3^2 , as detailed below in Figure 4.6c using a dashed-red line. The change of sign at $\alpha = 90^\circ$ - from negative to positive - commands the *auxetic* to *non-auxetic* behavior of the orthotropic effective Poisson's ratios. Further study on these properties is reported in subsection 4.1.2.

4. NUMERICAL SOLUTIONS IN 2D LATTICES

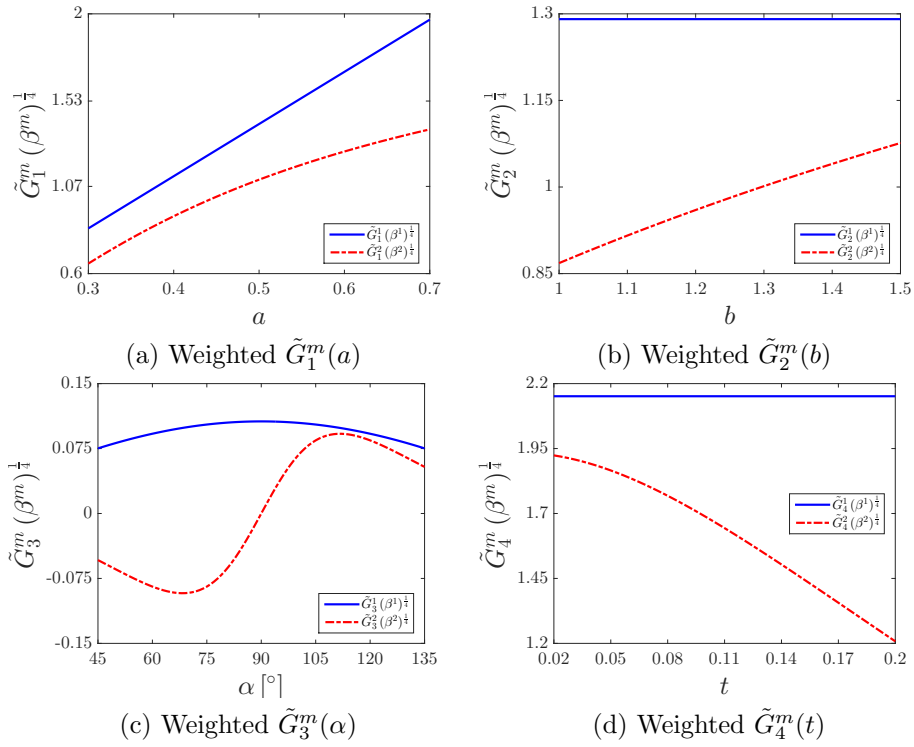


Figure 4.6: Unit-cell load case YY with PGD compression. Normalized parametric functions weighted for illustration.

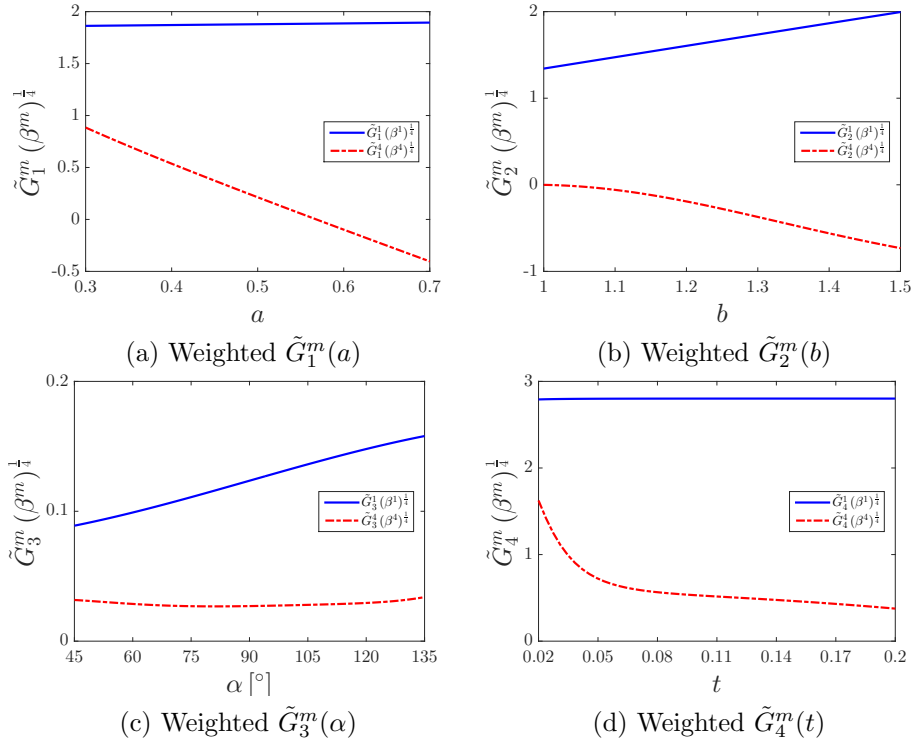


Figure 4.7: Unit-cell load case XY with PGD compression. Normalized parametric functions weighted for illustration.

The influence of parameter “ t ” shows almost a constant performance, as observed in Figures 4.5d, 4.6d and 4.7d for PGD mode 1 in all loading cases. This behavior is related to the fact that all unit-cell load cases are built upon prescribed displacements and not forces, therefore the change of stiffness associated to parameter “ t ” is mostly not reflected in the first modes. This is also the case for parameter “ b ”, which does not modify the first mode of load case YY , as seen in Figure 4.6b.

4.1.1 PGD solver performance

In order to compare how the added modes to the PGD solution conduct with respect to FE solutions, computed at different values of the parameters, the following relative error is defined:

$$\epsilon_{\text{FE}}(\boldsymbol{\mu} = \boldsymbol{\mu}_o) = \sqrt{\frac{(\mathbf{U}_{\text{PGD}} - \mathbf{U}_{\text{FE}})^{\text{T}} \mathbf{M} (\mathbf{U}_{\text{PGD}} - \mathbf{U}_{\text{FE}})}{\mathbf{U}_{\text{FE}}^{\text{T}} \mathbf{M} \mathbf{U}_{\text{FE}}}},$$

where $\mathbf{U}_{\text{PGD}}(\boldsymbol{\mu})$, $\mathbf{U}_{\text{FE}}(\boldsymbol{\mu})$ and $\mathbf{M}(\boldsymbol{\mu})$ are respectively the solution computed with the PGD solver, the one solved with FE and the unit-cell mass matrix. The dependence on $\boldsymbol{\mu}$ has been omitted to ease the notation in all these three, which are evaluated for different sets of random values of the parameters ($\boldsymbol{\mu} = \boldsymbol{\mu}_o$), outlined in Table 4.1:

Set	I	II	III	IV	V
b	1.31	1.47	1.21	1.09	1.01
a	0.39	0.53	0.32	0.69	0.61
α	106°	53°	134°	89°	66°
t	0.19	0.03	0.14	0.10	0.08

Table 4.1: Unit-cell sets of parameters where PGD error is evaluated against finite element solutions.

Figure 4.8 exposes the honeycomb unit-cell configurations for the five sets of random values of the parameters summarized above.

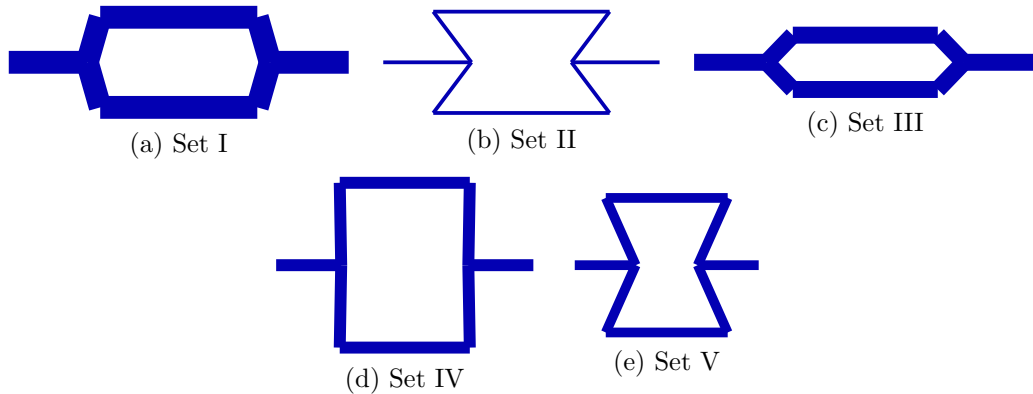


Figure 4.8: Honeycomb unit-cell configurations given by the sets of random values of the parameters.

4. NUMERICAL SOLUTIONS IN 2D LATTICES

Figure 4.9 shows the evolution of error $\epsilon_{\text{FE}}(\boldsymbol{\mu} = \boldsymbol{\mu}_o)$, computed for the unit-cell load cases. The PGD *vademecum* of solutions, evaluated at particular values of the parameters, shows excellent agreement when compared against FE solutions. Maximum errors below 2.5% in the L_2 norm are obtained for all loading cases. Although the same criterion has been used to stop the greedy computation of the modes, these errors behave different depending on the load case, showing that in general, the load case YY provides the minimum errors while XY the maximum. For all cases, errors tend to decrease fast for the first modes, and as the number of computed modes increases, the descend rate decays. Finally, the error trend of the PGD approximation does not present a monotonic decay, when compared to the FE solutions individually.

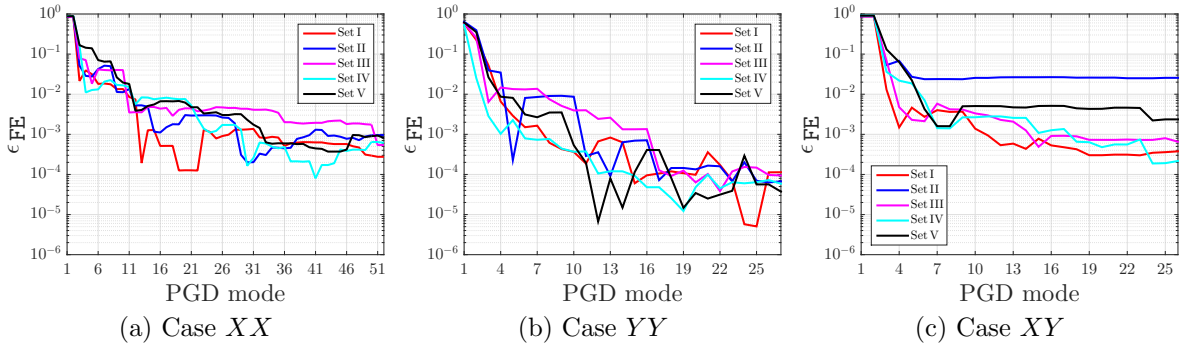


Figure 4.9: Unit-cell load cases: relative error of PGD solution against FE computed at different sets of parameters values.

However, the error of the PGD approximation can also be analyzed using a global measure in the parametric space. By means of the solution $\mathbf{U}(\boldsymbol{\mu})$ described in Appendix C, which is analytical in the parameters for each load case, a global relative error of the PGD is evaluated as:

$$\epsilon_{\text{glob}} = \sqrt{\frac{\sum_{\ell=1}^{14} \sum_{k=1}^{24} \sum_{j=1}^{14} \sum_{i=1}^{14} \|\mathbf{U}(\mu_1^i, \mu_2^j, \mu_3^k, \mu_4^\ell) - \mathbf{U}_{\text{PGD}}(\mu_1^i, \mu_2^j, \mu_3^k, \mu_4^\ell)\|^2}{\sum_{\ell=1}^{14} \sum_{k=1}^{24} \sum_{j=1}^{14} \sum_{i=1}^{14} \|\mathbf{U}(\mu_1^i, \mu_2^j, \mu_3^k, \mu_4^\ell)\|^2}}, \quad (4.1)$$

where the indexes i, j, k and ℓ range over the uniformly distributed points in the Cartesian $(I_1 \times I_2 \times I_3 \times I_4)$ multidimensional domain. As expressed in the summation limits above, a total of 14 points are used for parametric intervals I_1, I_2 and I_4 , whereas 24 for interval I_3 . Note that the global norm is calculated in an analogous way to the Frobenius norm of a matrix, extended here for the multidimensional parametric space. In addition, the vector norms above are computed using the L_2 norm such that $\|(\cdot)\|^2 = (\cdot)^\top \mathbf{M}(\boldsymbol{\mu}) (\cdot)$, with \mathbf{M} being properly evaluated at the corresponding values of the parameters $\boldsymbol{\mu} = \boldsymbol{\mu}_o = [\mu_1^i \mu_2^j \mu_3^k \mu_4^\ell]^\top$.

The results of the global relative PGD error convergence are shown in Figure 4.10 for the unit-cell load cases. Observing this Figure, the general trend indicates that each added mode contributes to reduce the error of the PGD solutions against the parametric analytical ones, when this one is measured in a global parametric norm.

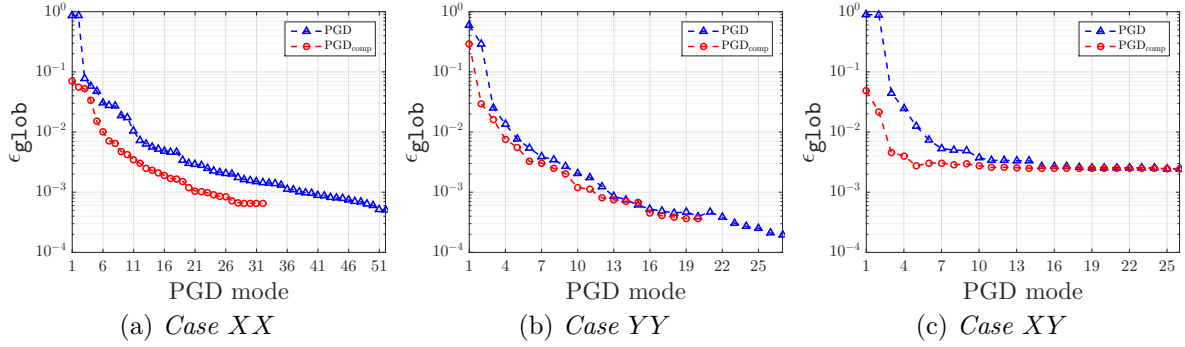


Figure 4.10: Relative error of $\mathbf{U}_{\text{PGD}}^n(\boldsymbol{\mu})$ in the unit-cell depending on the n number of PGD modes, measured in a global parametric norm.

For the unit-cell, all load cases show a maximum error below 0.2%, an excellent agreement with the parametric analytical solution for engineering purposes. However, it is also noted that depending on the nature of the solution, the same stopping criterion for the greedy algorithm - $\zeta = 10^{-4}$ - produces solutions with different error in the global relative norm. Particularly, it is noticed that in load case *XY*, the contribution of PGD modes to reduce the global error is notably decreased from mode 15 onwards. This suggests that further studies on PGD error indicators (Ammar et al. (2010)) are important to propose efficient algorithms (Nouy (2010)) and constructing adaptive PGD solutions (Chamoin et al. (2017)). With respect to PGD compression, it is noted that for a certain number of modes, the global error is lower than the original PGD solution, a fact that is especially appreciated for unit-cell load case *XX*. However, when the compressed solutions reach the same greedy stopping criteria $\zeta = 10^{-4}$, they show a slightly higher global error compared to the original ones.

4.1.2 Parametric effective properties with PGD

An interesting use of the PGD *vademecum* in the material design problem, is to exploit the unit-cell solutions to obtain explicit parametric material properties at the macro-scale. The components of the effective constitutive tensor can be constructed using the generalized displacement solutions of the parametric unit-cell problem, as described by the homogenization theory in equations (1.1) and (1.2). For the current problem, it can be shown that the effective mechanical properties result orthotropic (see the analytic parametric solutions in Appendix C). Being the material sheet orthotropic, two different parametric Poisson's ratios - $\nu_{12}^{\text{eff}}(\boldsymbol{\mu})$ and $\nu_{21}^{\text{eff}}(\boldsymbol{\mu})$ - are obtained following Bauchau and Craig (2009), which assumes a plane stress state and results:

$$\begin{aligned} \nu_{12}^{\text{eff}}(\boldsymbol{\mu}) &= \frac{C_{12}^{\text{eff}}(\boldsymbol{\mu})}{C_{22}^{\text{eff}}(\boldsymbol{\mu})} \quad \text{and} \\ \nu_{21}^{\text{eff}}(\boldsymbol{\mu}) &= \frac{C_{12}^{\text{eff}}(\boldsymbol{\mu})}{C_{11}^{\text{eff}}(\boldsymbol{\mu})}. \end{aligned} \quad (4.2)$$

In order to compute (4.2), it can be seen from equations (1.1) and (1.2), that the displacement solutions of the unit-cell problem, for load cases XX and YY , are needed. For this purpose, we use the PGD compressed solutions of the unit-cell that have 32 and 20 modes, see Figures 4.1a and 4.1b, when subjected to load cases XX and YY respectively.

It is appreciated in Figures 4.11 and 4.12, the orthotropic Poisson's ratios ν_{12}^{eff} and ν_{21}^{eff} respectively. These responses are displayed for the Cartesian parametric domain given by $I_1 \times I_3$ (that is, under variations of parameters $\mu_1 = a$ and $\mu_3 = \alpha$). In addition, for each of the response surfaces $\nu_{12}^{\text{eff}}(a, \alpha)$ and $\nu_{21}^{\text{eff}}(a, \alpha)$, four different snapshots are provided evaluating parameters $\mu_2 = b$ and $\mu_4 = t$ at the extremes of their intervals (I_2 and I_4 accordingly).

For both Poisson's ratios ν_{12}^{eff} and ν_{21}^{eff} , it is observed from Figures 4.11 and 4.12 that the unit-cell angle α rules the transition between positive to negative behavior, *non-auxetic* to *auxetic* and vice versa, independently on other values of the parameters. In addition, the extreme values of both Poisson's ratios are greatly diminished when the unit-cell beam thickness " t " is increased. This suggests that a proper mechanical engineering design should trade-off between extreme values of Poisson's ratio and the material stiffness that results at the macro-scale.

With respect to parameter " b ", it is observed that while increasing this length also increases the values of Poisson's ratio ν_{12}^{eff} , the opposite performance is observed for Poisson's ratio ν_{21}^{eff} . Moreover, the ranges obtained for ν_{12}^{eff} and ν_{21}^{eff} noted in Figures 4.11 and 4.12 are well beyond the Poisson's ratio limits for isotropic materials: $-1 < \nu < 0.5$. The possibility of obtaining a broader range of Poisson's ratio by design is a relevant physical property of orthotropic materials. Nevertheless, not any spectrum of orthotropic Poisson's ratios are necessarily thermodynamically consistent, see the work by Lempriere (1968). In our particular case, where the material is 2D-orthotropic, the following two conditions must be satisfied at the same time: ν_{12}^{eff} and ν_{21}^{eff} must be of the same sign, and the inequality $1 - \nu_{12}^{\text{eff}} \nu_{21}^{\text{eff}} > 0$ must hold.

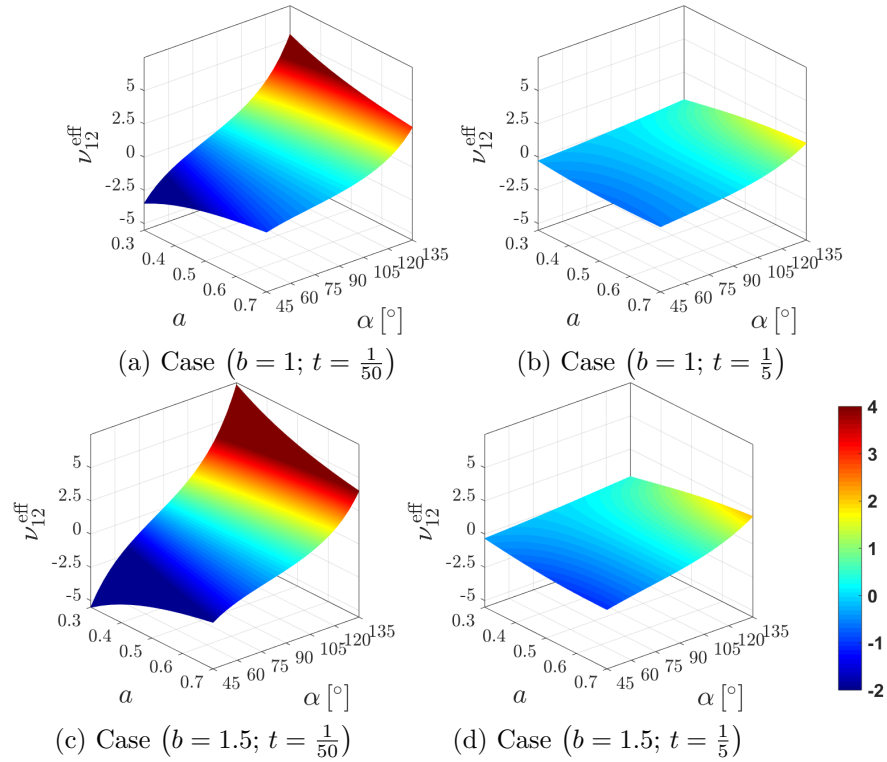


Figure 4.11: ν_{12}^{eff} response in $a \times \alpha$ for specified values of b and t .

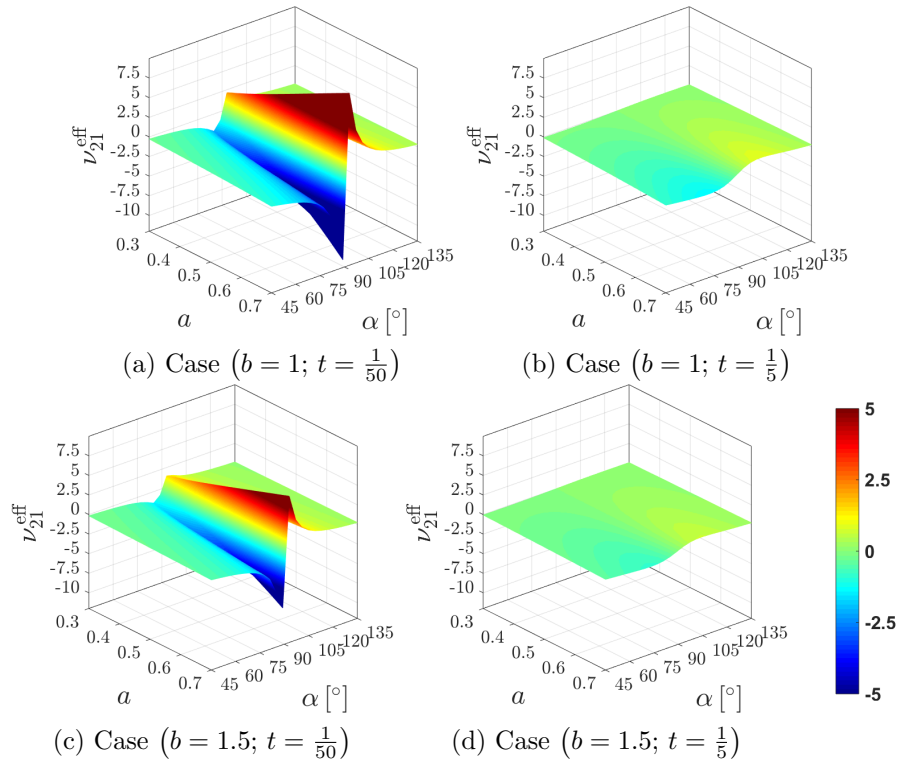


Figure 4.12: ν_{21}^{eff} response in $a \times \alpha$ for specified values of b and t .

4.2 Periodic pattern of hexagonal honeycomb cells

The PGD solver application is extended now to a lattice material structure made of a periodic array of $n_{\text{hor}} \times n_{\text{ver}}$ unit-cells. This material structure will be subjected to uni-axial tensile loads in the horizontal - X - and the vertical - Y - directions. Given the structural symmetry and the boundary conditions considered in both load cases (see Figure 4.13), it is possible to reduce the model to one quarter of the honeycomb sheet. The loads are applied by prescribing uniform displacements at the edges sketched in Figure 4.13, such that a 10% strain is implemented in all cases. Note that the load quantity is taken just as a reference for our linear model, given that it can be proportionally scaled. However, the imposition of an equal strain for the parametric material structure results in non-homogeneous Dirichlet boundary conditions, whose dependence on the parameters must be taken into account.

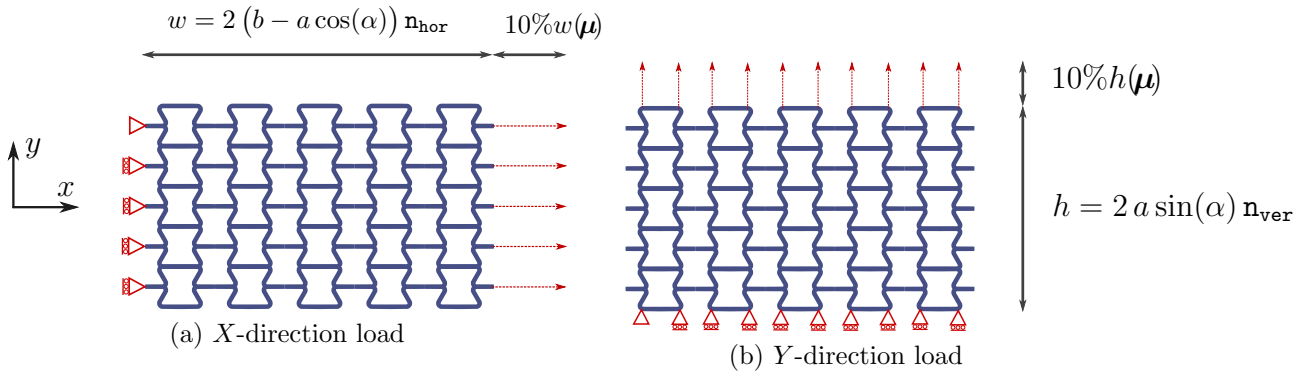


Figure 4.13: Periodic 5×5 array of honeycomb cells subjected to tensile loads.

Although the unit-cell model with homogenization is the standard approach for measuring the effective mechanical properties at the macro-scale, from the practical point of view, one may need to take into account the behavior of the full structure, for example in the case of highly inhomogeneous structural loads, or when boundary effects are important to take into account in the analysis. In our particular case, we observe that the auxetic behavior can be directly perceived visually from the deformation in the parametric full pattern, whereas in the unit-cell model is acknowledged indirectly after computing the material effective properties.

In the following, we analyze the PGD *vademecum* for the honeycomb sheet, subjected to the two uni-axial loads in consideration. In Figure 4.14, it is shown the evolution of the PGD modal amplitudes, comparing the direct output from the PGD solver and the other one after performing PGD compression. As it has been observed from numerical experiments, see for example the paper by Díez et al. (2018), the PGD compression is able to reduce the amount of modes in the original PGD solution, when the same criterion is used for stopping the greedy computation of new terms. It is also observed that the decaying response of the modal amplitudes is smoothed in the PGD compressed solution, for the two load cases detailed in Figure 4.14.

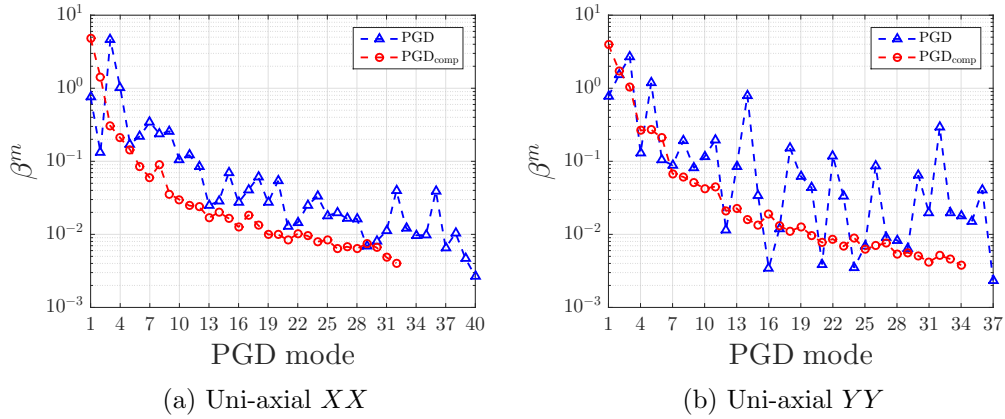


Figure 4.14: PGD modal amplitudes β^m , $m = 1, 2, \dots, n$ (with or without PGD compression). Honeycomb periodic structure subjected to uni-axial tensile loads.

In Figure 4.15, the first two spatial modes obtained with PGD compression in the honeycomb periodic structure are shown for the two uni-axial loads. It is observed that these two modes are very similar for both loads in X and Y directions, although they have distinct physical meanings. For example, the spatial modes corresponding to deformation across the transverse direction to the applied load are the second one $\tilde{\mathbf{u}}_x^2$ for loading direction X whereas the first one $\tilde{\mathbf{u}}_y^1$ for loading direction Y . Thus, these modes will contribute to the orthotropic Poisson's ratio behavior, ν_{12} and ν_{21} respectively, of the present honeycomb sheet.

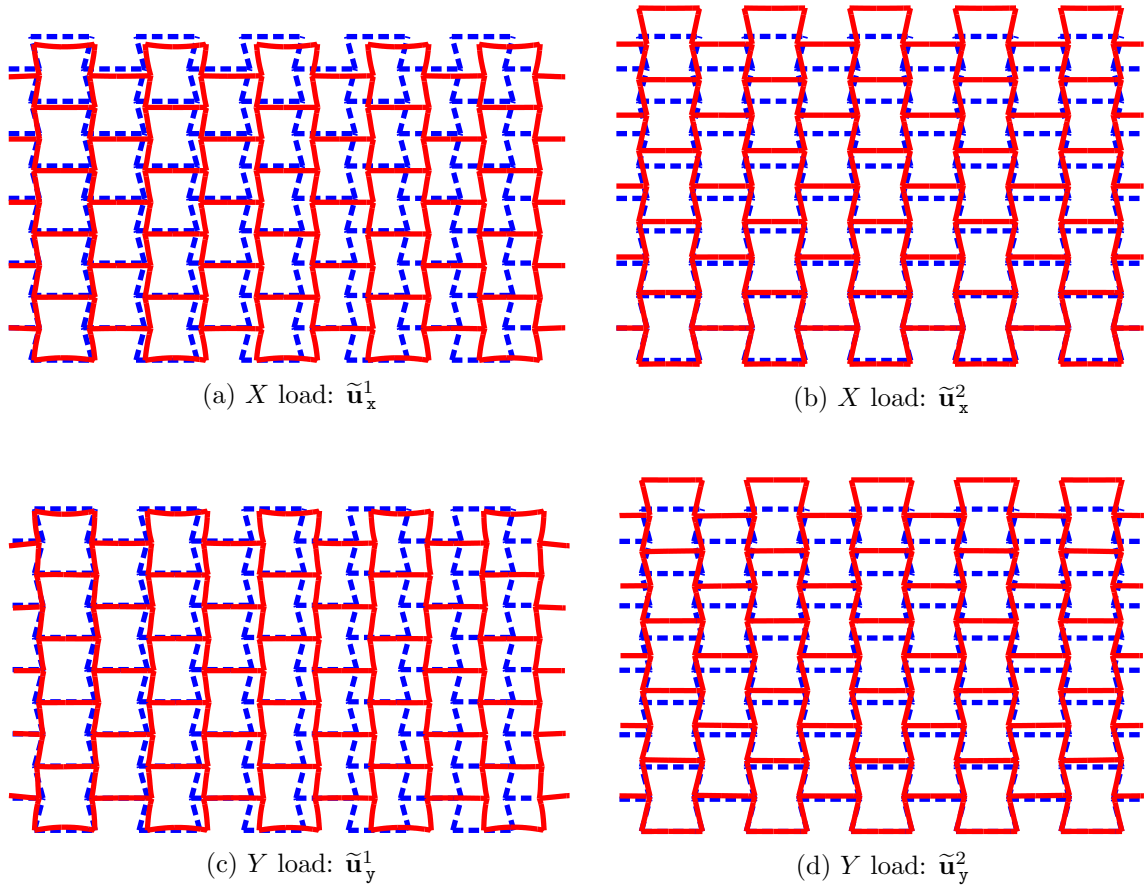


Figure 4.15: Normalized spatial modes 1 and 2 scaled for illustration. PGD compressed solution of the periodic honeycomb structure under uni-axial loads.

The parametric functions associated to these spatial modes give some insight on the behavior of the orthotropic Poisson's ratio. Noting for example the parametric function $\tilde{G}_3^2(\alpha)$ shown in a red dashed line in Figure 4.16c, it states that displacements given by $\tilde{\mathbf{u}}_x^2$ become zero for parameter $\alpha = 90^\circ$, changing sign from positive, for $\alpha < 90^\circ$, to negative, for $\alpha > 90^\circ$. This function shapes the *auxetic* to *non-auxetic* behavior observed in the effective properties studied for ν_{12}^{eff} in Figure 4.11.

On the other hand, the orthotropic Poisson's ratio ν_{21} of the modeled piece of honeycomb is related to the first spatial mode - $\tilde{\mathbf{u}}_y^1$ - for the Y-direction load. In this case, we should also observe that these displacements vanish when the parameter α tends to 90° , as observed from the parametric function $\tilde{G}_3^1(\alpha)$ shown in Figure 4.17c in blue, with positive and negative values for $\alpha < 90^\circ$ and $\alpha > 90^\circ$ respectively. In addition, the explicit function $\tilde{G}_4^1(t)$, see Figure 4.17d in blue, shows how spatial mode $\tilde{\mathbf{u}}_y^1$ decays as long as parameter “ t ” increases, an effect that has been observed as well in Figure 4.12 for ν_{21}^{eff} .

4.2. Periodic pattern of hexagonal honeycomb cells

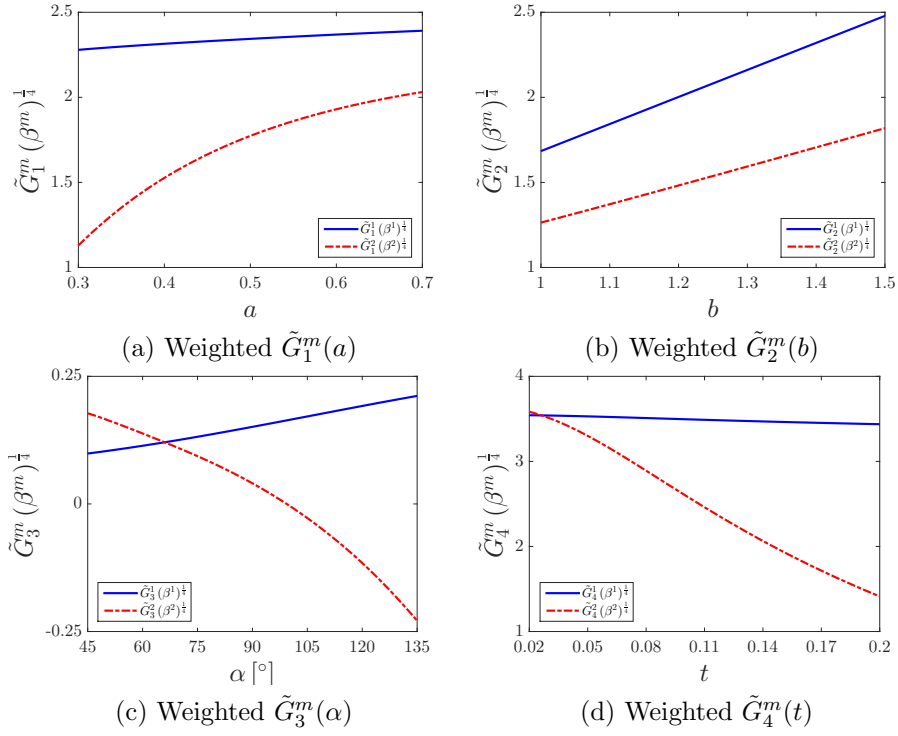


Figure 4.16: Periodic honeycomb structure under X-direction tensile load with PGD compression. Normalized parametric functions weighted for illustration.

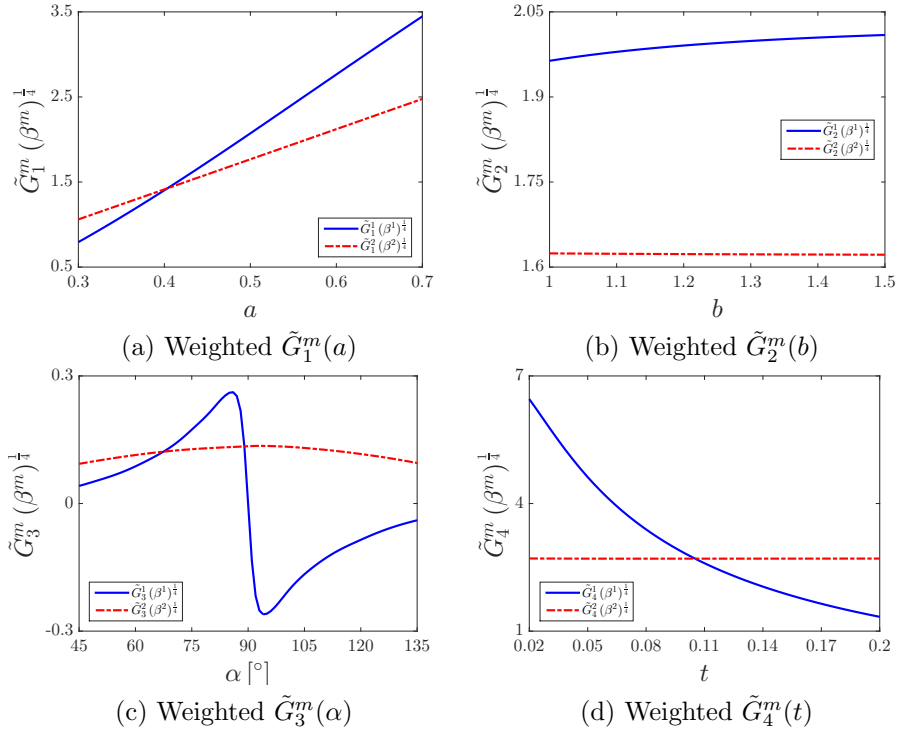


Figure 4.17: Periodic honeycomb structure under Y-direction tensile load with PGD compression. Normalized parametric functions weighted for illustration.

In all these physical descriptions, it is important to note that a single mode only contributes to a part of the mechanical response of the parametric structure, with a significance weighted by the modal amplitude. However, the parametric behavior is not comprehensively explained by a single mode. Instead, the precise response is recovered by summing all the inputs from the PGD modes in a solution.

A measurement of the orthotropic Poisson’s ratios in the parametric material sheet is done by averaging nodal displacements. For example, the PGD *vademecum* resulting from the X -direction tensile load is used to measure vertical displacements at the top and bottom edges of the honeycomb sheet (see Figure 4.18). Using the average of Y deformation along the honeycomb width $w_0(\boldsymbol{\mu})$, induced by a uniform strain along X direction, an estimation of the parametric $\nu_{12}(\boldsymbol{\mu})$ is obtained. The analogous idea is employed to estimate $\nu_{21}(\boldsymbol{\mu})$ in the honeycomb sheet, applying alternatively the PGD *vademecum* obtained from the uniform Y -direction loading case.

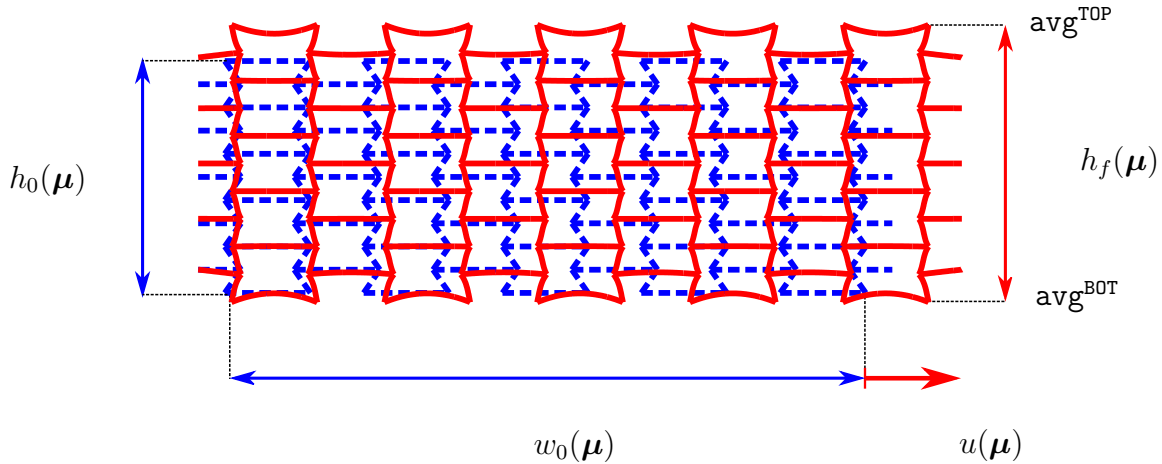


Figure 4.18: Measurement of ν_{12} in the honeycomb structure subjected to uniform load in X direction.

Figure 4.19 shows a comparison of the Poisson’s ratios estimated in the periodic material sheet against the effective ones. Note that the errors evolution along the increasing number of PGD modes are computed using a global norm in the multi-dimensional parametric space (in correlation to the Frobenius-like norm specified in equation (4.1)). For this purpose, the effective Poisson’s ratios are evaluated using analytical expressions in the parameters (see the solutions described in Appendix C).

The results in Figure 4.19 are obtained running three different honeycomb sheet patterns, made of 5×5 , 10×10 and 15×15 repetitions of unit-cells in the horizontal and vertical directions. The trends for both Poisson’s ratios confirm that the correlation between mechanical properties measured in the periodic structure should become closer to the homogenization response when the number of cells in the pattern is increased. In this sense, we have two sources of error in the analysis. One it is given by the actual PGD approximation, where accuracy is increased by enriching

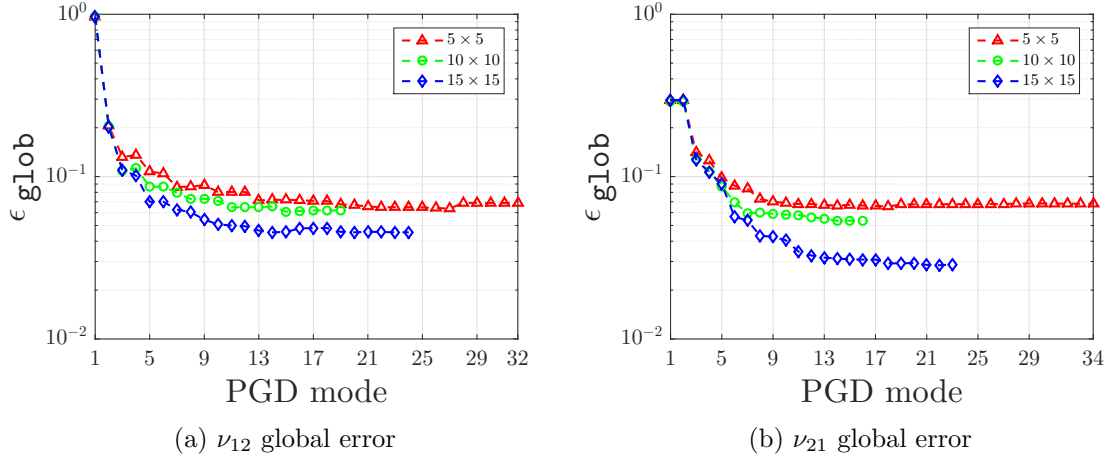


Figure 4.19: PGD modal evolution of relative error of Poisson's ratios computed in the full lattice material against the effective ones, measured in a global parametric norm.

the solution with higher number of modes. In addition, even if accurate estimations of the Poisson's ratios in the periodic structure do not represent exactly the effective values, they do approach them as long as the number of unit-cells modeled in the honeycomb is increased.

Finally, it is remarked that all PGD solutions for the honeycomb periodic structures are computed using the same stopping criterion - $\zeta = 10^{-3}$ - for the greedy algorithm, and post-processed with PGD compression to reduce the final number of modes. However, as shown in Figure 4.19, the final number of modes changes upon the different loading conditions and the number of unit-cells modeled in the periodic structures.

Chapter 5

Application to 3D lattices and nonlinear problems

In this chapter we present further models of parametric lattices structures that are solved within the same framework of the algebraic PGD solver. The results show the flexibility of the algebraic PGD approach, which in this case reduces the tasks only to properly arranging the input data into tensor structures with a separated representation of their parametric dependence. For this purpose, the beam model presented before is extended to 3D, which in the context of linear theory, this is a straightforward step. The 3D model is obtained basically by adding a new bending plane, orthogonal and totally uncoupled to the mechanics of the 2D model. In addition, the orientation of the beam elements is done with an extended arrangement of rotation matrices that no longer acts only on one plane but the complete 3D space, and takes care of the newly introduced degrees of freedom.

The mechanical problems here presented are based on two different parametric structures with relevant engineering applications. A parametric scaffold structure is first introduced, based on the hexagonal honeycomb unit-cell, suitably systematized in space as suggested by [Yang et al. \(2015\)](#). Engineered scaffolds exhibiting auxetic properties rise interest in biomedical applications ([Soman et al. \(2012\)](#)), since a tunable Poisson's ratio allows a better resembling of the native tissue's elastic behavior ([Timmins et al. \(2010\)](#)). With respect to the structural parametrization, a new parameter is introduced controlling the scaffold unit-cell depth in the third dimension. It is shown that the newly added constraints between parameters, ensuring that the unit-cell geometry has physical connotation, introduce a function that no longer depends on only one parameter. One possibility in these cases is to modify the PGD approach of [Chapter 3](#), which is uni-dimensional in all parametric spaces, and treat some of them in a multidimensional approach, as proposed by [Zou et al. \(2018\)](#). The advantage in these cases is that functions that are non separable in the parameters can be treated, or constraint parameter spaces that are not Cartesian domains can be fully explored, naturally at a higher computational cost. Our approach

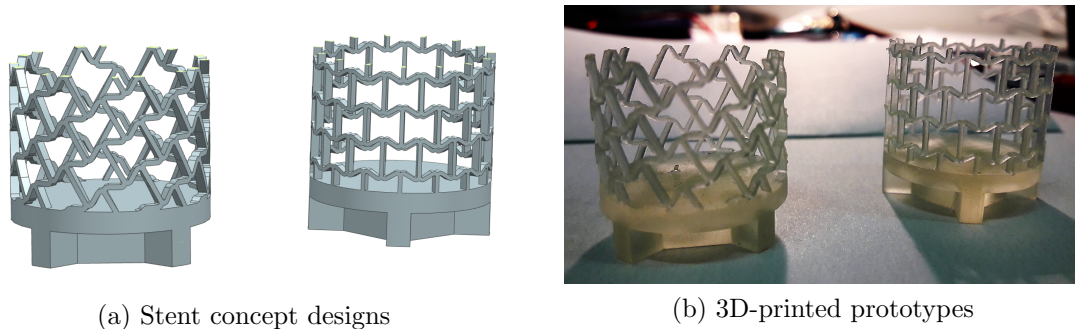


Figure 5.1: Auxetic stent-like structures.

is different, and in order to use the algebraic PGD solver without modifications, the non-separable function is computed first for all the chosen values of the parameters, and then a numerical separation is achieved by means of the SVD. This numerical pre-processing is already a new approximation to the problem, in the sense that the affine decomposition of input data, namely the parametric stiffness matrix and forcing term are no longer exactly the ones of the original structural problem.

The other parametric lattice structure that is explored in the following, is based on an identical parameterization of the honeycomb sheet previously characterized in detailed, but wrapped into a cylindrical tubular structure that resembles that of a medical stent, see Figure 5.1, a commonly used device in coronary heart interventions. Studies show that the choice of auxetic tubular structures provides an enhanced performance against kinking, suggesting that understanding the parametric response would provide valuable information for the mechanical design of medical devices such as angioplasty stents or annuloplasty rings (Karnesis and Burriesci (2013) and Scarpa et al. (2008)).

The proper assessment of kinking or in general buckling phenomena is a key aspect in the design of structures such as columns in civil engineering, railway tracks undergoing thermal expansion (also known as *sun kinking*) or pressure vessels subjected to external pressure. A comprehensive study of this aspect is out of the scope of the present work but we acknowledge it, on one hand, as a limitation of the parametric analysis within a linear beam model, and on the other hand as a motivation to explore a possible development of the PGD algebraic solver for the solution of nonlinear equations.

In particular with respect to lattice materials, as they are formed by slender elements, buckling appears like a meaningful effect to be addressed by design. In fact, Figure 5.2 shows a 3D-printed sample of a honeycomb sheet of dimensions $w = 107.25$ mm and $h = 84.44$ mm, made of 11×15 hexagonal cells with an angle $\alpha = 60^\circ$ and subjected to a uniform vertical load. The test specimen has been built and tested at the 3D@UniPV facilities, constructed with two materials using an Objet 260 Connex 3 printer. The honeycomb is fixed to the holds at the top and bottom

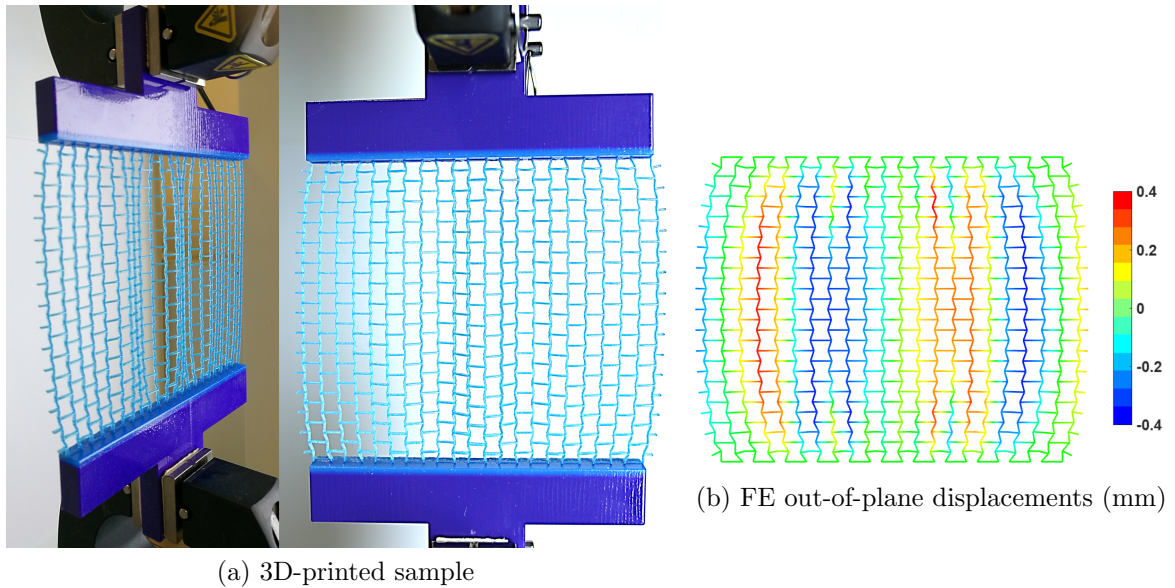


Figure 5.2: Buckling effect observed in a honeycomb sheet subjected to a tensile vertical load. Loaded strain is 9% for the 3D-printed sample and 10% for the FE simulation.

extremes, which are made of a significantly stiffer material. Thus, the boundary conditions at the test specimen are not only prescribed vertical displacements but also fixed horizontal displacements at their bottom and top tips. When the specimen is loaded, this induces compressive forces at the horizontal direction, which in turn generate out-of-plane displacements in a typical buckling configuration as observed from the photos in Figure 5.2a at a 9% of strain in the loading direction. This effect is also observed in a finite element simulation performed using the commercial software ADINA© R&D (2018), as shown in Figure 5.2b, where the pattern of out-of-plane displacements triggered by buckling is depicted, for a 10% of applied strain in the loading direction.

Moreover, buckling is not necessarily the only mechanical design issue that can be addressed by geometrically nonlinear models in the context of lattice materials. A more general argument is to answer how the effective material properties may change with the applied loading magnitude. The parametric analysis of effective material properties derived in previous chapters is valid in a context where the original and the deformed configurations of the structure resemble. Thus, in applications where this is arguable, it is of certain interest to evaluate the effective material properties also as a function of the applied load. Our first approach to a parametric analysis of this kind is presented in this chapter, where we use PGD to construct explicit parametric responses *a posteriori*, that include the loading factor itself as a parameter. In this case, PGD works as a least-squares approximation, in its particular separated form,

of a finite element response that is built *a priori* using simply a multidimensional sampling in the parameters space. Although in this particular case there is no gain in terms of computational cost, the results are promising because for our geometrically nonlinear parametric problem, the PGD response reflects very good accuracy without an excessive amount of computed modes. In this sense, we believe that future work could be built on a framework that uses the algebraic PGD solver inside an iterative loop, such that the approximation to nonlinear parametric systems of equations could be built *a priori* at a reduced cost.

5.1 Problem statement: 3D parametric lattices

5.1.1 3D beam element

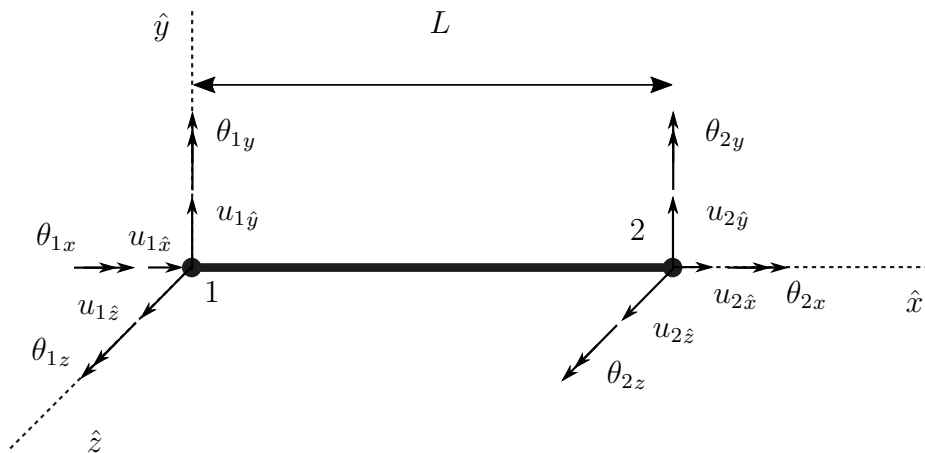


Figure 5.3: Local beam element system and nodal degrees of freedom.

It is here described the beam model used for the mechanical description of 3D lattice structures, whose parametric equilibrium is afterward worked out using the algebraic PGD solver. This model is a 3D version of the Euler-Bernoulli theory described in Chapter 2. Two displacements, $u_{\hat{y}}$ and $u_{\hat{z}}$, perpendicular to beam's axis direction \hat{x} , and two rotations $\theta_{\hat{z}}$ and $\theta_{\hat{y}}$, characterize the deformed beam's line of centroids. In addition, the axial displacement, $u_{\hat{x}}$, and the angle of twist, $\theta_{\hat{x}}$, complete the six degrees of freedom, which are all functions only of the beam's axial coordinate \hat{x} , and are measured with respect to the local beam axes $(\hat{x}, \hat{y}, \hat{z})$, see Figure 5.3.

Both $u_{\hat{x}}$ and $\theta_{\hat{x}}$ are uncoupled to the bending deformations, that are decomposed in two independent orthogonal planes $\hat{x}\hat{y}$ and $\hat{x}\hat{z}$. In each of these planes, there works a 2D bending problem exactly as described for the honeycomb, coupling displacement $u_{\hat{y}}$ and rotation $\theta_{\hat{z}}$ in plane $\hat{x}\hat{y}$, and independently, displacement $u_{\hat{z}}$ and rotation $\theta_{\hat{y}}$ in plane $\hat{x}\hat{z}$.

In the finite element formulation of Euler-Bernoulli beams, the displacements $u_{\hat{y}}$ and $u_{\hat{z}}$ are interpolated using cubic polynomials, functions of \hat{x} . Their coupled

rotations, θ_z and $\theta_{\hat{y}}$ respectively, are defined as their first derivatives with respect to \hat{x} , then quadratic polynomials interpolate them. Finally, $u_{\hat{x}}$ and $\theta_{\hat{x}}$ are interpolated with linear polynomials. The reader is referred to [Cook et al. \(2002, Chapter 2\)](#) and [Cook et al. \(2002, Chapter 4\)](#) for a detailed explanation on this topic.

5.1.2 Parametrization of a scaffold unit-cell

The parametric structure to be considered is the scaffold depicted in [Figure 5.4a](#), whose name has been coined by similar lattice structures applied, for example, in tissue engineering ([Soman et al. \(2012\)](#), [Lantada et al. \(2015\)](#) and [Wang et al. \(2016\)](#)), and orthopedic implants ([Khanoki and Pasini \(2012\)](#), [Arabnejad et al. \(2016\)](#) and [Arabnejad et al. \(2017\)](#)). The periodic arrangement characterized in [Figure 5.4a](#) is constituted by a pattern of $3 \times 3 \times 3$ unit-cells, repeated in the three directions of a rectangular system of coordinates. The replicated unit-cell is detailed in [Figure 5.4b](#), which has been trimmed from the periodic structure, as defined in homogenization theory, by three pairs of orthogonal planes colored in transparent green, red and blue. Precisely, note that the red and blue planes (and their opposite counterpart) must be placed at half of the elements thickness “ t ”. These planes define the unit-cell volume, which is a function of the parameters $\boldsymbol{\mu}$, and in particular we refer to the unit-cell width $w_c(\boldsymbol{\mu})$ as the length in x between opposite planes shaded in green, the unit-cell height $h_c(\boldsymbol{\mu})$ as the length in y between opposite planes shaded in red and the unit-cell pitch $p_c(\boldsymbol{\mu})$ as the length in z between opposite planes shaded in blue.

Furthermore, the 3D beam model is introduced to describe the mechanics of the scaffold unit-cell, a step that is illustrated in [Figure 5.4c](#). Note that the architecture of the scaffold is based on a tessellation of the hexagonal honeycomb cell, which in the xy planes, its frame is governed by the four parameters (a , b , α and t), proposed in subsection [2.1.2](#). In addition, the configuration is completed with an arrangement of hexagonal cells of the same topology, but placed in xz planes and shaped by two added parameters:

- c : the length of the obliquely oriented beam elements in xz planes,
- θ : the angle of the oblique elements placed in xz planes, oriented with respect to the x axis.

The first three parameters (a , b and α) are restricted to the inequality constraint from equation [\(2.1\)](#):

$$b > 2a \cos(\alpha). \quad (5.1)$$

In addition, there is an equality restrain to be considered:

$$\begin{aligned} a \cos(\alpha) &= c \cos(\theta), \\ \cos(\theta) &= \frac{a}{c} \cos(\alpha), \end{aligned} \quad (5.2)$$

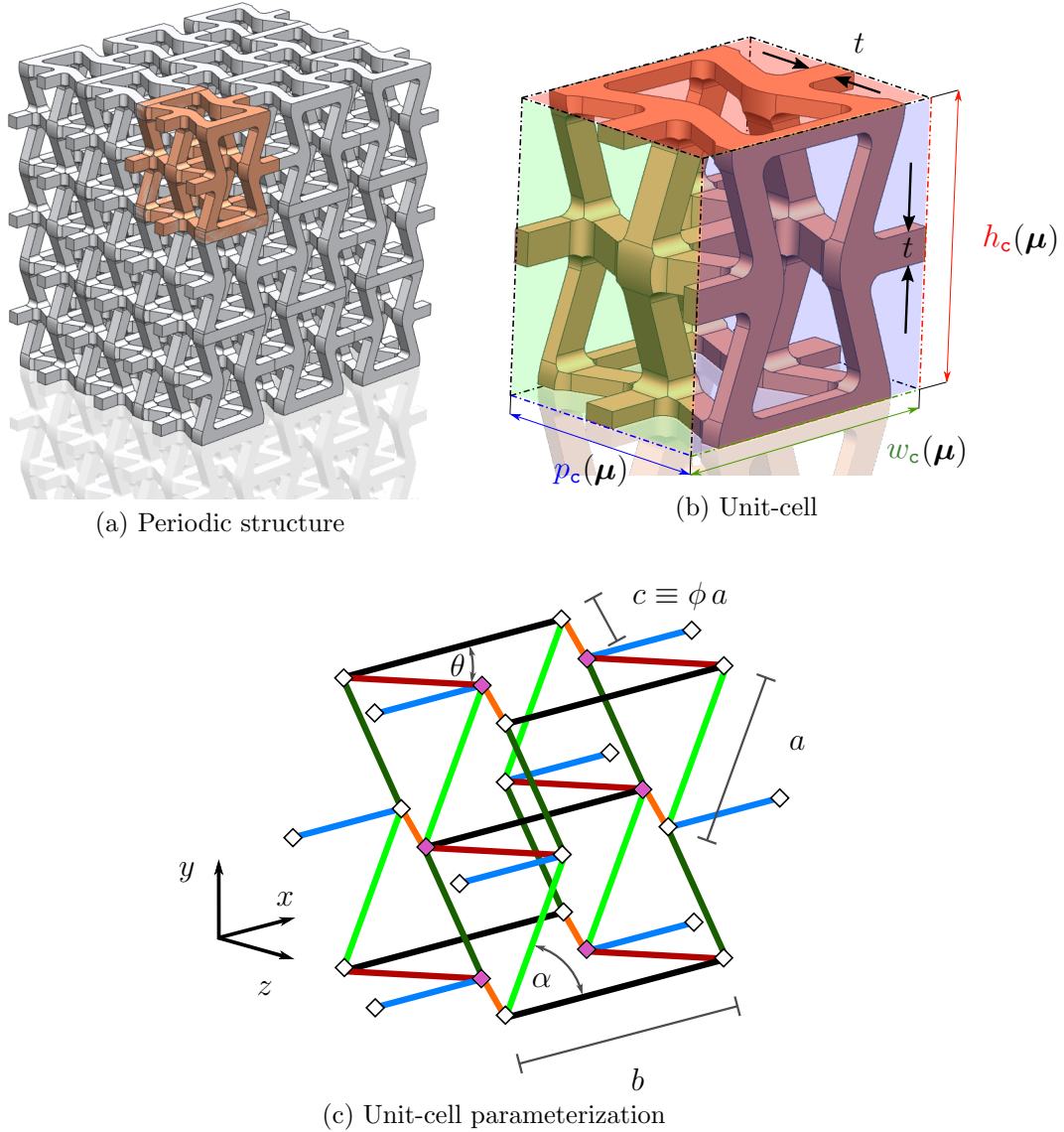


Figure 5.4: Parametrization of a scaffold unit-cell.

a condition that basically ensures the interconnection of the orthogonally located honeycomb cells at the points colored in magenta, in Figure 5.4c. From the equality expressed in (5.2) we first observe that θ is not an independent parameter, since it can be expressed as a function of parameters (a , α and c). Secondly, this function depends, on one hand on *alpha*, and on the other hand on the ratio of lengths a/c . Thus, rather than considering c itself, it makes sense to define ϕ as the newly introduced parameter, namely (Figure 5.4c):

$$\phi \equiv \frac{c}{a}. \quad (5.3)$$

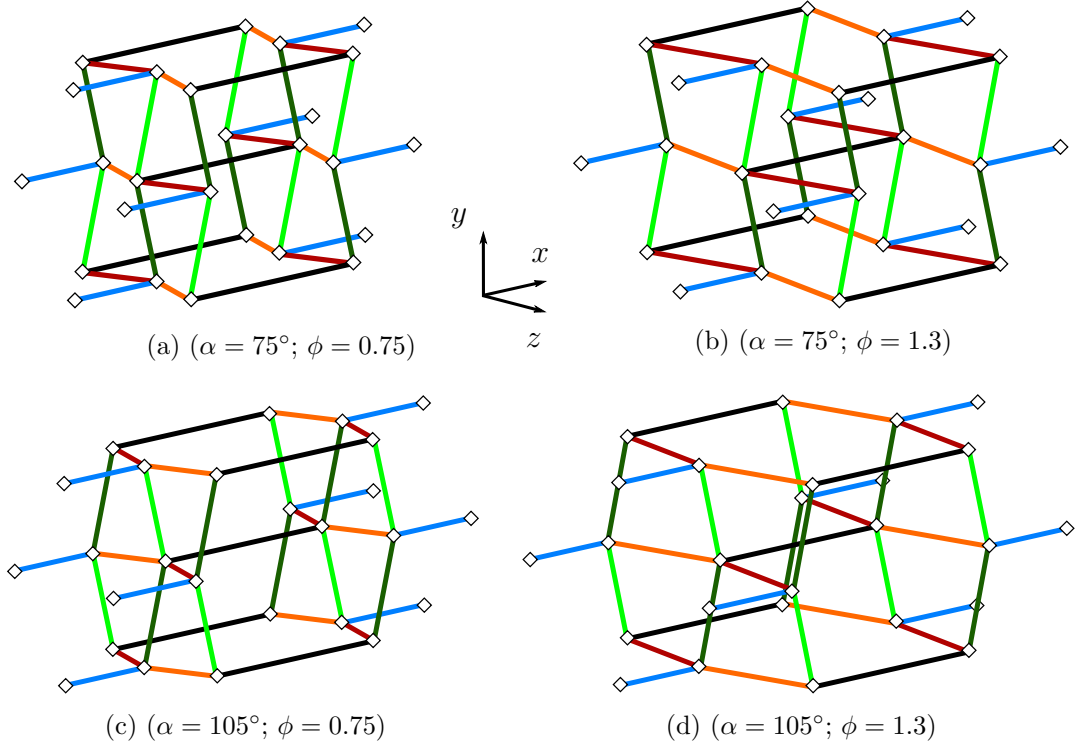


Figure 5.5: Scaffold unit-cell geometry for characteristic values of parameters α and ϕ , and fixed values of parameters $a = 0.5$ and $b = 1$.

Taking into account the previous, the total number of parameters is $n_p = 5$, which are collected in the vector $\boldsymbol{\mu}$:

$$\boldsymbol{\mu} = [\mu_1 \ \mu_2 \ \mu_3 \ \mu_4 \ \mu_5]^\top = [a \ b \ \alpha \ \phi \ t]^\top.$$

The parameters are chosen to range in the following intervals:

$$a \in I_1 = [0.3, 0.7], b \in I_2 = [1, 1.5], \alpha \in I_3 = \left[\frac{\pi}{4}, \frac{3\pi}{4}\right],$$

$$\phi \in I_4 = [0.75, 2] \text{ and } t \in I_5 = \left[\frac{1}{50}, \frac{1}{5}\right],$$

which are the same selected for the hexagonal honeycomb in subsection 2.1.2, plus interval I_4 for the newly introduced parameter ϕ . An illustration of the scaffold parametric geometry is shown in Figure 5.5, for characteristic values of α and ϕ .

In the present case, it is assured that all the parameters values in the multidimensional space formed by the Cartesian product $I_1 \times I_2 \times I_3 \times I_4$ fulfill the constraints given by equations (5.1) and (5.2). Then, input data assumes all parametric dependence as a product of separated 1D functions, which is the approach of the algebraic

PGD solver in Chapter 3. More details about handling the parametric input data are presented in section 5.2.

5.1.3 Finite Element formulation of 3D beams

The 3D beam element locates two nodes at its vertices, where each of them is correlated with six degrees of freedom, as sketched in Figure 5.3. The following ordering criteria is taken for the generalized displacement vector, collecting the degrees of freedom of a beam element, with respect to its local system of coordinates:

$$\widehat{\mathbf{u}} = \{u_{1\hat{x}} \ u_{1\hat{y}} \ u_{1\hat{z}} \ \theta_{1\hat{x}} \ \theta_{1\hat{y}} \ \theta_{1\hat{z}} \ u_{2\hat{x}} \ u_{2\hat{y}} \ u_{2\hat{z}} \ \theta_{2\hat{x}} \ \theta_{2\hat{y}} \ \theta_{2\hat{z}}\}^T. \quad (5.4)$$

Likewise, a generalized force vector gathers:

$$\widehat{\mathbf{f}} = \{N_{1\hat{x}} \ V_{1\hat{y}} \ V_{1\hat{z}} \ T_{1\hat{x}} \ M_{1\hat{y}} \ M_{1\hat{z}} \ N_{2\hat{x}} \ V_{2\hat{y}} \ V_{2\hat{z}} \ T_{2\hat{x}} \ M_{2\hat{y}} \ M_{2\hat{z}}\}^T, \quad (5.5)$$

where N and T represent axial forces and torque - aligned with the beam local \hat{x} direction -, and V and M are shear forces and bending moments respectively - either aligned with the beam local \hat{y} or \hat{z} directions -. The present 3D beam element uses the Bernoulli hypothesis, in two perpendicular bending curvatures, one coupling shear forces in \hat{y} and moments in \hat{z} , and in the same way but independently, another one links shear forces in \hat{z} and moments in \hat{y} . The remaining degrees of freedom stay uncoupled, in the local beam \hat{x} direction, assuming a uni-axial stress state given by forces N , and a pure shear state given by torques T .

The elemental stiffness matrix $\widehat{\mathbf{K}}_e$ relates the generalized force (5.5) and displacement vectors (5.4). In structural mechanics, this matrix is typically derived using a direct stiffness method (Cook et al., 2002, Chapter 2), and becomes:

$$\widehat{\mathbf{K}}_e = \begin{bmatrix} X_e & 0 & 0 & 0 & 0 & 0 & -X_e & 0 & 0 & 0 & 0 & 0 \\ Y_{1,e} & 0 & 0 & 0 & Y_{2,e} & 0 & 0 & -Y_{1,e} & 0 & 0 & 0 & Y_{2,e} \\ Z_{1,e} & 0 & -Z_{2,e} & 0 & 0 & 0 & 0 & 0 & -Z_{1,e} & 0 & -Z_{2,e} & 0 \\ S_e & 0 & 0 & 0 & 0 & 0 & 0 & 0 & 0 & -S_e & 0 & 0 \\ & & 2Z_{3,e} & 0 & 0 & 0 & 0 & 0 & Z_{2,e} & 0 & Z_{3,e} & 0 \\ & & & 2Y_{3,e} & 0 & 0 & 0 & -Y_{2,e} & 0 & 0 & 0 & Y_{3,e} \\ \hline & & & & & & X_e & 0 & 0 & 0 & 0 & 0 \\ & & & & & & Y_{1,e} & 0 & 0 & 0 & 0 & -Y_{2,e} \\ & & & & & & Z_{1,e} & 0 & Z_{2,e} & 0 & & \\ & & & & & & & S_e & 0 & 0 & & \\ & & & & & & & & 2Z_{3,e} & 0 & & \\ & & & & & & & & & & 2Y_{3,e} & \end{bmatrix}. \quad (5.6)$$

From a mathematical point of view, the same matrix is obtained by integrating in space a variational formulation, where the unknown displacements and rotations are interpolated with polynomials of different degrees (Cook et al., 2002, Chapter 4).

The superscript “ $\hat{}$ ” is marked above to denote the stiffness of a beam element “ e ” given in its local coordinate system. The stiffness matrix components in (5.6), X_e and $Y_{j,e}$, for $j = 1, 2, 3$, are exactly as defined for the 2D case in (2.3),

$$\begin{aligned} X_e &= \frac{E_e A_e}{L_e} & Y_{1,e} &= \frac{12E_e I_{\hat{z},e}}{L_e^3} \\ S_e &= \frac{G_e J_{\hat{t},e}}{L_e} & Y_{2,e} &= \frac{6E_e I_{\hat{z},e}}{L_e^2}, \\ & & Y_{3,e} &= \frac{2E_e I_{\hat{z},e}}{L_e} \end{aligned} \quad (5.7)$$

and a new property of the shape and size of the cross section $J_{\hat{t},e}$, the torsional constant, has been introduced for the 3D beam. The terms $Z_{j,e}$ are defined equally as $Y_{j,e}$, for $j = 1, 2, 3$, but switching \hat{z} to \hat{y} in the beam’s moments of inertia, for example: $Z_{1,e} = \frac{12E_e I_{\hat{y},e}}{L_e^3}$.

In our parametric scaffold, we have that the beams cross-section area, A_e , the centroidal moments of inertia, $I_{\hat{z},e}$ and $I_{\hat{y},e}$, and the torsional constant, $J_{\hat{t},e}$, are all functions of the parameter “ t ”. Depending on the element in the scaffold unit-cell model (Figure 5.4b), the previous beam properties may change, so it is distinguished in the notation by the subscript “ e ”.

Beams length L_e depends differently on the parameters, according to Figure 5.4c:

$$L_e = \begin{cases} b; & \text{for an element “}e\text{” oriented along }x\text{ direction,} \\ a; & \text{for an element “}e\text{” obliquely oriented in }xy\text{ planes,} \\ \phi a; & \text{for an element “}e\text{” obliquely oriented in }xz\text{ planes.} \end{cases} \quad (5.8)$$

The beams cross-section is assumed square with side t (Figure 5.4a). However, the unit-cell model considers that those elements contained in the boundary planes are either rectangular or square with side $t/2$ (Figure 5.4b). Regarding to material properties, the beams Young’s modulus E_e and shear modulus G_e are not parametrized, remaining constant for all elements in the structure, $E_e = 1$ and $G_e = 0.385$ (equally to an isotropic material with unitary Young’s modulus and Poisson’s ratio $\nu = 0.3$).

Given that all matrix coefficients from (5.7) depend on the parameters, the following notation is used: $X_e(\boldsymbol{\mu})$, $S_e(\boldsymbol{\mu})$, $Y_{j,e}(\boldsymbol{\mu})$ and $Z_{j,e}(\boldsymbol{\mu})$, for $j = 1, 2, 3$. This also implies - $\hat{\mathbf{K}}_e(\boldsymbol{\mu})$ - that the elemental stiffness matrix also depends on the parameters (see equation (5.6)). In addition, this matrix is expressed in its local coordinate system $(\hat{x}, \hat{y}, \hat{z})$, which can be arbitrarily oriented in space with respect to the global coordinate system, as presented in Figure 5.6.

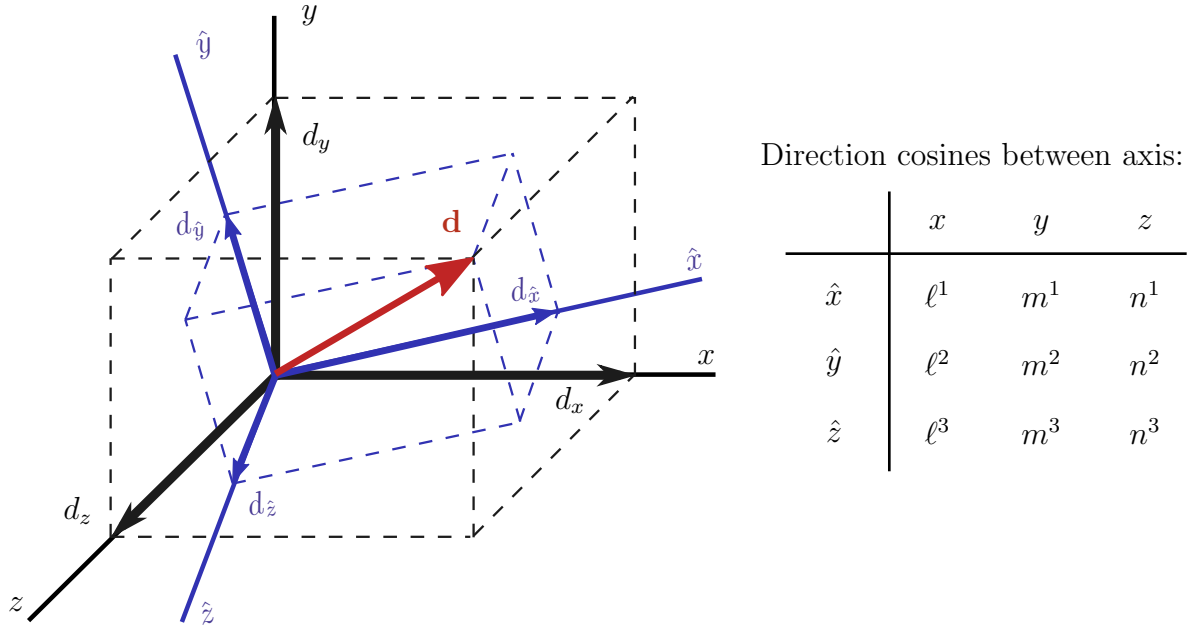


Figure 5.6: Vector \mathbf{d} expressed in components $[d_{\hat{x}} \ d_{\hat{y}} \ d_{\hat{z}}]^\top$ or $[d_x \ d_y \ d_z]^\top$, either in the coordinate system $(\hat{x}, \hat{y}, \hat{z})$ or (x, y, z) respectively.

For example, a rotational coordinate transformation for the vector quantity \mathbf{d} (Figure 5.6), can be expressed in terms of the matrix $\mathbf{\Lambda}$:

$$\mathbf{\Lambda} = \begin{bmatrix} \ell^1 & m^1 & n^1 \\ \ell^2 & m^2 & n^2 \\ \ell^3 & m^3 & n^3 \end{bmatrix}. \quad (5.9)$$

Rearranging $\mathbf{\Lambda}$ in blocks, to account for displacements and rotations of the two-noded beam, a transformation matrix is built to map the elemental matrix $\widehat{\mathbf{K}}_e$ into the global coordinate system (x, y, z) (Cook et al., 2002, Chapter 2):

$$\mathbf{K}_e(\boldsymbol{\mu}) = \mathbf{T}_e^\top(\boldsymbol{\mu}) \widehat{\mathbf{K}}_e(\boldsymbol{\mu}) \mathbf{T}_e(\boldsymbol{\mu}); \quad \mathbf{T}_e(\boldsymbol{\mu}) = \begin{bmatrix} \mathbf{\Lambda}_e(\boldsymbol{\mu}) & \mathbf{0} & \mathbf{0} & \mathbf{0} \\ \mathbf{0} & \mathbf{\Lambda}_e(\boldsymbol{\mu}) & \mathbf{0} & \mathbf{0} \\ \mathbf{0} & \mathbf{0} & \mathbf{\Lambda}_e(\boldsymbol{\mu}) & \mathbf{0} \\ \mathbf{0} & \mathbf{0} & \mathbf{0} & \mathbf{\Lambda}_e(\boldsymbol{\mu}) \end{bmatrix}. \quad (5.10)$$

The transformation matrix \mathbf{T}_e is written in the parametric framework, since depending upon the element, $\mathbf{\Lambda}_e$ becomes a function of the angles α or θ (Figure 5.4c). For elements oriented in xy planes, the rotation matrix is denoted by $\mathbf{\Lambda}_{e,xy}$, and results:

$$\mathbf{\Lambda}_{e,xy}(\alpha) = \begin{bmatrix} \cos(\vartheta_e(\alpha)) & \sin(\vartheta_e(\alpha)) & 0 \\ -\sin(\vartheta_e(\alpha)) & \cos(\vartheta_e(\alpha)) & 0 \\ 0 & 0 & 1 \end{bmatrix}.$$

In the case of elements oriented in xz planes, the rotation matrix is denoted by $\mathbf{\Lambda}_{e,xz}$, and becomes:

$$\mathbf{\Lambda}_{e,xz}(\theta) = \begin{bmatrix} \cos(\varrho_e(\theta)) & 0 & -\sin(\varrho_e(\theta)) \\ -\sin(\varrho_e(\theta)) & 0 & -\cos(\varrho_e(\theta)) \\ 0 & 1 & 0 \end{bmatrix}. \quad (5.11)$$

The information about the angles $\vartheta_e(\alpha)$ and $\varrho_e(\theta)$ can be distinguished from Figure 5.4c, depending on element “ e ”:

$$\vartheta_e(\alpha) = \begin{cases} \pi - \alpha, & \text{for depicted elements in dark green;} \\ \alpha, & \text{for depicted elements in light green;} \end{cases} \quad (5.12)$$

or

$$\varrho_e(\theta) = \begin{cases} \pi - \theta, & \text{for depicted elements in red;} \\ \theta, & \text{for depicted elements in orange.} \end{cases} \quad (5.13)$$

5.2 Affine decomposition of input data

The affine decomposition of input data refers to provide the algebraic PGD solver, with the parametric dependence of the stiffness matrix and forcing term, in a separated way (i.e. equations (3.4) and (3.5)). The 3D problems presented in the following adopt in general the same procedure described for the 2D honeycomb in section 2.2. Thus, only the particularities for the scaffold and the stent parametric structures are specified.

5.2.1 Parametric scaffold

To begin with, we recall that the affine decomposition of the elemental stiffness matrices in equation (5.10) must be constructed. The result is written in a general way by

$$\mathbf{K}_e(\boldsymbol{\mu}) = \sum_{d=1}^{n_{k_e}} \mathbf{K}_e^d \prod_{i=1}^{n_p} B_{i,e}^d(\mu_i). \quad (5.14)$$

With respect to their parametric dependence, we distinguish three types of elements:

- the horizontal elements, denoted by the set “ $e \in \text{hor}$ ” (colored in black and blue in Figure 5.4c).
- the oblique elements placed in xy planes, denoted by “ $e \in \text{xy}$ ” (colored in green in Figure 5.4c).

- the oblique elements placed in xz planes, denoted by “ $e \in \mathbf{xz}$ ” (colored in orange and red in Figure 5.4c).

To begin with, it is necessary to describe first the unrotated stiffness matrix $\widehat{\mathbf{K}}_e(\boldsymbol{\mu})$ as the following:

$$\widehat{\mathbf{K}}_e(\boldsymbol{\mu}) = \sum_{f=1}^{n_{\mathbf{k}}} \widehat{\mathbf{K}}_e^f \prod_{i=1}^{n_p} O_{i,e}^f(\mu_i). \quad (5.15)$$

The number of terms in the previous is always $n_{\mathbf{k}} = 4$, independently of the element type in the scaffold unit-cell. For example, for the set of oblique elements “ $e \in \mathbf{xz}$ ”, we have that $L_{\mathbf{xz}} = \phi a$. Using equation (5.7), we decompose $\widehat{\mathbf{K}}_{e,\mathbf{xz}}(\boldsymbol{\mu})$ in the following four terms:

$$\widehat{\mathbf{K}}_{e,\mathbf{xz}}(\boldsymbol{\mu}) = \widehat{\mathbf{K}}_{e,\mathbf{xz}}^1 \underbrace{\frac{t^2}{\phi a}}_{\Pi_i O_{i,\mathbf{xz}}^1} + \widehat{\mathbf{K}}_{e,\mathbf{xz}}^2 \underbrace{\frac{t^4}{\phi a}}_{\Pi_i O_{i,\mathbf{xz}}^2} + \widehat{\mathbf{K}}_{e,\mathbf{xz}}^3 \underbrace{\frac{t^4}{(\phi a)^2}}_{\Pi_i O_{i,\mathbf{xz}}^3} + \widehat{\mathbf{K}}_{e,\mathbf{xz}}^4 \underbrace{\frac{t^4}{(\phi a)^3}}_{\Pi_i O_{i,\mathbf{xz}}^4}. \quad (5.16)$$

We observe that the parametric functions depend only in the type of elements, then we use the notation $O_{i,\mathbf{xz}}^f(\mu_i)$ in equation (5.16). In addition, these parametric functions are summarized in Table 5.1. For other type of elements in the scaffold unit-cell, the procedure is alike but taking into account that the beams length depend differently on the parameters (equation (5.8)).

$\mu_i \setminus f$	1	2	3	4
μ_1	$1/a$	$1/a$	$1/a^2$	$1/a^3$
μ_2	1	1	1	1
μ_3	1	1	1	1
μ_4	$1/\phi$	$1/\phi$	$1/\phi^2$	$1/\phi^3$
μ_5	t^2	t^4	t^4	t^4

Table 5.1: Parametric functions $O_{i,\mathbf{xz}}^f(\mu_i)$ in the scaffold structure.

On the other hand, the subscript “ e ” is kept in equation (5.16) for matrices $\widehat{\mathbf{K}}_{e,\mathbf{xz}}^f$, indicating that these change within elements of the same type. This occurs, for example, for elements placed at the unit-cell boundary, which are cut at half thickness $t/2$.

So far, it remains to consider the parametric dependence of transformation matrices $\mathbf{T}_e(\boldsymbol{\mu})$. This is the next step in order to reach the affine decomposition of $\mathbf{K}_e(\boldsymbol{\mu})$ (equation (5.14)). We distinguish first, the transformation matrices for the set of oblique elements contained in xy planes, with this decomposition:

$$\mathbf{T}_{e,xy}(\boldsymbol{\mu}) = \sum_{g=1}^{\mathbf{n}_{T_{xy}}} \mathbf{T}_{e,xy}^g \prod_{i=1}^{\mathbf{n}_p} L_{i,xy}^g(\mu_i), \quad (5.17)$$

and for the set of oblique elements contained in xz planes:

$$\mathbf{T}_{e,xz}(\boldsymbol{\mu}) = \sum_{g=1}^{\mathbf{n}_{T_{xz}}} \mathbf{T}_{e,xz}^g \prod_{i=1}^{\mathbf{n}_p} L_{i,xz}^g(\mu_i). \quad (5.18)$$

Note that the subindex “ e ” is kept only in matrices $\mathbf{T}_{e,xy}^g$ and $\mathbf{T}_{e,xz}^g$, given that the parametric functions $L_{i,xy}^g$ and $L_{i,xz}^g$ remain the same for all elements in their corresponding sets.

The number of separated terms for $\mathbf{T}_{e,xy}$ is $\mathbf{n}_{T_{xy}} = 3$, which is obtained by decomposition of the rotation matrix $\boldsymbol{\Lambda}_{e,xy}$:

$$\boldsymbol{\Lambda}_{e,xy}(\alpha) = \begin{bmatrix} 0 & 0 & 0 \\ 0 & 0 & 0 \\ 0 & 0 & 1 \end{bmatrix} + \begin{bmatrix} 1 & 0 & 0 \\ 0 & 1 & 0 \\ 0 & 0 & 0 \end{bmatrix} \cos(\vartheta_e(\alpha)) + \begin{bmatrix} 0 & 1 & 0 \\ -1 & 0 & 0 \\ 0 & 0 & 0 \end{bmatrix} \sin(\vartheta_e(\alpha)).$$

Depending on the elements (5.12), the angle $\vartheta_e(\alpha)$ takes complementary values $(\pi - \alpha)$ or α . This exception, $\cos(\pi - \alpha) = -\cos(\alpha)$, is adopted by changing the sign of matrix $\mathbf{T}_{e,xy}^2$ accordingly.

On the other hand, the rotation matrix $\boldsymbol{\Lambda}_{e,xz}$ is decomposed in a similar way:

$$\boldsymbol{\Lambda}_{e,xz}(\theta) = \begin{bmatrix} 0 & 0 & 0 \\ 0 & 0 & 0 \\ 0 & 1 & 0 \end{bmatrix} + \begin{bmatrix} 1 & 0 & 0 \\ 0 & 0 & -1 \\ 0 & 0 & 0 \end{bmatrix} \cos(\varrho_e(\theta)) + \begin{bmatrix} 0 & 0 & -1 \\ -1 & 0 & 0 \\ 0 & 0 & 0 \end{bmatrix} \sin(\varrho_e(\theta)), \quad (5.19)$$

where in this case, see equation (5.13), $\varrho_e(\theta)$ takes complementary values $(\pi - \theta)$ or θ , and the sign of matrix $\mathbf{T}_{e,xz}^2$ is changed consistently. However, the orientation angle θ is not an independent parameter of our analysis, but a function of $\mu_3 = \alpha$ and $\mu_4 = \phi$, as imposed by the unit-cell geometric constraint (5.2), and equation (5.3). Using these two equations, $\cos(\theta)$ can be replaced by

$$\cos(\theta) := g(\alpha, \phi) = \frac{\cos(\alpha)}{\phi},$$

which is separable in the parameters α and ϕ . Using the trigonometric identity, and the fact that $\sin(\theta)$ is positive in all the parametric space of our study, this function results

$$\sin(\theta) := f(\alpha, \phi) = \sqrt{1 - \frac{\cos^2(\alpha)}{\phi^2}}. \quad (5.20)$$

$\mu_i \setminus g$	1	2	3	$\mu_i \setminus g$	1	2	3	...	$2 + \mathbf{n}_{\text{svd}}$
μ_1	1	1	1	μ_1	1	1	1	...	1
μ_2	1	1	1	μ_2	1	1	1	...	1
μ_3	1	$\cos(\alpha)$	$\sin(\alpha)$	μ_3	1	$\cos(\alpha)$	Ξ^1	...	$\Xi^{\mathbf{n}_{\text{svd}}}$
μ_4	1	1	1	μ_4	1	$1/\phi$	Ψ^1	...	$\Psi^{\mathbf{n}_{\text{svd}}}$
μ_5	1	1	1	μ_5	1	1	1	...	1

(a) $L_{i,xy}^g$
(b) $L_{i,xz}^g$

Table 5.2: Functions $L_{i,xy}^g$ and $L_{i,xz}^g$ describing the separated parametric dependence of transformation matrices $\mathbf{T}_{e,xy}(\boldsymbol{\mu})$ and $\mathbf{T}_{e,xz}(\boldsymbol{\mu})$.

Certainly, $\sin(\theta)$ is not separable in parameters α and ϕ . However, we propose a separable approximation by means of the Singular Value Decomposition (SVD), which is optimal for this case (i.e. a scalar function of two parameters). Appendix D describes this procedure, such that the following approximation holds:

$$\sin(\theta) := f(\alpha, \phi) \approx \sum_{\ell=1}^{\mathbf{n}_{\text{svd}}} \omega^\ell \Xi^\ell(\alpha) \Psi^\ell(\phi). \quad (5.21)$$

The previous implies that first, the function $\sin(\theta)$ is computed using (5.20) at all values of the parameters $\alpha \in I_3$ and $\phi \in I_4$, and then it is approximated by means of a SVD decomposition of \mathbf{n}_{svd} terms.

For each of the terms, $\ell = 1, \dots, \mathbf{n}_{\text{svd}}$, the SVD, see Appendix D, provides an amplitude ω^ℓ , and two vectors containing the values of functions $\Xi^\ell(\alpha)$ and $\Psi^\ell(\phi)$, at the 1D parametric meshes of size $\mathbf{n}_{d,3}$ and $\mathbf{n}_{d,4}$ (number of points chosen for intervals I_3 and I_4 respectively). Having considered this, the number of separated terms for $\mathbf{T}_{e,xz}(\boldsymbol{\mu})$ results from equations (5.19) and (5.21): $\mathbf{n}_{\mathbf{T}_{xz}} = 2 + \mathbf{n}_{\text{svd}}$.

For our analysis, we use five SVD terms - $\mathbf{n}_{\text{svd}} = 5$ - that in equation (5.21) account for an approximation with a maximum relative error of $1.92e^{-5}$ in the whole Cartesian domain $I_3 \times I_4$ (the global relative error being $5.43e^{-7}$). The reader is referred to Appendix D for further details about the SVD application.

Table 5.2 summarizes the parametric functions $L_{i,xy}^g$ and $L_{i,xz}^g$ describing the affine decomposition of $\mathbf{T}_{e,xy}(\boldsymbol{\mu})$ and $\mathbf{T}_{e,xz}(\boldsymbol{\mu})$ in equations (5.17) and (5.18). In one case, the transformation depends only on parameter (α) while in the other it depends on both (α, ϕ), the rest of the functions being naturally constant.

The parametric dependence of $\widehat{\mathbf{K}}_e(\boldsymbol{\mu})$, $\mathbf{T}_{e,xy}(\boldsymbol{\mu})$ and $\mathbf{T}_{e,xz}(\boldsymbol{\mu})$ has been described in a separated way by equations (5.15), (5.17) and (5.18). In the following, we focus on how we can use these descriptions, to recover the affine decomposition of $\mathbf{K}_e(\boldsymbol{\mu})$. This one is defined in equation (5.14), by means of $\mathbf{n}_{\mathbf{K}_e}$ number of terms, which depends

on the parametric dependence of an element in the scaffold structure.

To begin with, we note that the set of horizontal elements - $e \in \text{hor}$ - does not have a parametric orientation. This implies that $\mathbf{K}_{\text{hor}}(\boldsymbol{\mu}) = \widehat{\mathbf{K}}_{\text{hor}}(\boldsymbol{\mu})$, the parametric description of stiffness is readily obtained from (5.15), and the number of separated terms corresponds to $\mathbf{n}_{\mathbf{k}_{\text{hor}}} = \mathbf{n}_{\hat{\mathbf{k}}} = 4$. On the other hand, the set of oblique elements contained in xy and xz planes have a parametrized orientation. The number of terms involved in their parametric stiffness affine decomposition is higher, and the procedure to evaluate them is discussed in the following.

We replace in equation (5.10), the separated expressions for $\widehat{\mathbf{K}}_e(\boldsymbol{\mu})$ (equation (5.15)) and $\mathbf{T}_{e,xy}(\boldsymbol{\mu})$ (equation (5.17)), to obtain for the set of oblique elements in xy :

$$\mathbf{K}_{e,xy}(\boldsymbol{\mu}) = \sum_{f=1}^{\mathbf{n}_{\hat{\mathbf{k}}}} \sum_{h=1}^{\mathbf{n}_{\text{T}_{xy}}} \sum_{g=1}^{\mathbf{n}_{\text{T}_{xy}}} [\mathbf{T}_{e,xy}^{g\top} \widehat{\mathbf{K}}_{e,xy}^f \mathbf{T}_{e,xy}^h] \prod_{i=1}^{\mathbf{n}_p} (L_{i,xy}^g L_{i,xy}^h O_{i,xy}^f). \quad (5.22)$$

The equation above is referred to as a product of separated matrices. The maximum number of terms arising from the three nested sums is denoted by $\mathbf{n}_{\mathbf{k}_{xy}}^{\text{max}} = \mathbf{n}_{\text{T}_{xy}}^2 \mathbf{n}_{\hat{\mathbf{k}}}$. However, we note in advanced that many of the $\mathbf{n}_{\mathbf{k}_{xy}}^{\text{max}}$ terms share a common product of parametric functions $\prod_{i=1}^{\mathbf{n}_p} L_{i,xy}^g L_{i,xy}^h$. Precisely, this occurs once for each commutative combination of indexes $\{g, h\}$, when $g \neq h$, for $g, h = 1, \dots, \mathbf{n}_{\text{T}_{xy}}$. The reduced number of terms is $\mathbf{n}_{\mathbf{k}_{xy}}^{\text{red}} = \mathbf{n}_{\mathbf{q}_{xy}} \mathbf{n}_{\hat{\mathbf{k}}}$, where $\mathbf{n}_{\mathbf{q}_{xy}}$ is calculated as a binomial coefficient $\binom{\mathbf{n}_{\text{T}_{xy}}+1}{2}$:

$$\mathbf{n}_{\mathbf{q}_{xy}} := \binom{\mathbf{n}_{\text{T}_{xy}}}{2} = \binom{\mathbf{n}_{\text{T}_{xy}} + 1}{2} = \frac{(\mathbf{n}_{\text{T}_{xy}} + 1)!}{2! (\mathbf{n}_{\text{T}_{xy}} - 1)!}. \quad (5.23)$$

Given that $\mathbf{n}_{\text{T}_{xy}} = 3$, it results that $\mathbf{n}_{\mathbf{q}_{xy}} = 6$, which basically counts how many unordered pairs $\{g, h\}$ are built without repetitions, for $g, h = 1, \dots, \mathbf{n}_{\text{T}_{xy}} = 3$.

In addition, we define a one to one relation “ \mathcal{F} ” between the summing index $d = 1, \dots, \mathbf{n}_{\mathbf{k}_{xy}}^{\text{red}}$ in equation (5.14) and the multiple summing indexes from equation (5.22), being $f = 1, \dots, \mathbf{n}_{\hat{\mathbf{k}}}$ and the $\mathbf{n}_{\mathbf{q}_{xy}}$ unrepeated-unordered pairs $\{g, h\}$, that is summarized by the following equations:

$$d = \mathcal{F}(g, h, f) \quad \text{for } d = 1, \dots, \mathbf{n}_{\mathbf{k}_{xy}}^{\text{red}} \quad (5.24)$$

$$\mathbf{K}_{e,xy}^d = \begin{cases} \mathbf{T}_{e,xy}^{g\top} \widehat{\mathbf{K}}_{e,xy}^f \mathbf{T}_{e,xy}^h & \text{if } g = h, \\ \mathbf{T}_{e,xy}^{g\top} \widehat{\mathbf{K}}_{e,xy}^f \mathbf{T}_{e,xy}^h + \mathbf{T}_{e,xy}^{h\top} \widehat{\mathbf{K}}_{e,xy}^f \mathbf{T}_{e,xy}^g & \text{if } g \neq h, \end{cases} \quad (5.25)$$

$$B_{i,xy}^d = L_{i,xy}^g L_{i,xy}^h O_{i,xy}^f \quad \text{for } i = 1, \dots, \mathbf{n}_p \quad (5.26)$$

These equations actually provide the terms and parametric functions for the affine decomposition of $\mathbf{K}_{e,xy}(\boldsymbol{\mu})$.

Considering that $\mathbf{n}_{\mathbf{q}_{xy}} = 6$ and $\mathbf{n}_{\hat{\mathbf{k}}} = 4$, it results that $\mathbf{n}_{\mathbf{k}_{xy}}^{\text{red}} = 24$. However, after computing the separated matrices $\mathbf{K}_{e,xy}^d$ from (5.25), for $d = 1, \dots, \mathbf{n}_{\mathbf{k}_{xy}}^{\text{red}} = 24$, we recover that only $\mathbf{n}_{\mathbf{k}_{xy}} = 13$ of them are nonzero. Their associated parametric functions $B_{i,xy}^d$ are summarized in Table 5.3.

$\mu_i \setminus d$	1	2	3	4	5	6	7	8	9	10	11	12	13
μ_1	$\frac{1}{a}$	$\frac{1}{a}$	$\frac{1}{a}$	$\frac{1}{a}$	$\frac{1}{a}$	$\frac{1}{a}$	$\frac{1}{a}$	$\frac{1}{a^2}$	$\frac{1}{a^2}$	$\frac{1}{a^3}$	$\frac{1}{a^3}$	$\frac{1}{a^3}$	$\frac{1}{a^3}$
μ_2	1	1	1	1	1	1	1	1	1	1	1	1	1
μ_3	1	$\cos^2(\alpha)$	$\sin(2\alpha)$	$\sin^2(\alpha)$	$\cos^2(\alpha)$	$\sin(2\alpha)$	$\sin^2(\alpha)$	$\cos(\alpha)$	$\sin(\alpha)$	1	$\cos^2(\alpha)$	$\sin(2\alpha)$	$\sin^2(\alpha)$
μ_4	1	1	1	1	1	1	1	1	1	1	1	1	1
μ_5	t^4	t^2	t^2	t^2	t^4	t^4	t^4	t^4	t^4	t^4	t^4	t^4	t^4

Table 5.3: Parametric functions $B_{i,xy}^d$ describing stiffness of the oblique elements “ $e \in xy$ ” in the scaffold, for $d = 1, \dots, \mathbf{n}_{k_{xy}}$ and $i = 1, \dots, \mathbf{n}_p$.

Finally, the separated parametric stiffness matrix for the set of oblique elements in xz , is obtained following the same procedure. To begin with, we write the product of separated matrices that result in $\mathbf{K}_{e,xz}(\boldsymbol{\mu})$:

$$\mathbf{K}_{e,xz}(\boldsymbol{\mu}) = \sum_{f=1}^{\mathbf{n}_{\hat{\mathbf{k}}}} \sum_{h=1}^{\mathbf{n}_{\mathbf{T}_{xz}}} \sum_{g=1}^{\mathbf{n}_{\mathbf{T}_{xz}}} [\mathbf{T}_{e,xz}^{g\top} \hat{\mathbf{K}}_{e,xz}^f \mathbf{T}_{e,xz}^h] \prod_{i=1}^{\mathbf{n}_p} (L_{i,xz}^g L_{i,xz}^h O_{i,xz}^f). \quad (5.27)$$

The number of separated terms $\mathbf{n}_{\hat{\mathbf{k}}} = 4$ remains the same, but for the present element set “ $e \in xz$ ” we have that $\mathbf{n}_{\mathbf{T}_{xz}} = 2 + \mathbf{n}_{\text{svd}}$. Recall that \mathbf{n}_{svd} is the number of modes chosen for the SVD approximation in equation (5.21), and that for our analysis we select $\mathbf{n}_{\text{svd}} = 5$. Thus, we use equation (5.23) to determine that there are $\mathbf{n}_{\mathbf{q}_{xz}} = 28$ unique combinations of unrepeated-unordered pairs $\{g, h\}$, for $g, h = 1, \dots, \mathbf{n}_{\mathbf{T}_{xz}} = 7$. This in turn gives the number of separated terms $\mathbf{n}_{k_{xz}}^{\text{red}} = \mathbf{n}_{\mathbf{q}_{xz}} \mathbf{n}_{\hat{\mathbf{k}}} = 112$, and the following equations that allow to compute the terms and parametric functions for the affine decomposition of $\mathbf{K}_{e,xz}(\boldsymbol{\mu})$:

$$d = \mathcal{F}(g, h, f) \quad \text{for } d = 1, \dots, \mathbf{n}_{k_{xz}}^{\text{red}} \quad (5.28)$$

$$\mathbf{K}_{e,xz}^d = \begin{cases} \mathbf{T}_{e,xz}^{g\top} \hat{\mathbf{K}}_{e,xz}^f \mathbf{T}_{e,xz}^h & \text{if } g = h, \\ \mathbf{T}_{e,xz}^{g\top} \hat{\mathbf{K}}_{e,xz}^f \mathbf{T}_{e,xz}^h + \mathbf{T}_{e,xz}^{h\top} \hat{\mathbf{K}}_{e,xz}^f \mathbf{T}_{e,xz}^g & \text{if } g \neq h, \end{cases} \quad (5.29)$$

$$B_{i,xz}^d = L_{i,xz}^g L_{i,xz}^h O_{i,xz}^f \quad \text{for } i = 1, \dots, \mathbf{n}_p \quad (5.30)$$

Again, many separated terms from the total of $\mathbf{n}_{k_{xz}}^{\text{red}} = 112$ computed in equation (5.29), result in a null matrix. In fact, we recover only $\mathbf{n}_{k_{xz}} = 71$ of them that are nonzero. It is remarkable that expressing the separated parametric dependence in the least possible number of terms is relevant in the performance of the algebraic PGD solver. This is observed in Appendix A, where \mathbf{n}_k determines the size of the loop in the separated global stiffness matrices K^k , for $k = 1, \dots, \mathbf{n}_k$.

In fact, once we know how to construct the affine decomposition for the elemental stiffness in the parametric scaffold, the procedure to build the following global separated stiffness matrix is straightforward:

$$\mathbf{K}(\boldsymbol{\mu}) = \sum_{k=1}^{\mathbf{n}_k} \mathbf{K}^k \prod_{i=1}^{\mathbf{n}_p} B_i^k(\mu_i). \quad (5.31)$$

We recognize first that all the different parametric functions from the elemental stiffness collected together define the set of parametric functions for the global structure, namely $B_i^k(\mu_i)$ in equation (5.31). Therefore, the number of terms for the global stiffness matrix is obtained by the sum: $\mathbf{n}_k = \mathbf{n}_{k \text{ hor}} + \mathbf{n}_{k \text{ xy}} + \mathbf{n}_{k \text{ zz}} = 88$.

Each one of the separated matrices \mathbf{K}^k is associated to one of the products $\prod_{i=1}^{\mathbf{n}_p} B_i^k$. The ordering criterion for the $k = 1, \dots, \mathbf{n}_k$ separated terms, is built by assigning first the parametric functions $O_{i, \text{hor}}^f$, for $f = 1, \dots, \mathbf{n}_{k \text{ hor}} = 4$, then placing $B_{i, \text{xy}}^d$ from Table 5.3, for $d = 1, \dots, \mathbf{n}_{k \text{ xy}} = 13$, and finally taking functions $B_{i, \text{zz}}^d$, for $d = 1, \dots, \mathbf{n}_{k \text{ zz}} = 71$.

The way in which matrices K^k are built is fairly adopted from finite element procedures. With minor modifications, we can supplement finite elements with the parametric dimension in a separated approach. The lay out is presented in Algorithm 2, where the standard FE loop is sketched along with the peculiarities that arrange the affine decomposition of the parametric stiffness matrix, for our scaffold architecture.

Data: FE connectivities, $eType_e$: element type, for $e = 1, \dots, n_e$.

Parametric functions B_i^k , for $k = 1, \dots, n_k$.

Result: \mathbf{K}^k separated matrices, for $k = 1, \dots, n_k$.

for $e = 1 \dots n_e$ **do**

switch $eType_e$ **do**

case “ $e \in hor$ ” **do**

 • Compute $\widehat{\mathbf{K}}_e^f$ from (5.15), for $f = 1, \dots, n_{k\ hor}$.

 • Assign local $\widehat{\mathbf{K}}_e^f$ to global \mathbf{K}^k for $k = 1, \dots, n_{k\ hor}$.

end

case “ $e \in xy$ ” **do**

 • Compute $\mathbf{K}_{e,xy}^d$ from (5.25), for $d = 1, \dots, n_{k\ xy}$.

 • Assign local $\mathbf{K}_{e,xy}^d$ to global \mathbf{K}^k for
 $k = (n_{k\ hor}+1), \dots, (n_{k\ hor}+n_{k\ xy})$.

end

case “ $e \in xz$ ” **do**

 • Compute $\mathbf{K}_{e,xz}^d$ from (5.29), for $d = 1, \dots, n_{k\ xz}$.

 • Assign local $\mathbf{K}_{e,xz}^d$ to global \mathbf{K}^k for $k = (n_{k\ hor}+n_{k\ xy}+1), \dots, n_k$.

end

end

end

Build all sparse \mathbf{K}^k , for $k = 1, \dots, n_k$.

Algorithm 2: Adapted FE loop building the matrices \mathbf{K}^k that provide the parametric stiffness of the scaffold in a separated approach.

5.2.2 Stent

We present in the following how the parametric stiffness of a stent-like structure can be built in the separated form. The procedures are similar to those already explained, with a particular application to the cylindrical lattice (Figure 5.7b). The initial setup is the 2D hexagonal honeycomb (Figure 5.7a), whose structure is described by $\mathbf{n}_p = 4$ parameters:

$$\boldsymbol{\mu} = [\mu_1 \ \mu_2 \ \mu_3 \ \mu_4]^\top = [a \ b \ \alpha \ t]^\top.$$

The final parametric structure becomes 3D by wrapping the honeycomb sheet into a cylindrical shape (Figure 5.7b). Despite the figures present a periodic structure with $(\mathbf{n}_{\text{hor}} = 5) \times (\mathbf{n}_{\text{ver}} = 5)$ cell repetitions, the following procedure is general for any $\mathbf{n}_{\text{hor}} \times \mathbf{n}_{\text{ver}}$ structures of this type.

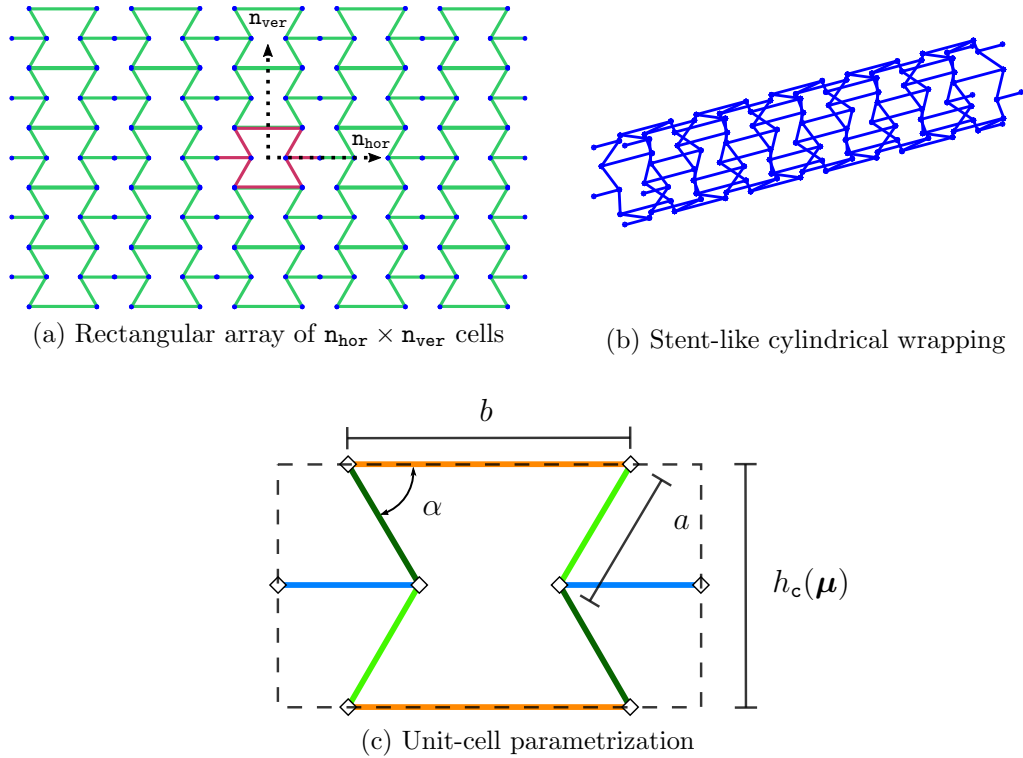


Figure 5.7: Stent unwrap and wrap configurations.

We assume that the stent cross-section (Figure 5.8a) is always formed by a regular polygon. The number of sides - \mathbf{n}_s - depends on the vertical number of cell repetitions - \mathbf{n}_{ver} - in the 2D setup, and the polygon circumradius - $r_0(\boldsymbol{\mu})$ - depends on the parameters:

$$\begin{aligned} \mathbf{n}_s &= 2 \mathbf{n}_{\text{ver}}, \\ r_0(\boldsymbol{\mu}) &= \frac{h_c(\boldsymbol{\mu})}{4 \sin\left(\frac{\pi}{\mathbf{n}_s}\right)}, \end{aligned} \quad (5.32)$$

where $h_c(\boldsymbol{\mu}) = 2a \sin(\alpha)$ is the honeycomb unit-cell height (Figure 5.7c).

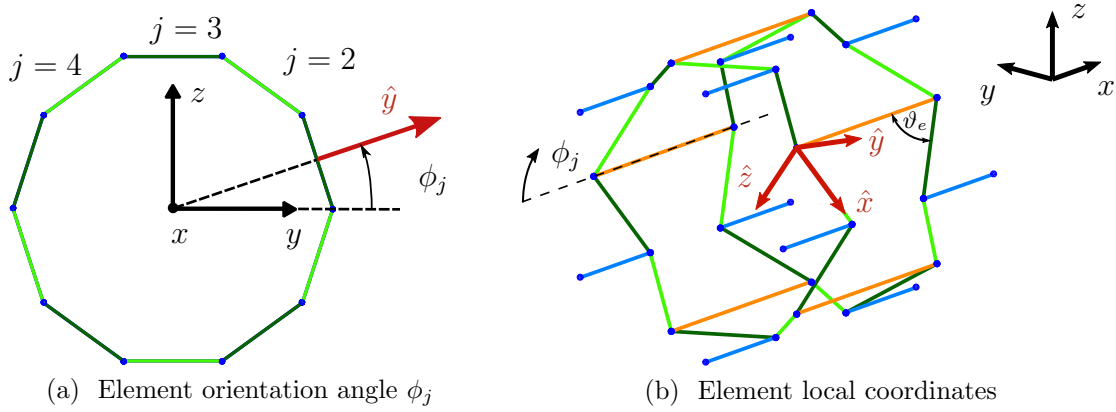


Figure 5.8: Orientation of the stent oblique elements.

Two types of elements are identified with respect to their parametric dependence:

- the horizontal elements, “ $e \in \text{hor}$ ”, colored in blue and orange (Figure 5.8b), have lengths depending on parameter b and a fixed orientation.
- the obliquely aligned elements, “ $e \in \text{ob}$ ”, colored in green (Figure 5.8b), have lengths depending on parameter a and a parametrized orientation by α .

In addition, we assume that all beam elements in the parametric stent have a circular cross-section of diameter “ t ”. This simplifies some treatments but it is definitely not a theoretical restriction to the following procedures. Material properties are not parametrized, remaining $E_e = 1$ and $G_e = 0.385$ for all elements.

The separated elemental stiffness matrices, for the horizontally aligned elements, are obtained from the unrotated stiffness matrix $\widehat{\mathbf{K}}_e(\boldsymbol{\mu})$:

$$\widehat{\mathbf{K}}_e(\boldsymbol{\mu}) = \sum_{f=1}^{\mathbf{n}_{\hat{\mathbf{k}}}} \widehat{\mathbf{K}}_e^f \prod_{i=1}^{\mathbf{n}_p} O_{i,e}^f(\mu_i), \quad (5.33)$$

given that the orientation is not parametrized, and the beams circular cross-section properties stay unchanged under x -axis rotations. This separation is obtained with $\mathbf{n}_{\hat{\mathbf{k}}} = 4$ terms, as explained in previous problems (5.16).

Regarding the obliquely aligned elements, their orientation is parametrized by α , but also depends on another angle, as explained in the following. These elements are placed at different planes in the stent cross-section (Figure 5.8a). The planes normal is oriented by an angle ϕ_j , measured as a positive rotation along x axis (Figure 5.8a). This angle is independent of the parameters $\boldsymbol{\mu}$, but depends on the vertical number of cells chosen in the initial 2D setup:

$$\phi_j = \left(j - \frac{1}{2}\right) \frac{\pi}{\mathbf{n}_{\text{ver}}}, \quad \text{for } j = 1, 2, \dots, 2 \mathbf{n}_{\text{ver}}. \quad (5.34)$$

Therefore, the obliquely aligned elements in the stent are oriented by a transformation that accounts first, for a rotation about an angle ϕ_j along global x axis, then followed by a rotation about an angle ϑ_e along the local axis \hat{y} (Figure 5.8b). This transformation is described by the following product of rotation matrices:

$$\mathbf{\Lambda}_e(\alpha) = \begin{bmatrix} \cos(\vartheta_e(\alpha)) & 0 & \sin(\vartheta_e(\alpha)) \\ 0 & 1 & 0 \\ -\sin(\vartheta_e(\alpha)) & 0 & \cos(\vartheta_e(\alpha)) \end{bmatrix} \begin{bmatrix} 1 & 0 & 0 \\ 0 & \cos(\phi_j) & \sin(\phi_j) \\ 0 & -\sin(\phi_j) & \cos(\phi_j) \end{bmatrix}, \quad (5.35)$$

where the subindex “ e ” indicates that the angle $\vartheta_e(\alpha)$ becomes:

$$\vartheta_e(\alpha) = \begin{cases} \pi - \alpha, & \text{for dark green elements in Figure 5.8b;} \\ \alpha, & \text{for light green elements in Figure 5.8b.} \end{cases} \quad (5.36)$$

Matrix $\mathbf{\Lambda}_e$ from (5.35) is decompose in three terms, that result

$$\begin{aligned} \mathbf{\Lambda}_e(\alpha) = & \begin{bmatrix} 0 & 0 & 0 \\ 0 \cos(\phi_j) \sin(\phi_j) & & \\ 0 & 0 & 0 \end{bmatrix} + \\ & + \begin{bmatrix} 1 & 0 & 0 \\ 0 & 0 & 0 \\ 0 & -\sin(\phi_j) \cos(\phi_j) & \end{bmatrix} \cos(\vartheta_e(\alpha)) + \begin{bmatrix} 0 & -\sin(\phi_j) \cos(\phi_j) \\ 0 & 0 & 0 \\ -1 & 0 & 0 \end{bmatrix} \sin(\vartheta_e(\alpha)). \end{aligned} \quad (5.37)$$

Using the equation above, we get the following transformation matrices in a separated form:

$$\mathbf{T}_e(\boldsymbol{\mu}) = \sum_{g=1}^{\mathbf{n}_T} \mathbf{T}_e^g \prod_{i=1}^{\mathbf{n}_p} L_i^g(\mu_i). \quad (5.38)$$

For all oblique elements, the number of terms - $\mathbf{n}_T = 3$ - and the parametric functions - L_i^g - do not change. Instead, according to the element orientation in the circumferential direction, ϕ_j (5.34), the separated matrices, \mathbf{T}_e^g , take different values (5.37). In addition, depending on the element (5.36), matrix \mathbf{T}_e^g changes its sign correspondingly.

The following steps are done in the same approach adopted for the previous problems. The product of separated matrices is obtain for the oblique elements “ $e \in \text{ob}$ ” by replacing equations (5.38) and (5.33) into (5.10):

$$\mathbf{K}_e(\boldsymbol{\mu}) = \sum_{f=1}^{\mathbf{n}_{\hat{\mathbf{k}}}} \sum_{h=1}^{\mathbf{n}_{\Gamma}} \sum_{g=1}^{\mathbf{n}_{\Gamma}} [\mathbf{T}_e^{g\top} \widehat{\mathbf{K}}_{\text{ob}}^f \mathbf{T}_e^h] \prod_{i=1}^{\mathbf{n}_p} (L_i^g L_i^h O_{i,\text{ob}}^f), \quad (5.39)$$

where the absence of the sub-index “ e ” implies that all parametric functions and matrices $\widehat{\mathbf{K}}_{\text{ob}}^f$ are the same for all elements in the set. A reduced number of terms $\mathbf{n}_{\text{k}_{\text{ob}}}^{\text{red}} = \mathbf{n}_q \mathbf{n}_{\hat{\mathbf{k}}} = 24$ result from (5.39), being $\mathbf{n}_{\hat{\mathbf{k}}} = 4$ (5.16) and $\mathbf{n}_q = 6$ (5.23). The affine decomposition for the stiffness matrices in (5.39) is finally written as

$$\mathbf{K}_e(\boldsymbol{\mu}) = \sum_{d=1}^{\mathbf{n}_{\text{k}_{\text{ob}}}} \mathbf{K}_e^d \prod_{i=1}^{\mathbf{n}_p} B_{i,\text{ob}}^d(\mu_i), \quad (5.40)$$

where the number of terms $\mathbf{n}_{\text{k}_{\text{ob}}}$ is a priori unknown but is recovered after performing the following computations for all the $\mathbf{n}_{\text{k}_{\text{ob}}}^{\text{red}} = 24$ separated matrices \mathbf{K}_e^d :

$$d = \mathcal{F}(g, h, f) \quad \text{for } d = 1, \dots, \mathbf{n}_{\text{k}_{\text{ob}}}^{\text{red}} \quad (5.41)$$

$$\mathbf{K}_e^d = \begin{cases} \mathbf{T}_e^{g\top} \widehat{\mathbf{K}}_{\text{ob}}^f \mathbf{T}_e^h & \text{if } g = h, \\ \mathbf{T}_e^{g\top} \widehat{\mathbf{K}}_{\text{ob}}^f \mathbf{T}_e^h + \mathbf{T}_e^{h\top} \widehat{\mathbf{K}}_{\text{ob}}^f \mathbf{T}_e^g & \text{if } g \neq h, \end{cases} \quad (5.42)$$

$$B_{i,\text{ob}}^d = L_i^g L_i^h O_{i,\text{ob}}^f \quad \text{for } i = 1, \dots, \mathbf{n}_p \quad (5.43)$$

As a result from the above, only $\mathbf{n}_{\text{k}_{\text{ob}}} = 13$ matrices computed from equation (5.42) result non-null. The parametric functions associated to these terms are the same as those reported in Table 5.3 for the set of elements “ $e \in \text{xy}$ ” in the scaffold, thus are not repeated here.

Once the parametric functions has been determined for all the elements, we can proceed to build the global separated stiffness matrices in the stent-like structure. The notation for the affine decomposition of the global stiffness matrix is repeated below,

$$\mathbf{K}(\boldsymbol{\mu}) = \sum_{k=1}^{\mathbf{n}_k} \mathbf{K}^k \prod_{i=1}^{\mathbf{n}_p} B_i^k(\mu_i), \quad (5.44)$$

where we recognize that the parametric functions $B_i^k(\mu_i)$ of the global structure are just the collection of the particular ones obtained for the different set of elements in the stent. Therefore, the total number of separated terms in equation (5.44) is given by the sum: $\mathbf{n}_k = \mathbf{n}_{\hat{\mathbf{k}}} + \mathbf{n}_{\text{k}_{\text{ob}}} = 17$. The ordering criteria for these terms is arbitrary, an we choose to place first the parametric functions governing the horizontally aligned elements, and then functions that govern the parametric behavior of the obliquely aligned elements.

The separated matrices \mathbf{K}^k that complete the affine decomposition in equation (5.44), are built following standard finite element procedures with slight considerations, as presented in Algorithm 3. This methodology builds finite element equations that supplement the parametric dimensions in a separated approach. Afterward, it serves as input data for the algebraic PGD solver that approximates the multidimensional solution at a reduced cost.

Data: FE connectivities, $eType_e$: element type, for $e = 1, \dots, n_e$. Unit-cell repetitions in 2D: $n_{hor} \times n_{ver}$. Parametric functions B_i^k , for $k = 1, \dots, n_k$.

Result: \mathbf{K}^k separated matrices, for $k = 1, \dots, n_k$.

```

for  $e = 1 \dots n_e$  do
    switch  $eType_e$  do
        case " $e \in hor$ " do
            • Compute  $\widehat{\mathbf{K}}_e^f$  from (5.33), for  $f = 1, \dots, n_{\hat{k}}$ .
            • Assign local  $\widehat{\mathbf{K}}_e^f$  to global  $\mathbf{K}^k$  for  $k = 1, \dots, n_{\hat{k}}$ .
        end
        case " $e \in ob$ " do
            • Compute  $\phi_j$  from (5.34).
            • Compute  $\mathbf{K}_e^d$  from (5.42), for  $d = 1, \dots, n_{k\ ob}$ .
            • Assign local  $\mathbf{K}_e^d$  to global  $\mathbf{K}^k$  for  $k = (n_{\hat{k}}+1), \dots, n_k$ .
        end
    end
end
Build all sparse  $\mathbf{K}^k$ , for  $k = 1, \dots, n_k$ .
    
```

Algorithm 3: Adapted FE loop that builds the separated matrices \mathbf{K}^k , providing an affine decomposition of the parametric stiffness in the stent-like structure.

5.3 3D parametric lattice structures solved with algebraic PGD

Once the affine decomposition of input data is defined, the algebraic PGD solver is used to solve the structures described before. For the parametric scaffold, we present a unit-cell problem with homogenization and a periodic structure made of $5 \times 5 \times 5$ repetitions of cells in three orthogonal directions.

The effective orthotropic 3D constitutive tensor coefficients can be recovered at the bulk using the unit-cell solutions with homogenization. We focus on the explicit

parametric response of the orthotropic Poisson's ratios, since this is the property of interest in auxetic materials.

In addition, the parametric stent is solved for two load cases, either subjected to internal pressure or axial loads. We use the generalized displacements solutions, to compute two explicit parametric responses in the stent. In the axially loaded case, we measure how the mean radius along the deformed cylinder changes with respect to the applied deformation. In contrast, we measure how the cylinder length varies when an internal pressure is applied to the stent.

The PGD solver tolerances are $\eta_{\text{tol}} = 10^{-6}$ for the alternated directions, and $\zeta = 10^{-3}$ or $\zeta = 10^{-4}$ are the typical ones used for the greedy computation modes.

Regarding the 3D beam models, the cross-section property for torsion, $J_{\text{t},e}$, is always function of the parameter "t", but it is modified according to the torsion theory for prismatic structures (Timoshenko and Goodier, 1951, Chapter 11). Therefore, in the scaffold problem it becomes either $J_{\text{t}}(t) = 0.141 t^4$ for square cross-sections or $J_{\text{t}}(t) = 0.029 t^4$ for rectangular cross-sections (cut elements at unit-cell boundary). In the stent problem, $J_{\text{t}}(t) = \frac{\pi t^4}{32}$ is simply the circular cross-section polar moment of inertia.

5.3.1 Parametric scaffold

The scaffold unit-cell is subjected to Periodic Boundary Conditions (PBC) and six load cases, as conceived by homogenization theory in 3D. These result in parametric non-homogeneous Dirichlet boundary conditions that are prescribed in the first mode or modes, depending on the number of terms needed. The remaining modes are solved by the algebraic PGD solver, where homogeneous essential conditions are enforced. Thus, the sum of all modes verify boundary conditions exactly, whereas equilibrium is satisfied by minimizing the residual in a global parametric sense.

Given that the PBC are enforced by Lagrange Multipliers, special care must be taken at the scaffold unit-cell boundary nodes, since they are all located at boundary edges (dotted lines in Figure 5.9). Typically, imposition of PBC at rectangular unit-cells are defined at their six boundary faces, those illustrated in Figure 5.9 in red, green and blue, and their opposites. For points that are contained in these faces, the resulting constraints are independent. This is no longer true for points that are contained at their edges, because these share two faces. We follow the systematic approach explained by Li and Wongsto (2004) to avoid dependent boundary constraints, which result in ill-conditioned systems.

In Figure 5.10, we present the evolution of the modal amplitudes that result from the algebraic PGD solver, for the solution of the scaffold unit-cell load cases. The stopping criteria for the Greedy computation of the modes is set with $\zeta = 10^{-4}$. We observe that in general, the PGD compression applied to the solution does not reduce the number of modes but presents a smoother evolution of modal amplitudes. In addition, the first five modal amplitudes observed in Figures 5.10c, 5.10e and 5.10f in

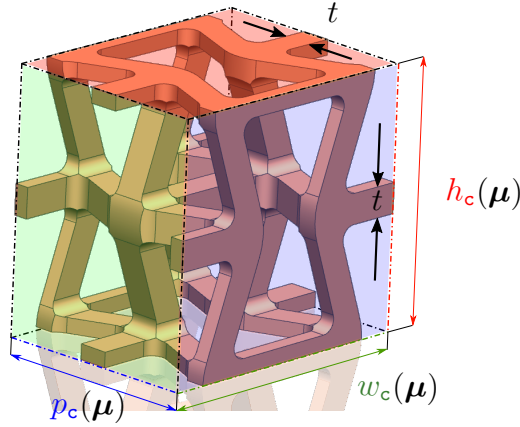


Figure 5.9: Scaffold unit-cell characterization.

blue, are related to the ω^ℓ modal amplitudes from the SVD approximation (5.21), for $\ell = 1, \dots, n_{\text{svd}} = 5$. This happens for load cases ZZ , XZ and YZ respectively, since the SVD modes are needed to prescribe the parametric non-homogeneous essential boundary conditions.

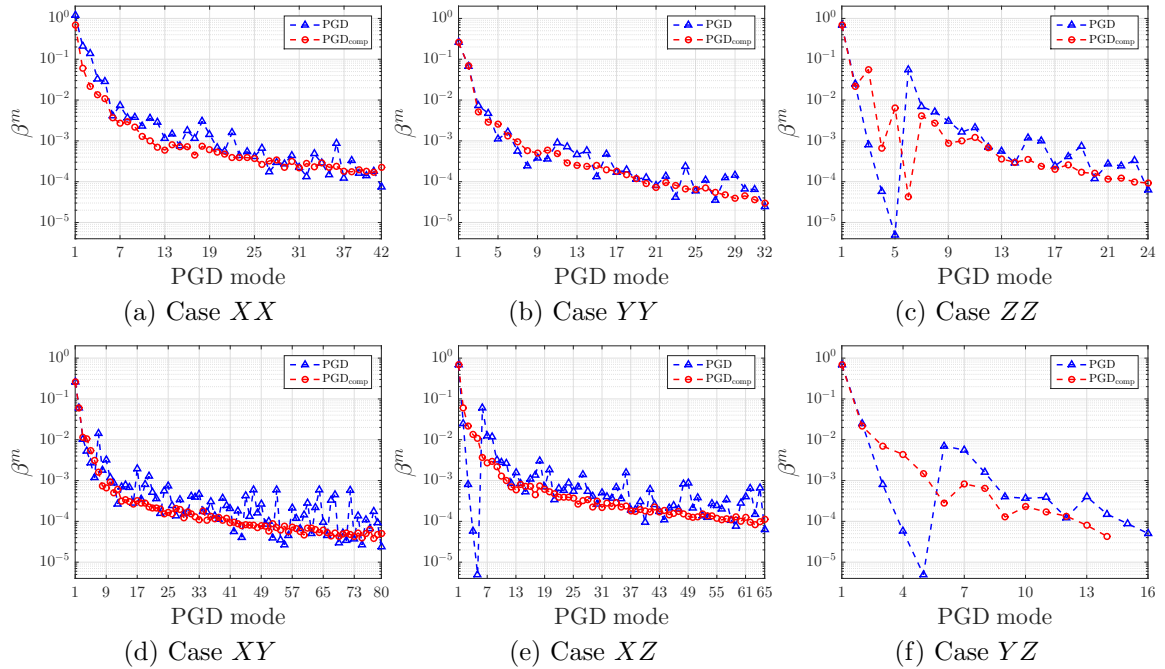


Figure 5.10: PGD modal amplitudes β^m , $m = 1, 2, \dots, n$ (with or without PGD compression). Parametric scaffold unit-cell model with homogenization.

Figure 5.11 collects the first two distinctive spatial modes, obtained using PGD compression and plotted normalized, for the scaffold unit-cell under prescribed normal strains. In order to represent their shape, we need to arbitrary select the unit-

cell undeformed configuration, depicted in dashed-blue lines for: $a = 0.4$, $b = 1$, $\alpha = 75^\circ$ and $\phi = 1.3$. Typically, the first mode in all cases describe the characteristic deformation given by the different prescribed strains.

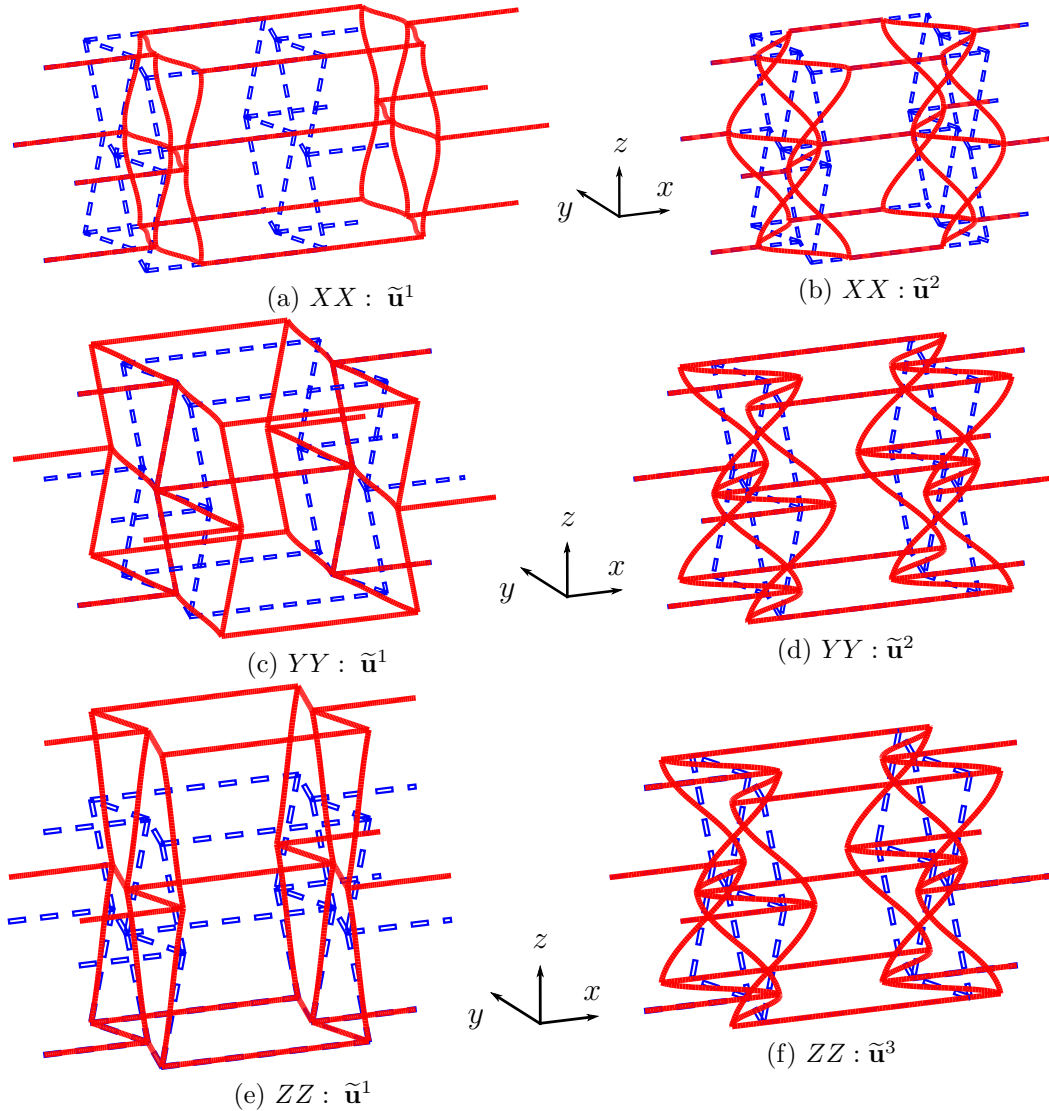


Figure 5.11: Scaffold unit-cell under normal strain load cases. Normalized spatial modes with PGD compression scaled for illustration.

The remaining spatial modes in Figure 5.11 are $\tilde{\mathbf{u}}^2$ for load cases XX and YY , and $\tilde{\mathbf{u}}^3$ for case ZZ . These latter practically represent the same shape, despite a sign change noted in Figure 5.11b for $\tilde{\mathbf{u}}^2$ in the XX load case. It does not seem accidental that these similar modes appear under different normal strains, given that for all load cases, the relation between degrees of freedom at opposite boundary faces of the unit-cell is the same, once the essential boundary conditions are set homogeneous. However, this does not mean that the parametric functions are the same for different

normal strain load cases. For each of the spatial modes shown in Figure 5.11, there are different functions providing the explicit parametric response. The reader is referred to Appendix E, where these parametric functions are shown.

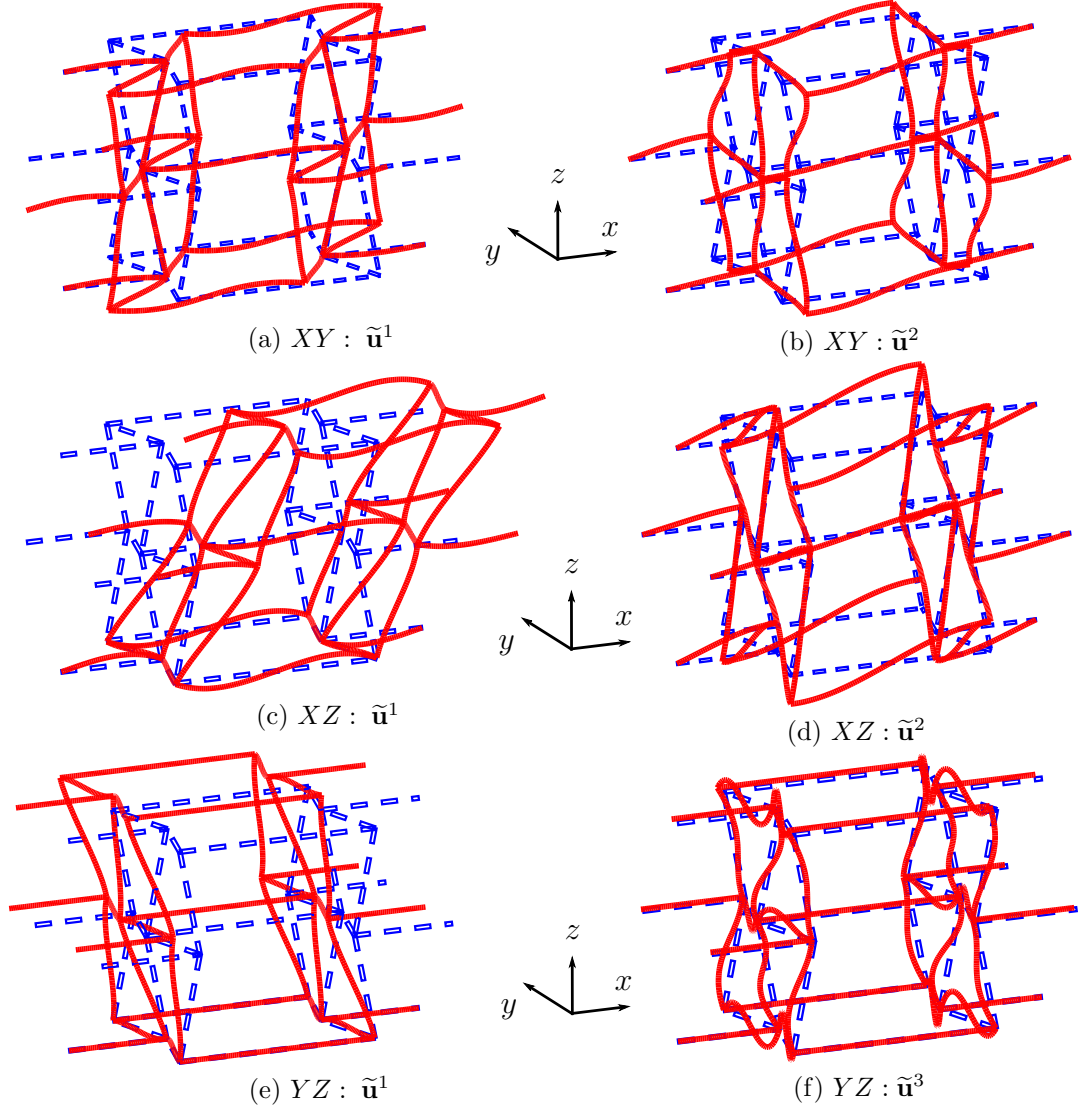


Figure 5.12: Scaffold unit-cell under shear strain load cases. Normalized spatial modes with PGD compression scaled for illustration.

In Figure 5.12 we also present the first two characteristic normalized spatial PGD modes with compression, but for the prescribed shear strain loads applied to the scaffold unit-cell. Again, the first mode in all cases take the distinctive deformation of the imposed strains. The other spatial modes selected in Figure 5.12 are $\tilde{\mathbf{u}}^2$ for load cases XY and XZ , and $\tilde{\mathbf{u}}^3$ for case YZ . In contrast with the normal strain cases, all spatial modes are clearly diverse between different shear strain cases. Also,

it is noticeable that these configurations activate rotational degrees of freedom of the beam elements in the lattice. The normalized parametric functions that correspond to all the spatial modes depicted in Figure 5.12 are given in Appendix E.

Explicit parametric mechanical effective properties: We begin by recalling which are the computations that provide the coefficients of the effective constitutive tensor. In the context of PGD, we can recover all of them as a computational *vademecum*, that is a sum of terms with an explicit parametric response. Then, we present how these coefficients can be related to engineering moduli of interest, in our specific case, the 3D orthotropic Poisson's ratio. We finish showing some results and analysis of the Poisson's ratios computational *vademecum*, evaluated at different values of the parametric space.

The effective constitutive tensor $\mathbf{C}^{\text{eff}}(\boldsymbol{\mu})$ is written for the particular case of a 3D orthotropic material, using Voigt notation:

$$\mathbf{C}^{\text{eff}}(\boldsymbol{\mu}) = \begin{bmatrix} C_{11}^{\text{eff}} & C_{12}^{\text{eff}} & C_{13}^{\text{eff}} & 0 & 0 & 0 \\ C_{21}^{\text{eff}} & C_{22}^{\text{eff}} & C_{23}^{\text{eff}} & 0 & 0 & 0 \\ C_{31}^{\text{eff}} & C_{32}^{\text{eff}} & C_{33}^{\text{eff}} & 0 & 0 & 0 \\ 0 & 0 & 0 & C_{44}^{\text{eff}} & 0 & 0 \\ 0 & 0 & 0 & 0 & C_{55}^{\text{eff}} & 0 \\ 0 & 0 & 0 & 0 & 0 & C_{66}^{\text{eff}} \end{bmatrix}, \quad (5.45)$$

where the dependency of the coefficients in the parameters $\boldsymbol{\mu}$ have been omitted for simplicity. This matrix is symmetric, and each one of its coefficients is calculated according to the homogenization theory:

$$C_{IJ}^{\text{eff}}(\boldsymbol{\mu}) = \frac{1}{V_c(\boldsymbol{\mu})} \mathbf{u}^I(\boldsymbol{\mu})^\top \mathbf{K}(\boldsymbol{\mu}) \mathbf{u}^J(\boldsymbol{\mu}), \quad \text{for } I, J = 1, \dots, 6, \quad (5.46)$$

where $V_c(\boldsymbol{\mu}) = w_c(\boldsymbol{\mu})h_c(\boldsymbol{\mu})p_c(\boldsymbol{\mu})$ is the scaffold unit-cell volume (Figure 5.9). The displacements in (5.46) are the PGD solutions for the unit-cell problem, using the following definitions: $\mathbf{u}^1 \equiv \mathbf{u}^{XX}$, $\mathbf{u}^2 \equiv \mathbf{u}^{YY}$, $\mathbf{u}^3 \equiv \mathbf{u}^{ZZ}$, $\mathbf{u}^4 \equiv \mathbf{u}^{XY}$, $\mathbf{u}^5 \equiv \mathbf{u}^{XZ}$ and $\mathbf{u}^6 \equiv \mathbf{u}^{YZ}$. In addition, the stiffness matrix $\mathbf{K}(\boldsymbol{\mu})$ must be used in its separated form, as built for the algebraic PGD solver input. In the PGD approach, the result from equation (5.46) is a new separated expression: the computational *vademecum* for each of the material effective constitutive tensor components. Actually, the computation of (5.46) is done by performing the product using the vectors and matrix in their separated form. A similar procedure is followed to that explained, for example, for equation (5.39) in the affine decomposition of input data.

The Poisson's ratio for a 3D orthotropic material is typically recovered from the material compliance - the inverse of the constitutive tensor - which takes the following form in Voigt notation:

$$\mathbf{S} = \begin{bmatrix} 1/E_1 & -\nu_{21}/E_2 & -\nu_{31}/E_3 & 0 & 0 & 0 \\ -\nu_{12}/E_1 & 1/E_2 & -\nu_{32}/E_3 & 0 & 0 & 0 \\ -\nu_{13}/E_1 & -\nu_{23}/E_2 & 1/E_3 & 0 & 0 & 0 \\ 0 & 0 & 0 & 1/G_4 & 0 & 0 \\ 0 & 0 & 0 & 0 & 1/G_5 & 0 \\ 0 & 0 & 0 & 0 & 0 & 1/G_6 \end{bmatrix}, \quad (5.47)$$

where by ν_{ij} - for $i, j = 1, 2, 3$; $\forall i \neq j$ - is denoted the Poisson's ratio of a transverse extensional strain in "j" direction, with respect to an axial strain in "i" direction (Lempriere (1968)). In addition, E_i - for $i = 1, 2, 3$ - stands for the Young's modulus in the three orthogonal directions corresponding to load cases XX , YY and ZZ , while G_j - for $j = 4, 5, 6$ - implies the shear modulus in three orthogonal planes XY , XZ and YZ . Poisson's ratios are not symmetric in its indexes, but using the symmetry of the compliance matrix, the following relations between off-diagonal terms hold:

$$\begin{aligned} \frac{\nu_{21}}{E_2} &= \frac{\nu_{12}}{E_1}, \\ \frac{\nu_{31}}{E_3} &= \frac{\nu_{13}}{E_1}, \\ \frac{\nu_{32}}{E_3} &= \frac{\nu_{23}}{E_2}. \end{aligned} \quad (5.48)$$

Therefore, using the relations above and the fact that the matrix in (5.47) is nothing but the inverse of matrix in (5.45), the parametric orthotropic effective Poisson's ratios can be derived from the constitutive matrix coefficients as:

$$\begin{aligned} \nu_{12}^{\text{eff}}(\boldsymbol{\mu}) &= \frac{C_{13}^{\text{eff}} C_{23}^{\text{eff}} - C_{12}^{\text{eff}} C_{33}^{\text{eff}}}{(C_{23}^{\text{eff}})^2 - C_{22}^{\text{eff}} C_{33}^{\text{eff}}}, \\ \nu_{21}^{\text{eff}}(\boldsymbol{\mu}) &= \frac{C_{13}^{\text{eff}} C_{23}^{\text{eff}} - C_{12}^{\text{eff}} C_{33}^{\text{eff}}}{(C_{13}^{\text{eff}})^2 - C_{11}^{\text{eff}} C_{33}^{\text{eff}}}, \\ \nu_{13}^{\text{eff}}(\boldsymbol{\mu}) &= \frac{C_{12}^{\text{eff}} C_{23}^{\text{eff}} - C_{13}^{\text{eff}} C_{22}^{\text{eff}}}{(C_{23}^{\text{eff}})^2 - C_{22}^{\text{eff}} C_{33}^{\text{eff}}}, \\ \nu_{31}^{\text{eff}}(\boldsymbol{\mu}) &= \frac{C_{12}^{\text{eff}} C_{23}^{\text{eff}} - C_{13}^{\text{eff}} C_{22}^{\text{eff}}}{(C_{12}^{\text{eff}})^2 - C_{11}^{\text{eff}} C_{22}^{\text{eff}}}, \\ \nu_{23}^{\text{eff}}(\boldsymbol{\mu}) &= \frac{C_{12}^{\text{eff}} C_{13}^{\text{eff}} - C_{11}^{\text{eff}} C_{23}^{\text{eff}}}{(C_{13}^{\text{eff}})^2 - C_{11}^{\text{eff}} C_{33}^{\text{eff}}}, \\ \nu_{32}^{\text{eff}}(\boldsymbol{\mu}) &= \frac{C_{12}^{\text{eff}} C_{13}^{\text{eff}} - C_{11}^{\text{eff}} C_{23}^{\text{eff}}}{(C_{12}^{\text{eff}})^2 - C_{11}^{\text{eff}} C_{22}^{\text{eff}}}. \end{aligned} \quad (5.49)$$

In order to compute the six Poisson's ratios from (5.49), the three PGD solutions of the unit-cell subjected to normal strains are needed. For these six quantities,

we present in the following their response surfaces to variations in their parametric domain.

Figures 5.13 and 5.14 show respectively Poisson's ratios ν_{12}^{eff} and ν_{21}^{eff} . For these two, we select to show their response in the parametric domain $I_1 \times I_3$, that is where $\mu_1 = a$ and $\mu_3 = \alpha$ range. We also provide four different snapshots of their response $\nu_{12}^{\text{eff}}(a, \alpha)$ and $\nu_{21}^{\text{eff}}(a, \alpha)$, by evaluating parameters $\mu_2 = b$ and $\mu_5 = t$ at their intervals I_2 and I_5 extreme values.

The same is done for ν_{13}^{eff} and ν_{31}^{eff} in Figures 5.15 and 5.16, and for ν_{23}^{eff} and ν_{32}^{eff} in Figures 5.17 and 5.18. For these cases though, we show the response in the parametric domain $I_3 \times I_4$, that is where $\mu_3 = \alpha$ and $\mu_4 = \phi$ range. The four snapshots instead are given by evaluating parameters $\mu_1 = a$ and $\mu_5 = t$ at their intervals I_1 and I_5 extreme values.

5.3. 3D parametric lattice structures solved with algebraic PGD

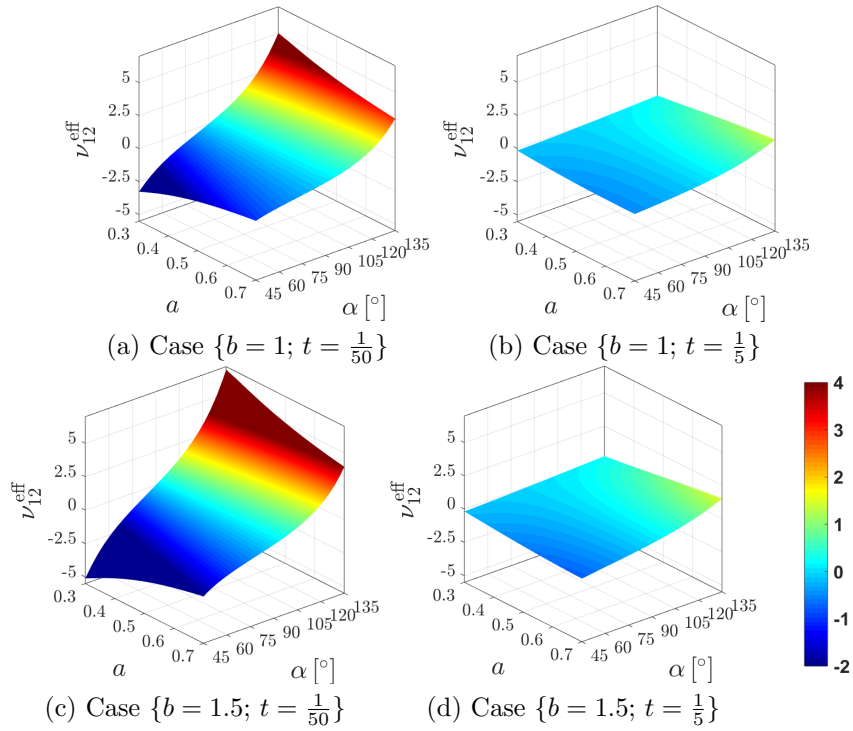


Figure 5.13: ν_{12}^{eff} in $a \times \alpha$ for specified values of b and t . Response for a scaffold unit-cell with a fixed value of $\phi = 1$.

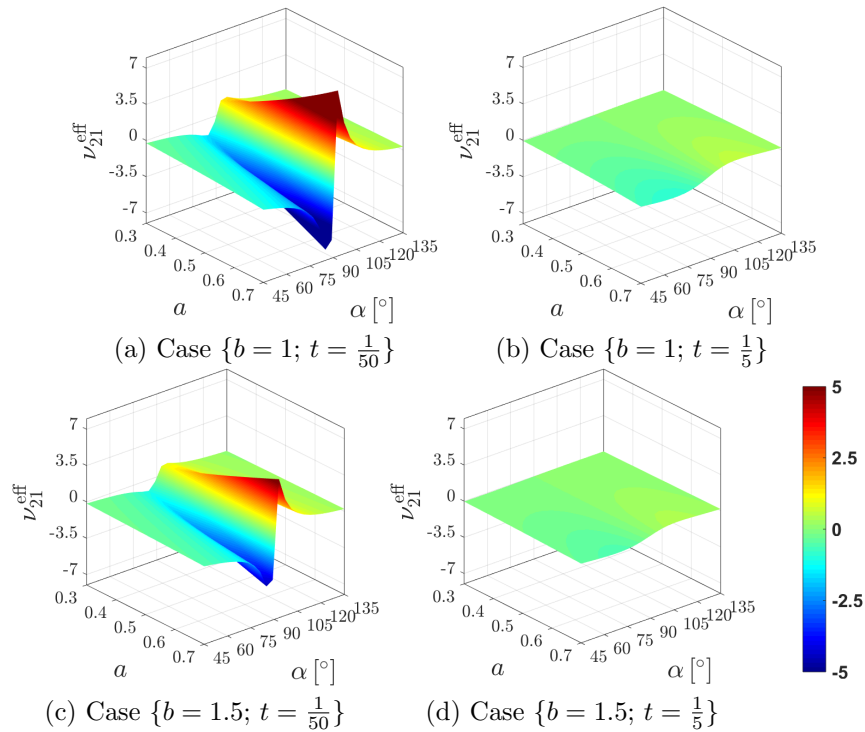


Figure 5.14: ν_{21}^{eff} in $a \times \alpha$ for specified values of b and t . Response for a scaffold unit-cell with a fixed value of $\phi = 1$.

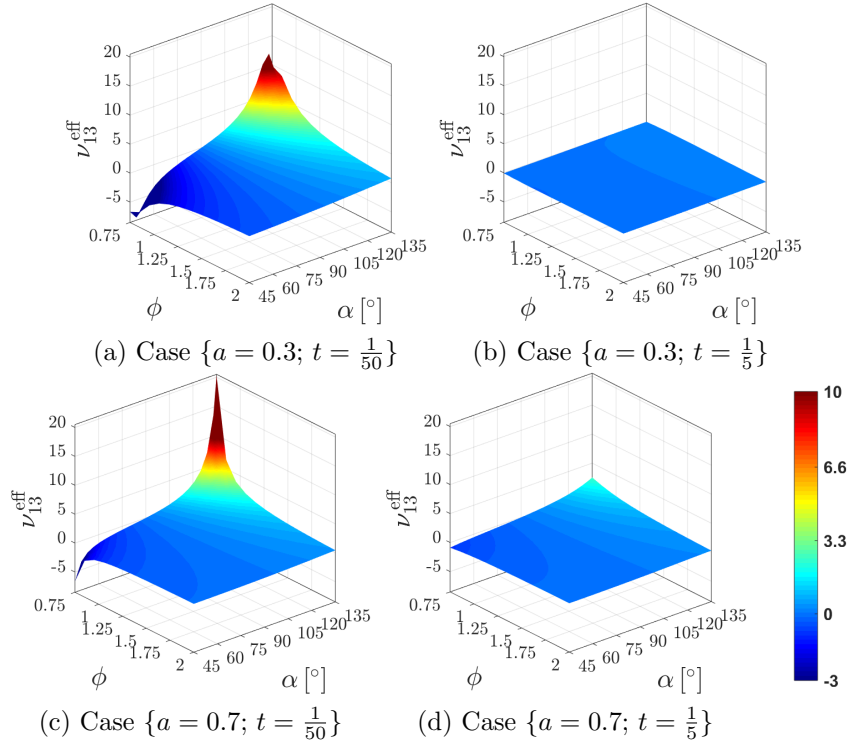


Figure 5.15: ν_{13}^{eff} in $\phi \times \alpha$ for specified values of a and t . Response for a scaffold unit-cell with a fixed value of $b = 1$.

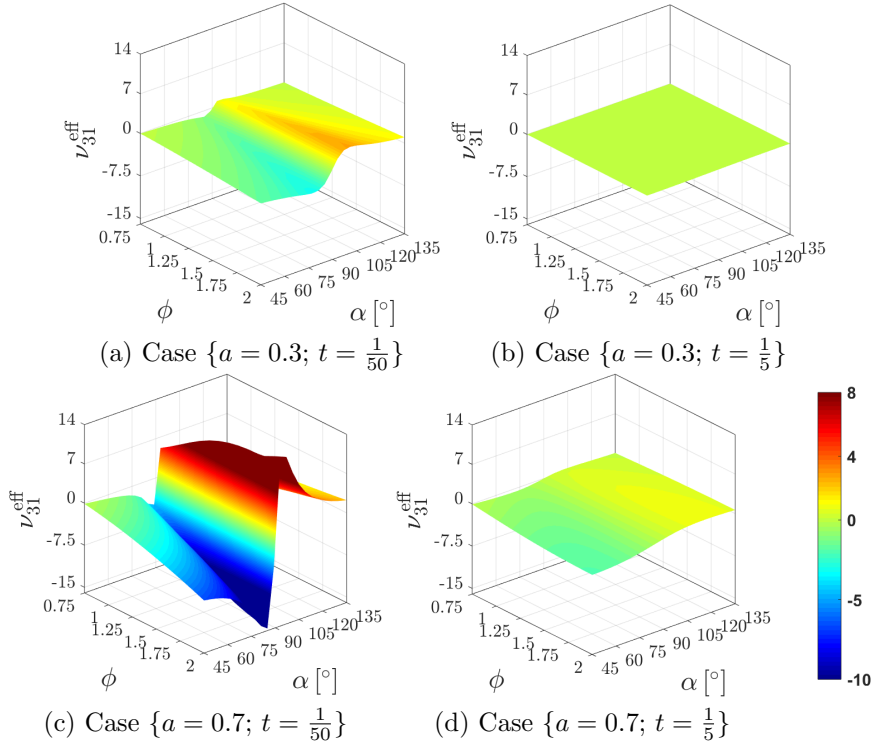


Figure 5.16: ν_{31}^{eff} in $\alpha \times \phi$ for specified values of a and t . Response for a scaffold unit-cell with a fixed value of $b = 1$.

5.3. 3D parametric lattice structures solved with algebraic PGD

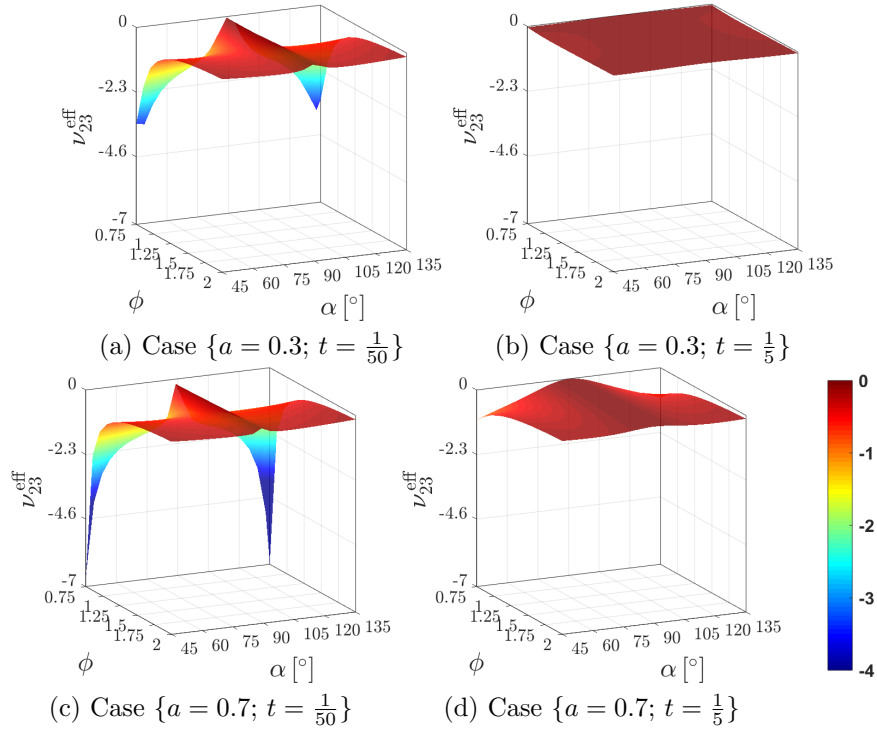


Figure 5.17: ν_{23}^{eff} in $\alpha \times \phi$ for specified values of a and t . Response for a scaffold unit-cell with a fixed value of $b = 1$.

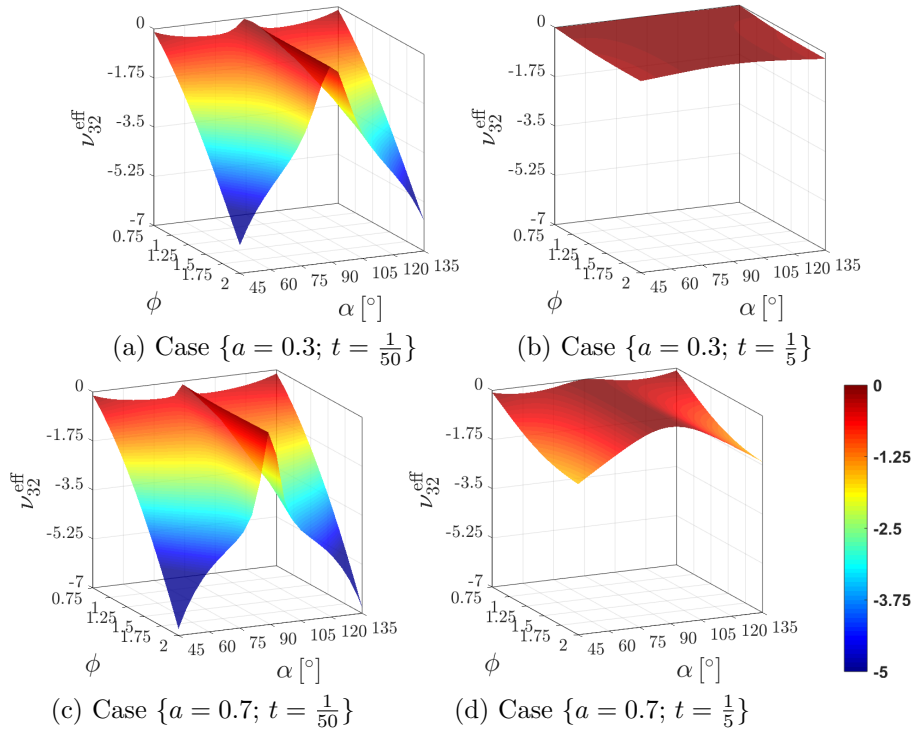


Figure 5.18: ν_{32}^{eff} in $\alpha \times \phi$ for specified values of a and t . Response for a scaffold unit-cell with a fixed value of $b = 1$.

In Figures 5.13 and 5.14 we observe the same behavior as in the 2D honeycomb, for Poisson's ratios ν_{12}^{eff} and ν_{21}^{eff} respectively, where the unit-cell angle α is the parameter that commands the transition between *non-auxetic* to *auxetic* performance and vice versa. With respect to the snapshots, these show that whereas an increase in length b magnifies the responses for Poisson's ratio ν_{12}^{eff} , the opposite occurs for ν_{21}^{eff} . In addition, both Poisson's ratios ν_{12}^{eff} and ν_{21}^{eff} are noticeably reduced when increasing the unit-cell beams thickness from its lowest $t = 1/50$ to its highest $t = 1/5$ values. This suggests that when designing an auxetic material for an engineering application, the inverse problem should approach a multi-objective or constrained optimization that trades off between the extreme values of Poisson's ratio and the effective material stiffness at the macro-scale.

In Figures 5.15 and 5.16 we present the response surfaces for the Poisson's ratios ν_{13}^{eff} and ν_{31}^{eff} . With respect to the previous analysis, we change the browsing parametric space to $\alpha \times \phi$. In fact, parameter ϕ works as the aspect ratio between the unit-cell pitch $p_c(\boldsymbol{\mu})$ and the other two dimensions, height $h_c(\boldsymbol{\mu})$ and width $w_c(\boldsymbol{\mu})$ (Figure 5.9). In general, there is an analogous behavior between the response of ν_{13}^{eff} and ν_{31}^{eff} compared with ν_{12}^{eff} and ν_{21}^{eff} . The snapshots also show that increasing the unit-cell beams thickness certainly reduces the extreme values of Poisson's ratios. In addition, parameter a is evaluated at their extreme values, showing that at its highest value, the responses of both ν_{13}^{eff} and ν_{31}^{eff} increase. However, it is particularly observed that, at the extremes of the range of α , and for the lowest values of ϕ , the response of ν_{13}^{eff} is dramatically amplified (see Figures 5.15a and 5.15c). We raise here the question about the accuracy of the algebraic PGD solver to capture these peak values and provide after some insight about it.

Regarding Poisson's ratios ν_{23}^{eff} and ν_{32}^{eff} , their results are shown in Figures 5.17 and 5.18, browsing the parametric space $\alpha \times \phi$ exactly as before. The peculiarity we observe here with respect to the previous ones is that either for values of $\alpha < 90^\circ$ or $\alpha > 90^\circ$, the behavior remains *auxetic*, and it also results symmetric along the range of parameter α . The snapshots show the same tendency as before, with respect to a decrease in the Poisson's ratio when thickness t is increased, and a magnification of the Poisson's ratios values when comparing results for the lowest value of a in contrast to those for the highest value of a . Moreover, it is observed that the response of ν_{23}^{eff} in Figures 5.17a and 5.17c is greatly magnified locally, at the interval extremes of parameter α and for the lowest values of ϕ .

PGD accuracy at the extreme values of Poisson's ratios: We here provide an insight of some cases where we observe that the algebraic PGD solver fails to provide an accurate result when computing extreme values of the effective Poisson's ratios in the scaffold. We focus on Poisson's ratios ν_{13}^{eff} and ν_{23}^{eff} since we have noticed that their response is greatly amplified locally at two corners of the Cartesian space $\alpha \times \phi$, specifically at $\{\alpha = 90^\circ \pm 45^\circ; \phi = 0.75\}$. In addition, we detect that the PGD response surfaces at these points are notably not smooth (see Figures 5.15a and 5.17a).

We begin by evaluating the algebraic PGD solutions (generalized displacements) at the prescribed set of parameters values shown in Table 5.4, where among them, are the extreme points considered before. The relative errors of the PGD solutions evaluated at these sets, compared against FE are shown in Figure 5.19. The results comprise the three normal strain cases XX , YY and ZZ , which are the ones involved in the calculation of the effective Poisson's ratios (5.49). Indeed, we note that all errors in Figure 5.19 are below 1%, which from the engineering point of view is an excellent performance. Note that these PGD vademecums provide a solution for a big number (exactly 568.75 millions) of different unit-cells in the present analysis.

Set	I	II	III	IV	V	VI	VII	VIII
a	0.3	0.3	0.3	0.3	0.7	0.7	0.7	0.7
α	45°	45°	135°	135°	45°	45°	135°	135°
ϕ	0.75	2	0.75	2	0.75	2	0.75	2

Table 5.4: Scaffold sets of parameters (a, α, ϕ) , where PGD against finite element error is computed (Figure 5.19). The remaining parameters are constant at $b = 1$ and $t = 0.11$.

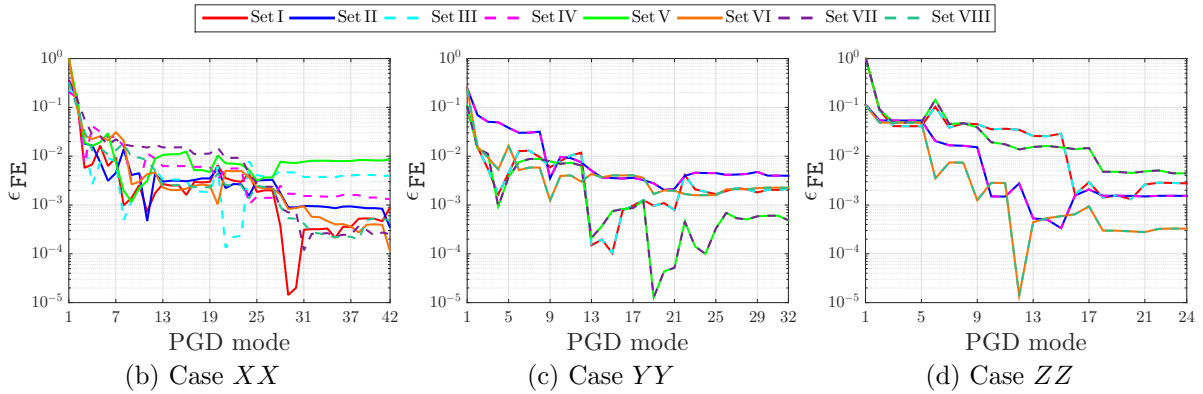


Figure 5.19: Scaffold unit-cell under uni-axial traction loads: relative error of PGD solution against FE computed at different sets of parameters values (Table 5.4).

On the other hand, we compute the relative error of the response surfaces of Poisson's ratios ν_{13}^{eff} (from Figure 5.15a) and ν_{23}^{eff} (from Figure 5.17a) against FE. The results, over the Cartesian domain $I_3 \times I_4$, are shown in Figure 5.20. A high increase in the error is observed where extreme values of ν_{13}^{eff} and ν_{23}^{eff} occur, reaching magnitudes above 60% (Figures 5.20a) and 40% (Figure 5.20b) respectively.

Being the error in displacements low, the response of the Poisson's ratios resulting from equation (5.49), is likely to be sensitive to other sources of error, for some particular values of the parameters. In fact, the total error outcoming from equation (5.49) is propagated from the displacements solutions - reported below 1% in Figure

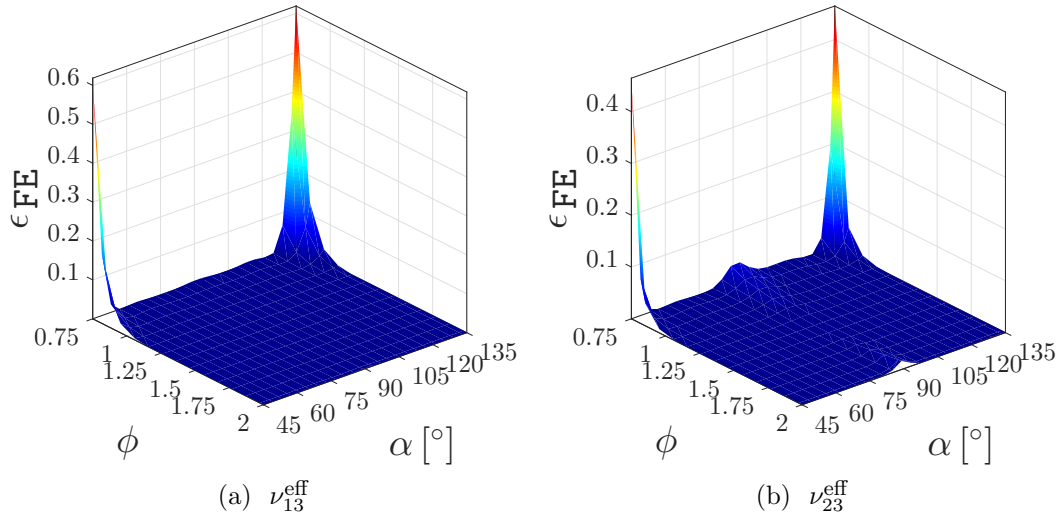


Figure 5.20: Relative error of Poisson's ratios PGD response in $\alpha \times \phi$ against FE, for a scaffold unit-cell with parameters values: $\{a = 0.3; b = 1; t = \frac{1}{50}\}$.

5.19 - together with that committed in the approximation of $\mathbf{K}(\boldsymbol{\mu})$ - where the maximum error of the function approximated by 5 SVD terms is $1.92e^{-5}$ in the whole parametric space $\alpha \times \phi$ - . These two sources of error, that are alone appreciated as excellent from an engineering point of view, are certainly magnified at the extreme values shown in Figure 5.20.

Scaffold made of a periodic arrangement of unit-cells: The unit-cell solution errors presented in Figure 5.19 are very low compared to the peak errors reported in Figure 5.20, at extreme values of the Poisson's ratios ν_{13}^{eff} and ν_{23}^{eff} . Therefore, one may think what would actually happen if instead of using homogenization, we solve with algebraic PGD, a scaffold made of periodic unit-cell repetitions, subjected to uni-axial loads. In any case, previous results from section 4.2 have shown that Poisson's ratios computed by averaging displacements at orthogonal faces, do correspond very well with the effective ones obtained by homogenization.

We consider a parametric scaffold made by $5 \times 5 \times 5$ repetitions of the unit-cell formerly described. Figure 5.21 shows one possible configuration of the parametric problem, which actually holds 568.75 millions of different cases, given by the product $\prod_{i=1}^{n_p} n_{d,i}$.

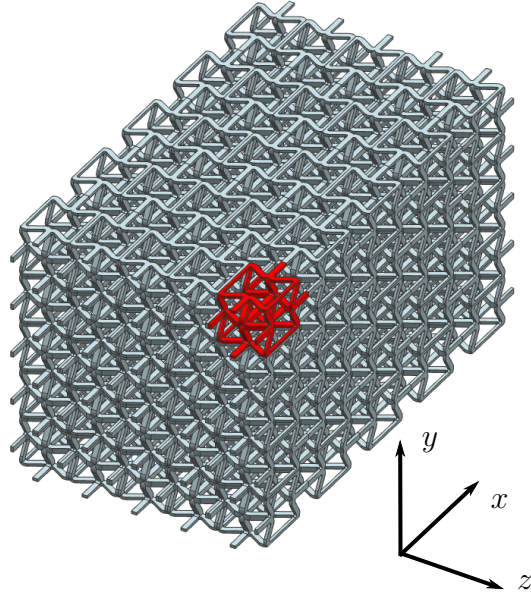


Figure 5.21: Parametric lattice scaffold made by a $5 \times 5 \times 5$ unit-cells composition.

In Figure 5.22, we present the evolution of the modal amplitudes given by the algebraic PGD solver, for the solution of the periodic scaffold subjected to three uni-axial loads. The stopping criteria for the Greedy computation of the modes is set with $\zeta = 10^{-3}$.

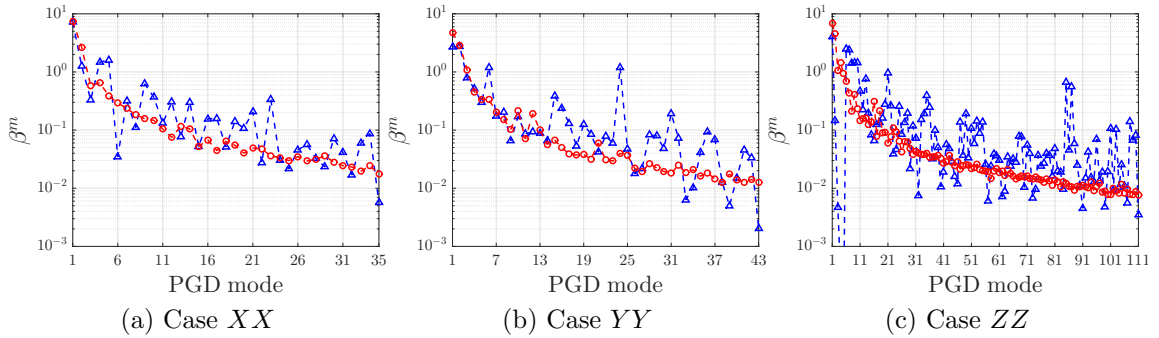


Figure 5.22: PGD modal amplitudes β^m , $m = 1, 2, \dots, n$ (with or without PGD compression). Parametric lattice scaffold subjected to uni-axial loads.

We focus on the accuracy of the algebraic PGD solver, compared to FE solutions. Especially, we evaluate the scaffold explicit parametric displacements, at the values where significant errors have been observed for the PGD effective Poisson's ratios, ν_{13}^{eff} and ν_{23}^{eff} , computed using homogenization.

The analysis confirms that the algebraic PGD solver lacks of accuracy for the displacements solutions of the periodic lattice, at the same critical points obtained using homogenization. For example, we present in Figure 5.23 a comparison of the generalized displacements obtained by the algebraic PGD against finite elements, for

the periodic scaffold subjected to uni-axial XX displacements, and evaluated at the set of parameters $\{a = 0.3; b = 1; \alpha = 45^\circ; \phi = 0.75; t = \frac{1}{50}\}$.

We observe from Figure 5.23 that the applied strain in x direction is notably magnified in z direction, given that this set of parameters corresponds to the extreme negative value of ν_{13}^{eff} in Figure 5.15a. However, when comparing Figures 5.23c and 5.23d from the PGD response against 5.23a and 5.23b computed by FE, the displacements in z direction are markedly diminished. Precisely, the L_2 relative error of displacements between these two solutions results 53.6%, which is well related to the corresponding one reported in Figure 5.20a for ν_{13}^{eff} .

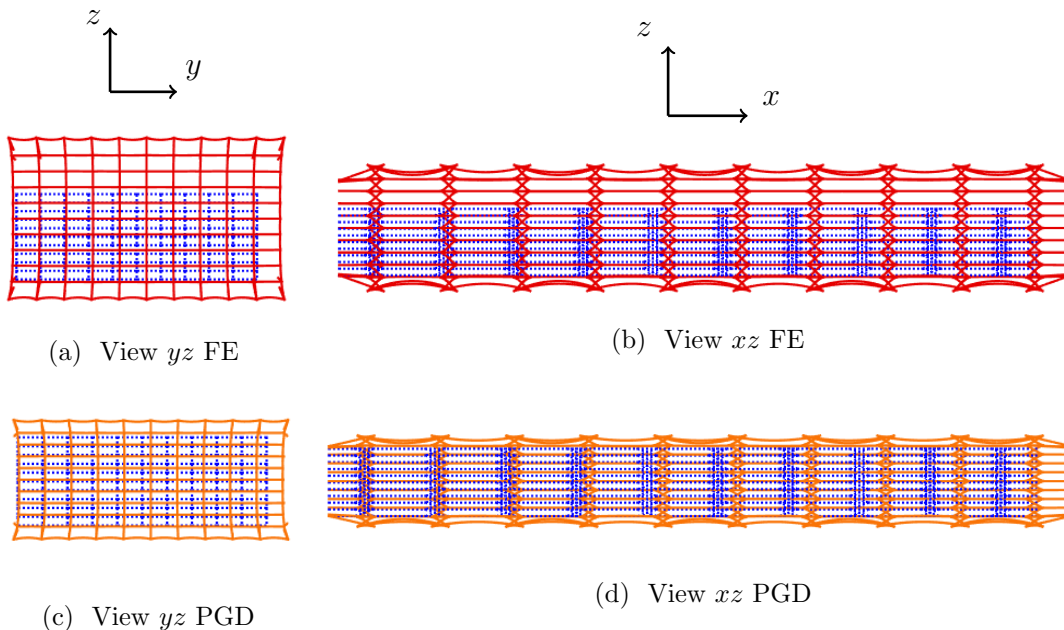


Figure 5.23: Periodic scaffold subjected to XX displacements (5% equivalent strain), comparing deformations using FE or PGD, for parameters $\{a = 0.3; b = 1; \alpha = 45^\circ; \phi = 0.75; t = \frac{1}{50}\}$

A similar case results in Figure 5.24 when comparing generalized displacements for the same set of parameters, but imposing the periodic scaffold to uni-axial YY displacements. For this applied strain, we focus on the magnification of strain in z direction, in accordance to one of the extreme negative values of ν_{23}^{eff} in Figure 5.18a. Again, we find that the PGD solution is considerably diminished when contrasting the generalized displacements from Figures 5.24c and 5.24d against those obtained using FE in 5.24a and 5.24b. Precisely, the L_2 relative error between these two becomes 49.7%, in correlation with the corresponding one reported in Figure 5.20b for ν_{23}^{eff} .

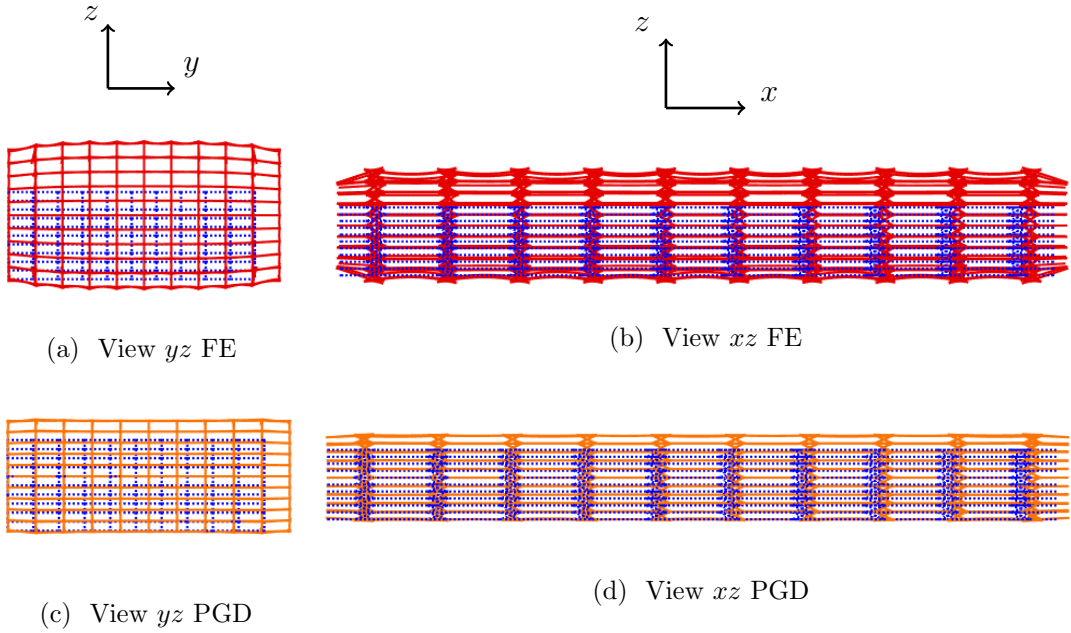


Figure 5.24: Periodic scaffold subjected to YY displacements (10% equivalent strain), comparing deformations using FE or PGD, for parameters $\{a = 0.3; b = 1; \alpha = 45^\circ; \phi = 0.75; t = \frac{1}{50}\}$

We finally propose some ideas that could serve as guidelines for future tasks on mitigating these cases. To begin with, it is true that the two points where we detect big errors in Figures 5.20a and 5.20a coincide with those where we find the biggest errors in the SVD approximation of input data (see Appendix D and Figure D.4b). However, the input error in the approximation is very low, in fact the maximum relative error for an entry in $\mathbf{K}(\boldsymbol{\mu})$ evaluated at the set of values $\{a = 0.3; b = 1; \alpha = 45^\circ; \phi = 0.75; t = \frac{1}{50}\}$ is only $1.32e - 6$. This suggests that in this case, adding more SVD modes to reduce the input error might not necessarily pay off the increased computational effort in accuracy (a bigger number of SVD modes increases \mathbf{n}_k , which makes the PGD solver loop in separated terms of $\mathbf{K}(\boldsymbol{\mu})$ longer). Actually, a possible remedy could be related to a richer parametric space, either by a local refinement or assuming higher order approximating functions, as proposed by Zou (2017). Another possible route would be to assume initially a more expensive approach by tidying parameters (α, ϕ) into a 2D parametric problem (Zou et al. (2018)), expecting a benefit in the final computational cost in terms of accuracy.

5.3.2 Parametric stent-like structure

We present in the following the results of a stent-like structure subjected to two load cases, a uni-axial load and an internal pressure (see Figures 5.25a and 5.25b). The parametrization behaves exactly as described for the planar honeycomb, with

the particularity that here an array of $(n_{\text{hor}} = 5) \times (n_{\text{ver}} = 10)$ cells is wrapped into a cylindrical shape. We focus on the parametric mechanical behavior, which is obtained after solving equilibrium by means of the algebraic PGD. In particular, we present for the uni-axial case, $\nu_{\text{ax-rad}}$: the ratio between strains in the radial direction against the applied deformation, and for the internal pressure load, $\nu_{\text{rad-ax}}$: the ratio between strains in the axial direction against the applied deformation. These two mechanical properties serve in the comparison against the same parametric structure, but modeled using a geometrically nonlinear beam model (Simo and Vu-Quoc (1988)).

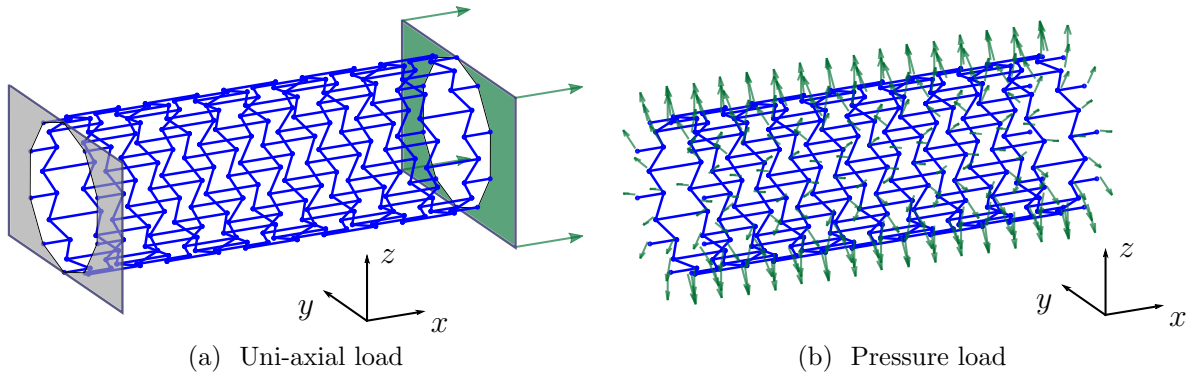


Figure 5.25: Stent-like structure under two different load cases.

In Figure 5.26 it is shown how the PGD modal amplitudes evolve, for the solution of the parametric stent-like structure under the two loading conditions. The stopping criteria for the Greedy computation of the modes is set with $\zeta = 10^{-3}$.

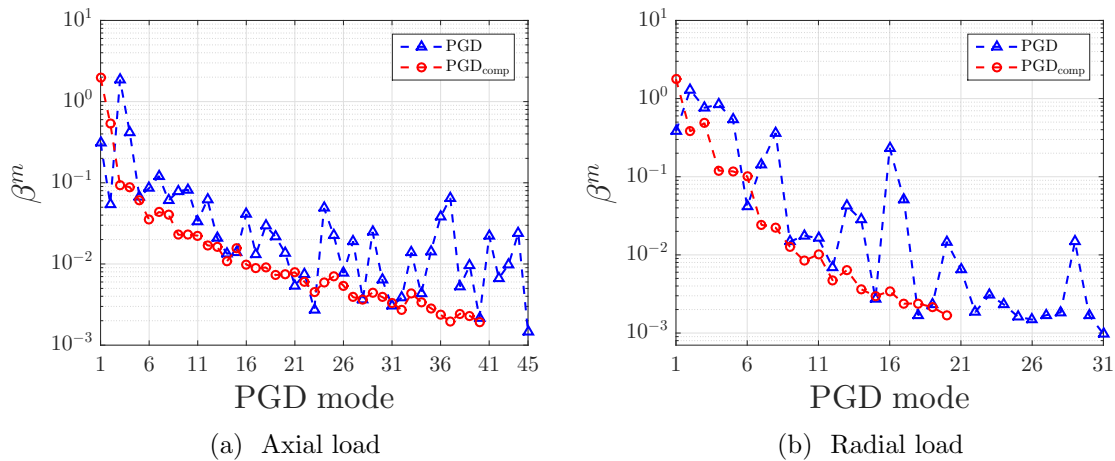


Figure 5.26: PGD modal amplitudes (with or without PGD compression), stent-like structure under axial and radial loads.

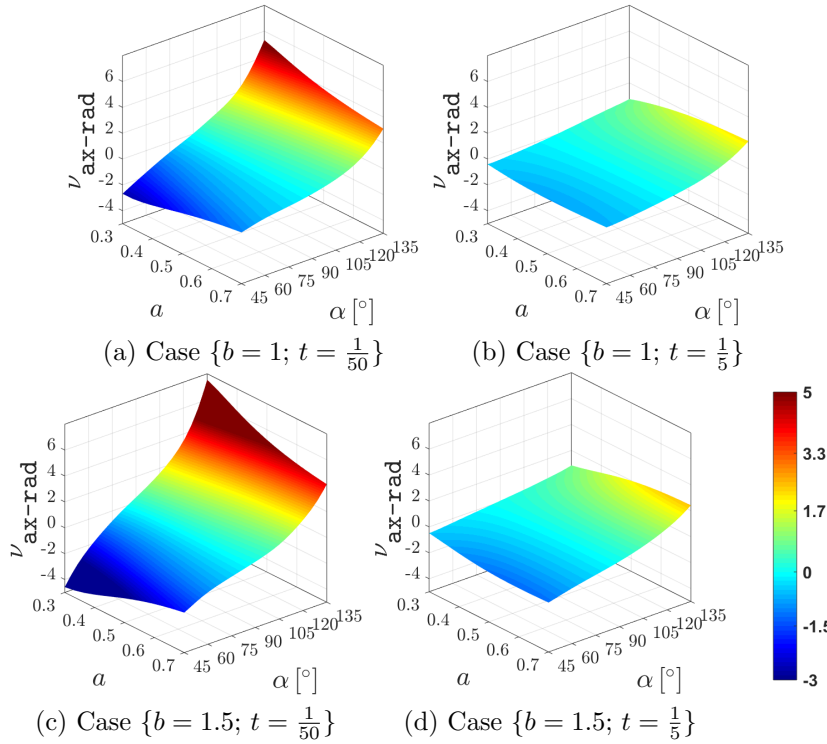


Figure 5.27: $\nu_{\text{ax-rad}}$ in $a \times \alpha$ for specified values of b and t in the stent-like structure.

Moreover, Figure 5.27 presents the parametric response of $\nu_{\text{ax-rad}}$ in the space of $a \times \alpha$, and taking different values of the remaining parameters b and t . The computation is obtained using the PGD displacements solution. The nodal positions of the deformed configuration are used to fit a value for the deformed radii, which is average along different coordinates of the cylindrical axis. A similar behavior to that of ν_{12} in the planar honeycomb is recovered.

Finally, Figure 5.28 presents the parametric response of $\nu_{\text{rad-ax}}$ in the same space of parameters as described before. In the present case, all radial displacements are imposed, and what is measured instead using the PGD solution is the distance between the cylinder tips. The observed performance is as expected, analogous to that of ν_{21} analyzed in the planar honeycomb.

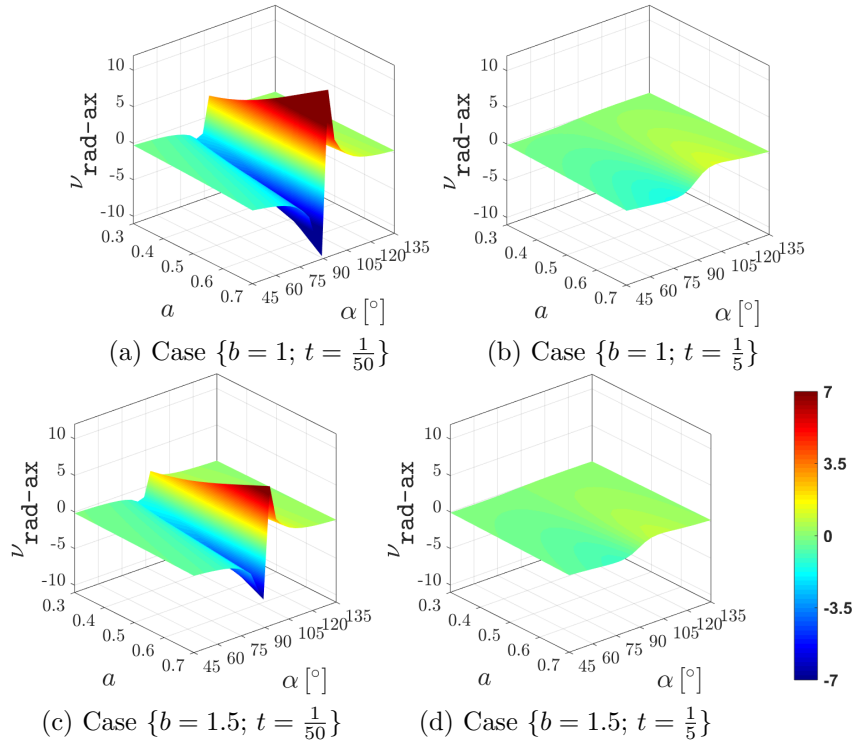


Figure 5.28: $\nu_{\text{rad-ax}}$ in $a \times \alpha$ for specified values of b and t in the stent-like structure.

In the following section, the parametric stent is solved using a nonlinear beam formulation (Simo and Vu-Quoc (1988)), at multiple values of the parameters. The explicit parametric response is recovered using PGD a posteriori, meaning that instead of solving an equilibrium problem, it interpolates the multiple finite element solutions in the particular separated form.

We focus in two aspects of interest in the application of lattices structures. On one hand, we have observed how these structures can work as a mechanical amplifier of the applied strain, for example the extreme values computed in Figure 5.28a. This mechanisms are of relevant interest in applications like soft actuators (Miriyeve et al. (2017)). However, the fact that an applied strain is magnified in its transverse directions, it could certainly imply a considerable modification of the structure's initial configuration. Whenever this condition is true, then the initially computed mechanical properties are no longer true. We asses an example of this in the following, and refer to as mechanical properties that depend on the applied loading magnitude as an extra parameter. Last but not least, we also analyze that buckling is prompt to show up in the stent-like structure subjected to axial loads. In addition, this effect is more likely to appear in designs associated to auxetic extreme values.

5.4 Multidimensional sampling of nonlinear parametric formulations and a posteriori separation using PGD

For the present analysis we use the free license of ADINA [ADINA© R&D \(2018\)](#), a commercial finite element software. The aim is to run a finite element model that considers large displacements (and small strains) of the same parametric stent-like structure. This framework is usually referred to as geometrical nonlinearities. In order to reduce the amount of finite element cases, the multidimensional space is restricted to two parameters only, then $\boldsymbol{\mu}_{n1} = [\mu_1 \ \mu_2]^\top = [a \ \alpha]^\top$. Compared to the linear model, the remaining parameters are fixed at $b = 1.2$ and $t = 2/25$. The intervals and sampling points for μ_1 and μ_2 are kept the same as described before for the PGD solver, then $n_{d,1} = 50$ and $n_{d,2} = 91$. The total number of cases to run - 4550 - is considerably big, then we approach it with a scripting strategy written in Matlab®. The parametric nodal coordinates of the stent initial configuration are already known from the linear problem, and the two loading cases are applied by prescribing displacements, in a series of incremental load steps for the nonlinear solver, up to an equivalent of 10% strain.

The generalized displacements solution are recovered for each of the converged configurations, at ten different load steps (corresponding to equivalent applied strains from 1% to 10%). Given that a finite element displacement solution is known for each of the prescribed values of the parameters, and for each of the load steps, a posteriori PGD least square approximation (LS-PGD) can be launched. The algorithm is based exactly on the same scheme used for PGD compression (see Appendix B), the difference being now that the parametric data is a full multidimensional tensor, and the LS-PGD provides as an output, a separable approximation of it. This becomes the explicit parametric solution, which depends on the loading magnitude as an extra parameter, and is typically less expensive in terms of storage. In fact, the number of modes computed by the LS-PGD is shown in Figure 5.29, associated to a modal amplitude decay of 10^{-3} .

We begin with the LS-PGD approximation of the stent subjected to internal pressure (radial loads). We observe from Figure 5.29b that the response decay much faster than its counterpart subjected to axial loads, in fact a modal amplitude decay of 10^{-3} is obtained by only 13 modes.

From the material design point of view, we present in Figure 5.30, $\nu_{\text{rad-ax}}$, the ratio between strains in the axial direction against the applied deformation. The novelty here is that this material property depends on the loading magnitude as an extra parameter. It is interesting to observe that the points in the parametric space $a \times \alpha$ that give rise to extreme values of $\nu_{\text{rad-ax}}$ for small deformations - 1% of applied strain in Figure 5.30a - do not provide them any more as long as the structural configuration is changed by effect of higher applied strains - 5% and 10% in Figures 5.30b and 5.30c respectively - .

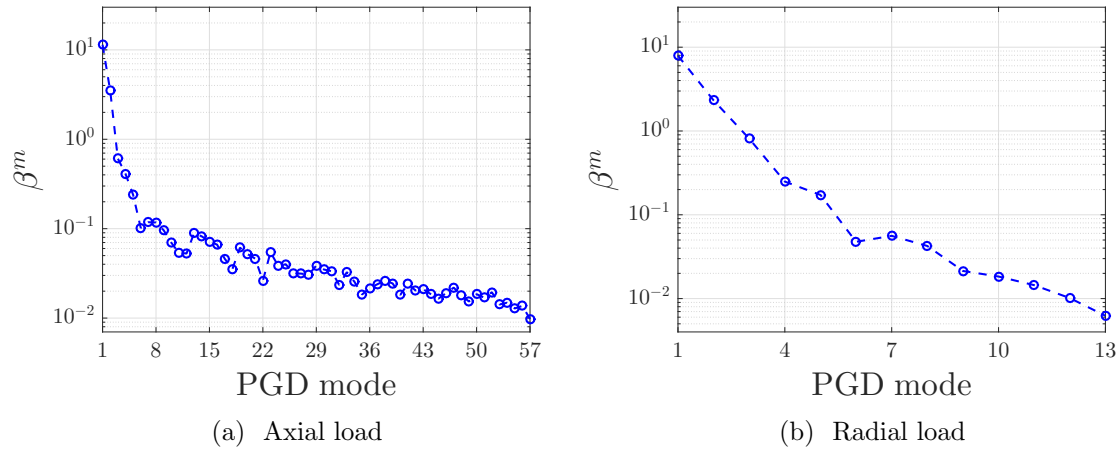


Figure 5.29: Modal amplitudes of the PGD least square approximation for the stent-like structure solved using nonlinear finite elements, sampled at points of the parametric space $a \times \alpha$, and subjected to axial and radial loads.

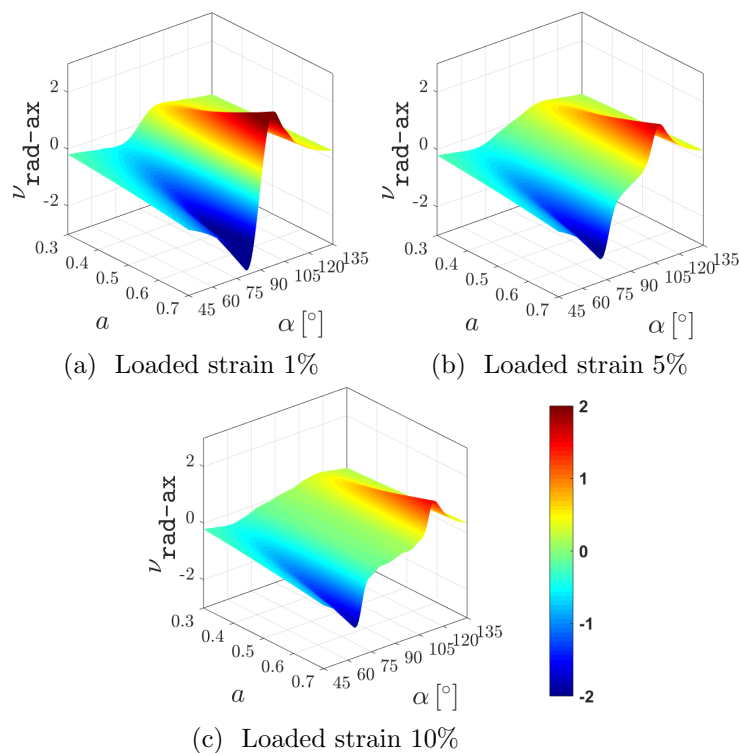


Figure 5.30: $\nu_{\text{rad-ax}}$ in $a \times \alpha$ for the PGD nonlinear solution of a stent-like structure, given at different load magnitudes.

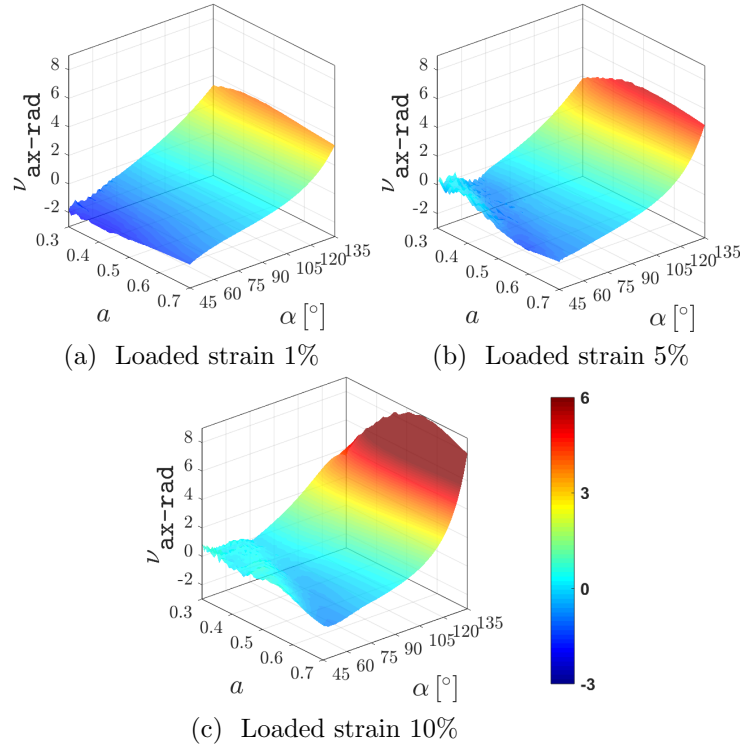
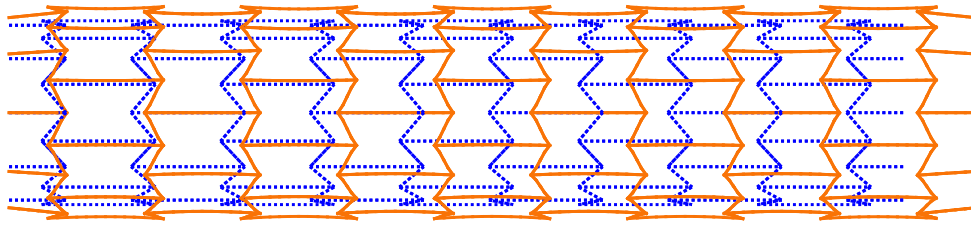


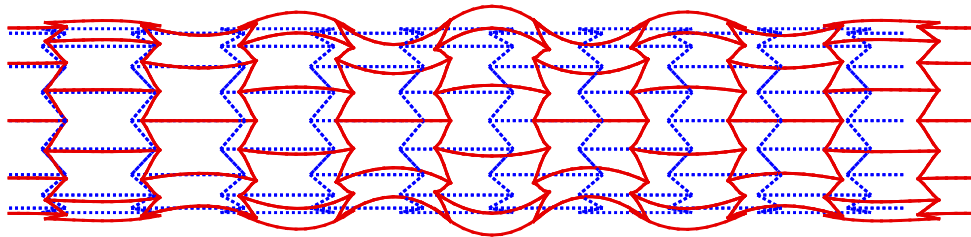
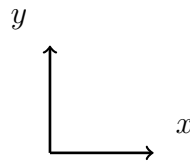
Figure 5.31: $\nu_{\text{ax-rad}}$ in $a \times \alpha$ for the PGD nonlinear solution of a stent-like structure, given at different load magnitudes.

With respect to the stent subjected to axial loads, in comparison to the radial load case, we observe from the modal amplitudes in Figure 5.29a that the LS-PGD approximation requires much more number of modes for the same decay. In fact, this load case result more challenging from the structural point of view given that is prompt to buckling, thus sudden modifications in the equilibrium configuration appear when loading magnitude is increased. Recovering from the LS-PGD the explicit parametric performance $\nu_{\text{ax-rad}}$, that is the ratio between strains in the radial direction against the applied deformation, it brings an insight as well on the parametric buckling behavior. Observing $\nu_{\text{ax-rad}}$ for higher applied strains in Figures 5.31b and 5.31c, compared to the smallest applied strain in 5.31a, we recover an unstable front that pushes the lowest values of Poisson's ratio up to zero, and grows with the increased loading magnitude.

From the mechanical point of view, the lowest auxetic values of $\nu_{\text{ax-rad}}$ implies higher elongations in the radial direction with respect to the applied axial load. Given that the structure is wrapped, the fact that the circumferential strain wants to grow implies that compressive forces appear in the tangent direction to the cylindrical shape. The lower the negative values of $\nu_{\text{ax-rad}}$ are, the higher the magnitude of this circumferential compression. These are the forces that induce local buckling configurations in the auxetic stent-like structure.



(a) View xy PGD linear



(b) View xy PGD nonlinear

Figure 5.32: Stent-like structure subjected to axial loads (8% equivalent strain), comparing deformed configurations obtained by PGD and LS-PGD of a nonlinear response affected by buckling. The set of parameters are: $\{a = 0.4; b = 1.2; \alpha = 50^\circ; t = \frac{2}{25}\}$

Figure 5.32 shows a comparison between deformed configurations obtained by PGD in the linear parametric framework and the LS-PGD approximation of the nonlinear response. Observing in Figure 5.32b the local contractions of the stent radius in the buckled shape, it explains how this configuration is reflected in values of $\nu_{\text{ax-rad}}$ tending to zero (Figure 5.31) - recall that $\nu_{\text{ax-rad}}$ is based on the average deformed radius along the cylinder axis -.

Chapter 6

PGD web app: displaying parametric solutions online

In the previous chapters, different parametric lattice material structures have been solved by means of a PGD approximation, such that the exponential cost associated with the increasing number of parameters could be greatly reduced. The collection of explicit parametric solutions, a.k.a. *PGD vademecum*, is formed by a tabulated structure given by spatial modes: in our problem, vectors of generalized displacements, coming along with associated parametric functions. Although each of these spatial modes do not have a precise physical meaning, this can be recovered by evaluating their accompanying modal functions at desired values of the parameters and performing a sum along all the terms in the PGD solution. Thus, the reconstruction of the parametric PDE solution for a prescribed value of the parameters implies accessing the *vademecum*, which can be done in a fast way, and performing a sum along PGD modes. In practice, it is commonly recognized that if these operations can be done within a minimum bandwidth of 20-60 Hz, it enables real-time solutions with a visual feedback. This is the inspiration behind developing a PGD post-processing tool which could allow the user interpret in an interactive way a parametric lattice structure response.

In this chapter, a post-processing solution for PGD is proposed and developed. The PGD solver provides as a result a copious amount of data, which is not ready to be visualized until properly post-processed, which can turn to be a tedious task, unless there is a way to display all the parametric results interactively. Moreover, the construction of a solution from the *PGD vademecum* for a prescribed value of the parameters requires certain familiarization with the method itself. In this sense, the PGD post-processing tool points to support a user without any PGD background to visualize how a parametric material structure behaves. Finally, the use is not restricted to parametric lattice structures, but can be potentially extended to any kind of PGD solution.

The PGD post-processing tool is developed in a standard web-based fashion. A

graphical interface is developed using a combination of HTML and CSS languages, which provide operability in a user-friendly environment. This is powered with the scripting language JavaScript, which has been used for years as a tool to provide functionality and dynamic features in websites. The graphical part of the tool is handled through WebGL (Web Graphics Library), which is included virtually in all popular available web browsers. In order to use the WebGL API (Application Programming Interface), an open source JavaScript library called “`three.js`” is used, which is designed to take advantage of the WebGL framework to provide 2D and 3D graphics without the need of adding third party add-ons.

The inception of the web application is a code, kindly provided by the AMB group at the University of Zaragoza, for displaying real-time solutions of a cantilever beam with a parametrized load position, using PGD (Cueto et al. (2016)). Moreover, the contents of this chapter have been developed by Alonzo (2018), a project in collaboration with the present thesis.

6.1 Program structure

The web application is organized by modules, such that distinct functionalities are placed in different folders, and the graphical interface is provided by the web-page (`index.html` file). Thus, by separating critical aspects of the application, it is intended that the development and maintenance of the software is simplified. In this section, the project structure is explained, which is constituted by:

```
| - cases/  
| - css/  
| - docs/  
| - js/  
| - resources/  
|  
| - index.html
```

The aim of this structure is that any new PGD solution that is intended to be post-processed could be added in the `cases` folder, while the others remain without modifications. The core of the application is provided in folders `css` and `js` while some additional data and information about the capabilities is kept in `resources` and `docs` folders. In addition, the contents of the web-page are defined in the `index.html` file, which is explained in the following.

6.1.1 Graphical interface

The graphical interface of the application is defined by the “Hypertext Markup Language” (HTML) file `index.html`, which specifies which are the elements that are

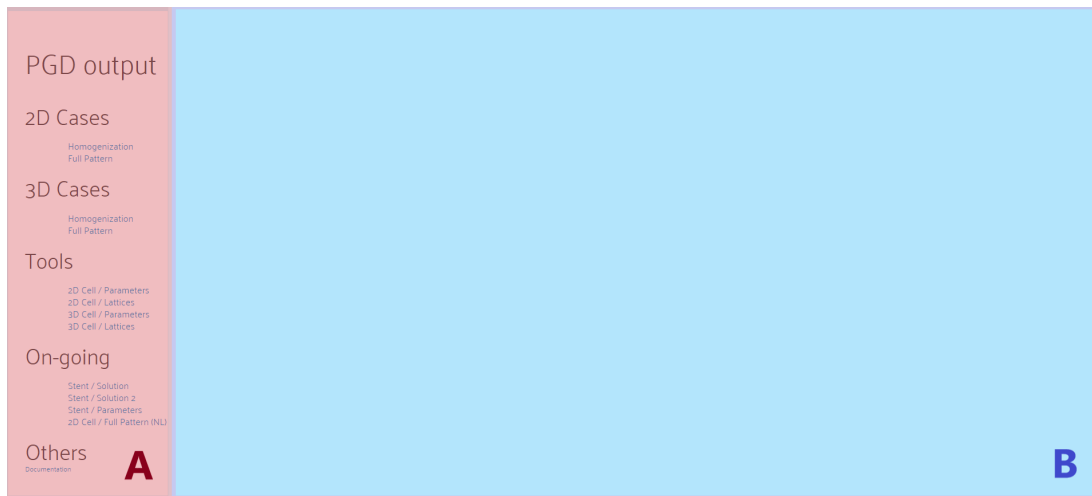


Figure 6.1: Main web-page graphical interface parts.

shown in the web-page, and the files contained inside the “Cascading Style Sheets” `css` folder. The latter commands the layout and displaying style of the elements within the web-page.

The stylish appearance of the graphical interface is shown in Figure 6.1, which is divided in two parts:

- Part A: Panel: it contains the labels of the precomputed PGD solutions that can be used. It is fixed at the left-hand side of the screen and by clicking in the different solutions, these are loaded into the working area, depicted with letter B in Figure 6.1. In here, the user can further interact with the parametric PGD solutions.
- Part B: Working area: it is defined in the `index.html` file as an `iframe`, which is an HTML element that admits content to import another resource into the interface. This dynamic loading of content (or “embedded content”) allows that each PGD solution is loaded into the `iframe` as a piece of HTML code, instead of loading a complete new web-page on its own. In this way, a generic interface is coded only once and loaded many times, avoiding the need of writing a new interface for each new solution added. Thus, post-processing new PGD solutions is simplified since the amount of files needed for the implementation is reduced.

Once a PGD solution has been loaded into the working area, the graphical interface looks like in Figure 6.2, displaying four distinct windows with particular purposes:

- Window 1: Graphical PGD: the post-processed PGD solution (in our case, a deformed lattice structure for a given value of the parameters) is depicted in the middle of the working area. The screen can change the visualization of the deformed

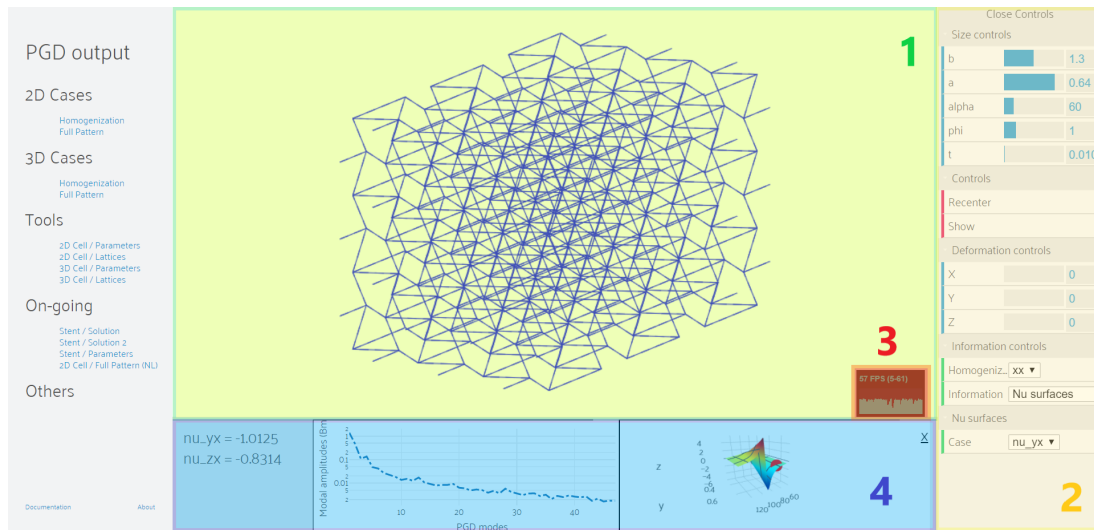


Figure 6.2: Different graphical interface windows for a PGD solution loaded into the working area.

structure either by using a mouse or the fingers in a touch-screen device. This allows the PGD solution being visible from different perspectives, accessed by the user through rotation, translation and zooming operations. In addition, the display of the PGD solution in this area works interactively with the control bar, since every change made in the parameters intervals displayed in Window 2 is immediately updated here, supporting the visual feedback for real-time simulations.

Window 2: Control bar: a set of values of the parameters involved in the PGD solution can be modified here, which works as an input to modify the deformed structure display in Window 1, without needing to reload the web-page. A detail of this control bar is shown in Figure 6.3. Depending on the PGD solution loaded into the working area, the control bar shows the appropriate parameters involved in the problem formulation. In addition, these are some of the typical actions that can be done through the control bar:

- Sliders: the natural and most common use is for ranging within the values of the parameters, accordingly to the intervals limits and number of points selected for the PGD solver. In addition, a slider also varies the deformation magnitude imposed to the parametric structure. This acts just as a magnifying plotting factor for the linear PGD cases, but in the nonlinear problems, it points to the particular parametric function that modifies the PGD modes, depending upon the loading magnitude.
- Switches: they admit the use of “true or false” binary statements, such as showing or hiding different solutions for comparison or selecting which loading case to display in the same parametric structure.

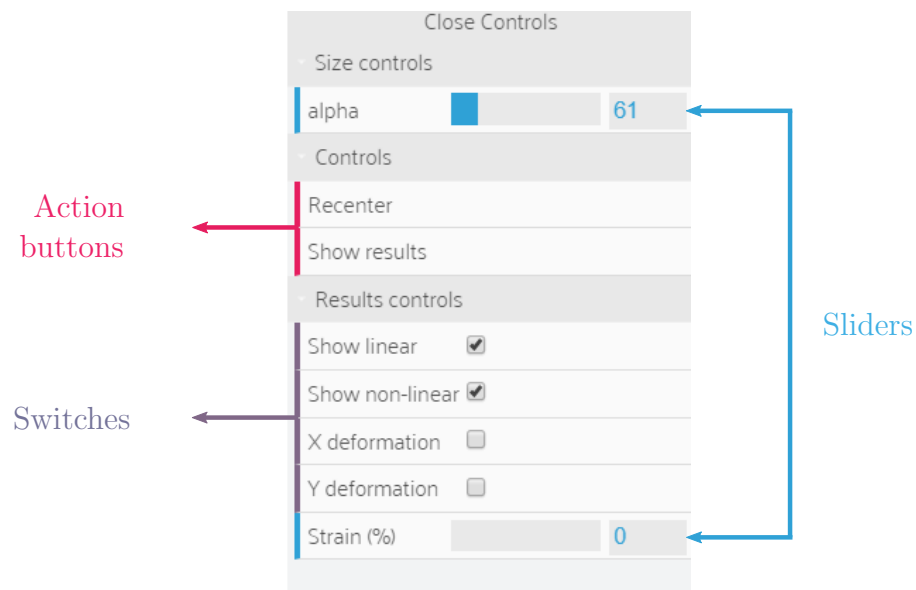


Figure 6.3: A detailed look at the Control bar.

- Action buttons: they are programmed to trigger either a re-centering operation for the deformed structure view or to show the results controls. The first one renders a new image of the deformed structure in the center of the working area such that all rotations, translations or zooming operations are reset. The results control opens new elements in the control bar associated to the PGD solution, such as modifying the loading magnitude or activating the information panel below the working area - Window 4 - that shows parametric material effective properties in real time.

Window 3: Stats bar: it assesses the rendering visual feedback by tracking the graphic engine performance, measured in frames per second (FPS) at which the image is updated. It works under an external library `stats.js`, whose developers are also the ones involved in `three.js`.

Window 4: Results panel: it is opened by the action button “Show results” in the control bar and has three reserved spaces. The first one on the left hand-side displays the values of the effective Poisson’s ratio, which are computed in real time depending upon the chosen values of the parameters in the control bar. The space in the middle always displays the evolution of the modal amplitudes for the chosen PGD solution, and the remaining one shows depending on the user’s choice, either the PGD parametric functions or the response surface of a selected Poisson’s ratio.

6.1.2 Web application core

The application is based on the programming language JavaScript, allowing possible execution in every modern web browser. The scripts (filename extensions “`.js`”) are organized such that those providing global functions are grouped inside the `js` folder, meaning that every loaded PGD solution uses them. On the other hand, scripts that support particular uses of a certain PGD solution are placed inside separated folders, which are in turn sorted within the folder `cases`. In this way, particular purposes do not affect the global functioning of the web application.

In addition, the `js` folder follows the structure

```
| - js/  
    | - core/  
    | - misc/
```

The `core` folder contains the following scripts:

- `three.js` is the main file of a JavaScript library and Application Programming Interface (API) of identical name, whose documentation, examples and forums, are found in threejs.org. It is focused on the creation of 3D computer graphics, and manages its display through WebGL library, meaning that this rendering process could be handled across different web browsers. The library is published online, allowing modifications and redistribution under the [MIT license](https://opensource.org/licenses/MIT), a permissive free software license, and its main asset is providing an easy way of defining geometries and their associated displaying properties.
- `CanvasRenderer.js` is a module of `three.js` designed for drawing 2D graphics, and displaying them by means of *Canvas 2D Context* API. It is also used in 3D graphics since it features the possibility of exhibiting changes in line widths, which is practical to show variations of the lattice material thickness. However, it is acknowledged that the performance with 3D graphics is slower than the WebGL renderer.
- `OrbitControls.js` is another module of `three.js`, controlling how the PGD solution illustration (Window 1) is seen from a 3D space. In desktop computers, it supports the usage of the mouse left button to let the camera orbit around the displayed graphics, the right button to enable the camera panning, and the scrolling wheel to do zooming. In portable devices, panning is admitted when using three fingers while zooming is done with two, as usual.
- `jQuery.js` is a free and open-source JavaScript library using the MIT license, which in fact is reported to be used by the 71.5% of the top ten thousand websites, and being the most widely adopted JavaScript library for a large margin ([Ltd \(2019\)](#); [Libscore \(2019\)](#)). It is designed to manipulate the Document Object Model (DOM), which is the tree-structure that represents the HTML

elements of a web-page. Thus, it effectively reduces the amount of coding needed to produce dynamic web-pages, by simplifying the finding operations of an element in the DOM, the handling of events, the creation of animations and eliminating incompatibilities between different web browsers.

- `plotly.js` is a JavaScript open source graphing library, enabling the creation of sophisticated scientific charts and animations in a scalable vector format (SVG), which gives compatibility across web browsers and publication of high-quality exported images. It has a simple framework since it only takes data and instructions, whereas the actual production of vector graphics is externally done. This plain structure also facilitates the adoption of this library as a browser-based graphing library for [Python](#), [R](#), or [Matlab](#).
- `math.js` is an open source library that extends the JavaScript's built-in Math capabilities, allowing for example to work with matrices or high dimensional arrays.
- `dat.gui.min.js` is a user platform that allows changing the value of variables in JavaScript using a graphical interface. This replaces the need of making modifications inside the code or having to provide continuously these values as inputs. In the context of post-processing a PGD solution, it admits a modification of the set of values of the parameters that triggers real-time changes in the solution in an interactive way. The following process is required in order to account for this feature:
 - The parameters values can be changed using the sliders in the control bar, while the variables associated to each of them are overwritten accordingly.
 - A function is called each time a parameter value is modified, to refresh all the graphics and results shown in the working area (Windows 1 and 4). For this purpose, all data depending on the new values must be recomputed, starting for example from the parametric structure coordinates matrix. In addition, the PGD *vademecum* is evaluated by summing all the spatial modes, weighted by the parametric functions contribution, whose arrays must be properly accessed using the new pointers to the parameters values.
- `loader.js` is a function that loads the content of each PGD solution in the `iframe`, which is the HTML element that displays the graphical results in the working area (Part B). By “content” we mean the basic ingredients needed for the PGD solution post-processing to properly work, constituted by: a basic HTML structure, some functions coded in JavaScript, and data stored in files; these latter also written in a proper JavaScript syntax. For this purpose, each PGD solution - or link - in the side panel (Part A) is defined with a unique ID (specified in `index.html`). When the links are clicked, the actual function `loader.js` is called and inserts all the specified content into the `iframe`. It is

worth noting that each PGD solution post-processing may need to load different data files (among which there is always a PGD *vademecum*). Thus, the required file names must be defined in the `json.js` file under the unique ID (this file, written in the JavaScript Object Notation - **JSON** - format, is kept inside the `resources` folder).

With respect to the `misc` folder, it contains the following:

- `anim.js` is the script that manages the interactive PGD graphical results, by means of two functions:
 - `init()` defines the main elements that the library `three.js` requires to initialize the PGD solution rendering:
 - ★ The scene, holding the different geometries that create an image inside the container.
 - ★ The container, being the physical part of the screen where the animation takes place. Technically, it is an HTML element that links the web-page HTML code and the graphical elements produced by the renderer.
 - ★ The renderer, working inside the container, is in charge of translating the written orders in JavaScript into different graphical elements that generates the visible image or *the scene*.
 - `animate()` does the animation, which in practice means providing the scene with a new image or frame at a frequency of 60 Hz, a number that might get slower whenever the CPU/GPU usage increases. It is performed as an infinite background loop, requesting the renderer for the execution of a new image, which in fact is built using the actual set of values of the parameters selected by the user in the control bar sliders.
- `events.js` is the script containing some functions which are not essential to the PGD solution rendering but provide some useful functionalities. For example, the possibility to recenter the displayed image to the original view, avoiding the need of reloading, or an automatic adjustment of the image whenever the web-browser window is resized, allowing to keep the same image view in the working area.

6.1.3 Briefing: input of a PGD vademecum for interactive post-processing

The goal here is to briefly present what are the ingredients needed to post-process a PGD solution using the core of the web application explained before, and how these two interact to produce the displayed graphics. Each one of the PGD solutions that

appear in the web-page side panel (Part A) is identified with a unique ID, which is referred to as `caseName`, for the sake of explanation in the following.

Each PGD solution must contain three basic ingredients to be post-processed, being the `caseName` main file, the PGD *vademecum* file and the mesh file, which are all coded in a JavaScript format.

The `caseName` main file

The generic name of the PGD solution is used to invoke the main JavaScript file as `caseName.js`. The objective here is to define *local* functions that complement the *global* functions used by the core. Thus, the *local* functions can be modified, added or skipped depending on the specific purposes of the PGD solution to be post-processed. Typically, the following functions are coded in the `caseName.js` file:

- `createGUI()` customizes the control bar that is displayed in the working area (Window 2). This control bar contains, for example, the sliders that set the parameters values. Thus, it is natural to define this function as *local*, given that each PGD solution could contain different parameters (or different parameters intervals). Other functionalities, boxes or buttons of the control bar are also defined here.
- `recreate()` performs the update of the nodal coordinates at the deformed configuration, depending upon the load magnitude and the values of the parameters. The computations are prompted by tracking if there are any changes in the parameters or loading magnitude, set through the control bar sliders.
- `results()` loads the results panel (Window 4), and commands the display of effective mechanical properties in real time.

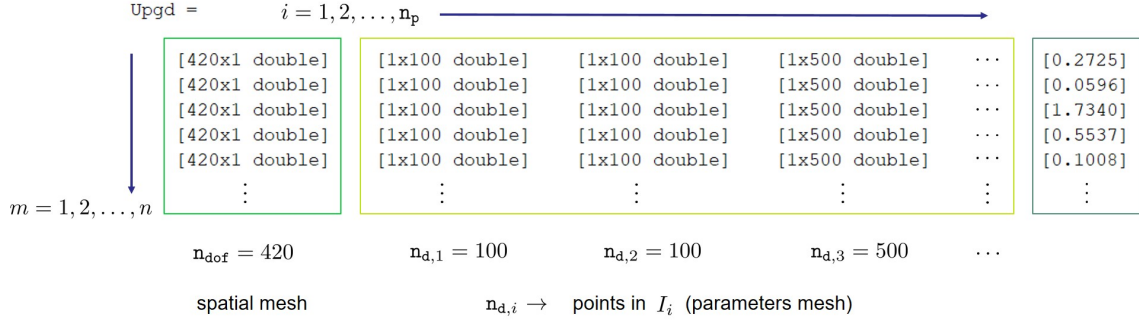
The PGD *vademecum* file

In this file we provide the post-processing app with the explicit parametric solution obtained by PGD. As described in Chapter 3, the PGD provides an approximation of the problem solution by means of a separated representation. From the point of view of the structure of this data, the particularity is that the PGD solution in the whole multidimensional space is stored in a smart way, preventing the exponential memory requirement for a problem with an increasing number of parameters. In addition, reconstructing the solution for a particular set of values is limited to a weighted sum of all the PGD spatial modes, making this computationally cheap operation suitable for displaying parametric responses of a PDE in real time.

In our case, the PGD solver has been coded in Matlab, where cell arrays provide an indexed data type storing arrays of numbers with different sizes. Recall from equation (3.11) that the PGD solution is given by

$$\mathbf{U}_{\text{PGD}}^n(\boldsymbol{\mu}) = \sum_{m=1}^n \beta^m \tilde{\mathbf{u}}^m \prod_{i=1}^{n_p} \tilde{G}_i^m(\mu_i),$$

being the sum of all PGD modes from $m = 1$ to n , containing at each addend, the product from $i = 1$ to n_p of all their corresponding parametric functions. In a Matlab cell array, for example, such a solution could be stored as:



where Upgd is the tabulated solution accommodating one row for each of the n modes, placing the normalized spatial modes $\tilde{\mathbf{u}}^m$ (column vectors of size $n_{\text{dof}} = 420$) and modal amplitudes β^m at the first and last columns, and in between, the discrete version of the normalized parametric functions $\tilde{G}_i^m(\cdot)$, taking values in the parameter's mesh of size $n_{d,i}$ (row vectors of size $n_{d,i}$).

This data must be transferred to the web application to serve the PGD solution post-processing, which in practice demands a translation into a JavaScript file (*.js). Given that JavaScript does not support cell arrays in the Matlab fashion, multidimensional arrays are defined instead to sidestep this issue. As an example, for a given parameter $i = 4$, the modal functions $\tilde{G}_4^m(\cdot)$ taking values in the parameter's mesh are written in a 2D array:

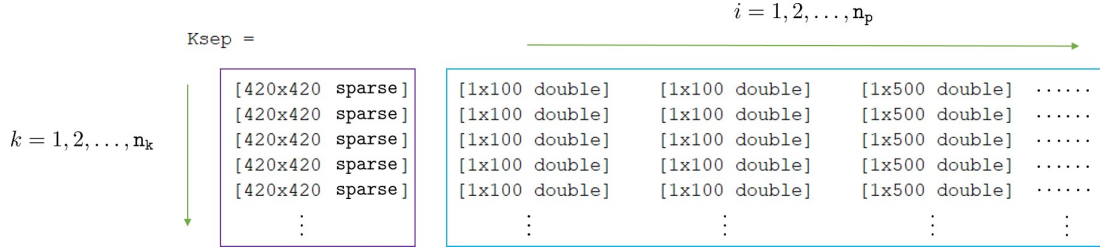
$$\mathbf{G4}[\mathbf{m}][\mathbf{j}] = \left[\left[\mathbf{G4}^{\wedge 1}_{_1}, \mathbf{G4}^{\wedge 1}_{_2}, \dots, \mathbf{G4}^{\wedge 1}_{_n_{d,4}} \right], \right. \\ \left. \left[\mathbf{G4}^{\wedge n}_{_1}, \mathbf{G4}^{\wedge n}_{_2}, \dots, \mathbf{G4}^{\wedge n}_{_n_{d,4}} \right] \right]$$

being $\mathbf{j}=1, 2, \dots, n_{d,4}$ a pointer to the discrete values of function $\tilde{G}_4^m(\cdot)$, and $\mathbf{m}=1, 2, \dots, n$ the index for the PGD modes. A 2D array that follows this format must be written for each parameter involved in the PGD solution.

In addition, the parametric unit-cell stiffness matrix is provided to the web application, since it is required for the material effective properties computations. The separated form of this matrix has been already used in the PGD solver, recalling equation (3.4):

$$\mathbf{K}(\boldsymbol{\mu}) = \sum_{k=1}^{n_k} \mathbf{K}^k \prod_{i=1}^{n_p} B_i^k.$$

In a Matlab cell array, for example, this data structure could be stored as:



In the multidimensional array format for JavaScript, the separated matrices \mathbf{K}^k are input as:

$$\begin{aligned}
 \mathbf{K}[k][1][j] = & \left[\left[\left[\mathbf{K}^{1_11} \quad \mathbf{K}^{1_12} \quad \dots \quad \mathbf{K}^{1_1 n_{\text{dof}}} \right], \right. \right. \\
 & \left. \left. \begin{array}{c} \vdots \\ \mathbf{K}^{1_{n_{\text{dof}}1}} \quad \mathbf{K}^{1_{n_{\text{dof}}2}} \quad \dots \quad \mathbf{K}^{1_{n_{\text{dof}} n_{\text{dof}}} \end{array} \right] \right] \\
 & \left. \left[\mathbf{K}^{n_k_11} \quad \mathbf{K}^{n_k_12} \quad \dots \quad \mathbf{K}^{n_k_1 n_{\text{dof}}} \right], \right. \\
 & \left. \left[\mathbf{K}^{n_k_{n_{\text{dof}}1}} \quad \mathbf{K}^{n_k_{n_{\text{dof}}2}} \quad \dots \quad \mathbf{K}^{n_k_{n_{\text{dof}} n_{\text{dof}}} \right] \right] \right]
 \end{aligned}$$

being $1, m=1, 2, \dots, n_{\text{dof}}$ the subindices for the matrix \mathbf{K}^k elements, and $k=1, 2, \dots, n_k$ the pointer to the stiffness matrix separated terms. Thus, a 3D array of size $n_k \times n_{\text{dof}} \times n_{\text{dof}}$ is composed.

The mesh file

As it is frequently done in finite element codes, here are provided the coordinates and connectivities of the lattice structure. In addition, the notion of mesh must also be extended to the parameters, meaning that their interval limits and the number of equally distributed points therein must be here supplied as well. The idea of having a mesh file releases all this data from the `caseName` main file, remaining simpler and easier to modify. However, it is recommended to code both files side by side, given that all variables required by the `caseName` main file are constructed in the mesh file. In addition, there are variables that are used not only by the functions defined for a PGD solution in the `caseName` file but also by some of the application core. Therefore, special care must be taken by setting a naming convention that allows compatibility across all of them, typically:

- `NUM_NODES`: number of nodes in the parametric lattice structure.
- `NUM_ELEMS`: number of elements in the parametric lattice structure.
- `DIM3`: boolean variable to set if the PGD solution is 2D or 3D ($n_{\text{dim}} = 2, 3$).

- **CONNECT**: connectivity matrix, defined as a 2D array in the JavaScript format.
- **COORS**: parametric coordinates matrix, which is constructed using the PGD separated style, therefore becoming a 3D array of size $\mathbf{n}_x \times \text{NUM_NODES} \times \mathbf{n}_{\text{dim}}$, being \mathbf{n}_x the amount of terms in which the parametric coordinates matrix is separated.

6.2 A PGD interactive post-processing example

PGD provides a *vademecum* of solutions whose spatial modes do not represent any physical solution of the parametric problem but instead, the physical solution of the problem can be reconstructed for any set of values of the parameters with minimal computational resources. This however could result in a tedious task using conventional packages for sophisticated scientific charts like Matlab[®]. Instead, capabilities for real-time solutions can be provided by the current web application, where the modifications of the parameters and animations are provided at the same time on the screen, as shown below:

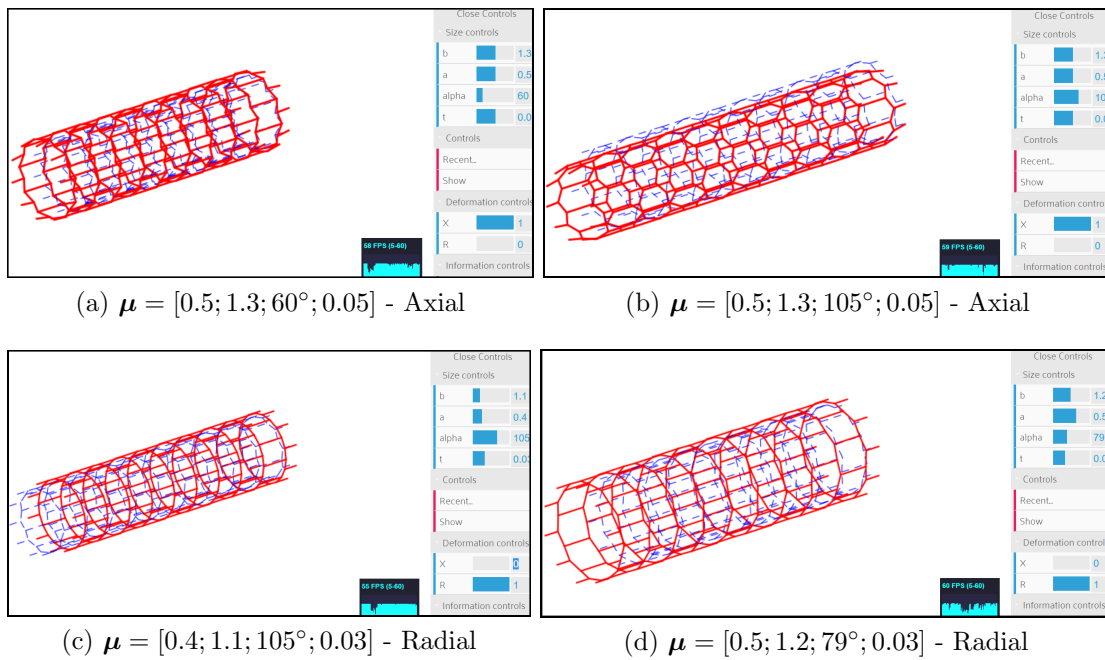


Figure 6.4: Interactive PGD solution of a parametric stent-like structure subjected to axial and radial load cases. The set of values of the parameters is indicated using the notation: $\boldsymbol{\mu} = [\mu_1; \mu_2; \mu_3; \mu_4] = [a; b; \alpha; t]$

Chapter 7

Conclusions

7.1 Contributions of the present thesis

This work presents lattice material structures whose mechanical properties can be tailored in term of their parameters values. We address this problem by means of an algebraic PGD solver, that allows us to browse the parametric mechanical response in an efficient way. In particular, we find extreme negative values of the materials Poisson's ratios, a feature that attracts our attention regarding the outperforming of some *auxetic* properties compared to conventional materials.

The algebraic PGD solver is developed in Chapter 3. It is conceived in a way that in principle, the solution of any parametric linear system of equations can be approached. In this sense, the distinctive contribution here is that different parametric material structures can be treated with exactly the same solver. Moreover, its use is not limited to structural problems but in general, any discrete form of a parametrized linear PDE.

In order to exploit the versatility of the algebraic PGD solver approach as a *black box*, there remains an intrusive part to be devised by the user. We refer to this part as the affine decomposition of the solver input data. In practice, this means that the discrete form resulting from the PDE (i.e. stiffness matrix and forcing term) must express its parametric dependence in a separated fashion. We propose for our structural problems, a systematic methodology to supplement finite elements with the parametric dimension. In Chapter 2, these procedures are described for a 2D parametric honeycomb and in Chapter 5 for a 3D scaffold and a stent-like structure.

The 2D parametric honeycomb is solved in Chapter 4, accounting for more than 11 millions of different configurations. Using the PGD *vademecum*, an explicit parametric response of the effective mechanical properties can be recovered for the unit-cell problem with homogenization. The accuracy of the solver against finite elements is assessed for random values of the parameters, achieving a maximum error of 2.5% in the L_2 norm among all load cases, with an average number of 35 PGD modes.

The parametrization of a 3D scaffold that considers more than 568 millions of configurations is treated in Chapter 5, where a geometric constraint between parameters

imposes a non-separable function between them. Therefore, a separable approximation for this function is constructed by means of the Singular Value Decomposition (SVD). This step is incorporated in the systematic approach that builds the affine decomposition of input data for the algebraic PGD solver. The error committed in the SVD approximation is low, for example for 5 modes, a maximum relative error below $2e-5$ is retrieved in the whole 2D space of the related parameters. Despite this, we note that the algebraic PGD solver lacks of accuracy, in particular when the response is evaluated at some particular values of the parameters where extreme values of the Poisson's ratios occur at the material bulk. Some possibilities are suggested to overcome this issue in future works.

A stent-like structure is parametrized in Chapter 5, based on the 2D honeycomb wrapped into a cylindrical shape, thus the same number of diverse configurations are treated (above 11 millions). The mechanical parametric response under axial and pressure loads is determined using the algebraic PGD solver. This serves as a comparison against another analysis, developed for the same structure, considering fewer parameters but using geometrically nonlinear finite elements. In this case, we exploit PGD as an interpolation method of the finite element response, providing an explicit parametric solution with the loading magnitude as an extra parameter.

7.2 Concluding remarks

1. The spatial dimension of the problem (2D, 3D) is kept by the algebraic PGD solver, and the parametric dimensions are treated separately. At each fixed-point solver iteration, the system of equations for the spatial dimension (typically the size of the finite element mesh) and those for each of the parametric ones can be solved in parallel.
2. The algebraic PGD solver is applied to different parametric structural problems. In this sense it works as a non-intrusive solver, where its parametric input data takes the intrusive part. This requires to build the standard finite elements equations but taking care of their parametric dependence in a separated manner. We believe that this part can be done systematically, following a proposed framework with familiar procedures for finite element programmers. In addition, this could certainly ease the path for further research on algebraic PGD.
3. An analytical solution in the parameters is constructed for the 2D unit-cell three load cases, by means of symbolic computations. In this case, the algebraic PGD solver accuracy is analyzed in a global parametric norm. In all cases, we observe that every PGD mode contributes to reduce the global error, whose maximum value results below 0.2% (average number of modes: 35, associated to a $\zeta = 10^{-4}$ decay in amplitude).

4. The PGD *vademecum* of mechanical properties shows extreme values of the Poisson's ratios in orthotropic materials for particular values of the geometric parameters. The material in these cases actually works as a mechanical amplifier in the transverse directions to the applied strain. In addition, the parametric response shows that for an engineering application, these extreme values of the Poisson's ratios should be traded off with respect to the material stiffness at the bulk.
5. Geometrically nonlinear behavior in a stent-like structure under two load cases is recovered by a least-square PGD interpolation. The number of modes for a $\zeta = 10^{-3}$ decay in amplitude are considerably low, 13 for the internal pressure case and 57 for the axially loaded case, are built upon 4550 finite element configurations run for each load case. The PGD *vademecum* shows mechanical properties and buckling effects as an explicit function, not only of the geometrical parameters but also the loading magnitude.

7.3 Future works

1. It has been shown that each new computed mode in the algebraic PGD solver contributes to decrease the error in a global parametric sense. However, we recognize two questions where further research efforts could be addressed. First, an error estimation of the residual or some quantity of interest would provide a precise criterion to stop the greedy computation of modes. In addition, different routes to the residual minimization could improve the rate at which each mode reduces the solution error.
2. The PGD *vademecum* of effective material properties shows a notable lack of accuracy when evaluated at some of the extreme values of the Poisson's ratios in the scaffold. We identify this as a case where the parametric response gets locally a sudden change with respect to the global behavior. A local refinement in the parametric space or higher order approximating functions would surely overcome this concern.
3. Regarding a material design with tailored properties, this thesis presents a groundwork on top of which the PGD *vademecum* could be exploited for multi-objective and constrained optimizations. In this context, the solutions and its derivatives with respect to the parameters (sensitivities) are supplied as a trivial post-process, for the whole multidimensional space.
4. The low number of modes retrieved in the PGD interpolation of the geometrically nonlinear responses is promising to believe that a scheme where the algebraic PGD solver is used inside an iterative loop, could successfully build the approximation to nonlinear parametric systems of equations "on the fly", and at a reduced cost. The feasibility of this concept is subjected mainly to the

affine decomposition of the residual (which now depends on the parametric solution itself). In addition, the separable dependence on the parameters should also extend to the tangent stiffness matrix if a full Newton-Raphson method is sought.

5. In structural analysis, a standard procedure to assess buckling by means of a linear model implies the solution of an eigenvalue problem. For this, the structure stiffness matrix is augmented with a so-called *stress stiffness matrix*, which is a function of the initial configuration and the applied loads. The resulting eigenvalues define a magnification factor at which the applied loads reach a critical state (with their eigenvectors characterizing the shape of the buckled structure). Adopting this framework to our parametric setting, and efficiently solve the eigenvalue problem as a function of the geometric parameters, would result in a highly valuable tool for the design of lattice structures and materials.

Bibliography

- ADINA© R&D, I. (2018). Adina v9.4. <http://www.adina.com/n900.shtml>.
- Alfaro, I., González, D., Zlotnik, S., Díez, P., Cueto, E., and Chinesta, F. (2015). An error estimator for real-time simulators based on model order reduction. *Advanced Modeling and Simulation in Engineering Sciences*, 2(1):30.
- Almgren, R. F. (1985). An isotropic three-dimensional structure with Poisson's ratio = -1. *J. Elasticity*, 15(4):427–430.
- Alonzo, G. V. (2018). Reduced order models for 3d parametric lattice structures: computation and post-processing in portable devices. Master's thesis, Universitat Politècnica de Catalunya.
- Amendola, A., Smith, C., Goodall, R., Auricchio, F., Feo, L., Benzoni, G., and Fraternali, F. (2016). Experimental response of additively manufactured metallic pentamode materials confined between stiffening plates. *Composite Structures*, 142:254–262.
- Ammar, A., Chinesta, F., Díez, P., and Huerta, A. (2010). An error estimator for separated representations of highly multidimensional models. *Computer Methods in Applied Mechanics and Engineering*, 199(25):1872–1880.
- Andreassen, E., Lazarov, B. S., and Sigmund, O. (2014). Design of manufacturable 3d extremal elastic microstructure. *Mechanics of Materials*, 69(1):1–10.
- Anthoine, A. (1995). Derivation of the in-plane elastic characteristics of masonry through homogenization theory. *Int. J. Solids Structures*, 32(2):137–163.
- Arabnejad, S., Johnston, B., Tanzer, M., and Pasini, D. (2017). Fully porous 3d printed titanium femoral stem to reduce stress-shielding following total hip arthroplasty. *Journal of Orthopaedic Research*, 35(8):1774–1783.
- Arabnejad, S., Johnston, R. B., Pura, J. A., Singh, B., Tanzer, M., and Pasini, D. (2016). High-strength porous biomaterials for bone replacement: A strategy to assess the interplay between cell morphology, mechanical properties, bone ingrowth and manufacturing constraints. *Acta biomaterialia*, 30:345–356.

- Bauchau, O. A. and Craig, J. I. (2009). *Structural analysis: with applications to aerospace structures*, volume 163. Springer Science & Business Media.
- Benssousan, A., Lions, J. L., and Papanicolaou, G. (2011). *Asymptotic analysis for periodic structures*, volume 374. American Mathematical Soc.
- Black, N. and Moore, S. (2019). Gauss-seidel method. <http://mathworld.wolfram.com/Gauss-SeidelMethod.html>.
- Blum, A., Hopcroft, J., and Kannan, R. (2019). *Foundations of Data Science*.
- Bogner, B., Bordeu, F., Chinesta, F., Leygue, A., and Poitou, A. (2012). Advanced simulation of models defined in plate geometries: 3d solutions with 2d computational complexity. *Computer Methods in Applied Mechanics and Engineering*, 201:1–12.
- Brûlé, S., Javelaud, E., Enoch, S., and Guenneau, S. (2013). Seismic metamaterial: how to shake friends and influence waves? *arXiv preprint arXiv:1301.7642*.
- Bückmann, T., Thiel, M., Kadic, M., Schittny, R., and Wegener, M. (2014). An elasto-mechanical unfeelability cloak made of pentamode metamaterials. *Nature communications*, 5:4130.
- Chamoin, L., Pled, F., Allier, P.-E., and Ladevèze, P. (2017). A posteriori error estimation and adaptive strategy for pgd model reduction applied to parametrized linear parabolic problems. *Computer Methods in Applied Mechanics and Engineering*, 327:118–146.
- Chinesta, F., Ammar, A., and Cueto, E. (2010). Recent advances and new challenges in the use of the proper generalized decomposition for solving multidimensional models. *Archives of Computational methods in Engineering*, 17(4):327–350.
- Chinesta, F. and Ladevèze, P. (2014). Separated representations and pgd-based model reduction. *Fundamentals and Applications, International Centre for Mechanical Sciences, Courses and Lectures*, 554.
- Chinesta, F., Ladeveze, P., and Cueto, E. (2011). A short review on model order reduction based on proper generalized decomposition. *Archives of Computational Methods in Engineering*, 18(4):395.
- Chinesta, F., Leygue, A., Bordeu, F., Aguado, J. V., Cueto, E., González, D., Alfaro, I., Ammar, A., and Huerta, A. (2013). Pgd-based computational vademecum for efficient design, optimization and control. *Archives of Computational Methods in Engineering*, 20(1):31–59.
- Christensen, J., Kadic, M., Kraft, O., and Wegner, M. (2015). Vibrant times for mechanical metamaterials. *MRS Communications*, 5:453–462.

- Cook, R. D., Malkus, D. S., Plesha, M. E., and Witt, R. J. (2002). *Concepts and Applications of Finite Element Analysis*. John Wiley & Sons, Inc., USA, fourth edition.
- Courard, A., Néron, D., Ladevèze, P., and Ballere, L. (2016). Integration of pgd-virtual charts into an engineering design process. *Computational Mechanics*, 57(4):637–651.
- Cremonesi, M., Néron, D., Guidault, P.-A., and Ladevèze, P. (2013). A pgd-based homogenization technique for the resolution of nonlinear multiscale problems. *Computer Methods in Applied Mechanics and Engineering*, 267:275–292.
- Cueto, E., González, D., and Alfaro, I. (2016). *Proper generalized decompositions: an introduction to computer implementation with Matlab*. Springer.
- Deshpande, V., Ashby, M., and Fleck, N. (2001a). Foam topology: bending versus stretching dominated architectures. *Acta materialia*, 49(6):1035–1040.
- Deshpande, V. S., Fleck, N. A., and Ashby, M. F. (2001b). Effective properties of the octet-truss lattice material. *Journal of the Mechanics and Physics of Solids*, 49(8):1747–1769.
- Díez, P., Zlotnik, S., García-González, A., and Huerta, A. (2018). Algebraic pgd for tensor separation and compression: An algorithmic approach. *Comptes Rendus Mécanique*, 346(7):501–514.
- Díez, P., Zlotnik, S., and Huerta, A. (2017). Generalized parametric solutions in stokes flow. *Computer Methods in Applied Mechanics and Engineering*, 326:223–240.
- El Halabi, F., González, D., Chico, A., and Doblaré, M. (2013). Fe2 multiscale in linear elasticity based on parametrized microscale models using proper generalized decomposition. *Computer Methods in Applied Mechanics and Engineering*, 257:183–202.
- Elipe, J. C. Á. and Lantada, A. D. (2012). Comparative study of auxetic geometries by means of computer-aided design and engineering. *Smart Materials and Structures*, 21(10):105004.
- Evans, K. (1991). The design of doubly curved sandwich panels with honeycomb cores. *Composite Structures*, 17(2):95–111.
- Evans, K. E. and Alderson, A. (2000). Auxetic materials: functional materials and structures from lateral thinking! *Advanced materials*, 12(9):617–628.
- Evans, K. E., Nkansah, M., Hutchinson, I., and Rogers, S. (1991). Molecular network design. *Nature*, 353(6340):124.

- Farhat, M., Guenneau, S., and Enoch, S. (2009). Ultrabroadband elastic cloaking in thin plates. *Physical review letters*, 103(2):024301.
- Ferrer, A., Oliver, J., Cante, J. C., and Lloberas-Valls, O. (2016). Vademecum-based approach to multi-scale topological material design. *Advanced Modeling and Simulation in Engineering Sciences*, 3(1):23.
- Feyel, F. and Chaboche, J.-L. (2000). Fe2 multiscale approach for modelling the elastoviscoplastic behaviour of long fibre sic/ti composite materials. *Computer methods in applied mechanics and engineering*, 183(3-4):309–330.
- Ganapathysubramanian, B. and Zabaras, N. (2007). Modeling diffusion in random heterogeneous media: Data-driven models, stochastic collocation and the variational multiscale method. *Journal of Computational Physics*, 226(1):326–353.
- García-Blanco, R., Díez, P., Borzacchiello, D., and Chinesta, F. (2018). Algebraic and parametric solvers for the power flow problem: towards real-time and accuracy-guaranteed simulation of electric systems. *Archives of Computational Methods in Engineering*, 25(4):1003–1026.
- Gatt, R., Wood, M. V., Gatt, A., Zarb, F., Formosa, C., Azzopardi, K. M., Casha, A., Agius, T. P., Schembri-Wismayer, P., Attard, L., et al. (2015). Negative poisson’s ratios in tendons: an unexpected mechanical response. *Acta biomaterialia*, 24:201–208.
- Gibson, L. J. and Ashby, M. F. (1999). *Cellular solids: structure and properties*. Cambridge University Press, US, second edition.
- Gómez-Moriana, R. (2012). Gaudí’s hanging chain models: parametric design avant la lettre? <https://criticalista.com/2012/08/16/gaudis-hanging-chain-models-parametric-design-avant-la-lettre/>.
- Greaves, G. N., Greer, A. L., Lakes, R. S., and Rouxel, T. (2011). Poisson’s ratio and modern materials. *Nat. Mater.*, 10(11):823–837.
- Grima, J. N., Casha, A. R., and Rybicki, J. (2015). Natural architectural design.
- Guenneau, S. and Amra, C. (2013). Anisotropic conductivity rotates heat fluxes in transient regimes. *Optics Express*, 21(5):6578–6583.
- Guenneau, S., Amra, C., and Veynante, D. (2012). Transformation thermodynamics: cloaking and concentrating heat flux. *Optics Express*, 20(7):8207–8218.
- Guest, J. K. and Prévost, J. H. (2006). Optimizing multifunctional materials: design of microstructures for maximized stiffness and fluid permeability. *International Journal of Solids and Structures*, 43(22-23):7028–7047.

- Guest, S. (2000). Tensegrities and rotating rings of tetrahedra: a symmetry viewpoint of structural mechanics. *Philosophical Transactions of the Royal Society of London A: Mathematical, Physical and Engineering Sciences*, 358(1765):229–243.
- Gustavo Méndez, C., Podestá, J. M., Lloberas-Valls, O., Toro, S., Huespe, A. E., and Oliver, J. (2017). Computational material design for acoustic cloaking. *International Journal for Numerical Methods in Engineering*, 112(10):1353–1380.
- Hernández, J., Oliver, J., Huespe, A. E., Caicedo, M., and Cante, J. (2014). High-performance model reduction techniques in computational multiscale homogenization. *Computer Methods in Applied Mechanics and Engineering*, 276:149–189.
- Hexcel, C. (1999). Hexweb™ honeycomb attributes and properties.
- Hopkins, J. B., Lange, K. J., and Spadaccini, C. M. (2013). Designing Microstructural Architectures With Thermally Actuated Properties Using Freedom, Actuation and Constraint Topologies. *Journal of Mechanical Design. ASME*, 135(6):061004.
- Kadic, M., Bückmann, T., Schittny, R., and Wegener, M. (2013). Metamaterials beyond electromagnetism. *Reports on Progress in Physics*, 76(12):126501.
- Kadic, M., Bückmann, T., Stenger, N., Thiel, M., and Wegener, M. (2012). On the practicability of pentamode mechanical metamaterials. *Appl. Phys. Lett.*, 100(19):191901.
- Karnesis, N. and Burriesci, G. (2013). Uniaxial and buckling mechanical response of auxetic cellular tubes. *Smart Materials and Structures*, 22(8):084008.
- Khanoki, S. A. and Pasini, D. (2012). Multiscale design and multiobjective optimization of orthopedic hip implants with functionally graded cellular material. *Journal of biomechanical engineering*, 134(3):031004.
- Kolda, T. G. and Bader, B. W. (2009). Tensor decompositions and applications. *SIAM review*, 51(3):455–500.
- Ladevèze, P. and Chamoin, L. (2011). On the verification of model reduction methods based on the proper generalized decomposition. *Computer Methods in Applied Mechanics and Engineering*, 200(23-24):2032–2047.
- Lamari, H., Ammar, A., Cartraud, P., Legrain, G., Chinesta, F., and Jacquemin, F. (2010). Routes for efficient computational homogenization of nonlinear materials using the proper generalized decompositions. *Archives of Computational methods in Engineering*, 17(4):373–391.
- Lantada, A. D., Muslija, A., and García-Ruíz, J. P. (2015). Auxetic tissue engineering scaffolds with nanometric features and resonances in the megahertz range. *Smart Materials and Structures*, 24(5):055013.

- Leblond, C. and Allery, C. (2014). A priori space–time separated representation for the reduced order modeling of low reynolds number flows. *Computer Methods in Applied Mechanics and Engineering*, 274:264–288.
- Lempriere, B. (1968). Poisson’s ratio in orthotropic materials. *AIAA J*, 6(11):2226–2227.
- Leonhardt, U. (2006). Optical conformal mapping. *Science*, 312(5781):1777–1780.
- Li, S. and Wongsto, A. (2004). Unit cells for micromechanical analyses of particle-reinforced composites. *Mechanics of materials*, 36(7):543–572.
- Libscore (2019). Javascript library usage. <http://libscore.com/#libs>.
- Ltd, B. P. (2019). jQuery usage statistics. <https://trends.builtwith.com/javascript/jquery>.
- Michel, J. C., Moulinec, H., and Suquet, P. (1999). Effective properties of composite materials with periodic microstructure: a computational approach. *Comput. Methods Appl. Mech. Engrg.*, 172:109–143.
- Milton, G. W. (2002). *The Theory of Composites*. Cambridge University Press, UK.
- Milton, G. W., Briane, M., and Willis, J. R. (2006). On cloaking for elasticity and physical equations with a transformation invariant form. *New Journal of Physics*, 8(10):248.
- Milton, G. W. and Cherkaev, A. (1995). Which Elasticity Tensors are Realizable? *J. Eng. Mater-T. ASME*, 117:483–493.
- Mindlin, R. D. (1951). Influence of rotatory inertia and shear on flexural motions of isotropic, elastic plates. *J. appl. Mech.*, 18:31–38.
- Miriyev, A., Stack, K., and Lipson, H. (2017). Soft material for soft actuators. *Nature communications*, 8(1):596.
- Modesto, D., Zlotnik, S., and Huerta, A. (2015). Proper Generalized Decomposition for parameterized helmholtz problems in heterogeneous and unbounded domains: application to harbor agitation. *Comput. Methods Appl. Mech. Eng.*, 295:127–149.
- Mosby, M. and Matouš, K. (2015). Hierarchically parallel coupled finite strain multi-scale solver for modeling heterogeneous layers. *International Journal for Numerical Methods in Engineering*, 102(3-4):748–765.
- Nachman, A. I. (1988). Reconstructions from boundary measurements. *Annals of Mathematics*, 128(3):531–576.

- Narayana, S. and Sato, Y. (2012). Heat flux manipulation with engineered thermal materials. *Physical review letters*, 108(21):214303.
- Nguyen, V. D., Béchet, E., Geuzaine, C., and Noels, L. (2011). Imposing periodic boundary condition on arbitrary meshes by polynomial interpolation. *Computational Materials Science*, 00:1–28.
- Niroomandi, S., González, D., Alfaro, I., Bordeu, F., Leygue, A., Cueto, E., and Chinesta, F. (2013). Real-time simulation of biological soft tissues: a pgd approach. *International journal for numerical methods in biomedical engineering*, 29(5):586–600.
- Nouy, A. (2010). A priori model reduction through proper generalized decomposition for solving time-dependent partial differential equations. *Computer Methods in Applied Mechanics and Engineering*, 199(23-24):1603–1626.
- Osanov, M. and Guest, J. K. (2016). Topology optimization for architected materials design. *Annual Review of Materials Research*, 46:211–233.
- Pendry, J. B., Schurig, D., and Smith, D. R. (2006). Controlling electromagnetic fields. *science*, 312(5781):1780–1782.
- Poisson, S. D. (1811). *Traité de Mécanique.*, volume 2, page 476. Chez Mme veuve Courcier, Paris.
- Prud’Homme, C., Rovas, D. V., Veroy, K., Machiels, L., Maday, Y., Patera, A. T., and Turinici, G. (2002). Reliable real-time solution of parametrized partial differential equations: Reduced-basis output bound methods. *Journal of Fluids Engineering*, 124(1):70–80.
- Reis, P. M., Jaeger, H. M., and van Hecke, M. (2015). Designer Matter: A perspective. *Extreme Mechanics Letters*, 5:25–29.
- Reissner, E. (1945). The effect of transverse shear deformation on the bending of elastic plates. *J. appl. Mech.*, pages A69–A77.
- Rozza, G., Huynh, D. B. P., and Patera, A. T. (2007). Reduced basis approximation and a posteriori error estimation for affinely parametrized elliptic coercive partial differential equations. *Archives of Computational Methods in Engineering*, 15(3):1.
- Rozza, G., Huynh, D. P., and Manzoni, A. (2013). Reduced basis approximation and a posteriori error estimation for stokes flows in parametrized geometries: roles of the inf-sup stability constants. *Numerische Mathematik*, 125(1):115–152.
- Saa-Seoane, J., Nguyen, N.-C., Men, H., Freund, R., and Peraire, J. (2012). Binary optimization techniques for linear pde-governed material design. *Applied Physics A*, 109(4):1023–1030.

- Sánchez-Palencia, E. (1980). Non-homogeneous media and vibration theory. *Lecture Notes in Physics*, 127.
- Scarpa, F., Smith, C., Ruzzene, M., and Wadee, M. (2008). Mechanical properties of auxetic tubular truss-like structures. *physica status solidi (b)*, 245(3):584–590.
- Schaedler, T. A. and Carter, W. B. (2016). Architected cellular materials. *Annual Review of Materials Research*, 46:187–210.
- Schittny, R., Kadic, M., Guenneau, S., and Wegener, M. (2013). Experiments on transformation thermodynamics: molding the flow of heat. *Physical review letters*, 110(19):195901.
- Shelby, R. A., Smith, D. R., and Schultz, S. (2001). Experimental verification of a negative index of refraction. *Science*, 292(5514):77–79.
- Sievenpiper, D., Sickmiller, M., and Yablonovitch, E. (1996). 3d wire mesh photonic crystals. *Physical Review Letters*, 76(14):2480.
- Sigmund, O. (1994a). *Design of Material Structures using Topology Optimization*. PhD thesis, Technical University of Denmark.
- Sigmund, O. (1994b). Materials with prescribed constitutive parameters: An inverse homogenization problem. *I. J. Solids Struct.*, 31(17):2313–2329.
- Sigmund, O. (1995). Tailoring materials with prescribed elastic properties. *Mech. Mater.*, 20:351–368.
- Sigmund, O. and Torquato, S. (1997). Design of materials with extreme thermal expansion using a three-phase topology optimization method. *Journal of the Mechanics and Physics of Solids*, 45(6):1037–1067.
- Signorini, M., Zlotnik, S., and Diez, P. (2017). Proper generalized decomposition solution of the parameterized helmholtz problem: application to inverse geophysical problems. *International Journal for Numerical Methods in Engineering*, 109(8):1085–1102.
- Simo, J. and Vu-Quoc, L. (1988). On the dynamics in space of rods undergoing large motions -a geometrically exact approach. *Comput. Methods Appl. Mech. Engng*, 53:125–161,.
- Soman, P., Lee, J. W., Phadke, A., Varghese, S., and Chen, S. (2012). Spatial tuning of negative and positive poisson’s ratio in a multi-layer scaffold. *Acta biomaterialia*, 8(7):2587–2594.
- Soukoulis, C. M. and Wegener, M. (2011). Past achievements and future challenges in the development of three-dimensional photonic metamaterials. *Nature photonics*, 5(9):523.

- Stenger, N., Wilhelm, M., and Wegener, M. (2012). Experiments on elastic cloaking in thin plates. *Physical Review Letters*, 108(1):014301.
- Theerakittayakorn, K. and Nanakorn, P. (2013). Periodic boundary conditions for unit cells of periodic cellular solids in the determination of effective properties using beam elements. In *The 2013 World Congress on Advances in Structural Engineering and Mechanics (ASEM13)*, pages 3738–3748.
- Timmins, L. H., Wu, Q., Yeh, A. T., Moore Jr, J. E., and Greenwald, S. E. (2010). Structural inhomogeneity and fiber orientation in the inner arterial media. *American Journal of Physiology-Heart and Circulatory Physiology*, 298(5):H1537–H1545.
- Timoshenko, S. and Goodier, J. (1951). *Theory of Elasticity*. McGraw-Hill Book Company, Inc., New York, second edition.
- Vidal, P., Gallimard, L., and Polit, O. (2013). Proper generalized decomposition and layer-wise approach for the modeling of composite plate structures. *International Journal of Solids and Structures*, 50(14-15):2239–2250.
- Wang, Y., Luo, Z., Zhang, N., and Qin, Q. (2016). Topological shape optimization of multifunctional tissue engineering scaffolds with level set method. *Structural and Multidisciplinary Optimization*, 54(2):333–347.
- Xia, L. and Breitkopf, P. (2014). A reduced multiscale model for nonlinear structural topology optimization. *Computer Methods in Applied Mechanics and Engineering*, 280:117–134.
- Xia, L., Raghavan, B., Breitkopf, P., and Zhang, W. (2013). Numerical material representation using proper orthogonal decomposition and diffuse approximation. *Applied Mathematics and Computation*, 224:450–462.
- Yang, L., Harrysson, O., West, H., and Cormier, D. (2015). Mechanical properties of 3d re-entrant honeycomb auxetic structures realized via additive manufacturing. *International Journal of Solids and Structures*, 69:475–490.
- Yvonnet, J. and He, Q.-C. (2007). The reduced model multiscale method (r3m) for the non-linear homogenization of hyperelastic media at finite strains. *Journal of Computational Physics*, 223(1):341–368.
- Zlotnik, S., Díez, P., González, D., Cueto, E., and Huerta, A. (2015). Effect of the separated approximation of input data in the accuracy of the resulting PGD solution. *Adv. Model. Simul. Eng. Sci.*, 2(28).
- Zou, X. (2017). *Simulation Tools for Biomechanical Applications with PGD-Based Reduced Order Models*. PhD thesis, Universitat Politècnica de Catalunya.

Zou, X., Conti, M., Díez, P., and Auricchio, F. (2018). A nonintrusive proper generalized decomposition scheme with application in biomechanics. *International Journal for Numerical Methods in Engineering*, 113(2):230–251.

Appendix A

Algebraic PGD solver: Algorithm

Data: $\mathbf{K}^k, B_i^k, \mathbf{f}^\ell, S_i^\ell$ and $\mathbf{U}_{\text{PGD}}^{n-1}(\boldsymbol{\mu})$: \mathbf{u}^m, G_i^m , for $m = 1, 2, \dots, n-1$,
 $k = 1, 2, \dots, n_k, \ell = 1, 2, \dots, n_f$
Result: \mathbf{u} and G_i , for $i = 1, 2, \dots, n_p$
Initialize: tolerance η_{tol} ; variables ε, ζ ; initial guess \mathbf{u} and G_i .

while $\varepsilon > \zeta$ **do**

 Compute $\tilde{\mathbf{u}} = \frac{\mathbf{u}}{\|\mathbf{u}\|}$, $\tilde{G}_i = \frac{G_i}{\|G_i\|}$ and $\beta = \|\mathbf{u}\| \prod_{i=1}^{n_p} \|G_i\|$.

for $k = 1 \dots n_k$ **do**

 Compute $c^k := \prod_{i=1}^{n_p} \int_{I_i} B_i^k (G_i)^2 d\mu_i$.

for $i = 1 \dots n_p$ **do**

 Compute $d_i^k(\cdot) := \left(\prod_{\substack{j=1 \\ j \neq i}}^{n_p} \int_{I_j} B_j^k (G_j)^2 d\mu_j \right) B_i^k(\cdot)$.

end

for $m = 1 \dots (n-1)$ **do**

 Compute $c^{k,m} := \prod_{i=1}^{n_p} \int_{I_i} B_i^k G_i^m G_i d\mu_i$.

for $i = 1 \dots n_p$ **do**

 Compute $d_i^{k,m}(\cdot) := \left(\prod_{\substack{j=1 \\ j \neq i}}^{n_p} \int_{I_j} B_j^k G_j^m G_j d\mu_j \right) B_i^k(\cdot) G_i^m(\cdot)$.

end

end

end

for $\ell = 1 \dots n_f$ **do**

 Compute $\hat{c}^\ell := \prod_{i=1}^{n_p} \int_{I_i} S_i^\ell G_i d\mu_i$.

for $i = 1 \dots n_p$ **do**

 Compute $\hat{d}_i^\ell(\cdot) := \left(\prod_{\substack{j=1 \\ j \neq i}}^{n_p} \int_{I_j} S_j^\ell G_j d\mu_j \right) S_i^\ell(\cdot)$.

end

end

 Solve \mathbf{u}^{new} ; $[\sum_{k=1}^{n_k} \mathbf{K}^k c^k] \mathbf{u}^{\text{new}} = \sum_{\ell=1}^{n_f} \mathbf{f}^\ell \hat{c}^\ell - \sum_{m=1}^{n-1} [\sum_{k=1}^{n_k} \mathbf{K}^k c^{k,m}] \mathbf{u}^m$.

for $i = 1 \dots n_p$ **do**

 Update $G_i^{\text{new}}(\cdot) = \frac{\sum_{\ell=1}^{n_f} (\mathbf{u}^\top \mathbf{f}^\ell) \hat{d}_i^\ell(\cdot) - \sum_{m=1}^{n-1} \sum_{k=1}^{n_k} (\mathbf{u}^\top \mathbf{K}^k \mathbf{u}^m) d_i^{k,m}(\cdot)}{\sum_{k=1}^{n_k} (\mathbf{u}^\top \mathbf{K}^k \mathbf{u}) d_i^k(\cdot)}$.

end

 Compute $\tilde{\mathbf{u}}^{\text{new}} = \frac{\mathbf{u}^{\text{new}}}{\|\mathbf{u}^{\text{new}}\|}$, $\tilde{G}_i^{\text{new}} = \frac{G_i^{\text{new}}}{\|G_i^{\text{new}}\|}$ and $\beta^{\text{new}} = \|\mathbf{u}^{\text{new}}\| \prod_{i=1}^{n_p} \|G_i^{\text{new}}\|$.

 Compute $\varepsilon^2 = (\beta^{\text{new}})^2 + \beta^2 - 2\beta^{\text{new}}\beta (\tilde{\mathbf{u}}^\top \mathbf{M}_u \tilde{\mathbf{u}}^{\text{new}}) \prod_{i=1}^{n_p} \int_{I_i} \tilde{G}_i^{\text{new}} \tilde{G}_i d\mu_i$.

 Update values $\mathbf{u} \leftarrow \mathbf{u}^{\text{new}}$; $G_i \leftarrow G_i^{\text{new}}$; $\beta \leftarrow \beta^{\text{new}}$ and $\zeta = \eta_{\text{tol}} \beta^{\text{new}}$

end

Algorithm 4: Algebraic PGD alternated directions nonlinear solver.

Appendix B

PGD compression: Algorithm

Data: $\mathbf{U}_{\text{PGD}}^n(\boldsymbol{\mu})$: \mathbf{u}^m, G_i^m , for $m = 1, 2, \dots, n$
 $\mathbf{U}_{\text{com}}^{\hat{n}-1}$: $\hat{\mathbf{u}}^{\hat{m}}, \hat{G}_i^{\hat{m}}$, for $\hat{m} = 1, 2, \dots, (\hat{n} - 1)$
Result: $\hat{\mathbf{u}}, \hat{G}_i$, for $i = 1, 2, \dots, n_p$
Initialize: tolerance η_{tol} ; variables ε, ζ ; initial guess $\hat{\mathbf{u}}$ and \hat{G}_i .

while $\varepsilon > \zeta$ **do**

Compute $\tilde{\mathbf{u}} = \frac{\hat{\mathbf{u}}}{\|\hat{\mathbf{u}}\|}$, $\tilde{G}_i = \frac{\hat{G}_i}{\|\hat{G}_i\|}$ and $\psi = \|\hat{\mathbf{u}}\| \prod_{i=1}^{n_p} \|\hat{G}_i\|$.

Compute $\lambda = \prod_{i=1}^{n_p} (\hat{G}_i, \hat{G}_i)$

for $i = 1 \dots n_p$ **do**

Compute $\eta_i = (\hat{\mathbf{u}}^\top \mathbf{M}_u \hat{\mathbf{u}}) \prod_{\substack{j=1; \\ j \neq i}}^{n_p} (\hat{G}_j, \hat{G}_j)$

end

for $m = 1 \dots (n - 1)$ **do**

Compute $\gamma^m = \prod_{i=1}^{n_p} (\hat{G}_i, G_i^m)$

for $i = 1 \dots n_p$ **do**

Compute $\xi_i^m = (\hat{\mathbf{u}}^\top \mathbf{M}_u \mathbf{u}^m) \prod_{\substack{j=1; \\ j \neq i}}^{n_p} (\hat{G}_j, G_j^m)$

end

end

for $\hat{m} = 1 \dots (\hat{n} - 1)$ **do**

Compute $\phi^{\hat{m}} = \prod_{i=1}^{n_p} \int_{I_i} \hat{G}_i \hat{G}_i^{\hat{m}} d\mu_j$.

for $i = 1 \dots n_p$ **do**

Compute $\kappa_i^{\hat{m}} = (\hat{\mathbf{u}}^\top \mathbf{M}_u \hat{\mathbf{u}}^{\hat{m}}) \prod_{\substack{j=1; \\ j \neq i}}^{n_p} \int_{I_j} \hat{G}_j \hat{G}_j^{\hat{m}} d\mu_j$.

end

end

Update $\hat{\mathbf{u}}^{\text{new}} = \sum_{m=1}^n \hat{\mathbf{u}}^m \left(\frac{\gamma^m}{\lambda}\right) - \sum_{\hat{m}=1}^{\hat{n}-1} \hat{\mathbf{u}}^{\hat{m}} \left(\frac{\phi^{\hat{m}}}{\lambda}\right)$.

for $i = 1 \dots n_p$ **do**

Update $\hat{G}_i^{\text{new}}(\cdot) = \sum_{m=1}^n \left(\frac{\xi_i^m}{\eta_i}\right) G_i^m(\cdot) - \sum_{\hat{m}=1}^{\hat{n}-1} \left(\frac{\kappa_i^{\hat{m}}}{\eta_i}\right) \hat{G}_i^{\hat{m}}(\cdot)$.

end

Compute $\hat{\mathbf{u}}^{\text{new}} = \frac{\hat{\mathbf{u}}^{\text{new}}}{\|\hat{\mathbf{u}}^{\text{new}}\|}$, $\tilde{G}_i^{\text{new}} = \frac{\hat{G}_i^{\text{new}}}{\|\hat{G}_i^{\text{new}}\|}$ and $\psi^{\text{new}} = \|\hat{\mathbf{u}}^{\text{new}}\| \prod_{i=1}^{n_p} \|\hat{G}_i^{\text{new}}\|$.

Compute

$$\varepsilon^2 = (\psi^{\text{new}})^2 + \psi^2 - 2\psi^{\text{new}}\psi \left((\tilde{\mathbf{u}}^{\text{new}})^\top \mathbf{M}_u \tilde{\mathbf{u}} \right) \left(\prod_{i=1}^{n_p} \int_{I_i} \tilde{G}_i^{\text{new}} \tilde{G}_i d\mu_j \right).$$

Update values $\hat{\mathbf{u}} \leftarrow \hat{\mathbf{u}}^{\text{new}}$; $\hat{G}_i \leftarrow \hat{G}_i^{\text{new}}$; $\psi \leftarrow \psi^{\text{new}}$ and $\zeta = \eta_{\text{tol}}\psi^{\text{new}}$

end

Algorithm 5: Least-Squares PGD alternated directions nonlinear solver.

Appendix C

Parametric honeycomb unit-cell analytical solution

It is here explained that the systems of equations of the unit-cell in 2D using homogenization can be reduced by prescribing the periodic boundary conditions using the Direct Method (Cook et al., 2002, Chapter 13). This transformation of the global stiffness matrix and forcing terms into a reduced system allows the possibility of solving the three load cases of homogenization in the 2D problem symbolically in the parameters. Then, the generalized displacements of the unit-cell as function of the parameters are obtained, which can be further post-processed to obtain the effective elastic properties as a function of the parameters. This analytical solutions are evaluated for different values of the parameters and compared against the PGD *vademecum* to provide an insight of the PGD solver convergence (measured in the multidimensional parameters space).

Given the unit-cell global stiffness matrix built by Bernoulli beam elements, $\mathbf{K}(\boldsymbol{\mu})$, the equations

$$\begin{aligned}\mathbf{K}(\boldsymbol{\mu}) \mathbf{U}(\boldsymbol{\mu}) &= \mathbf{0}, \\ \mathbf{C} \mathbf{U}(\boldsymbol{\mu}) &= \mathbf{Q}(\boldsymbol{\mu}),\end{aligned}$$

contain equilibrium and periodicity conditions, given a specific load case in the unit-cell. If the constraints are applied using a direct method (Cook et al., 2002, Chapter 13), then the system unknowns can be split into released and constrained:

$$[\mathbf{C}_R \quad \mathbf{C}_C] \begin{Bmatrix} \mathbf{U}_R(\boldsymbol{\mu}) \\ \mathbf{U}_C(\boldsymbol{\mu}) \end{Bmatrix} - \{\mathbf{Q}(\boldsymbol{\mu})\} = \{\mathbf{0}\}.$$

In addition, the constrained unknowns can be solved in terms of the released:

$$\begin{Bmatrix} \mathbf{U}_R(\boldsymbol{\mu}) \\ \mathbf{U}_C(\boldsymbol{\mu}) \end{Bmatrix} = \underbrace{\begin{bmatrix} \mathbf{I} \\ -\mathbf{C}_C^{-1}\mathbf{C}_R \end{bmatrix}}_{\boldsymbol{\varphi}} \{\mathbf{U}_R(\boldsymbol{\mu})\} + \underbrace{\begin{Bmatrix} \mathbf{0} \\ \mathbf{C}_C^{-1}\mathbf{Q}(\boldsymbol{\mu}) \end{Bmatrix}}_{\mathbf{Q}_0(\boldsymbol{\mu})}.$$

Then, a reduced system can be expressed in terms of the released unknowns only:

$$\mathbf{K}_R(\boldsymbol{\mu}) \mathbf{U}_R(\boldsymbol{\mu}) = \mathbf{F}_R(\boldsymbol{\mu}),$$

where

$$\begin{aligned} \mathbf{K}_R(\boldsymbol{\mu}) &= \boldsymbol{\varphi}^T \mathbf{K}(\boldsymbol{\mu}) \boldsymbol{\varphi} \quad \text{and} \\ \mathbf{F}_R(\boldsymbol{\mu}) &= -\boldsymbol{\varphi}^T \mathbf{K}(\boldsymbol{\mu}) \mathbf{Q}_0(\boldsymbol{\mu}). \end{aligned}$$

While $\forall \boldsymbol{\mu} \in \mathcal{D} = I_1 \times I_2 \times \dots \times I_{n_p}$, $\mathbf{K}(\boldsymbol{\mu}) \in \mathbb{R}^{(n_{\text{dof}} \times n_{\text{dof}})}$, $\mathbf{K}_R(\boldsymbol{\mu}) \in \mathbb{R}^{(n_R \times n_R)}$. In the unit-cell problem, $n_{\text{dof}} = 24$ is reduced to $n_R = 13$. Now the system can be solved symbolically as functions of the parameters $\boldsymbol{\mu} = [a \ b \ \alpha \ t]^T$.

With this, the parametric solution of released unknowns for case *XX* results:

$$\mathbf{U}_R^{\text{xx}}(\boldsymbol{\mu}) = \begin{Bmatrix} u_2 \\ v_2 \\ \theta_2 \\ u_3 \\ v_3 \\ \theta_3 \\ u_4 \\ v_4 \\ \theta_4 \\ u_5 \\ v_5 \\ \theta_5 \\ \theta_6 \end{Bmatrix} = \begin{Bmatrix} \frac{b(a \cos(\alpha) - b) ((a^2 - 4t^2) \sin^2(\alpha) - a^2)}{a^2(a + 2b) - 2b(a^2 - 4t^2) \sin^2(\alpha)} \\ 0 \\ 0 \\ -\frac{(a \cos(\alpha) - b) (a^2(a + b) - b(a^2 - 4t^2) \sin^2(\alpha))}{a^2(a + 2b) - 2b(a^2 - 4t^2) \sin^2(\alpha)} \\ 0 \\ 0 \\ -\frac{(a \cos(\alpha) - b) (a^2(a + 3b) - 3b(a^2 - 4t^2) \sin^2(\alpha))}{a^2(a + 2b) - 2b(a^2 - 4t^2) \sin^2(\alpha)} \\ 0 \\ 0 \\ -\frac{(a \cos(\alpha) - b) (a^2(2a + 3b) - 3b(a^2 - 4t^2) \sin^2(\alpha))}{a^2(a + 2b) - 2b(a^2 - 4t^2) \sin^2(\alpha)} \\ 0 \\ 0 \\ 0 \end{Bmatrix}.$$

Figure C.1 shows a scaled solution $\mathbf{U}_R^{\text{xx}}(a = 0.5, b = 1, \alpha = 60^\circ, t = \frac{1}{40})$.

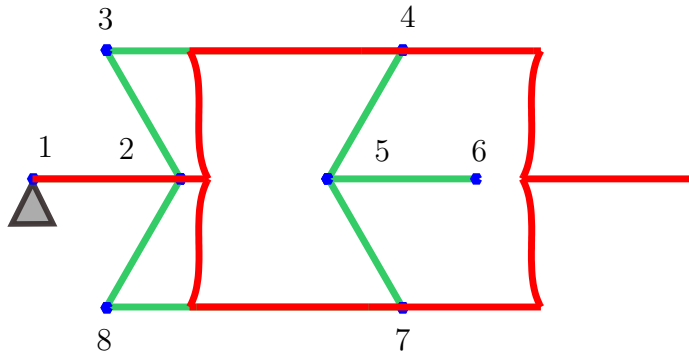


Figure C.1: Scaled $\mathbf{U}_R^{\text{xx}}(\boldsymbol{\mu})$ evaluated at $(a = 0.5, b = 1, \alpha = 60^\circ, t = \frac{1}{40})$.

The parametric solution of released unknowns for load case YY becomes:

$$\mathbf{U}_R^{yy}(\boldsymbol{\mu}) = \begin{Bmatrix} u_2 \\ v_2 \\ \theta_2 \\ \theta_3 \\ u_4 \\ v_4 \\ \theta_4 \\ u_5 \\ v_5 \\ \theta_5 \\ u_6 \\ v_6 \\ \theta_6 \end{Bmatrix} = \begin{Bmatrix} -\frac{2ab(a^2 - 4t^2)\cos(\alpha)\sin^2(\alpha)}{a^3 + a^2b + 4bt^2 + b(a^2 - 4t^2)\cos(2\alpha)} \\ a\sin(\alpha) \\ 0 \\ 0 \\ -\frac{2ab(a^2 - 4t^2)\cos(\alpha)\sin^2(\alpha)}{a^3 + a^2b + 4bt^2 + b(a^2 - 4t^2)\cos(2\alpha)} \\ 2a\sin(\alpha) \\ 0 \\ 0 \\ a\sin(\alpha) \\ 0 \\ -\frac{ab(a^2 - 4t^2)\cos(\alpha)\sin^2(\alpha)}{a^3 + a^2b + 4bt^2 + b(a^2 - 4t^2)\cos(2\alpha)} \\ a\sin(\alpha) \\ 0 \end{Bmatrix}.$$

Figure C.2 shows a scaled solution $\mathbf{U}_R^{yy}(\boldsymbol{\mu})$ evaluated at $\boldsymbol{\mu}=[a = 0.5, b = 1, \alpha = 60^\circ, t = \frac{1}{40}]$.

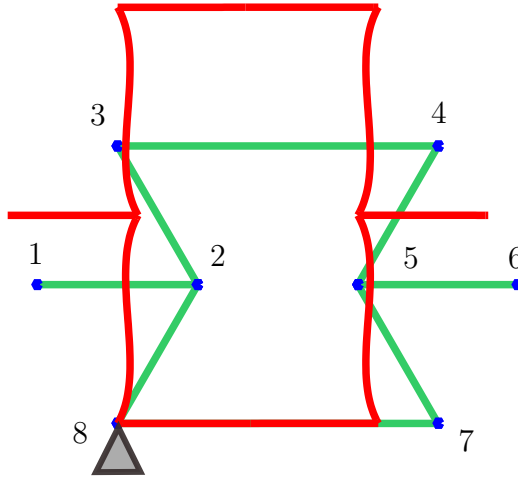


Figure C.2: Scaled $\mathbf{U}_R^{yy}(\boldsymbol{\mu})$ evaluated at $\boldsymbol{\mu}=[a = 0.5, b = 1, \alpha = 60^\circ, t = \frac{1}{40}]$.

Finally, solving for case XY , the released unknowns result:

$$\mathbf{U}_R^{xy}(\boldsymbol{\mu}) = \begin{pmatrix} u_2 \\ v_2 \\ \theta_2 \\ u_3 \\ v_3 \\ \theta_3 \\ u_4 \\ v_4 \\ \theta_4 \\ u_5 \\ v_5 \\ \theta_5 \\ \theta_6 \end{pmatrix} = \begin{pmatrix} 0 \\ \frac{b(a \cos(\alpha) - b) (8t^2 \cos(\alpha)a + b (-a^2 - 2ab - 4t^2 + (a^2 + 2ab - 4t^2) \cos(2\alpha)))}{2(8t^2a^2 + a^2b^2 - 16t^2 \cos(\alpha)ab + 5ab^3 + 4t^2b^2 - b^2(a^2 + 5ab - 4t^2) \cos(2\alpha))} \\ \frac{(a \cos(\alpha) - b) (8t^2 \cos(\alpha)a + b (-a^2 - 4t^2 + (a^2 - 4t^2) \cos(2\alpha)))}{8t^2a^2 + a^2b^2 - 16t^2 \cos(\alpha)ab + 5ab^3 + 4t^2b^2 - b^2(a^2 + 5ab - 4t^2) \cos(2\alpha)} \\ 0 \\ \frac{(a \cos(\alpha) - b) (16t^2a^2 + a^2b^2 - 24t^2 \cos(\alpha)ab + 2ab^3 + 4t^2b^2 - b^2(a^2 + 2ab - 4t^2) \cos(2\alpha))}{2(8t^2a^2 + a^2b^2 - 16t^2 \cos(\alpha)ab + 5ab^3 + 4t^2b^2 - b^2(a^2 + 5ab - 4t^2) \cos(2\alpha))} \\ \frac{(a \cos(\alpha) - b) (8t^2 \cos(\alpha)a + b (-a^2 - 4t^2 + (a^2 - 4t^2) \cos(2\alpha)))}{8t^2a^2 + a^2b^2 - 16t^2 \cos(\alpha)ab + 5ab^3 + 4t^2b^2 - b^2(a^2 + 5ab - 4t^2) \cos(2\alpha)} \\ 0 \\ \frac{(a \cos(\alpha) - b) (16t^2a^2 + 3a^2b^2 - 40t^2 \cos(\alpha)ab + 18ab^3 + 12t^2b^2 - 3b^2(a^2 + 6ab - 4t^2) \cos(2\alpha))}{2(8t^2a^2 + a^2b^2 - 16t^2 \cos(\alpha)ab + 5ab^3 + 4t^2b^2 - b^2(a^2 + 5ab - 4t^2) \cos(2\alpha))} \\ \frac{(a \cos(\alpha) - b) (8t^2 \cos(\alpha)a + b (-a^2 - 4t^2 + (a^2 - 4t^2) \cos(2\alpha)))}{8t^2a^2 + a^2b^2 - 16t^2 \cos(\alpha)ab + 5ab^3 + 4t^2b^2 - b^2(a^2 + 5ab - 4t^2) \cos(2\alpha)} \\ 0 \\ \frac{(a \cos(\alpha) - b) (32t^2a^2 + 3a^2b^2 - 56t^2 \cos(\alpha)ab + 18ab^3 + 12t^2b^2 - 3b^2(a^2 + 6ab - 4t^2) \cos(2\alpha))}{2(8t^2a^2 + a^2b^2 - 16t^2 \cos(\alpha)ab + 5ab^3 + 4t^2b^2 - b^2(a^2 + 5ab - 4t^2) \cos(2\alpha))} \\ \frac{2(a \cos(\alpha) - b) (-4a \cos(\alpha)t^2 + b(4t^2 + (a^2 - 4t^2) \sin^2(\alpha)))}{8t^2a^2 + a^2b^2 - 16t^2 \cos(\alpha)ab + 5ab^3 + 4t^2b^2 - b^2(a^2 + 5ab - 4t^2) \cos(2\alpha)} \\ \frac{(a \cos(\alpha) - b) (8t^2 \cos(\alpha)a + b (-a^2 - 3ab - 4t^2 + (a^2 + 3ab - 4t^2) \cos(2\alpha)))}{8t^2a^2 + a^2b^2 - 16t^2 \cos(\alpha)ab + 5ab^3 + 4t^2b^2 - b^2(a^2 + 5ab - 4t^2) \cos(2\alpha)} \end{pmatrix}.$$

Figure C.3 shows a scaled analytical solution $\mathbf{U}_R^{xy}(\boldsymbol{\mu})$, evaluated at $\boldsymbol{\mu}=[a = 0.5, b = 1, \alpha = 60^\circ, t = \frac{1}{40}]$.

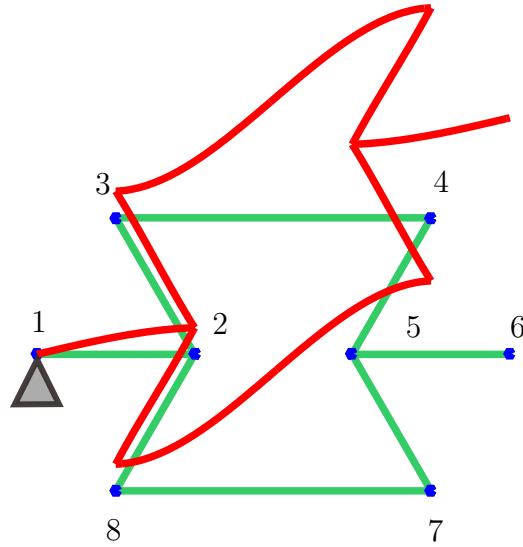


Figure C.3: Scaled $\mathbf{U}_R^{xy}(\boldsymbol{\mu})$ evaluated at $\boldsymbol{\mu}=[a = 0.5, b = 1, \alpha = 60^\circ, t = \frac{1}{40}]$.

At this point, it is worth mentioning that the parametric analytical solutions have the size of a 2D unit-cell, reduced by its periodic constraints. For a full structure done by repetitions of unit-cells, the cost of obtaining such expressions becomes computationally unfeasible.

Finally, the components of the effective elasticity matrix can be calculated from homogenization theory (1.1) and (1.2), and are shown in equations (C.1) to (C.6). It is noteworthy that, considering all elements in the unit-cell are made of the same constituent material, all these results are proportional to E , the Young's modulus. However, this is taken as unitary for the present analysis and is omitted in the following expressions for the sake of clarity:

$$C_{11}^{\text{eff}}(\boldsymbol{\mu}) = -\frac{t \csc(\alpha)(a \cos(\alpha) - b) ((a^2 - 4t^2) \cos(2\alpha) + a^2 + 4t^2)}{a (a^3 + b (a^2 - 4t^2) \cos(2\alpha) + a^2b + 4t^2b)} \quad (\text{C.1})$$

$$C_{22}^{\text{eff}}(\boldsymbol{\mu}) = -\frac{t \sin(\alpha) (a^3 - a (a^2 - 4t^2) \cos(2\alpha) + 4at^2 + 16t^2b)}{(a \cos(\alpha) - b) (a^3 + b (a^2 - 4t^2) \cos(2\alpha) + a^2b + 4t^2b)} \quad (\text{C.2})$$

$$C_{33}^{\text{eff}}(\boldsymbol{\mu}) = -\frac{16t^3 \sin(\alpha)(a \cos(\alpha) - b)}{-b^2 (a^2 + 5ab - 4t^2) \cos(2\alpha) + 8a^2t^2 + a^2b^2 - 16ab t^2 \cos(\alpha) + 5ab^3 + 4t^2b^2} \quad (\text{C.3})$$

$$C_{12}^{\text{eff}}(\boldsymbol{\mu}) = \frac{t (4t^2 - a^2) \sin(2\alpha)}{a^3 + b (a^2 - 4t^2) \cos(2\alpha) + a^2b + 4t^2b} \quad (\text{C.4})$$

$$C_{13}^{\text{eff}}(\boldsymbol{\mu}) = 0 \quad (\text{C.5})$$

$$C_{23}^{\text{eff}}(\boldsymbol{\mu}) = 0 \quad (\text{C.6})$$

Using (C.1), (C.2) and (C.4) the orthotropic Poisson's ratios can be calculated as follows, assuming a state of plane stress (Bauchau and Craig, 2009, Chapter 2):

$$\nu_{12}^{\text{eff}}(\boldsymbol{\mu}) = \frac{C_{12}^{\text{eff}}(\boldsymbol{\mu})}{C_{22}^{\text{eff}}(\boldsymbol{\mu})} = \frac{2 (a^2 - 4t^2) \cos(\alpha)(a \cos(\alpha) - b)}{a^3 - a (a^2 - 4t^2) \cos(2\alpha) + 4a t^2 + 16t^2b} \quad (\text{C.7})$$

$$\nu_{21}^{\text{eff}}(\boldsymbol{\mu}) = \frac{C_{12}^{\text{eff}}(\boldsymbol{\mu})}{C_{11}^{\text{eff}}(\boldsymbol{\mu})} = \frac{a (a^2 - 4t^2) \sin(\alpha) \sin(2\alpha)}{(a \cos(\alpha) - b) ((a^2 - 4t^2) \cos(2\alpha) + a^2 + 4t^2)} \quad (\text{C.8})$$

Appendix D

Singular Value Decomposition (SVD)

In this Appendix, we explain the use of the SVD applied to approximate a parametric function describing the geometry of the scaffold, which is not separable in their variables (the parameters α and ϕ). We recall the geometric constraint between parameters in the scaffold structure and provide a brief explanation about the implemented methodology. For further references and applications of the SVD, the reader is referred to (Blum et al., 2019, Chapter 3).

D.1 Geometrical parameters constraint in the scaffold structure

The geometric parametrization of the scaffold unit-cell (Figure D.1), implies a constraint in the orientation angle θ , such that

$$\begin{aligned} a \cos(\alpha) &= c \cos(\theta), \\ \cos(\theta) &= \frac{a}{c} \cos(\alpha), \\ \cos(\theta) &= \frac{\cos(\alpha)}{\phi}, \end{aligned}$$

ensuring that the hexagonal honeycomb cells, placed at orthogonal planes, do interconnect at the points colored in magenta (Figure D.1). This implies that θ itself is

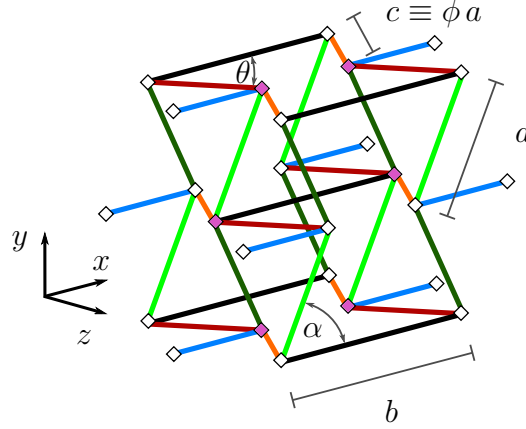


Figure D.1: Scaffold unit-cell parameterization ($\boldsymbol{\mu} = [a \ b \ \alpha \ \phi \ t]^\top$).

not an independent parameter but a function of α , and the ratio between element lengths defined as $\phi \equiv c/a$.

The parametrized orientation of the elements red and orange (Figure D.1) depend on trigonometric functions of θ :

$$\cos(\theta) = \frac{\cos(\alpha)}{\phi}, \quad (\text{D.1})$$

and using the trigonometric identity:

$$\sin(\theta) = \sqrt{1 - \frac{\cos^2(\alpha)}{\phi^2}}, \quad (\text{D.2})$$

where $\sin(\theta)$ takes always positive values in the unit-cell geometric parametrization. The parametric stiffness matrix of the scaffold is described in terms of functions (D.1) and (D.2). While in (D.1) there is a separable parametric dependence in α and ϕ , it must be constructed for (D.2) by means of the SVD.

D.2 Application

The SVD is a numerical method that produces the factorization of any real matrix $\mathbf{M} \in \mathbb{R}^{m \times n}$ into the product of three matrices:

$$\mathbf{M} = \mathbf{U} \boldsymbol{\Sigma} \mathbf{V}^\top,$$

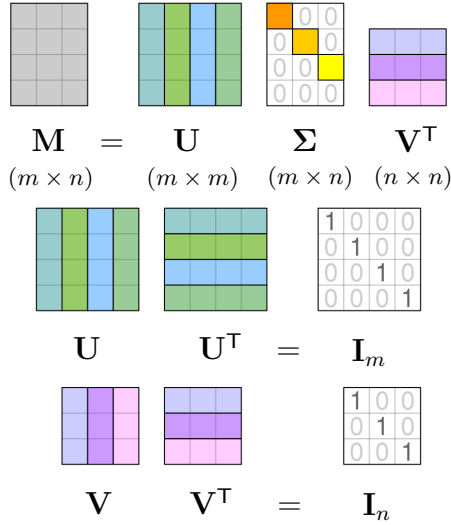


Figure D.2: SVD factorization of \mathbf{A} into the product of three matrices. Adapted from Wiki Commons.

whose characterization is shown in Figure D.2. The SVD is useful in many tasks (Blum et al. (2019, Chapter 3)), since for any “ k ” the SVD of \mathbf{M} gives the best rank- k approximation to \mathbf{M} , that is

$$\mathbf{M} \approx \mathbf{M}_k := \sum_{i=1}^k \sigma_{ii} \mathbf{u}_i \mathbf{v}_i^T, \quad (\text{D.3})$$

where \mathbf{u}_i and \mathbf{v}_i are the columns of \mathbf{U} and \mathbf{V} respectively, and σ_{ii} the diagonal elements of $\mathbf{\Sigma}$, placed in a descending order according to their magnitude, for $1 = 1, \dots, k$. When k reaches the rank of \mathbf{M} : $\min(m, n)$, equation (D.3) provides an exact decomposition of the matrix, a.k.a. the *singular value decomposition*.

We want to approximate the scalar function $\sin(\theta)$ (D.2) as a separable contribution of functions in their variables α and ϕ , as we have proposed in (5.21):

$$\sin(\theta) := f(\alpha, \phi) \approx \sum_{\ell=1}^{\text{nsvd}} \omega^\ell \Xi^\ell(\alpha) \Psi^\ell(\phi). \quad (\text{D.4})$$

Despite their different notations, the similarity between equations (D.3) and (D.4) is noticeable, and guides the following course of action:

1. Compute $f(\alpha, \phi)$ in $I_3 \times I_4$, at a discrete set of points values, and collect them in a matrix $\mathbf{M} \in \mathbb{R}^{\mathbf{n}_{d,3} \times \mathbf{n}_{d,4}}$, where $\mathbf{n}_{d,i}$ are the number of points chosen for the interval I_i (1D parametric meshes).

2. Use the SVD of \mathbf{M} , where each of the columns of \mathbf{U} : \mathbf{u}_i (D.3), corresponds to one of the functions $\Xi^\ell(\alpha)$ (D.4), evaluated at the $\mathbf{n}_{d,3}$ points of I_3 . Analogously, each of the columns of \mathbf{V} : \mathbf{v}_i , corresponds to one of the functions $\Psi^\ell(\phi)$, evaluated at $\mathbf{n}_{d,4}$ points of I_4 .
3. Asses the accuracy of the approximation \mathbf{M}_k against \mathbf{M} by choosing \mathbf{n}_{svd} (D.4), i.e. the number of SVD terms to consider. For our problem, \mathbf{n}_{svd} enlarges (almost quadratically) the number of \mathbf{n}_k separated terms of the parametric stiffness matrix, thus slowing down the algebraic PGD solver performance.

D.3 Results

The domain of $f(\alpha, \phi)$, where the SVD is applied, is given by $I_3 \times I_4 = [45^\circ, 135^\circ] \times [0.75, 2]$. The parameters mesh sizes are $\mathbf{n}_{d,3} = 91$ and $\mathbf{n}_{d,4} = 50$. Thus, the SVD of \mathbf{M} have 50 diagonal values of Σ , as shown in Figure D.3a. In addition, we present the parametric functions $\Xi^\ell(\alpha)$ (Figure D.3b) and $\Psi^\ell(\phi)$ (Figure D.3c), for $\ell = 1, \dots, \mathbf{n}_{\text{svd}} = 5$. In order to visualized the significance of a SVD term, the parametric functions are weighted by $\sqrt{\omega^\ell}$.

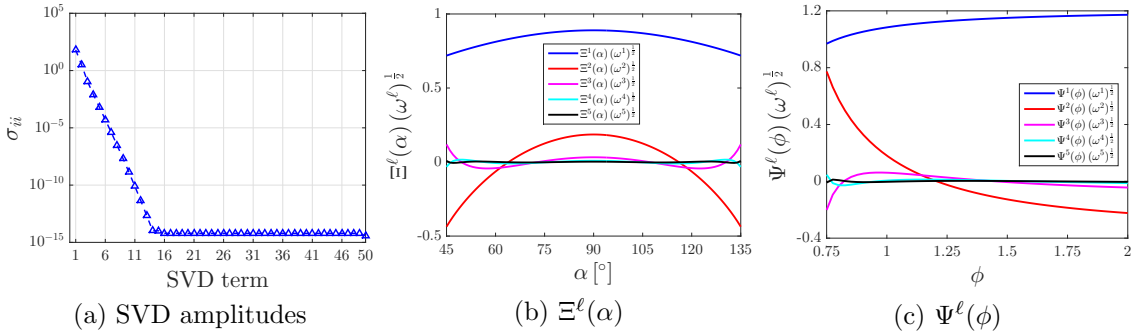


Figure D.3: SVD evolution of modal amplitudes and parametric functions, these latter shown for $\ell = 1, \dots, \mathbf{n}_{\text{svd}} = 5$.

In addition, Figure D.4a plots function $f(\alpha, \phi)$ in the domain $I_3 \times I_4$, and the relative error committed by the SVD approximation with $\mathbf{n}_{\text{svd}} = 5$ (Figure D.4b). The maximum relative error reported is $1.92e^{-5}$, located at points nearby $(\alpha = 90^\circ \pm 45^\circ, \phi = 0.75)$, Figure D.4b bottom left/right corners. Measuring instead the relative error in an average sense of the whole domain, we recover $5.43e^{-7}$.

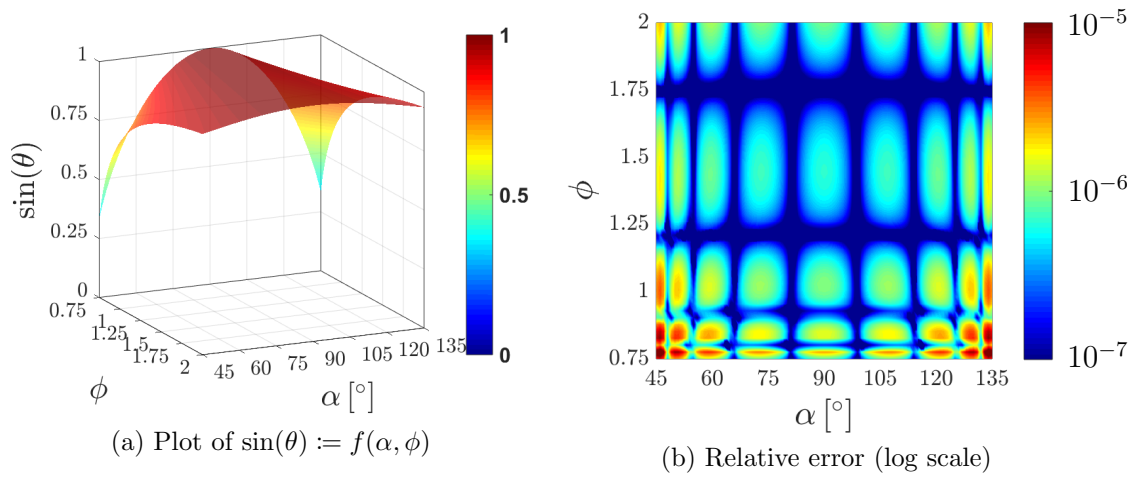


Figure D.4: Plot of the function $f(\alpha, \phi)$ and relative error of an approximation with $n_{\text{svd}} = 5$ SVD terms.

Appendix E

Explicit parametric functions for the scaffold unit-cell problem using homogenization

We present in the following, the normalized functions \tilde{G}_i^m - being $i = 1, \dots, n_p = 5$ - that supply the parametric behavior of the PGD spatial modes introduced in Figures 5.11 and 5.12. These are shown for the six different load cases - in Figures E.1, E.2, E.3, E.4, E.5 and E.6 for cases XX , YY , ZZ , XY , XZ and YZ respectively - of the scaffold unit-cell problem with homogenization. In order to visualize the PGD mode importance, each normalized parametric function \tilde{G}_i^m is weighted by $(\beta^m)^{\frac{1}{n_p}}$, being β^m the amplitude of mode m and $n_p = 5$ the number of parameters.

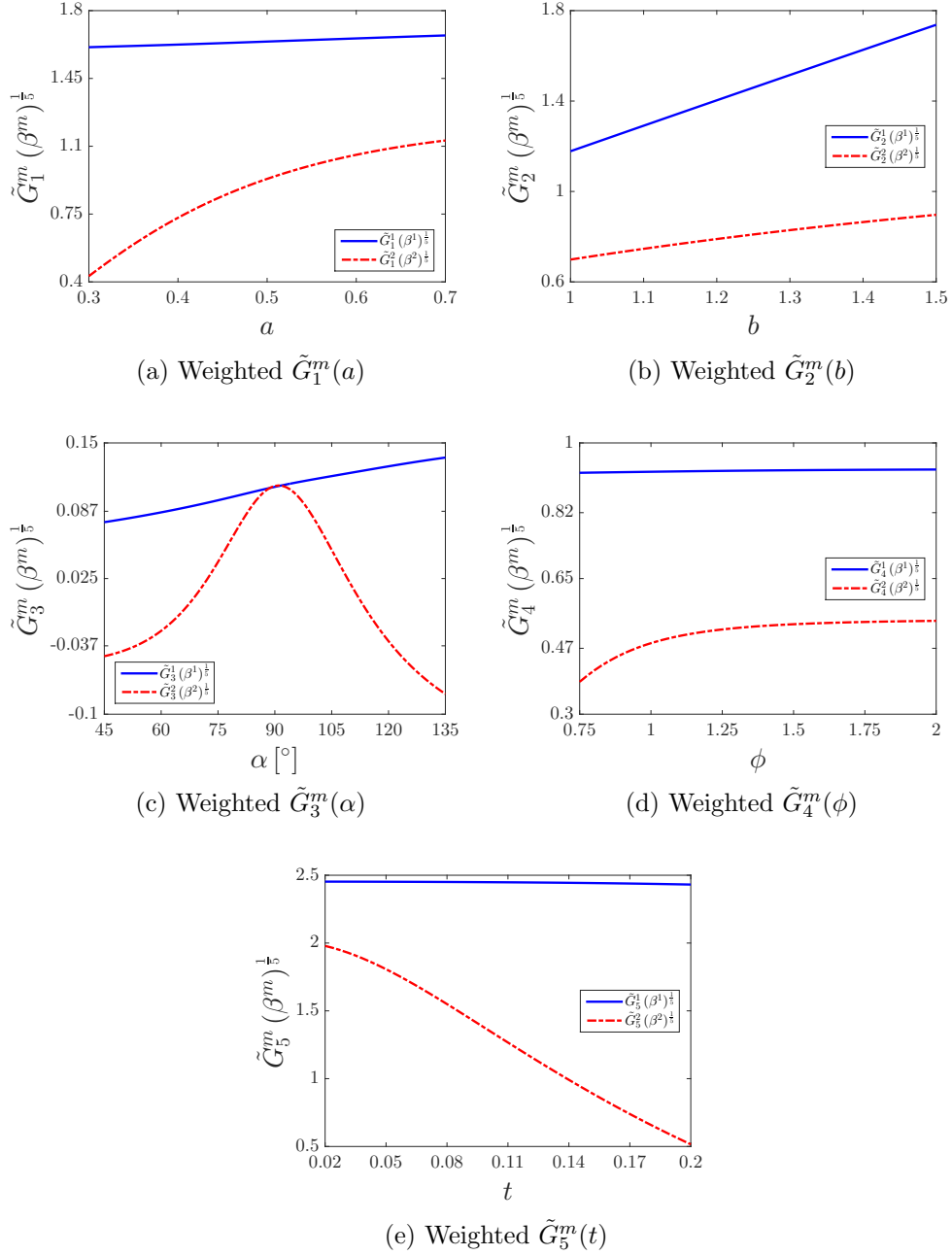


Figure E.1: Scaffold unit-cell load case XX with PGD compression. Normalized parametric functions weighted for illustration.

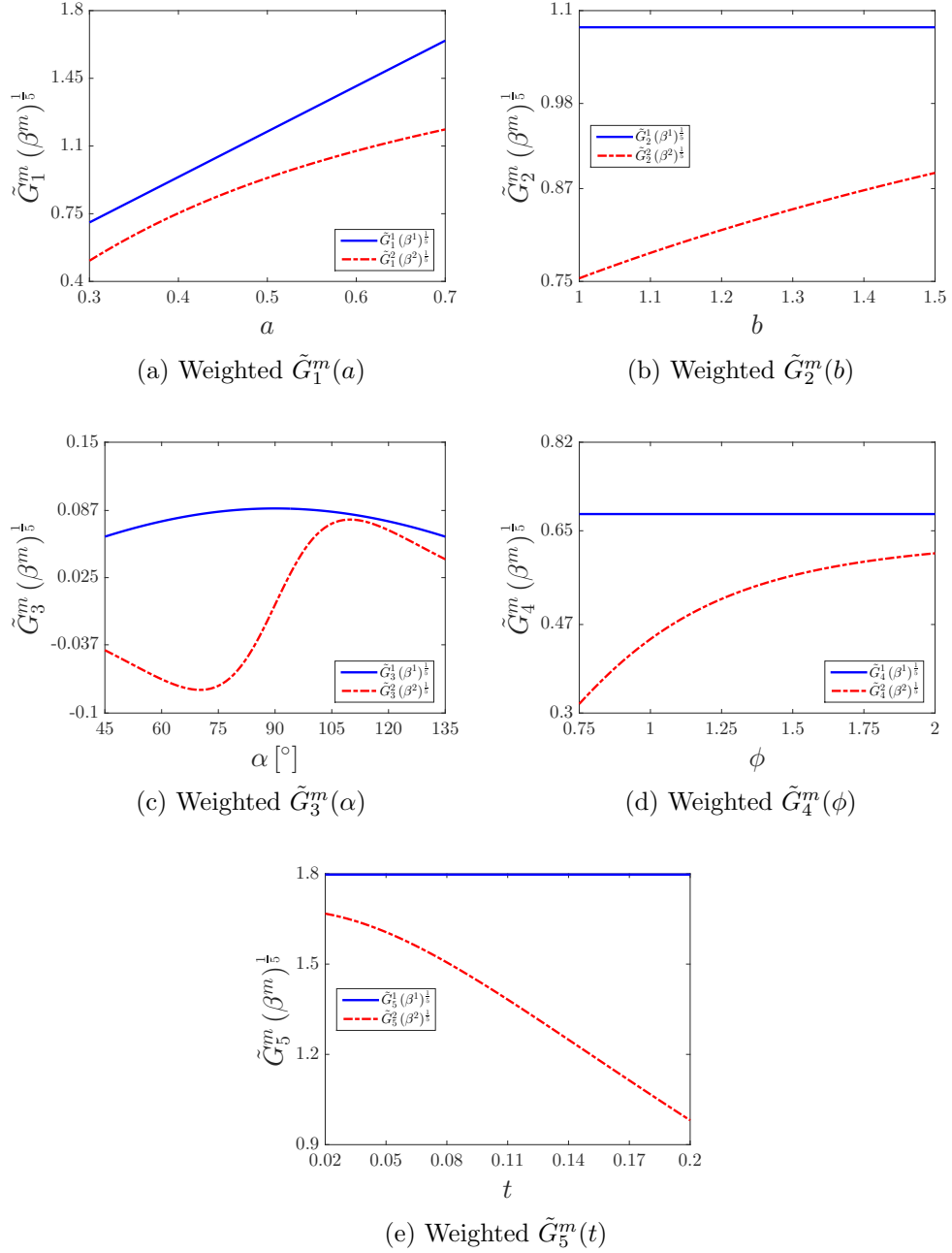


Figure E.2: Scaffold unit-cell load case YY with PGD compression. Normalized parametric functions weighted for illustration.

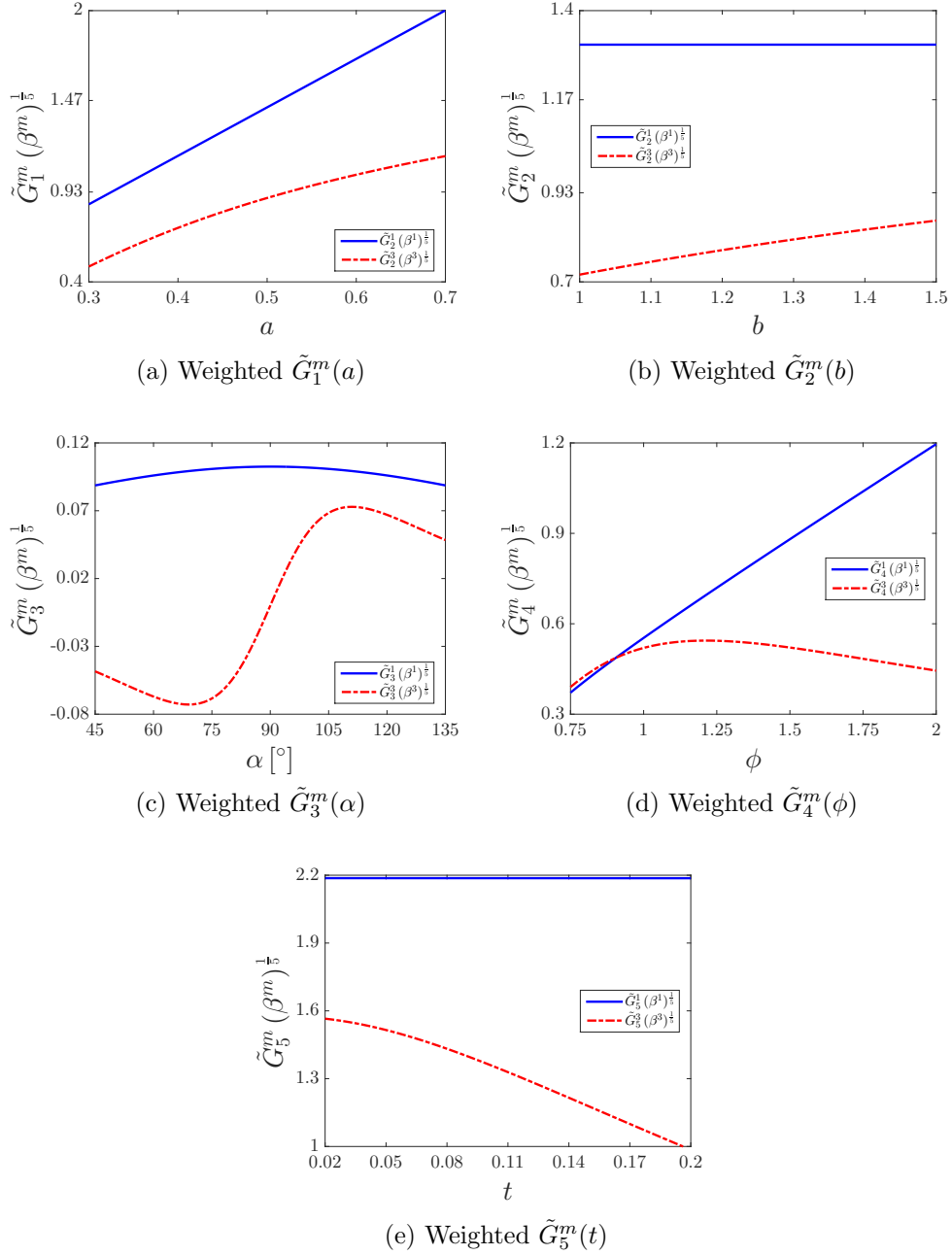


Figure E.3: Scaffold unit-cell load case ZZ with PGD compression. Normalized parametric functions weighted for illustration.

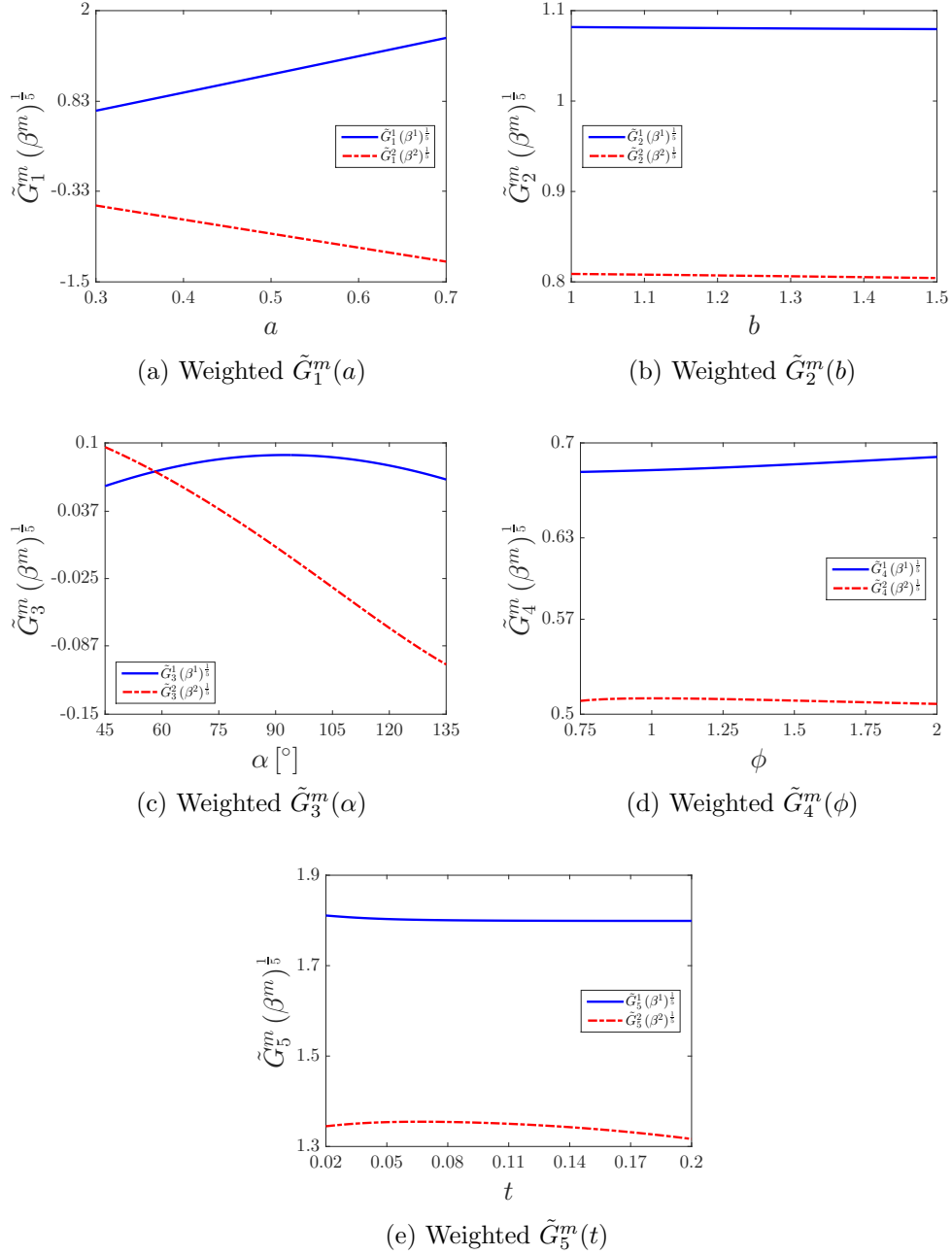


Figure E.4: Scaffold unit-cell load case XY with PGD compression. Normalized parametric functions weighted for illustration.

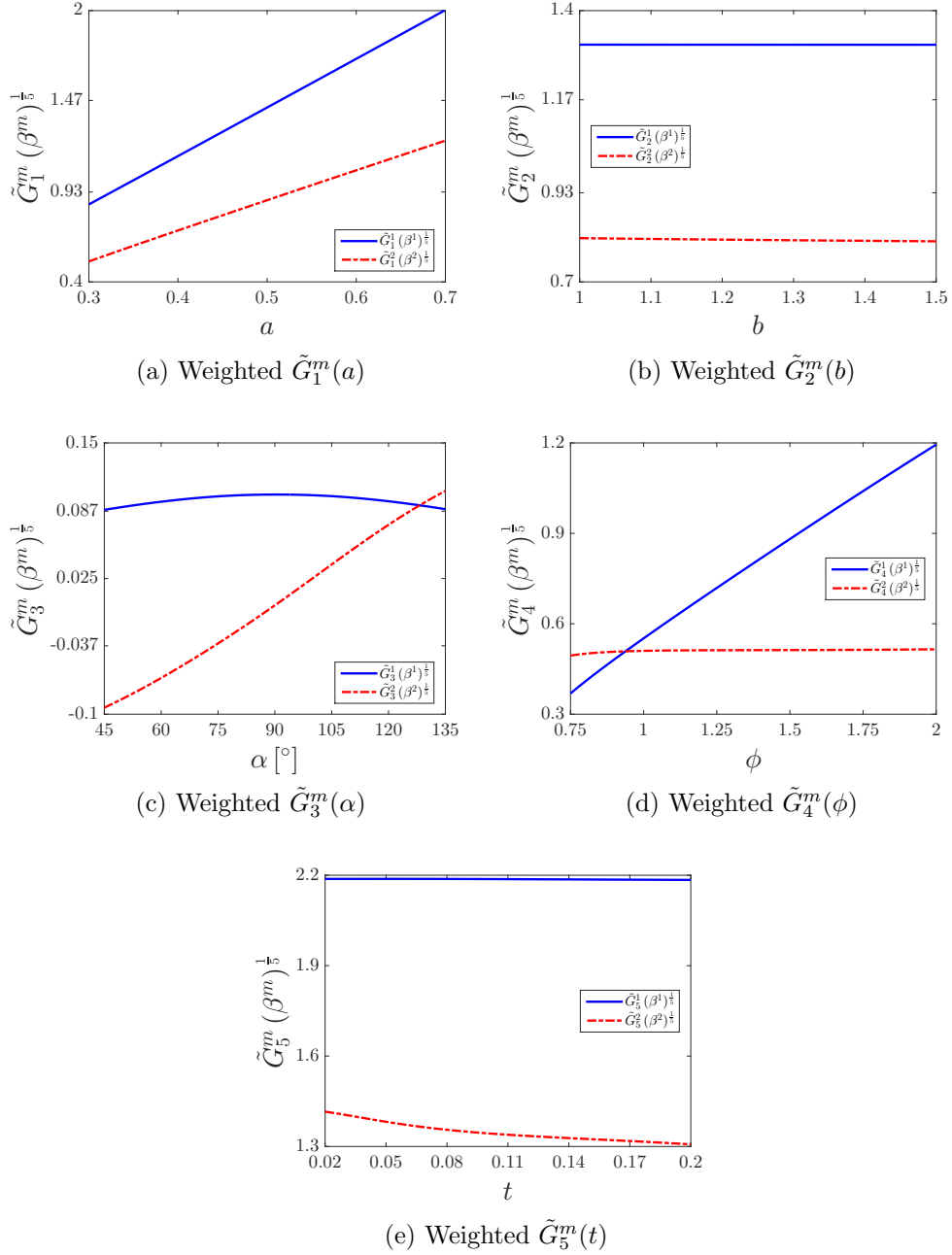


Figure E.5: Scaffold unit-cell load case XZ with PGD compression. Normalized parametric functions weighted for illustration.

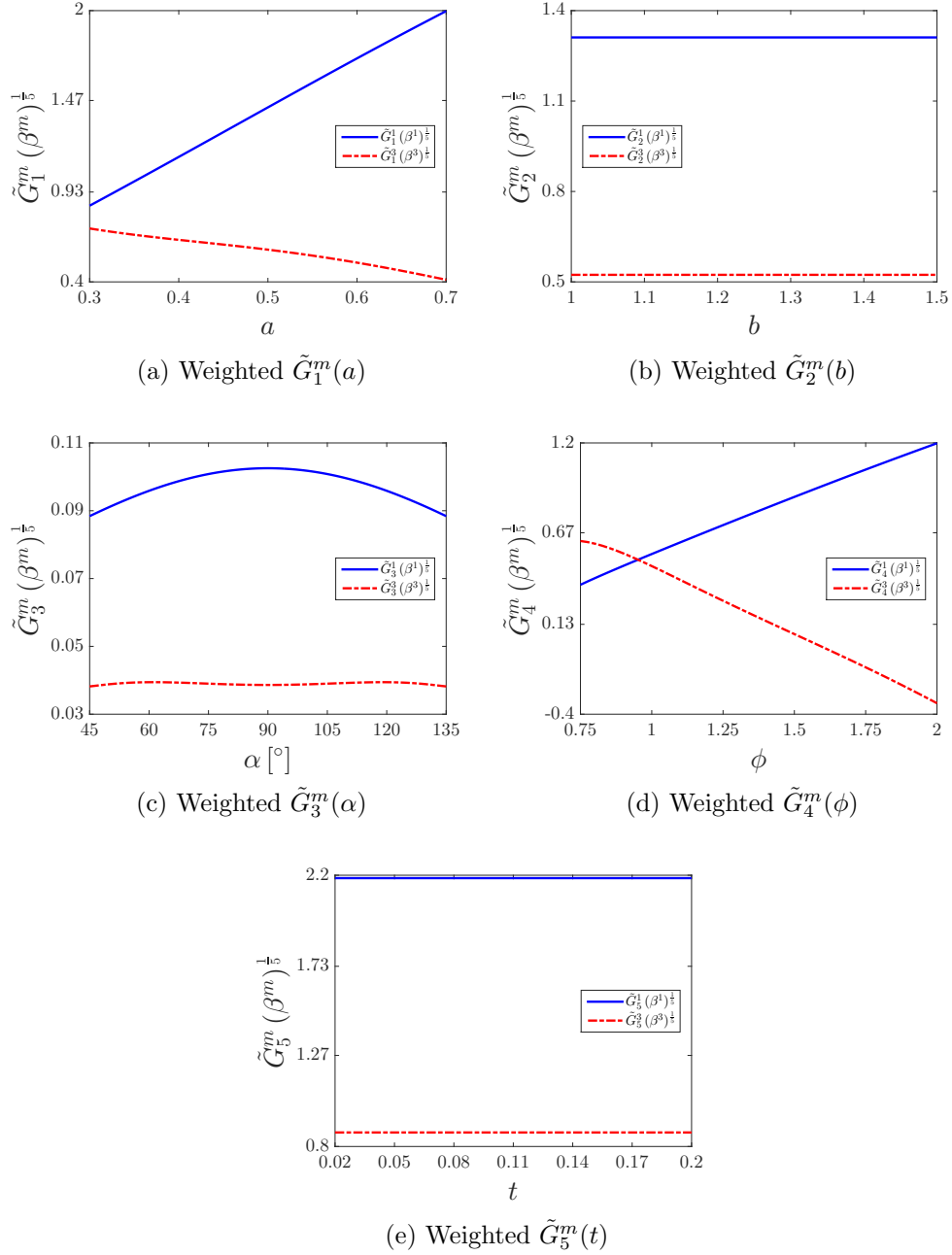


Figure E.6: Scaffold unit-cell load case YZ with PGD compression. Normalized parametric functions weighted for illustration.

